Exciton Transport in Organic Semiconductors

A Dissertation
SUBMITTED TO THE FACULTY OF THE
UNIVERSITY OF MINNESOTA
BY

Stephen Matthew Menke

IN PARTIAL FULFILLMENT OF THE REQUIREMENTS
FOR THE DEGREE OF
DOCTOR OF PHILOSOPHY

Russell J. Holmes, Advisor

June, 2015

Acknowledgements

Funding for this work was provided by a University of Minnesota Doctoral Dissertation Fellowship, the National Science Foundation, University of Minnesota NSF Materials Research Science and Engineering Center, University of Minnesota Initiative for Renewable Energy and the Environment, and Raytheon Vision Systems. Material was partially provided by Sigma-Aldrich New Products R&D.

I would like to acknowledge Professor Russell J. Holmes for his mentorship and steadfast support. I would like to acknowledge Professor David A. Blank for his insight and helpful discussions. I would like to acknowledge all the members, past and present, of the Holmes and Frisbie research groups for engaging dialogue and coffee runs. I would like to especially acknowledge Christopher D. Lindsay, an undergraduate student in Materials Science and Engineering at the University of Minnesota, for his assistance with experiments.

—On a personal note, I am indebted to my wife, Julie, for
her constant love, friendship, and encouragement.

—*I dedicate this dissertation to my Family.*

Abstract

Photovoltaic cells based on organic semiconductors are attractive for their use as a renewable energy source owing to their abundant feedstock and compatibility with low-cost coating techniques on flexible substrates. In contrast to photovoltaic cells based traditional inorganic semiconductors, photon absorption in an organic semiconductor results in the formation of a coulombically bound electron-hole pair, or exciton. The transport of excitons, consequently, is of critical importance as excitons mediate the interaction between charge and light in organic photovoltaic cells (OPVs).

In this dissertation, a strong connection between the fundamental photophysical parameters that control nanoscopic exciton energy transfer and the mesoscopic exciton transport is established. With this connection in place, strategies for enhancing the typically short length scale for exciton diffusion (L_D) can be developed. Dilution of the organic semiconductor boron subphthalocyanine chloride (SubPc) is found to increase the L_D for SubPc by 50%. In turn, OPVs based on dilute layers of SubPc exhibit a 30% enhancement in power conversion efficiency. The enhancement in power conversion efficiency is realized via enhancements in L_D, optimized optical spacing, and directed exciton transport at an exciton permeable interface.

The role of spin, energetic disorder, and thermal activation on L_D are also addressed. Organic semiconductors that exhibit thermally activated delayed fluorescence and efficient intersystem and reverse intersystem crossing highlight the balance between singlet and triplet exciton energy transfer and diffusion. Temperature dependent measurements for L_D provide insight into the inhomogeneously broadened exciton density of states and the thermal nature of exciton energy transfer. Additional topics include energy-cascade OPV architectures and broadband, spectrally tunable photodetectors based on organic semiconductors.

Table of Contents

List of Tables

List of Figures

1. Renewable energy and photovoltaics

The search for renewable sources of energy needs little justification. As the demand for energy increases and the supply of fossil-fuel based energy sources dwindle, the global energy market is on the verge of a historic transformation. Many sources of renewable energy exist, including solar, wind, and hydroelectric power among others. While a global energy solution will likely include a suite of these technologies, they are all driven by the sun. As the most direct means for conversion, photovoltaic devices, or solar cells, directly convert solar radiation into electrical power. This chapter will begin by briefly introducing the basic concepts of solar energy harvesting and conclude by reviewing traditional and emerging photovoltaic materials and technologies.

1.1. Harvesting solar radiation

As the largest source of energy in our solar system, the sun emits radiation across a broad range of the electromagnetic spectrum. The bulk of the radiation that strikes the earth has a photon wavelength (λ) from λ=(10^{-7}–10^{-3}) m. The highest energy of these photons (λ=10^{-7}–10^{-6}) m represent light suitable for energy harvesting. Figure 1.1 shows the spectrum of solar radiation for this wavelength range. Owing to absorption in the

Earth's atmosphere, only a fraction of solar radiation reaches the surface. Figure 1.1 also shows a standard solar radiation spectrum for an absolute air mass of 1.5 at a global 37° south facing tilt (AM1.5G).

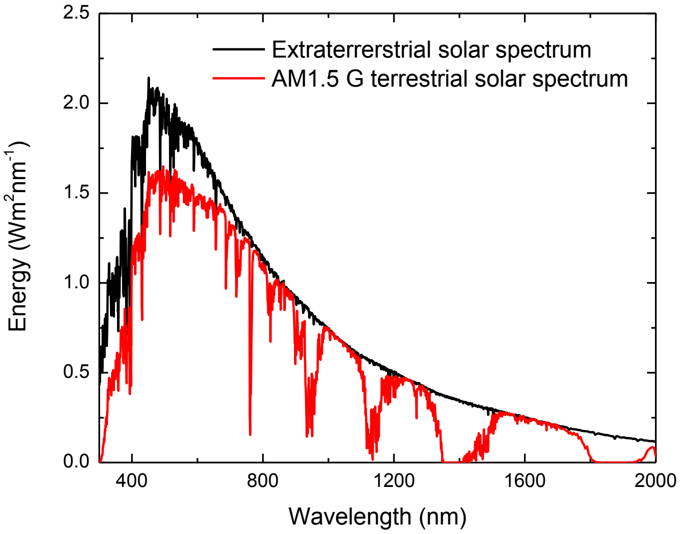

Figure 1.1. Extraterrestrial and terrestrial solar radiation spectra highlighting the effect of atmospheric absorption on the available light solar energy conversion.

To harvest this solar energy, photovoltaic devices must absorb in the solar spectrum. Semiconducting materials with energy gaps (E_g) between E_g=0.5–2.5 eV are well suited for this application [1]. Semiconducting materials also can be made to have very large charge mobility and conductivity, thereby allowing for efficient charge carrier movement and increased device efficiency [2]. In a photovoltaic device incorporating a single semiconductor material, or junction, the theoretical efficiency is limited by the E_g. Absorbed photons with energy greater than the band gap will quickly thermalize with the energy difference being lost to heat. Described by Shockley and Queisser, the theoretical maximum efficiency for a single junction device is 33.7% [3]. At this efficiency, a 10^4 mi^2 plot of land in the American southwest could meet the *entire* annual energy demand of the United States. While impractical for a multitude of reasons, including inefficient electrical storage and difficulty in transmission, this example highlights the potential importance of continually improving photovoltaic device efficiency.

1.2. Traditional photovoltaic technologies

Sometimes categorized as first and second generation photovoltaics, traditional photovoltaic technologies are based on the well-established understanding and characterization of inorganic semiconductor heterojunctions [4]. The first generation of photovoltaic devices is based on silicon wafers [5]. As this technology has matured, record device efficiencies have plateaued and the price per unit Watt of power produced is chiefly dictated by the cost of the starting materials, namely the single and polycrystalline silicon, toughened low-iron glass cover sheets, and required encapsulants [6]. Nonetheless, the optimized, high volume production of modules based on crystalline silicon has enabled widespread implementation and accounts for the strong majority of installed photovoltaic power in the United States and the world.

Currently, however, the photovoltaic industry is on the verge of entering a second generation [7]. Inspired by advancements in thin-film semiconductor processing, second generation photovoltaic technologies currently operate at slightly reduced device efficiencies with a reduced materials cost, reducing the overall price per unit Watt of power produced. This basic relationship is captured in Figure 1.2 which demonstrates the efficiency-cost tradeoff for first and second generation photovoltaic technologies [8]. To continue driving down the price per unit Watt of power produced, increases in efficiency or further reductions in cost are required.

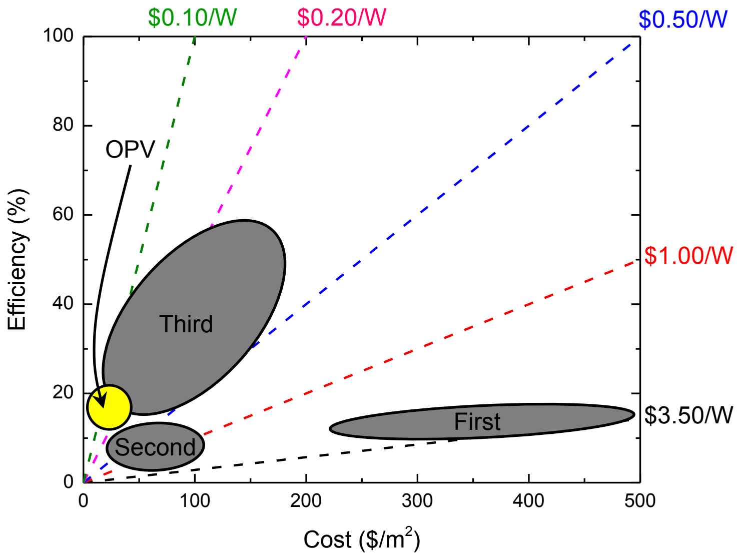

Figure 1.2. Efficiency-cost tradeoff for the three generations of photovoltaic technology as well as the position for organic photovoltaic devices (OPVs) based on organic semiconductors described in Sec. 1.3.

1.3. Emerging photovoltaic technologies

In order to meet these demands, third generation photovoltaic technologies are being extensively investigated on the laboratory scale [6,9]. Broadly categorized, third generation technologies incorporate advanced device architectures to exceed the Shockley-Queisser limit and typically incorporate rapidly developing, new classes of materials including, for example, graphene and quantum dots. A subset of third generation photovoltaic technologies incorporates organic semiconductors [10–12]. Organic photovoltaic devices (OPVs) have the potential to be fabricated at low-cost on flexible substrates owing to their compatibility with rapid-throughput, room temperature manufacturing technologies [13]. Furthermore, the photoactive materials can be synthesized from non-toxic, abundant feedstock similar to many current specialty chemicals [14]. While current state-of-the-art OPV device efficiencies lag with regard to first and second generation photovoltaic technologies, improvements in efficiency stand to significantly impact the competitiveness of OPVs, motivating the immense research effort in the scientific community.

This dissertation begins by introducing the fundamental physics associated with organic semiconductors and the operation of an OPV. This discussion will highlight a specific limitation of OPVs, namely the consequences of spatially localized excited states intrinsic to this family of materials. The remainder of the dissertation focuses on specific studies in the characterization and development of methodologies to overcome this constraint with the overall goal of leveraging an improved fundamental understanding of organic semiconductor physics to enhance the power conversion efficiency of OPV devices.

2. The physics of organic semiconductors

This chapter will serve to introduce the basic physical processes inherent to organic semiconductors as relevant to the study of organic photovoltaic devices (OPVs). A foundational knowledge of these processes will be critical in the forthcoming chapters in order to fully characterize material systems under investigation. Interestingly, many of the properties and processes intrinsic to organic semiconductors have inorganic parallels. These parallels will be discussed briefly, but the reader is encouraged to reference *Principles of Electronic Materials and Devices* by Kasap and *Solid State Physics* by Ashcroft and Mermin for a complete description of inorganic electronic material properties and processes.

2.1. Light-matter interactions

An organic semiconductor is characterized by the large degree of conjugated bonds within the molecule [15]. Weak intermolecular bonding is dominated by van der Waals interactions. For carbon containing molecules, such as anthracene, sp^2 orbital hybridization occurs between the carbon atoms where the remaining p_z orbitals are free to form π-bonds (Figure 2.1) [16]. The delocalized electron density associated with these π-bonds lies above and below the plane of the anthracene rings. Electrons that reside in these delocalized orbitals have quantized energy levels in analogy with solutions to the Schrödinger equation for electron(s) within a potential well. Unlike traditional inorganic semiconductors, however, the electrons in organic molecular solids are typically localized to individual molecules or conjugation centers [16]. This precludes the formation of a valence or conduction band. The organic semiconductor analog to the valence band is described as the highest occupied molecular orbital (HOMO). The difference between the HOMO and the lowest unoccupied molecular orbital (LUMO) for organic semiconductors is typically in the range of 0.5–3 eV, making these solids a promising material for near-UV, visible, and near-IR optoelectronic applications [17].

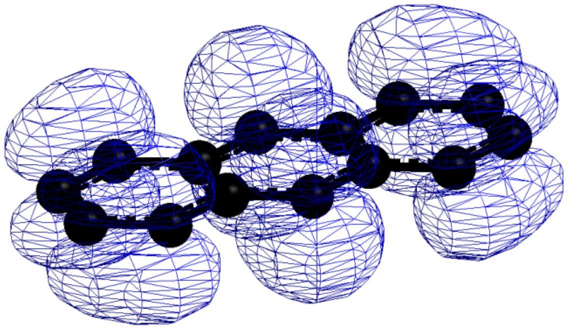

Figure 2.1 Chemical structure of the archetypical organic semiconductor anthracene where the outermost, bonding electron orbitals (HOMO) are shown residing above and below the molecular plane.

For each energetic state in which the molecule can reside there are vibrational and rotational sub-levels [15]. While electronic transitions are usually in the near-UV to near-IR regions of the electromagnetic spectrum, vibrational transitions are much smaller with energies of ~10^{-1} eV while rotational transitions are even smaller with energies of ~10^{-3} eV. In the solid state, rotational transitions are typically suppressed. The combinations of electronic and vibronic transitions play an important role in determining the spectral nature of absorption and emission in organic semiconductor materials.

2.1.1. Absorption and luminescence

Absorption of a photon in an organic semiconductor leads to the promotion of an electron from the HOMO to the LUMO. Under the Born-Oppenheimer approximation, nuclear motion is assumed to be much slower than the movement of electrons [18]. Such an approximation is valid in these systems because the nuclear mass is much larger than the mass of an electron. In this way, electrons are treated as reacting instantly to changes in nuclear arrangement, allowing for the calculation of molecular energy states as a function of nuclear position.

In the case of weakly coupled states, the strength of the absorption, or more precisely the rate, can be easily understood by examining Fermi's golden rule [15]:

Eq. 2.1 $$k = \frac{2\pi\rho}{\hbar} |< \Psi_2 | P_{1\rightarrow 2} | \Psi_1 >|$$

where Ψ_1 and Ψ_2 are the wavefunctions of the initial and final state, $P_{1\rightarrow 2}$ is the perturbation acting on Ψ_1, and ρ is the density of states of Ψ_2 that are of the same energy as Ψ_1. Consequently, Fermi's golden rule provides a platform for accessing the relative rates for weak interactions; if the matrix element in Eq. 2.1 is zero the transition is defined as forbidden.

For organic molecules, the most important perturbation acting on the molecular wavefunctions is vibronic nuclear motion [19]. This motion corresponds to the orbital motion of electrons and plays a deterministic role on the spectral nature of an organic molecule's absorption spectrum. To understand this effect more clearly, Eq. 2.1 can be separated to reflect the vibrational coupling and the vibrational overlap, sometimes referred to as the Franck-Condon (FC) factor [15,19].

Eq. 2.2 $$k = \left[\frac{k_{max}^{0} |<\Psi_2 | P_{vib} | \Psi_1 >|}{\Delta E_{12}^{2}}\right] \times |\chi_2 | \chi_1|$$

The first part of the equation represents the vibrational coupling and is determined from the vibronic coupling matrix element (P_{vib}) where k_{max}^{0} is the zero-point-motion-limited rate constant and ΔE_{12} is the separation in energy between the two states. The second part of the equation, then, only refers to the vibrational wavefunction overlap between the two states. When the initial and final states are similar, the transition will occur faster. Figure 2.2 visualizes this overlap and schematically demonstrates the effect on the absorption spectrum for an exemplary organic molecule. Here, the ground and first excited state wavefunctions are represented along the nuclear coordinate. In this schematic potential well, the first few vibronic energy levels within each state are shown. Absorption of a photon is assumed to occur from the lowest energy vibronic of Ψ_1 since it is the most populated ground state level. In this schematic, a large FC factor is achieved for the 0-3 transition. Transitions to the lower vibronic energy levels of Ψ_2 are progressively weaker. A possible resulting absorption spectrum accounting for only FC overlap shows how these changes in overlap can manifest in vibronic progressions with variable intensities.

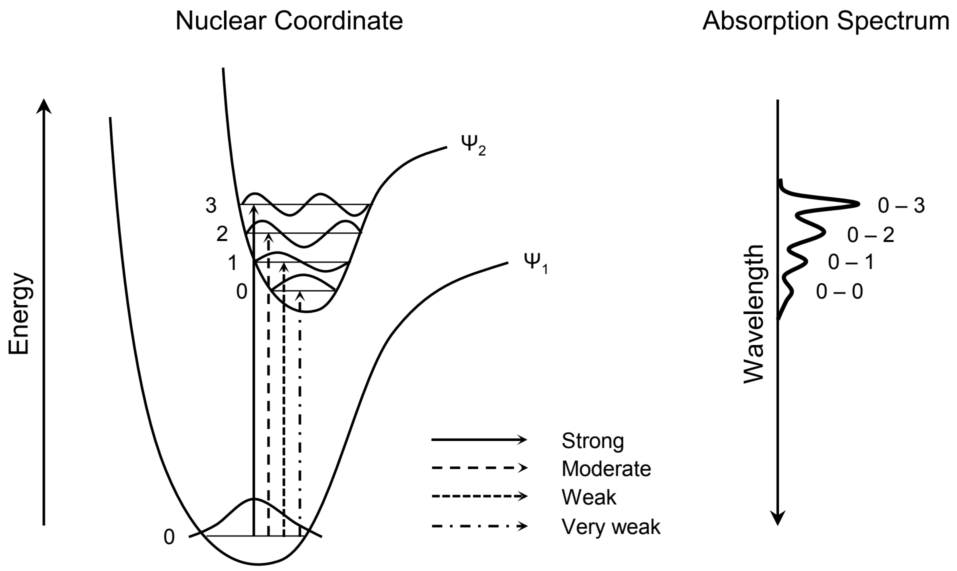

Figure 2.2 Nuclear coordinate and possible absorption spectrum for a prototypical organic molecule where the overlap in vibronic wavefunctions dictates the strength and spectral nature of absorption.

After absorption, the molecule now contains an excited electron in the LUMO and an electron vacancy, or hole, in the HOMO. Owing to the large dielectric constants representative of organic molecules, the photogenerated electron and hole will experience a large Coulombic attraction, leading to binding energies (E_B) of E_B~0.5–1.5 eV [20]. This correlated electron-hole quasiparticle is defined as an exciton, the dynamics of which will be discussed later in this chapter. Additionally, nuclear rearrangement occurs after the initial formation of the excited state, minimizing energy and shifting the excited state nuclear coordinate. Importantly, the optical energy gap (E_g) is defined as the HOMO-LUMO difference minus the E_B. Spectraphotometry used to characterize the absorption spectra will result in a measurement for the optical E_g whereas photoelectron spectroscopy to characterize the molecular density of states will result in a measurement for the true E_g (i.e. HOMO-LUMO difference) [21].

The same principles for absorption apply to luminescence. The key difference being, however, the important vibrational overlap is now between the lowest energy vibronic of Ψ_2 and the various vibronic energy levels of Ψ_1. According to Kasha's rule, electrons in higher energy vibronics of Ψ_2 will quickly relax to the lowest energy vibronic energy level on a timescale much shorter than the exciton lifetime ($\sim 10^{-15}$–10^{-12} s) [22]. In this way, luminescence will typically occur at a lower energy than absorption for a given transition. This shift in energy is defined as the Franck-Condon shift. This behavior is depicted schematically in Figure 2.3.

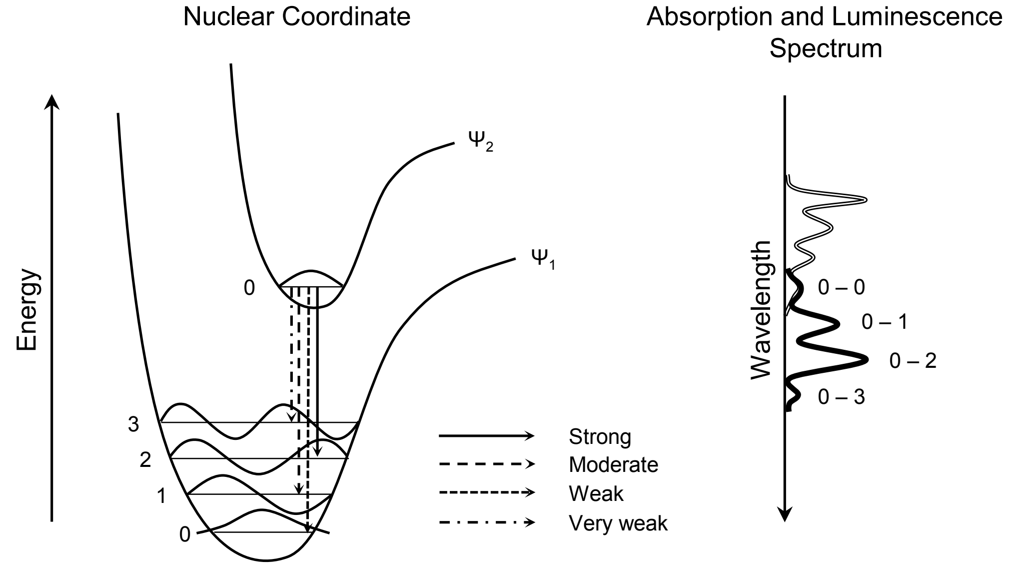

Figure 2.3 Nuclear coordinate, possible absorption spectrum, and possible luminescence spectrum for a prototypical organic molecule where, as with absorption, the vibronic wavefunction overlap after nuclear rearrangement dictates the spectral nature of luminescence.

2.1.2. Exciton spin

Another important aspect of an exciton is the spin state. Each electron in the molecule has spin angular momentum [1]. According to the Pauli Exclusion Principle, electrons occupying the same orbital must have opposite spin quantum numbers (+½ or -½). When an exciton is formed via the absorption of a photon, a particle that carries zero spin angular momentum, the promoted electron in the LUMO and the remaining electron in the HOMO retain their original, opposite spins. These spins are out of phase and exactly cancel with each other giving the photogenerated exciton a total spin state of zero [15]. This type of exciton is defined as a singlet exciton. If the exciton is formed from the collision of an uncorrelated electron and hole, each fermion has a random spin state [23]. The resulting exciton spin state will be either zero or one. An exciton spin of one is achieved when the constituent spins are in phase, and is termed a triplet exciton owing to the triple degeneracy of the spin state. To visualize this effect, Figure 2.4 shows the four possible spin configurations for a pair of electrons. Also shown are the total spin (S) and the spin quantum number (M_S).

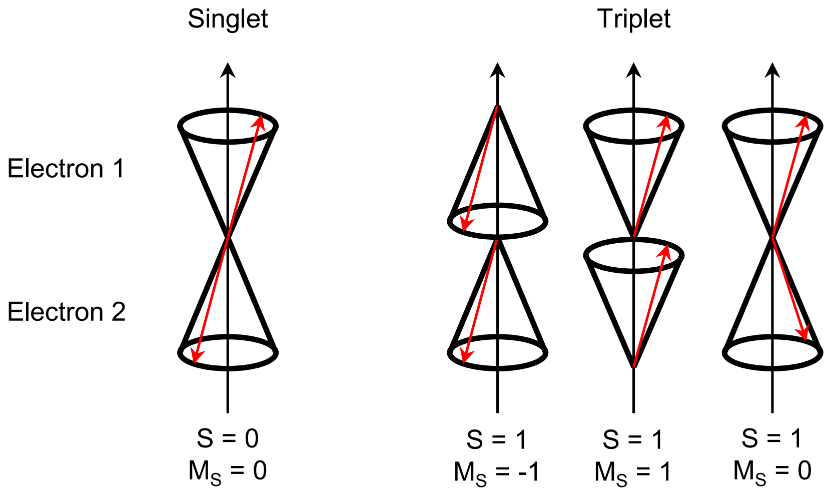

Figure 2.4 Vector representation of singlet and triplet spin states for molecular excitons. For a singlet, the two electron spins are exactly out of phase, resulting in S=0. For triplets, the two electron spins do not cancel, thus S=1.

Triplet excitons are unique because their non-zero spin state makes difficult transitions between the excited and ground states of the molecule [15]. In theory, triplet excited states do not radiatively couple to the singlet ground state because the photon cannot introduce or dissipate any spin angular momentum required for the conservation of spin angular momentum. In practice, however, weak, radiative coupling of the triplet excited state with the ground state is possible in the presence of spin-orbit coupling [15,24]. Spin-orbit coupling is an important interaction that couples two spin states, providing a means of conserving the total angular momentum of the system by coupling the electron spin angular momentum with the orbital angular momentum. The spin-orbit matrix operator for an electron in an atom is [15]:

Eq. 2.3
$$P_{SO} = \frac{Zke^2}{2m^2c^2}\frac{1}{r^3}\boldsymbol{L}\cdot\boldsymbol{S}$$

where Z mass number of the nucleus, k is the Coulomb constant, e is the charge of an electron, m is the mass of an electron, c is the speed of light, r is the radius of the electron-orbit, and **L·S** is the dot product of the orbital angular and spin angular momentum, respectively. Two important parts of this equation should be recognized. First, **L·S** results in the mixing of the singlet and triplet states. Second, the operator is directly proportional to Z. Hence, a larger atom will allow for more effective spin-orbit coupling. While this situation is more complex for a multi-atom molecule, these same principles apply. The total rate equation for absorption and luminescence from the triplet state follows neatly from Eq. 2.2 as [15]:

Eq. 2.4
$$k = \left[\frac{k_{max}^{0}|<\Psi_2|P_{vib}|\Psi_1>|}{\Delta E_{12}^{2}}\right] \times |\chi_2|\chi_1| \times |<\Psi_2|P_{so}|\Psi_1>|$$

2.1.3. Intersystem crossing

In the same way that spin-orbit coupling allows for a spin flip during radiative triplet decay, it can also enable the conversion of a singlet exciton to a triplet exciton. This process is called intersystem crossing. The conversion of a triplet exciton to a singlet exciton is adeptly called reverse intersystem crossing. Inspection of the spin-orbit coupling operator lends intuition.

For a two electron system, each with spin-$\frac{1}{2}$, the **L·S** component of the spin-orbit operator can be written as:

Eq. 2.5 $$P_{SO} \propto \boldsymbol{l_1} \cdot \boldsymbol{s_1} + \boldsymbol{l_2} \cdot \boldsymbol{s_2}$$

This equation can be rearranged by separating the orbital and angular momenta as:

Eq. 2.6 $$P_{SO} \propto \frac{1}{2}(\boldsymbol{l_1} + \boldsymbol{l_2}) \cdot (\boldsymbol{s_1} + \boldsymbol{s_2}) + \frac{1}{2}(\boldsymbol{l_1} - \boldsymbol{l_2}) \cdot (\boldsymbol{s_1} - \boldsymbol{s_2})$$

Here, both $\mathbf{s_1}$ and $\mathbf{s_2}$ have x-, y-, and z-components. Commutation with the total spin operator (S^2) will identify which of these spin operators, ($\mathbf{s_1}$+$\mathbf{s_2}$) or ($\mathbf{s_1}$–$\mathbf{s_2}$), can affect the spin component of the wavefunction. For example, ($s_{1,z}$+$s_{2,z}$) commutes with S^2 as:

Eq. 2.7 $$\left[(s_{1,z} + s_{2,z}), S^2\right] = (s_{1,z} + s_{2,z}) \cdot S^2 |\psi_S\rangle$$
$$-S^2 \cdot (s_{1,z} + s_{2,z}) |\psi_S\rangle = 0$$

When two operators commute, the order in which the operators act upon the same eigenstate is independent of the result, and both orders will return the same eigenvalue. Since S^2 will return the total spin of the system and not change the spin component of the wavefunction, so too must ($s_{1,z}$+$s_{2,z}$). Thus, if ($s_{1,z}$+$s_{2,z}$) commutes with S^2, it cannot mix states with different multiplicity.

In contrast, ($s_{1,z}$–$s_{2,z}$) does not commute with S^2. To confirm that this operator can change the multiplicity of a spin eigenstate (i.e. convert between singlet and triplet), one can operate ($s_{1,z}$–$s_{2,z}$) on a singlet eigenstate for a simple, two electron system. In doing this, however, care must be taken with the notation. While S^2 operates on the composite spin eigenstate, $s_{1,z}$ and $s_{2,z}$ operate on each electron's spin eigenstate. Tensor notation can be used to provide consistency.

For the two spin-$\frac{1}{2}$ particles, the four unique, composite eigenstates are:

Eq. 2.8
$$|\tfrac{1}{2}\tfrac{1}{2}\rangle\otimes|\tfrac{1}{2}\tfrac{1}{2}\rangle=\begin{pmatrix}1\begin{pmatrix}1\\0\end{pmatrix}\\0\begin{pmatrix}1\\0\end{pmatrix}\end{pmatrix}=\begin{pmatrix}1\\0\\0\\0\end{pmatrix}$$

Eq. 2.9
$$|\tfrac{1}{2}\tfrac{1}{2}\rangle\otimes|\tfrac{1}{2}\ -\tfrac{1}{2}\rangle=\begin{pmatrix}1\begin{pmatrix}0\\1\end{pmatrix}\\0\begin{pmatrix}0\\1\end{pmatrix}\end{pmatrix}=\begin{pmatrix}0\\1\\0\\0\end{pmatrix}$$

Eq. 2.10
$$|\tfrac{1}{2}\ -\tfrac{1}{2}\rangle\otimes|\tfrac{1}{2}\tfrac{1}{2}\rangle=\begin{pmatrix}0\begin{pmatrix}1\\0\end{pmatrix}\\1\begin{pmatrix}1\\0\end{pmatrix}\end{pmatrix}=\begin{pmatrix}0\\0\\1\\0\end{pmatrix}$$

Eq. 2.11
$$|\tfrac{1}{2}\ -\tfrac{1}{2}\rangle\otimes|\tfrac{1}{2}\ -\tfrac{1}{2}\rangle=\begin{pmatrix}0\begin{pmatrix}0\\1\end{pmatrix}\\1\begin{pmatrix}0\\1\end{pmatrix}\end{pmatrix}=\begin{pmatrix}0\\0\\0\\1\end{pmatrix}$$

Similarly, the operators for $(s_{z,1}-s_{z,2})$ and S^2 can be written as:

Eq. 2.12
$$s_{z,1}-s_{z,2}=S_z\otimes\mathbb{1}-\mathbb{1}\otimes S_z=\frac{\hbar}{2}\begin{pmatrix}0&0&0&0\\0&2&0&0\\0&0&-2&0\\0&0&0&0\end{pmatrix}$$

Eq. 2.13
$$S^2=\left(S_{x,total}\right)^2+\left(S_{y,total}\right)^2+\left(S_{z,total}\right)^2=(S^2\otimes\mathbb{1})+$$
$$(\mathbb{1}\otimes S^2)+2\left(S_x\otimes S_x+S_y\otimes S_y+S_z\otimes S_z\right)=\hbar^2\begin{pmatrix}2&0&0&0\\0&1&1&0\\0&1&1&0\\0&0&0&2\end{pmatrix}$$

where:

Eq. 2.14
$$S^2=\frac{3}{4}\hbar^2\begin{pmatrix}1&0\\0&1\end{pmatrix}$$

Eq. 2.15
$$S_x=\frac{\hbar}{2}\begin{pmatrix}0&1\\1&0\end{pmatrix}$$

Eq. 2.16
$$S_y=\frac{\hbar}{2}\begin{pmatrix}0&-i\\i&0\end{pmatrix}$$

Eq. 2.17 $$S_z = \frac{\hbar}{2}\begin{pmatrix} 1 & 0 \\ 0 & -1 \end{pmatrix}$$

A singlet eigenstate will be a linear difference of Eq. 2.9 and Eq. 2.10. It can therefore be shown that a singlet eigenstate can be transformed into a triplet eigenstate (a linear sum of Eq. 2.9 and Eq. 2.10) with the ($s_{1,z}$–$s_{2,z}$) operator as:

Eq. 2.18 $$\frac{\hbar}{2}\begin{pmatrix} 0 & 0 & 0 & 0 \\ 0 & 2 & 0 & 0 \\ 0 & 0 & -2 & 0 \\ 0 & 0 & 0 & 0 \end{pmatrix}\left| \frac{1}{\sqrt{2}}\begin{pmatrix} 0 \\ 1 \\ -1 \\ 0 \end{pmatrix}\right\rangle = \frac{\hbar}{\sqrt{2}}\begin{pmatrix} 0 \\ 1 \\ 1 \\ 0 \end{pmatrix}$$

The converse is also true and a triplet eigenstate can be converted to a singlet eigenstate with the ($s_{1,z}$–$s_{2,z}$). Interestingly, the ($s_{1,x}$–$s_{2,x}$) operator can be used to transform a pure triplet to a singlet and vice versa. While the ($s_{1,x}$+$s_{2,x}$) cannot change state multiplicity, it can convert a triplet between its three degenerate eigenstates.

The rate of intersystem crossing is further affected by the remaining constants in P_{SO} and ΔE_{12}^2. Importantly, as in the case of triplet radiative decay, a larger Z will result in faster intersystem crossing. This relationship has motivated the use of heavy metal atoms (e.g. Pt and Ir) in the design of phosphorescent dopants for organic light-emitting devices (OLEDs) [25]. The rate of intersystem crossing can also be enhanced if there is a very small singlet-triplet energy splitting [26]. This relationship will be further discussed in Chapter 8.

2.1.4. Single molecule exciton state diagram

Based on the discussion presented hereto, a state diagram for the photogenerated exciton on a single molecule can be constructed as seen in Figure 2.5. Here, the ground state (S_0) is shown as well as the first (S_1) and second (S_2) excited singlet states. Upon photon absorption into either of these two states, rapid internal conversion (10^{-14}–10^{-11} s) occurs to the lowest energy vibronic level of S_1. Photoluminescence from the singlet state, or fluorescence, occurs at a rate $k_{R,S}$. The associated rate of non-radiative decay for a singlet state ($k_{NR,S}$) will depend on the vibrational energy and chemical environment of the molecule. As these two rates compete to deactivate S_1 the photoluminescence efficiency of the singlet state can be defined as:

Eq. 2.19 $$\eta_{PL,S} = \frac{k_{R,S}}{k_{R,S}+k_{NR,S}}$$

This efficiency describes the probability that an exciton in S_1 decays radiatively. The lifetime of the singlet state is defined as the inverse of all deactivating rates:

Eq. 2.20 $$\tau_S = \frac{1}{k_{R,S}+k_{NR,S}}$$

In systems that demonstrate intersystem crossing rates competitive with the rates of singlet radiative and non-radiative decay, population of the triplet state (T_1) is possible. Since triplet excitons require spin-orbit coupling to couple radiatively ($k_{R,T}$) and non-radiatively ($k_{NR,T}$) to the ground state, triplet photoluminescence, or phosphorescence, and non-radiative triplet decay are often much slower than their singlet counterparts [15]. In a similar fashion, the triplet state photoluminescence efficiency can be defined as:

Eq. 2.21 $$\eta_{PL,T} = \frac{k_{R,T}}{k_{R,T}+k_{NR,T}}$$

and the triplet state lifetime can be defined as:

Eq. 2.22 $$\tau_T = \frac{1}{k_{R,T}+k_{NR,T}}$$

Not shown on the diagram is direct photo-population of T_1. While this process is quantum mechanically allowed for systems with spin-orbit coupling, absorption into the triplet state is also quite slow and therefore not competitive with absorption into the singlet manifolds. It should be noted that higher lying unoccupied energy levels can be populated with very high energy excitations.

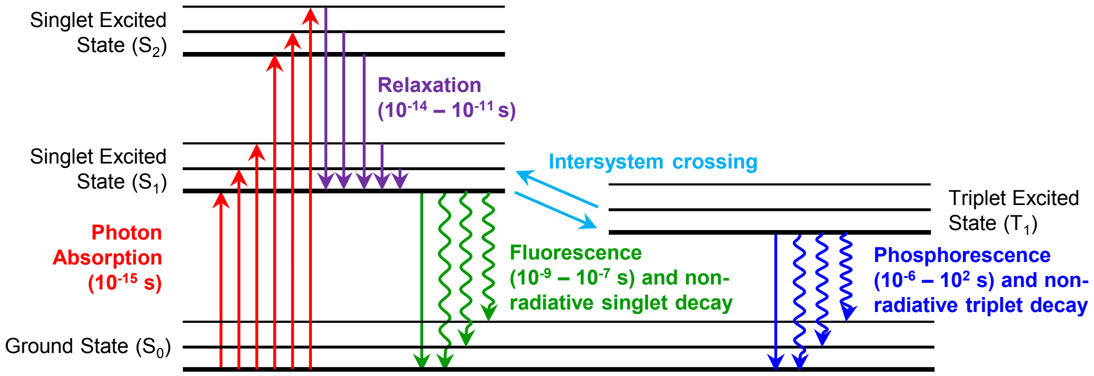

Figure 2.5 Exciton state diagram showing the relevant excitation pathways and timescales resulting from solar illumination and photogeneration. Each level is depicted as having multiple vibronic sublevels.

2.2. Exciton energy transfer

Once an exciton has been created, it is not necessarily confined to the molecule upon which it was generated. Exciton energy transfer between molecules is the transference of the exciton between conjugation centers within the organic solid [27]. In a solid composed of disordered small molecules, a conjugation center likely exists near the center of each molecule. In a solid composed of polymeric organic semiconductors, regions of crystallinity, kinks, and torsion create a variety of conjugation centers, each with their own chemical and excitonic environment [28–30]. In more ordered systems, such as organic single crystals, the exciton is thought to become more delocalized and different physical interpretations for exciton energy transport may need to be considered [31].

Considering an organic solid with localized excitations, there are three primary types of energy transfer that are responsible for exciton migration: cascade energy transfer, Förster transfer, and Dexter transfer [15].

2.2.1. Cascade

Cascade energy transfer involves the emission and subsequent absorption of a photon between two molecules [32]. This occurs over long length scales, comparable to the absorption path length, and is sometimes referred to as reabsorption or radiative energy transfer. For organic thin films, this mechanism should be considered when there is a reasonable overlap between the absorption and emission spectra of the given material. The rate of cascade energy transfer decreases as the Stokes shift between absorption and emission increases and as the film thickness decreases. Additionally, the effect of reabsorption can be neglected if the lifetime of the exciton is much longer than the inverse of the total hopping rate from other, shorter-range mechanisms such as Förster and Dexter energy transfer.

2.2.2. Förster

Förster transfer is a non-radiative energy transfer mechanism that takes place via the Coulombic coupling of the electromagnetic field between a donor and acceptor molecule [27]. Förster's pioneering work on Coulombic energy transfer approximates the transfer rate for a pair of weakly coupled point dipoles [33]. Mechanistically, this can be thought of as the emission and subsequent absorption of a virtual photon. Hence, there must be spectral overlap between the luminescent excited state donor molecule and the nearby ground state acceptor molecule. Since dipole-dipole interactions involve fields and not the direct exchange of electrons, they occur non-radiatively through empty or molecularly occupied space. The rate equation for Förster energy transfer is written in terms of the intermolecular separation (d), the exciton lifetime (τ), and the Förster radius for energy transfer (R_0) as [33]:

Eq. 2.23 $$k_F(d) = \frac{1}{\tau}\left(\frac{R_0}{d}\right)^6$$

At a separation $d=R_0$, the rate of Förster energy transfer equals the sum of all other rates for excited state decay for the exciton. The term R_0 is defined as [33]:

Eq. 2.24 $$R_0^6 = \frac{9\eta_{PL}\kappa^2}{128\pi^5 n^4}\int \lambda^4 F_D[\lambda]\sigma_A[\lambda]d\lambda$$

where κ^2 is the dipole orientation factor, η_{PL} is the photoluminescence efficiency of the excited state, n is the refractive index at the wavelength where the spectral overlap integral is maximized, λ is the wavelength, F_D is the area-normalized donor fluorescence, and σ_A is the acceptor absorption cross-section. A schematic representation of spectral overlap is shown in Figure 2.6. It is important to note that Förster transfer by dipole-dipole interactions requires that the molecule be capable of emitting light ($k_R \neq 0$). Förster energy transfer typically occurs over a relatively long length scale of R_0=(1–10) nm as compared to typical intermolecular spacing on the order of d=1 nm or less.

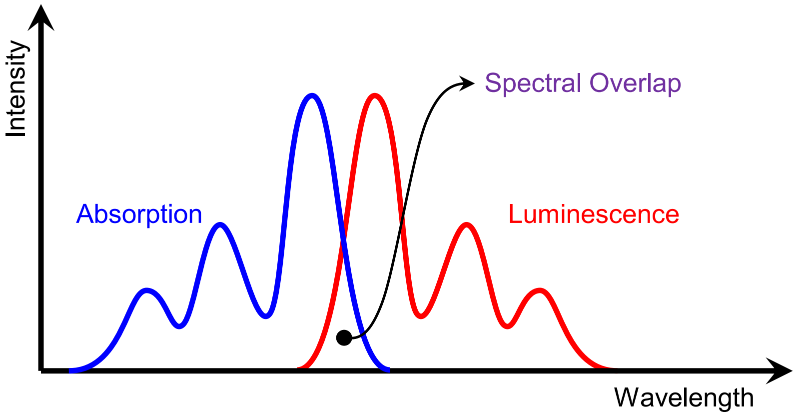

Figure 2.6 Schematic representation of the spectral overlap between absorption and photoluminescence that is required for Förster energy transfer to take place.

As the intermolecular spacing is reduced, the assumption of weakly coupled dipoles begins to breakdown. At distances on the order of the electronic density, higher order multi-pole contributions may play a significant role in determining the Coulombic interaction between molecules [27,34]. In this regime, the shape of the molecule and its associated electron density will determine how the Coulombic interaction should be represented because it will affect the essential shape of the transition densities [35]. Additionally, whenever the associated electron densities of the donor and acceptor molecules overlap, direct electron exchange coupling should also be considered.

2.2.3. Dexter

Dexter energy transfer theory can effectively describe the orbital interactions that govern electron exchange [36]. Since this mechanism involves the direct exchange of electrons, it requires overlap between the electron densities of both the excited donor molecule and the nearby ground state acceptor molecule. The rate equation for Dexter energy transfer is expressed as [15,36]:

Eq. 2.25 $$k_D(d) = KJe^{\left(-\frac{2d}{L}\right)}$$

where K is related to specific orbital interaction, J is a spectral overlap integral normalized for the extinction coefficient of the ground state molecule, and L is the van der Waals radius of the molecules. It is important to note that this equation assumes the electronic distributions of the donor and acceptor molecules decrease exponentially in the radial direction. Additionally, in contrast to Förster energy transfer the rate of Dexter energy transfer does not depend on the magnitude of the extinction coefficient of the accepting molecule. Dexter energy transfer is a nearest-neighbor process with a typical length scale of 0.1–1 nm, a shorter range interaction than Förster energy transfer. Since Dexter energy transfer is the physical exchange of electrons, it may occur between states that are weakly- or non-radiative. For this reason, triplet excitons are thought to migrate by electron exchange interactions described by Dexter theory.

Figure 2.7 schematically compares the movement of excited and ground state electrons for both the Förster and Dexter energy transfer mechanisms.

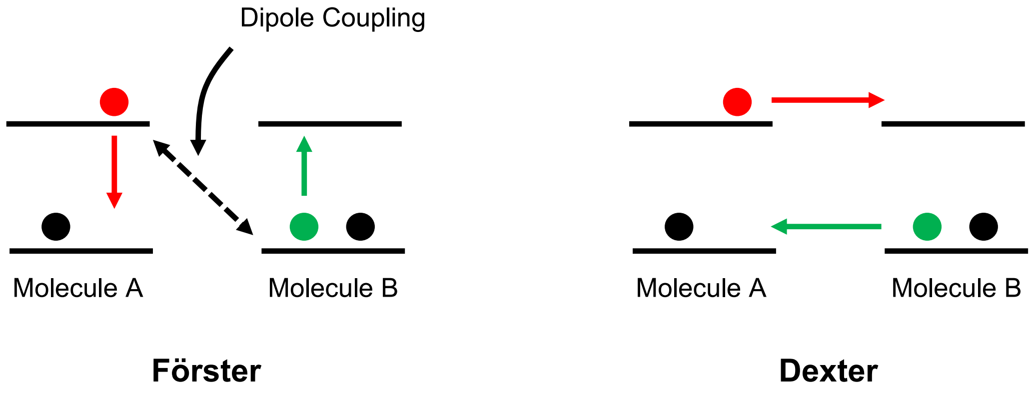

Figure 2.7 Schematic representation of electron pathways for both Förster and Dexter exciton energy transfer. The key difference is that Förster energy transfer proceeds via a Coulombic (dipole) coupling whereas Dexter energy transfer is the direct exchange of electrons.

2.3. Exciton transport

At the molecular level, exciton transport proceeds via successive energy transfer events [32]. At the device level, however, mesoscopic modeling of exciton transport as a diffusive process aides in the optimization and development of new device architectures [37]. Models describing exciton diffusion often have varying degrees of complexity. In the simplest terms, exciton diffusion is described as an ensemble of nearest neighbor hopping events identical to a random walk [38]. In these models, there is a rate of exciton energy transfer between molecules on a regular lattice. More complex models account for the dispersive nature of energy transfer events by considering the disorder present in the system, namely the energetic, spatial, and orientational disorder [39,40]. While more exact, these models often require a detailed knowledge of the local, ultrafast kinetic pathways for a given system as well as advanced computational resources to integrate local energy transfer rate calculations into a mesoscopic system.

For the plurality of this dissertation, focus will be placed on a more simplistic view of exciton transport. Note that even when the complexity due to disorder is neglected, analysis of energy transfer rate formalism can still be instructive and, in many cases, fairly accurate.

2.3.1. Normal diffusion

In order to connect a nanoscopic energy transfer event to mesoscopic transport, exciton diffusion can be modeled as an ensemble of self-energy transfer hopping events on a cubic lattice. A generalized diffusion coefficient can be written as [32,37]:

Eq. 2.26 $$D = \frac{A}{6}\sum_{N} d^2 k_{ET}[d]$$

where A is a factor accounting for disorder in the thin film (order unity), d is the distance of a single step or hop, and k_{ET} is the energy transfer rate to a specified lattice point of set N. It is important to note that as defined in Eq. 2.26, k_{ET} is the rate as rigorously defined, for example, in Eq. 2.23 or Eq. 2.25. An analogous expression for k_{ET} is the mean time between hops (τ_H), which is the inverse of the ensemble of hopping rates under consideration (Note: $\tau_H \neq k_{ET}^{-1}$ due to the availability of multiple hopping sites). Simplification of Eq. 2.26 for a simple cubic lattice leads to $D=Ad^2k_{ET}$ when only nearest neighbor interactions are considered which is identical to $D=Ad^2\tau_H^{-1}/6$.

In the absence of second order processes (e.g. annihilation, fission etc…), exciton diffusion is modeled with a second order differential equation as:

Eq. 2.27 $$\frac{dn}{dt} = D\nabla^2 n[\boldsymbol{r_n}] - \frac{n[\boldsymbol{r_n}]}{\tau} + G[\boldsymbol{r_n}]$$

where n is the exciton density, τ is the exciton lifetime, r is the position at point n, and G is the exciton generation rate. The first term represents exciton motion by diffusion, the second term represents exciton recombination, and the third term represents exciton generation by light absorption. Here, the exciton generation rate is the time average of the energy dissipated per second in the material [41]. This value is proportional to the intensity of the optical field in the material which can be determined explicitly from optical interference models [41]. In one-dimension, Eq. 2.27 reduces to:

$$\text{Eq. 2.28} \qquad \frac{dn}{dt} = D\frac{d^2n[x]}{dx^2} - \frac{n[x]}{\tau} + G[x]$$

In cases where there is long-range Förster energy transfer to another layer extra quenching terms can be added to Eq. 2.28:

$$\text{Eq. 2.29} \qquad \frac{dn}{dt} = D\frac{d^2n[x]}{dx^2} - \frac{n[x]}{\tau} + G[x] - n[x]k_F[d_F]$$

where d_F is the distance from a given point in a layer (x) to the quenching site. For quenching to an external layer, k_F is defined as [42]:

$$\text{Eq. 2.30} \qquad k_F = \frac{\rho_A}{\tau}\frac{\pi {R_0}^6}{6{d_F}^3}$$

where ρ_A is the molecular density of the acceptor. Alternative definitions of k_F should be used as dictated by the geometry of the system [42,43]. The characteristic length scale for diffusion is the exciton diffusion length:

$$\text{Eq. 2.31} \qquad L_D = \sqrt{D\tau}$$

The L_D for a given organic active material in an OPV is then a critical device parameter as it reflects a characteristic distance over which an exciton can migrate before it decays. The dimensionality of this characteristic length scale is sometimes included where a coefficient of $\sqrt{2}$, $\sqrt{4}$, or $\sqrt{6}$ is added for diffusion in one, two, and three dimensions, respectively. While the exact definition of L_D does not change its physical interpretation, care should be taken when comparing measured values across multiple sources to ensure it is defined consistently.

2.3.2. Anomalous diffusion

When considering an exciton moving along an infinite, one-dimensional lattice the average displacement will be exactly zero. This is because there will be an equal probability for the exciton to move to the left and to the right. The mean-squared displacement, however, will be non-zero as:

Eq. 2.32 $$\langle x^2 \rangle = Dt$$

where t is the time. This simple relationship states that the mean-squared displacement increases linearly in time for purely diffusive motion. Deviations from this relationship represent anomalous diffusion. A more general version of this equation can be written as [44]:

Eq. 2.33 $$\langle x^2 \rangle = \beta t^\alpha$$

where β is similar to D and $\alpha<1$ represents sub-diffusive motion and $\alpha>1$ represents super-diffusive motion. As before, $\alpha=1$ represents purely diffusive motion. Traces for normal and anomalous diffusion can be seen in Figure 2.8.

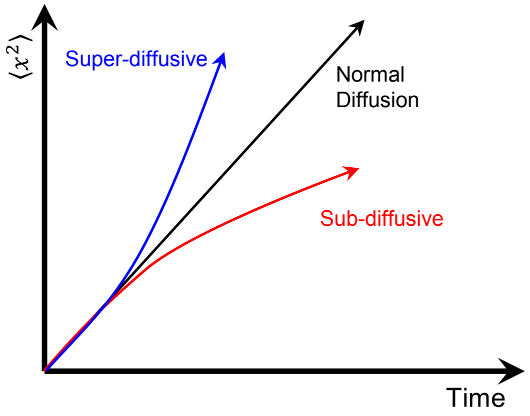

Figure 2.8 Diagram for the mean-squared displacement versus time highlighting the difference between normal diffusive, sub-diffusive, and super-diffusive motion.

Spatial, orientational, and energetic disorder within the organic solid are commonly cited as sources of sub-diffusive motion [45]. If the volume sampled by the exciton is large enough to average out all the sources of disorder, however, diffusive motion can be reestablished, albeit with a lower D (L_D) than would be measured without any disorder present. This is a common situation for amorphous thin-films of small molecule organic semiconductors, where the short-range nature of the spatial and orientational disorder can sometimes be incorporated into the energy transfer rate [46].

Instances of super-diffusion represent cases where the exciton is preferentially moving away from the referenced location faster than it is moving towards. This symmetry breaking phenomena has the potential to achieve fast, high-fidelity exciton transport and will be discussed more thoroughly in Chapter 6.

2.4. Charge transport

Similar to excitons, unpaired electrons and holes, or polarons, can also exist within an organic solid [16,47]. Unlike the charge neutral molecular exciton, polarons carry a positive or negative charge and can be envisioned as molecular ions. Transport of these species is critical to the operation of OPV devices as efficient extraction of these charge particles precludes production of an external current [17].

Many models exist to describe the electrical conductivity in organic solids, particularly due to the extensive research into charge carrier phenomena for inorganic semiconductors [48,49]. In one extreme is band-like transport which dominates in materials with long-range order, such as organic single crystals. In the other extreme, hopping transport dominates in materials which exhibit highly localized charge carriers, such as amorphous thin films consisting of disordered small molecules.

2.4.1. Band transport

Band transport is a well-established theory for describing the movement of charges in metals and single crystalline inorganic semiconductors [4]. In this framework, the interactions of two orbital wavefunctions results in the formation of two, distinct energy levels. When the ensemble of interactions between orbital wavefunctions for an entire solid or thin film are considered, the energy splittings are so closely spaced that a continuous band is formed [50]. In terms of organic semiconductors, this occurs for both the HOMO and the LUMO which carry hole and electron polarons, respectively.

The simplest model that describes charge transport within a band is the Drude model [1]. In this model, charged particles moving under an applied field (E) experience scattering events causing the charged particle to lose kinetic energy and change direction. The net drift velocity (υ_D) for these charge particles is then related to E and the average time between scattering events (τ_{SC}) as:

Eq. 2.34 $$\nu_D = \left(\frac{e\tau_{SC}}{m^*}\right) E$$

where e is the elemental charge and m^* is the effective mass. As a common metric for charge transport, the mobility is written as:

Eq. 2.35 $$\mu = \frac{\nu_D}{E} = \frac{e\tau_S}{m^*}$$

The major sources of scattering events are lattice vibrations, or phonons, and impurities. In highly pure, undoped organic single crystals, impurity levels are often very low. In this circumstance, the mobility tends to increase as the temperature is lowered due to weaker lattice vibrations. A power law dependence for mobility versus temperature follows as:

Eq. 2.36 $$\mu(T) \propto T^{-n}$$

where n>1. When this behavior is measured, “band-like” transport is often claimed. Interestingly, unlike crystalline metals or inorganic semiconductors where the charge particles are delocalized across the entire solid, organic single crystals exhibiting “band-like” transport still show mean free paths are the order of several nm, only slightly larger than the intermolecular separation [51]. This implies that the charge carriers are, perhaps, only delocalized over several unit cells and not the entire crystal.

2.4.2. Hopping transport

When large amounts of disorder are present in the organic solid, band theory is not applicable because delocalized orbital wavefunctions are not achieved. Similar to excitons, polarons then become localized to states on individual molecules or conjugation centers [52]. Under and applied field, polaron motion is represented as hopping between these energy states that are both spatially and energetically separated. The hopping rate is typically described as the Miller-Abrahams type where the overlap of electronic wavefunctions is combined with a Boltzmann factor for hopping upward in energy. The hopping rate between from site *i* to *j* follows as [53]:

Eq. 2.37
$$\upsilon_{ij} = \upsilon_0 exp\left[-2\gamma a\frac{\Delta R_{ij}}{a}\right]\begin{cases} exp\left[-\frac{E_j-E_i}{2k_BT}\right], & E_j - E_i > 0 \\ 1, & E_j - E_i < 0 \end{cases}$$

where υ_0 is a prefactor, γ is the decay constant of the exponentially decreasing wavefunction, a is the average lattice distance, ΔR_{ij} is the spatial distance between electronic site *i* and *j*, E_i and E_j are the site energies in zero field, k_B is Boltzmann’s constant, and T is the temperature. In the case of an applied field, an electrostatic energy is included in the site energies for cases when $E_j - E_i > 0$. The electric field is not thought to accelerate downward hops.

To connect this hopping rate to mobility, a density of states (DOS) for the electronic sites must be assumed. While many DOS can be rationalized based on a given material and temperature range, here a Gaussian DOS is considered where the energy distribution of sites is:

$$\text{Eq. 2.38} \qquad N(E) = (2\pi\sigma^2)^{-\frac{1}{2}} exp\left[-\frac{E}{2\sigma^2}\right]$$

where σ is the width of the DOS and E is the energy relative to the center of the distribution. The mobility at low applied electric field becomes:

$$\text{Eq. 2.39} \qquad \mu(T) = \mu_0 exp\left[-\left(\frac{T_0}{T}\right)^2\right]$$

where $T_0=2\sigma/3k_B$ and μ_0 is the disorder free mobility achieved as T→∞. A schematic representation of both band and hopping transport can be seen in Figure 2.9.

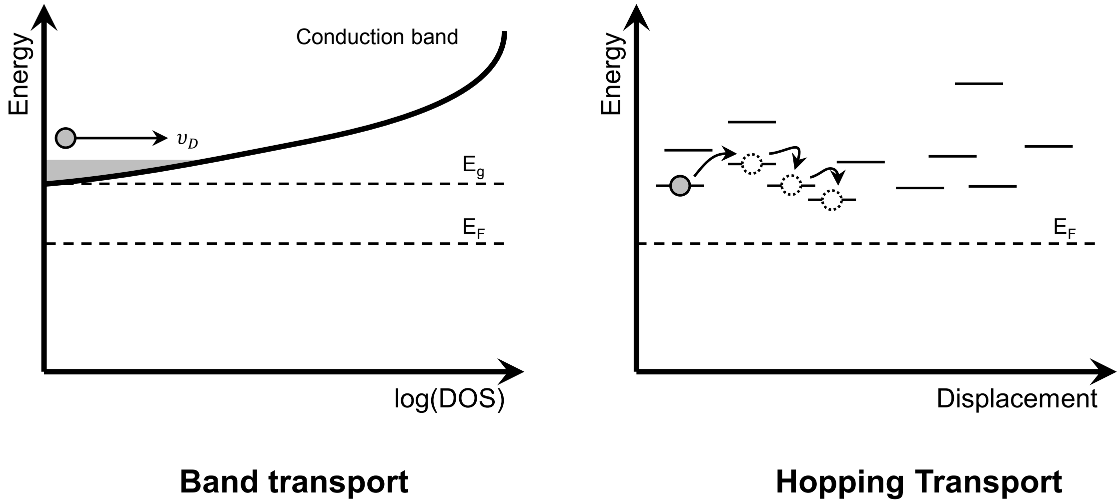

Figure 2.9 Shematic representations of band and hopping transport. While these are the extremes of the charge transport spectrum, intermediate mechanisms are possible depending on the degree of intermolecular interaction and chemical doping.

2.5. Summary

Owing to the localized nature of energy and charge in organic semiconductors, efficient photoconversion in organic photovoltaic devices (OPVs) requires a detailed knowledge of the photophysical pathaways described hereto in this chapter. The remaining focus of this dissertation will examine methods to enhanced nanoscopic exciton energy transfer and mesoscopic exciton diffusion in organic thin-films for application in OPVs. Chapter 3 will describe the methods for thin-film preparation and characterization techniques used throughout. Chapters 4–9. will describe studies undertaken in order to directly probe and enhance the exciton diffusion length by optimizing, for example, intermolecular interaction, anamolous diffusion, and intersystem crossing. Chapter 11 will describe future research directions in the continued optimizatin of exiton diffusion and tranport in OPVs and other organic optoelectronic devices.

3. Characterization of organic semiconductors films and devices

The short range nature of exciton and polaron transport inherent to organic semiconductors motivates the implementation of these materials as thin-films (i.e. 1–100 nm-thick). In fact, much of the progress made in the characterization of the materials and their subsequent implementation into OPV devices has relied on parallel advances in thin-film formation and morphological control. In this chapter, the primary methods for the fabrication of organic semiconductor thin-films will be discussed. Characterization techniques relevant for this dissertation will also be introduced.

3.1. Sample fabrication techniques

The techniques available for the processing and fabrication of an organic semiconductor thin-film depend strongly on the chemical nature of the material. Polymeric and oligomeric organic semiconductors with molecular weight (M_w) of M_w~(10^3–10^5) gmol^{-1} typically display good solubility in a variety of solvents [14]. The relatively high solution viscosities enable a wide-range of solution based deposition techniques such as spin-coating, slot-die coating, doctor-blade, etc [13,54]. On the other hand, the solubility of small molecule organic semiconductors (M_w~100 $gmol^{-1}$) can vary. Further, low solution viscosities make difficult solution based deposition techniques [54]. The low M_w, however, enables the use of vacuum based deposition techniques which require the sublimation or evaporation of the target molecule at very low pressure. While a variety of techniques exist on both ends of the spectrum, this dissertation will focus on the most representative for each respective class, vacuum thermal sublimation and spin-coating [10].

3.1.1. Vacuum thermal sublimation

In vacuum thermal sublimation, small molecule organic semiconductors are heated to temperatures of approximately 250-350°C in a vacuum chamber (Figure 3.1). This section will describe the technique and equipment used to fabricate samples used in this dissertation. The chamber is evacuated in two stages. A rotary vane pump first brings the chamber pressures down to 5×10^{-2} Torr. Below this pressure, a Helium-cooled, cryogenic pump is utilized to bring chamber the pressures down to $\sim10^{-8}$ Torr. Upon resistive heating, there is sufficient thermal energy to initiate the physical transformation from a solid to gas, sublimation. In this configuration, a voltage is applied between two Copper posts connected on each end of a resistive, Tungsten source boat. The boat resistively heats as current flows, thereby heating the organic source powder loaded inside.

At these pressures, the mean free path between molecular collisions is much greater than the distance between the organic source and the target deposition area. Molecules travel ballistically, impacting a room- or elevated-temperature substrate where they solidify and form a thin-film. The deposition rate, typically 0.1-5 $Ås^{-1}$, is measured with quartz crystal microbalances located near the source boat. A floating “tooling factor” adjusts the deposition rate to account for the geometry of the chamber. The measured deposition rate is controlled by adjusting the power supplied to the source boat. A key advantage of the system is the proportional-integral-derivative (PID) controlled deposition rate can be held remarkably constant (< 5% deviation) or even varied linearly throughout the course of film formation. Up to four materials can be deposited simultaneously, allowing for the deposition of mixed and gradient thin-films. Target substrates are pinned to the underside of a rotating Copper holder. Rotation allows for the deposition of uniform films across a large target area (~ 200 cm^2). A heating lamp can optionally be installed to heat the Copper holder. Deposition onto a heated stage allows for additional molecular motion during film formation, assisting in physical processes such as crystallization and annealing [55].

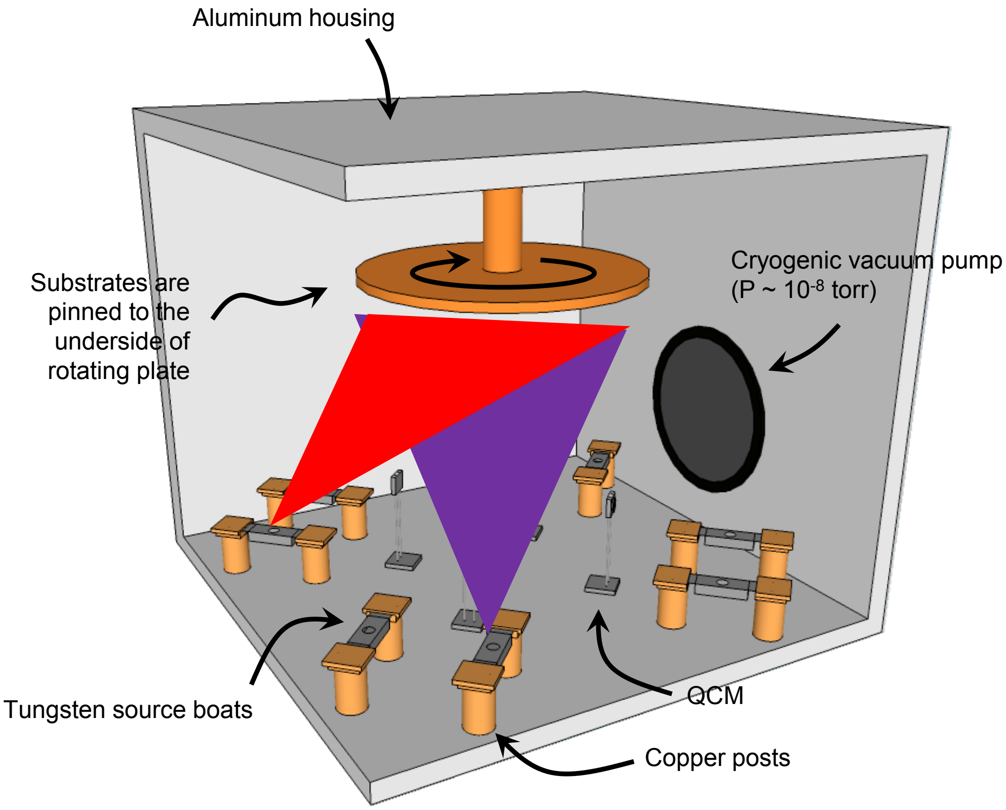

Figure 3.1 Schematic showing the chamber design used for the growth of small molecular thin-films via vacuum thermal sublimation.

3.1.2. Spin-coating

For organic semiconductors that demonstrate good solubility and moderate solution viscosities in the range of 20-500 cP, spin-coating is an excellent technique for the rapid formation of thin-films [54]. In this technique, the substrate is spun around a vertical axis as speeds in the range of 500-10,000 rpm. The dissolved organic semiconductor solution (~1-100 mgml^{-1}) can be added before the substrate has begun spinning (static) or during rotation (dynamic). The centrifugal forces combined with material parameters such as viscosity determine the thickness of the initial, wet coating that covers the surface of the substrate. As spinning continues, the solvent begins to dry. The formation of a dense, skin layer is common as the surface of the film will dry more rapidly. For high boiling-point solvents, the application of heat is necessary to fully dry the film and drive off excess solvent [54]. Figure 3.2 details the process of spin-coating schematically.

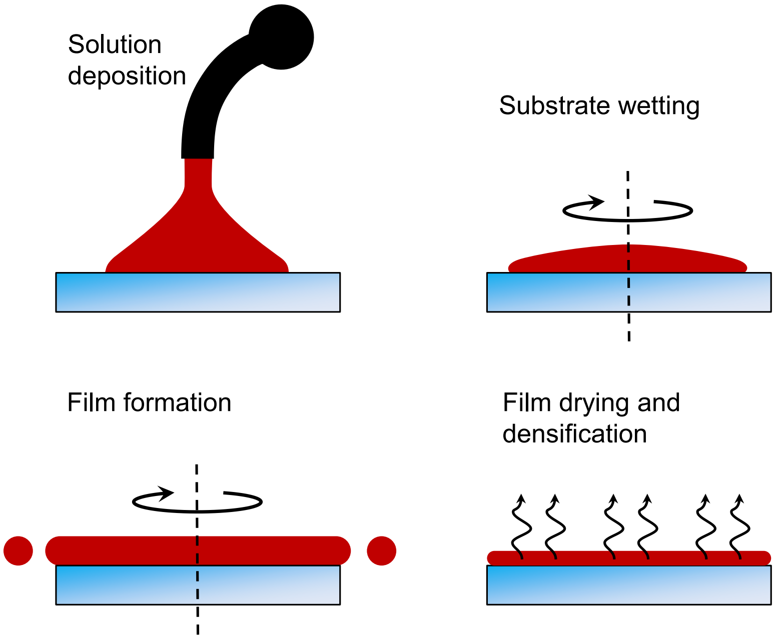

Figure 3.2 Schematic showing the basic process flow for the spin-coating of solvated organic semiconductors.

3.2. Film characterization

Simple thin-films of an organic semiconductor or mixtures thereof must first be characterized before implementation in multi-layer stacks or OPV devices. While a variety of characterization techniques exist for the measurement of the optical, electrical, and morphological characterization of organic semiconductor thin-films, only those used extensively throughout the course of this dissertation will be introduced. The reader is encouraged to reference the case studies presented in *Physics of Organic Semiconductors* by Brütting and Adachi for further information regarding the complete characterization of these materials.

3.2.1. Visible-light spectroscopy

The measurement of the absorption and luminescence for an organic thin-film provides a wealth of photophysical information. Further, characterization in the visible range of the electromagnetic spectrum provides information relevant the operation of OPV devices.

The absorption spectrum of an organic thin-film is commonly measured with a ultra-violet (UV) to near infra-red (NIR) spectrophotometer. In this technique the transmission of an organic thin film is compared to that of a bare substrate. Differences in the transmission spectrum are counted as absorption within the film. Overestimates of absorption can occur if there is a significant amount of additional reflection at the thin-film/substrate interface. This measurement is typically performed at normal incidence and fit assuming a Beer-Lambert type absorption where the transmission (T) of the absorptive sample is:

Eq. 3.1 $$T = \frac{I}{I_0} = e^{-\alpha t}$$

where I is the transmission of the sample, I_0 is the transmission of the bare substrate, t is the thickness of the film, and α is the absorption coefficient of the thin-film.

Light emitted from an organic thin-film after absorption is referred to as photoluminescence. The photoluminescence spectrum is typically measured with a spectrofluorometer. In this technique the photoluminescence is directed through a monochromator into a detector, commonly a Silicon photodiode or photomultiplier tube (PMT). Typically, materials with photoluminescence efficiency >1% can be readily measured. By scanning the monochromator across all the wavelengths of interest, a photoluminescence spectrum can be generated. A calibrated spectrometer can also be utilized which measures all wavelengths simultaneously, however does not have the same level of sensitivity. A monochromated Xenon arc lamp is used as the excitation. It is ideal to use as thin a film as possible when measuring photoluminescence spectra as very thick films (>100 nm) can have appreciable self-absorption and bias the measured spectrum towards longer wavelengths.

While the two previous techniques readily measure the steady state absorption and photoluminescence spectra, time-resolved photoluminescence measurements give information about the kinetic pathways for excitons. In this technique, a fast response (~10^{-9} – 10^{-6} s) Silicon photodiode is read by a fast oscilloscope. A 50 Ω terminated connection should be made to ensure that the detector's response is not resistance-capacitance (RC) limited. More advanced time-resolved photoluminescence techniques can measure photoluminescence on the ultrafast time scale (10^{-13} – 10^{-10} s). Ultrafast transient absorption spectroscopy is a technique that measures changes in the thin-film absorption spectrum upon illumination, providing information about higher-energy exciton states without the requirement of measurable photoluminescence.

3.2.2. Ellipsometry

Variable angle spectroscopic ellipsometry (VASE) is a technique used to measure the thickness and optical properties of materials. In this technique, light at a known wavelength and polarization is incident upon an organic thin-film at a known angle. As light interacts with the sample, the polarization changes due to optical effects such as reflection, refraction, interference, and absorption. The reflectivity is measured and its polarization analyzed. When broken down into x- and y-components, the tan(Ψ) is defined as the ratio between x- and y-amplitudes and Δ is the phase shift. The tan(Ψ) and

Δ are then measured at a variety of angles and wavelengths in order to build a unique data set representative of a given film. Optical models for predicting tan(Ψ) and Δ can then be used to fit the experimental data and extract meaningful parameters.

The Cauchy model is commonly used to fit for organic thin-film thicknesses. In this model the extinction coefficient (k) is assumed to be zero while the index of refraction (n) is expressed as [56]:

Eq. 3.2 $$n[\lambda] = A + \frac{B}{\lambda^2} + \frac{C}{\lambda^4}$$

where λ is the wavelength and A,B, and C are empirical fitting parameters. This dispersion relation serves as an input into an optical propagation model that can predict values for tan(Ψ) and Δ. The film thickness, A, B, and C are then fit iteratively, until a global minimum in the mean-squared error (MSE) is achieved. Extracted film-thicknesses typically have error bars of <1 nm. To use this model, however, the film cannot absorb in the spectral region over which the measurements and fitting are being performed. This requires some advance knowledge of the spectral absorption, but measurements between λ=(800 – 1,100) nm can typically be used provided the molecule does not absorb in the NIR.

Sometimes it is also necessary to know n and k for an organic thin-film, especially for the purposes of optical modeling. VASE can extract these constants provided the film thickness is known or previously extracted. By definition, a VASE measurement is performed over a variety of angles and wavelengths at which the molecule absorbs light. A global fit for n and k can then be performed to determine the optical constants. However, care must be taken before these values can be deemed trustworthy. A requirement for good optical constants is that they follow Kramers-

Kronig consistency [57]. This mathematical relationship between n and k holds because they are related to the real and imaginary parts of the complex dielectric function, ε.

Eq. 3.3 $$\mathrm{Re}\left[\frac{\epsilon(\lambda)}{\epsilon_0}\right] = 1 + \frac{1}{\pi} P \int_{-\infty}^{\infty} \frac{1}{2\pi c} \cdot \frac{\mathrm{Im}\left[\frac{\epsilon(\lambda)}{\epsilon_0}\right]}{\frac{1}{\lambda'} - \frac{1}{\lambda}} d\lambda'$$

Eq. 3.4 $$\mathrm{Im}\left[\frac{\epsilon(\lambda)}{\epsilon_0}\right] = -\frac{1}{\pi} P \int_{-\infty}^{\infty} \frac{1}{2\pi c} \cdot \frac{\mathrm{Re}\left[\frac{\epsilon(\lambda)}{\epsilon_0}\right] - 1}{\frac{1}{\lambda'} - \frac{1}{\lambda}} d\lambda'$$

where P is the Cauchy principle value. These transformations are also referred to as Hilbert transformations and allow the n to be determined from k and vice versa. If the fit optical constants follow this relationship, they can be assumed to well-reflect the optical properties of the material.

It should be noted that VASE is also sensitive to anisotropy and birefringence. By fitting the material with biaxial or uniaxial optical constants, the degree of optical anisotropy can be determined [58].

3.3. Optical modeling

Once, the optical constants of an organic thin-film are known, the propagation of light can be predicted with optical modeling. Optical modeling is an enabling step for many subsequent characterization techniques, namely the measurement of the exciton diffusion length (L_D) and prediction of OPV performance.

A transfer matrix formalism is used for the modeling of light propagation in layered systems [41]. The important assumptions made for the application of this modeling technique are (1) layers included in the system are considered to be homogeneous and isotropic such that their optical response can be described with a scalar, complex n, (2) interfaces are assumed parallel and flat compared to the wavelength of light, and (3) the light incident on the system can be described by plane waves. If these assumptions are met, optical modeling can be used to predict the spatial profile of the optical field within a layered, organic system.

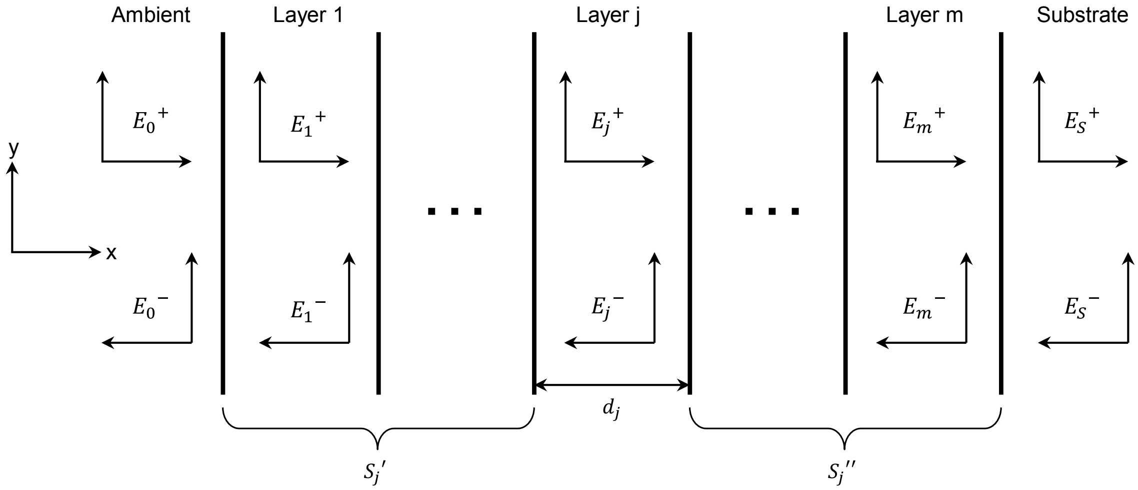

Figure 3.3 Schematic layer structure for an m-layer optical substrate on an arbitrary substrate. The electric field for the light incident from the ambient is separated into rightward and leftward propagating components.

Figure 3.3 depicts a generic, multi-layer structure for a series of m films on a given substrate. The ambient layer reflects the source of optical illumination. The given layer (j) is then described by its thickness (d_j) and complex index of refraction ($\widetilde{n_j} = n_j + ik_j$). The optical field at any point in any layer can be described by two components propagating in opposite directions, one in the positive x-direction and one in the negative x-direction.

At each interface, light can transmit or be reflected. These phenomena are described by the Fresnel complex transmission and reflection coefficients (r_{jk} and t_{jk}) for an interface between layer j and layer k. For light with the electric field perpendicular to the plane of the interface (s-polarized):

Eq. 3.5 $$r_{jk} = \frac{q_j - q_k}{q_j + q_k} \quad \text{and} \quad t_{jk} = \frac{2q_j}{q_j + q_k}$$

For light with the electric field parallel to the plane of the interface (p-polarized):

Eq. 3.6
$$r_{jk} = \frac{-\tilde{n}_k{}^2 q_j + \tilde{n}_j{}^2 q_k}{\tilde{n}_k{}^2 q_j + \tilde{n}_j{}^2 q_k} \quad \text{and} \quad t_{jk} = \frac{2\tilde{n}_k{}^2 \tilde{n}_j{}^2 q_j}{\tilde{n}_k{}^2 q_j + \tilde{n}_j{}^2 q_k}$$

where

Eq. 3.7
$$q_j = \tilde{n}_j cos\phi_j = \sqrt{\tilde{n}_j{}^2 - \eta_0{}^2 sin^2\phi_0}$$

and φ_j is the angle of refraction in layer j, η_0 is the refractive index of the transparent ambient, and φ_0 is the angle of incidence.

With these coefficients, 2x2 matrices for light propagation at the interfaces can be developed as:

Eq. 3.8
$$I_{jk} = \frac{1}{t_{jk}} \begin{bmatrix} 1 & r_{jk} \\ r_{jk} & 1 \end{bmatrix}$$

Light propagation through a layer can be developed as:

Eq. 3.9
$$L_j = \begin{bmatrix} e^{-i\xi_j d_j} & 0 \\ 0 & e^{i\xi_j d_j} \end{bmatrix}$$

where

Eq. 3.10
$$\xi_j = \frac{2\pi}{\lambda} q_j$$

A total transfer matrix (S) can then be developed which describes light propagation through a given layered system. It is simply the product, in order, of the interfaces and layers with which light interacts upon illumination.

Eq. 3.11
$$S = \begin{bmatrix} S_{11} & S_{12} \\ S_{21} & S_{22} \end{bmatrix} = \left(\prod_{v=1}^{m} I_{(v-1)v} L_v\right) \cdot I_{m(S)}$$

Partial system transfer matrices can also be developed as:

Eq. 3.12
$$S = S_j{}' L_j S_j{}''$$

The total transfer matrix describes the propagation of the electric field through the entire system as:

Eq. 3.13 $$\begin{bmatrix} {E_0}^{+} \\ {E_0}^{-} \end{bmatrix} = S \begin{bmatrix} {E_S}^{+} \\ {E_S}^{-} \end{bmatrix}$$

Finally, through extension of Eq. 3.5 to Eq. 3.13, the electric field in layer j as a function of x can be written as:

Eq. 3.14

$$E_j(x) = {E_j}^{+}(x) + {E_j}^{-}(x) = \frac{{S_{j11}}'' e^{-i\xi_j(d_j - x)} + {S_{j21}}'' e^{-i\xi_j(d_j - x)}}{{S_{j11}}' {S_{j11}}'' e^{-i\xi_j d_j} + {S_{j12}}' {S_{j21}}'' e^{-i\xi_j d_j}} {E_0}^{+}$$

Apart, from the optical field, additional optical parameters that can be derived from this treatment are the system reflection and transmission as well as the spatial profile of absorption. The absorption (Q) is proportional to the modulus-squared of the optical field as:

Eq. 3.15 $$Q(x) = \frac{1}{2} c \varepsilon_0 \alpha_j n_j \left| E_j(x) \right|^2$$

where α_j is the absorption coefficient of layer j and ε_0 is the vacuum permittivity. In this way, transfer matrix modeling of the incident optical field can predict the spatial profile of absorption in an organic thin-film or OPV. This absorbed power is the dissipation of the electric field and can be converted to formation of molecular excitons within the system. The rate of exciton generation (G from Eq. 2.28) is then directly proportional to the modulus-squared of the incident optical field.

3.4. Organic photovoltaic devices

The first examples of OPV devices employed a single organic semiconductor layer sandwiched between two dissimilar metallic electrodes [59]. In these devices, the work function difference between the two metals creates a Schottky-type potential barrier at the metal-organic interface. The resulting built-in potential separates molecular excitons into electron and hole polarons. These devices exhibited, however, very low performance attributed to a large series resistance or an inefficient field-dependent generation of charge carriers. In 1986, a major breakthrough was reported by C.W. Tang while working at the Eastman Kodak Company [60]. In this seminal letter, the interface between two organic semiconductor thin-films was used to separate excitons. Over the past three decades, an intense amount of research has been focused on elucidating the nature of this organic heterojunction. This section will focus on the evolution of OPV device architectures and the electrical characterization of OPV performance.

3.4.1. Evolution of device architecture

Figure 3.4 shows a schematic OPV architecture. In this configuration, a planar heterojunction exists between an electron-donating organic semiconductor (donor) and an electron-accepting organic semiconductor (acceptor). At the donor-acceptor (D-A) interface, there is sufficient energetic offset to dissociate photogenerated excitons into an electron and hole polaron [61]. Consequently, only excitons that are able to diffuse to the D-A interface are able to contribute to photocurrent. In this architecture, there exists a critical tradeoff between exciton diffusion and optical absorption. If the layers are made very thick ($d>50$ nm), the typically short $L_D \sim 10$ nm limits the fraction of excitons that can reach the D-A interface. If the layers are made quite thin ($d \sim L_D$), incomplete optical absorption will typically result. Sometimes referred to as the exciton diffusion bottleneck, this tradeoff limited OPV performance for nearly a decade.

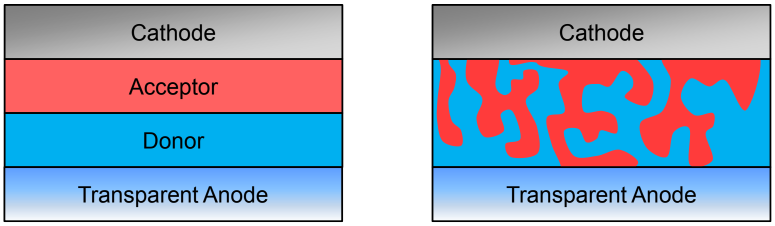

Figure 3.4 Archetypical device architectures for a planar heterojunction OPV (left) and a bulk or mixture heterojunction OPV (right). The critical difference in these architectures is the amount of DA interfacial area.

In 1990, Hiramoto *et al.* saw enhanced photocurrents upon mixing two distinct organic semiconductors [62,63]. In 1995, the combined efforts from the groups of Wudl and Heeger at the University of California at Santa Barbara made a critical discovery. By blending a polymeric donor and a small molecule, fullerene acceptor, significant increases in efficiency were realized [64]. In this configuration, the interface area between the donor and acceptor is significantly increased such that excitons are generated closer, on average, to the D-A interface (Figure 3.4) [65]. In contrast to planar heterojunction devices, these bulk heterojunction devices circumvent the typically short L_D and associated exciton diffusion bottleneck. Since this initial discovery, extensive research has been completed in the optimization of the bulk heterojunction OPV [66]. For the most part, improved synthetic and morphological control has been key to further increases in efficiency with state-of-the-art bulk heterojunction OPVs demonstrating efficiencies >10% [67].

In parallel with the development of efficient active layers, anode and cathode buffer layers have also been developed that are now instrumental the efficient operation of both planar and bulk heterojunction OPVs [17,68]. Ideally, both anode and cathode buffer layers prevent deleterious exciton quenching to the electrodes while still allowing for efficient charge collection. Further, the molecular orbital energy levels can be chosen such that the buffer layers are selective for a specific charge carrier, improving the diode like character of the device and improving performance.

3.4.2. Current-density voltage characterization

Current-density voltage measurements characterize the electrical power output of an OPV under standard operating conditions. AM1.5G solar simulated illumination is used as a standard. Figure 3.5 shows the current-density voltage traces for a prototypical OPV under illumination and in the dark.

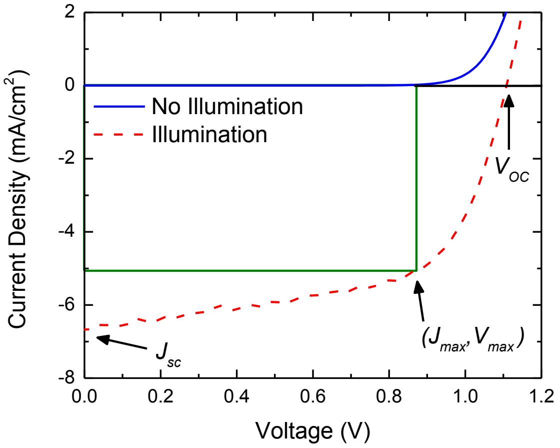

Figure 3.5 Example current-density voltage characteristics for an OPV in the dark and under illumination.

In the dark, diode-like behavior is measured. The dark current-density is often modeled akin to an ideal diode described by the Shockley equation:

Eq. 3.16 $$J = J_S \left(\exp[\frac{eV}{nk_BT}] - 1\right)$$

where J is the current-density, J_S is the reverse bias saturation current-density, V is the voltage across the diode, and n is the ideality factor. Upon illumination the current density-voltage characteristics shifts downwards and into the power-generating, fourth quadrant. If the photocurrent is assumed to be independent of voltage, the Shockley equation can be rewritten as:

Eq. 3.17 $$J = J_S \left(exp[\frac{eV}{nk_BT}] - 1 \right) - J_{SC}$$

where J_{SC} is the short-circuit current-density.

There are three special points to be considered which assist in the evaluation of OPV performance. The J_{SC} is located at V=0. The open-circuit voltage (V_{OC}) is located at J=0. The maximum power point (V_{max},J_{max}) is located between V=0 and V_{OC} where the JV product is maximized. The fill factor (FF) is defined as:

Eq. 3.18 $$FF = \frac{J_{max}V_{max}}{J_{SC}V_{OC}}$$

The power conversion efficiency (η_P) is then a product of these 3 parameters as:

Eq. 3.19 $$\eta_P = \frac{J_{SC}V_{OC}FF}{P_0}$$

where P_0 is the optical power incident upon the device. Under standard conditions OPVs are compared under AM1.5G with P_0=100 mW/cm^2, alternatively referred to as 1 sun illumination. As an alternative definition for J_{SC}, the device responsivity (R) is written as:

Eq. 3.20 $$R = \frac{J_{SC}}{P_0}$$

Typical values for the V_{OC} of an OPV range between V_{OC}=0.5–1.1 V while the FF ranges from FF=0.5–0.7 in state-of-the-art OPVs.

3.4.3. External quantum efficiency and device operation

The external quantum efficiency (η_{EQE}) is an important parameter because it deconvolutes the spectral nature of the J_{SC}. Figure 3.6 shows the energy level landscape for a typical OPV. The η_{EQE} is the product of four critical efficiencies in the conversion of a photon to electrical current. The absorption efficiency (η_A) is the probability than a photon incident upon the device is absorbed. Optical field modeling can be used to determine the η_A for a given OPV device architecture. The exciton diffusion efficiency (η_D) is the probability that a photogenerated exciton reaches the dissociating interface. Longer L_D are then correlated with large η_D. Excitons that reach the interface can then be dissociated by charge transfer (η_{CT}). In material systems where there is a large offset in molecular energy levels, η_{CT} can be near unity. Finally, the charge collection efficiency (η_{CC}) is the probability that photogenerated charge carriers are able to exit the device at the electrodes before recombining. Geminate recombination is defined as recombination of the correlated electron and hole polaron from the same exciton. Non-geminate recombination is defined as all other electron and hole polaron recombination events. The η_{EQE} is then:

Eq. 3.21 $$\eta_{EQE} = \eta_A \eta_D \eta_{CT} \eta_{CC}$$

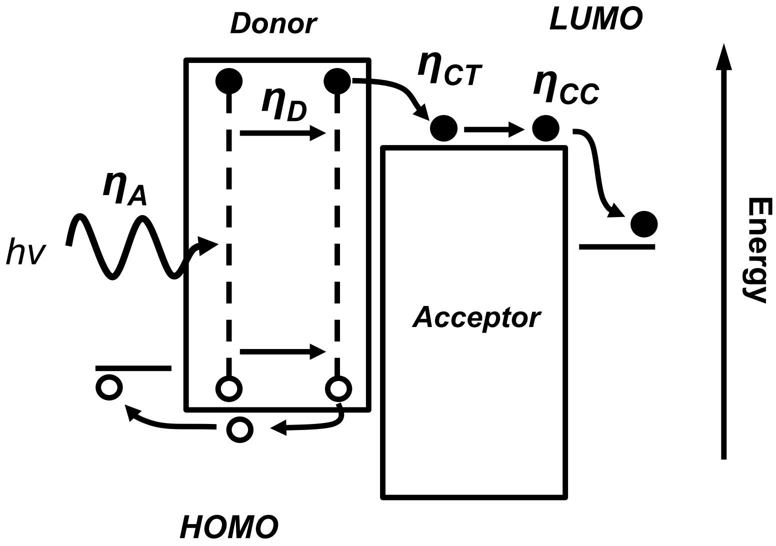

Figure 3.6 Schematic of OPV operation in an energy landscape. In the simplest circumstances, the η_{EQE} is the product of four critical efficiencies: absorption (η_A), exciton diffusion (η_D), exciton dissociation by charge transfer (η_{CT}), and charge collection (η_{CC}).

The η_{EQE} is implicitly a function of illumination wavelength because the incident optical field will dictate both the η_A and η_D. The η_{EQE} is then measured by measuring the photocurrent at zero applied bias while illuminated from a monochromated white light source. A lock-in measurement technique is commonly utilized in order to measure with η_{EQE} with greater sensitivity. The measurement of η_{EQE} also allows for the prediction of J_{SC} as

Eq. 3.22 $$J_{SC} = \frac{e}{hc}\int \lambda \eta_{EQE}[\lambda]S[\lambda]d\lambda$$

where h is Planck's constant and S is the solar spectrum (e.g. AM 1.5G). Self-consistent electrical characterization is achieved when the J_{SC} measured from current-density voltage measurements is equal to that as tabulated from the measured $\eta_{EQE.}$

3.5. Measurement of the exciton diffusion length

The accurate measurement of the L_D is of critical importance. An accurate measurement allows for comparisons to be made and provide a foundation for further experiments. The basic premise behind many measurements of L_D is combining experimental measurements of exciton quenching with mathematical solutions to the exciton diffusion equation [37]. The most general form of the exciton diffusion appears in Eq. 2.27. Further first and second order terms like exciton-exciton annihilation reactions should be added as needed. This premise holds as long as the diffusion equation in use reflects all relevant excitonic generation, transport, and decay pathways. Misrepresenting or not accounting for all the pathways in the system may lead to under- and over-estimates of L_D. In many instances, this equation can be reduced to a single dimension (Eq. 2.28). Additionally, appropriate boundary conditions can be selected to properly reflect the system's exciton dynamics.

It should be noted that in the steady state limit, only the product Dτ can be determined when solving Eq. 2.27. As such, L_D is typically the more commonly reported exciton transport parameter. Separate measurements of τ can be used to tabulate D. Conversely, transient measurement techniques are capable of separately measuring both D and τ.

The techniques available to measure L_D can be broadly categorized into two groups: spectroscopic techniques that measure re-radiated photons from unquenched excitons and charge carrier based techniques that measure photogenerated charges resulting from quenched excitons.

3.5.1. Spectroscopic techniques

Photoluminescence quenching is perhaps the most common method used to measure L_D [42,43,69–72,46,73–75]. The advantage of this method is that simple embodiments can be performed easily, at steady state, and in a fluorimeter. Coupled to this advantage is the obvious requirement that the material of interest be luminescent. The premise of the technique is to measure the photoluminescence of an organic semiconductor with and without the presence of a quenching medium (Figure 3.7). A photoluminescence ratio (PL ratio) can be defined as the measured photoluminescence of the quenched sample divided by the photoluminescence of the unquenched sample as:

Eq. 3.23
$$Exp.PL\ Ratio \equiv \frac{\int PL_Q d\lambda}{\int PL_{UQ} d\lambda}$$

A calculated PL Ratio is generated by modeling the exciton density in both samples, here represented in 1-D.

Eq. 3.24
$$Calc.PL\ Ratio \equiv \frac{\int n[x]_Q dx}{\int n[x]_{UQ} dx}$$

Hence, PL ratios reflect the reduction in exciton density incurred when diffusive motion to a quenching boundary is added to the system. Generally, values of PL ratios will be less than unity. Large differences in the optical field between the quenched and unquenched sample may, in some cases, drive the PL ratio over unity. Another advantage of this technique is that the absolute photoluminescence efficiency (η_{PL}) need not be measured for each sample. As long as the light collection geometry and η_{PL} are constant between the quenched and unquenched samples, both of these quantities divide out when the ratio is taken.

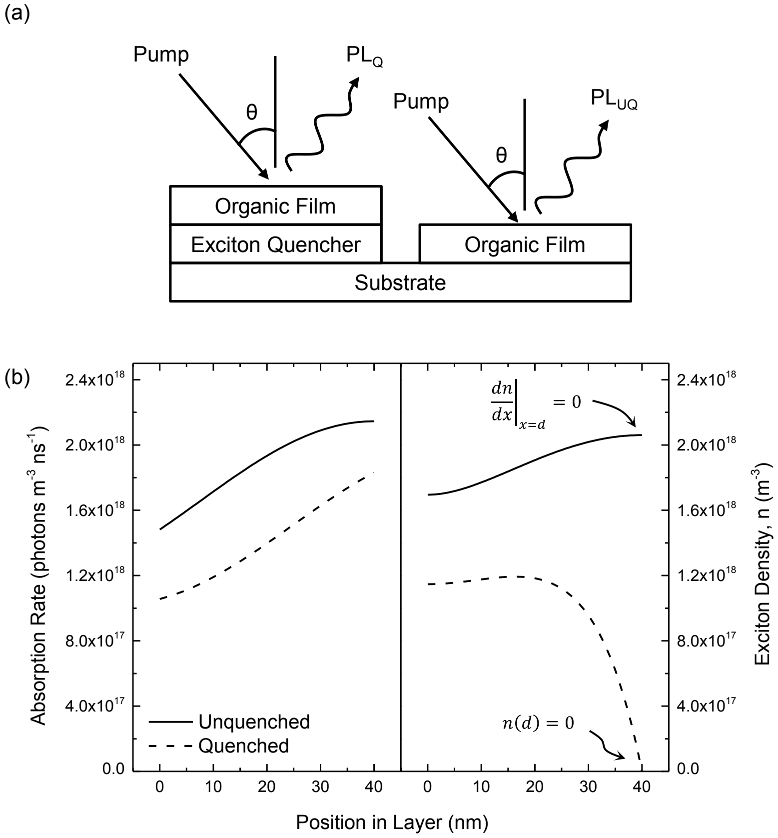

Figure 3.7 (a) Scheme for the basis of photoluminescence (PL) quenching experiments to measure L_D. (b) Optical modeling results for prototypical PL quenching samples.

Typically, PL ratios are measured over a statistically significant number of samples and film thicknesses, making for a more confident measurement of L_D. Measurements of L_D can then be made by solving Eq. 2.27 for both structures. Iterative fits of the measured PL ratios are used to determine L_D. Figure 3.7 shows sample results for solving Eq. 2.27 in 1-D for the quenched and unquenched structures. Here, boundary conditions are used to set the quenching behavior. A non-dissociating, or reflective boundary condition sets the first derivative of exciton density to zero at the substrate interface. A quenching boundary condition sets the exciton density to zero at the quenching interface. Increasing the layer thickness to values much larger than L_D, for example, will increase the PL ratio. This is because most excitons will not be able to travel to the quenching interface in their lifetime. In contrast, layers thinner than L_D will show reduced PL ratios since most of the photogenerated excitons can be quenched. Figure 3.8 shows calculated PL ratios versus sample thickness for a variety of L_D.

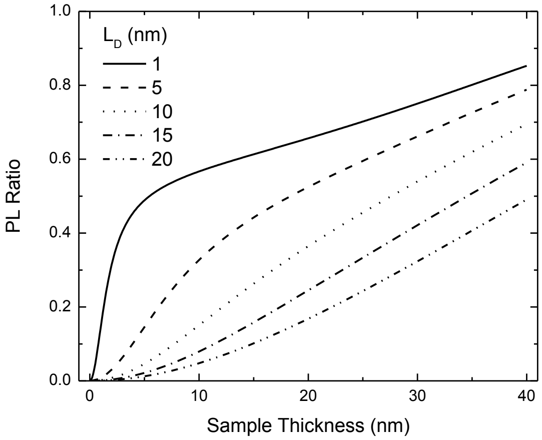

Figure 3.8 Sample calculated PL ratios for a prototypical thickness dependent PL quenching experiment at various L_D. The generated PL ratios tend towards unity for smaller L_D.

Sample layer thicknesses should be chosen such that they span a large range of PL ratios, resulting in confident fit values. Typically, choosing sample layer thicknesses both above and below the expected or predicted L_D will provide a sufficient range.

The number of samples can be reduced by varying other parameters in the system such as the wavelength of incident light [46] or by measuring the transient photoluminescence [71]. Varying the incident wavelength of light is typically referred to as spectrally resolved photoluminescence quenching (SRPLQ) and has the property of altering the exciton generation profile, G[x], in Eq. 2.28. Spectrally resolved photoluminescence quenching is best used when significant changes in the shape of the generation profile can be achieved with changes in incident wavelength [73]. Such changes ensure that the spectral structure of the PL ratios is clearly resolvable. Commonly, the sample thickness can be selected to ensure such a situation occurs. Examples of both an ideal and non-ideal situation are compared in Figure 3.9 where simulated PL ratios are compared to the generation profiles for two samples of different thicknesses. When the film is 80-nm-thick, significant changes to the generation profile are achieved between the unquenched (solid lines) and quenched (dashed line) samples. Further, changes to the incident wavelength show additional unique character. When the film is only 10-nm-thick, the generation profiles remain remarkable similar for each sample at all incident wavelengths. This situation translates to invariant PL ratios versus incident wavelength as seen in Figure 3.9. The thicker film, however, shows clearly resolved spectral structure that will provide confident, unique fits to experimental data sets.

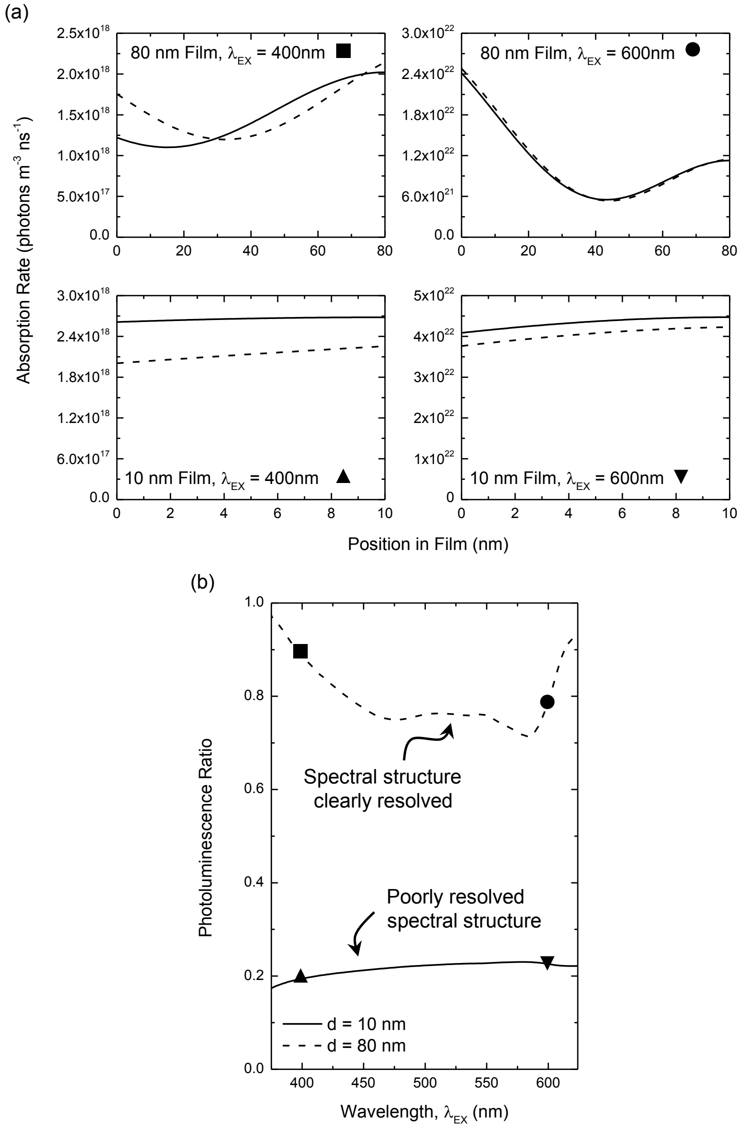

Figure 3.9 Experimental considerations for correctly selecting sample film thicknesses in spectrally resolved photoluminescence quenching (SRPLQ) measurements of L_D. (a) Optical field simulations for a 80-nm and 10nm-thick film at excitation wavelength of λ_{EX} = 400 nm and λ_{EX} = 600 nm. Solid lines represent unquenched films and dashed lines represent quenched samples. (b) Calculated PL ratios as a function of excitation wavelength for a 80-nm (solid) and 10-nm-thick (dashed) film.

Selection of the quenching medium is of utmost importance in photoluminescence quenching measurements as well as the rest of the measurements discussed hereafter. An implicit assumption in the use of a dissociating boundary condition is that the dissociation efficiency of excitons is unity at the quenching interface. If this condition does not hold, underestimates of L_D will result. Typically, quenching materials are chosen such that there is sufficient energetic offset at the quenching interface to overcome the binding energy of the exciton in the layer of interest.

If the quenching material has a smaller energy gap than the material of interest, longer range exciton energy transfer to the quencher is additionally possible [43,69]. This behavior is common when fullerene C_{60} is used to quench OPV donor materials which couple to C_{60} via long-range Förster energy transfer arising from good spectral overlap between film emission and C_{60} absorption (Figure 3.10) [76]. To correctly fit for L_D, Eq. 2.28 must be correctly modified to reflect this additional quenching pathway. If this is not accounted for, overestimates in L_D may result. Figure 3.10 demonstrates this effect by showing how the quenched exciton density profile is impacted by varying the R_0 with C_{60} in a quenched structure. Also displayed is the L_D that would be measured if Förster energy transfer to the quencher was not taken into account. An effective way to circumvent this added complexity is to use a wide energy gap quenching material that neither absorbs incident photons nor couples to the material of interest.

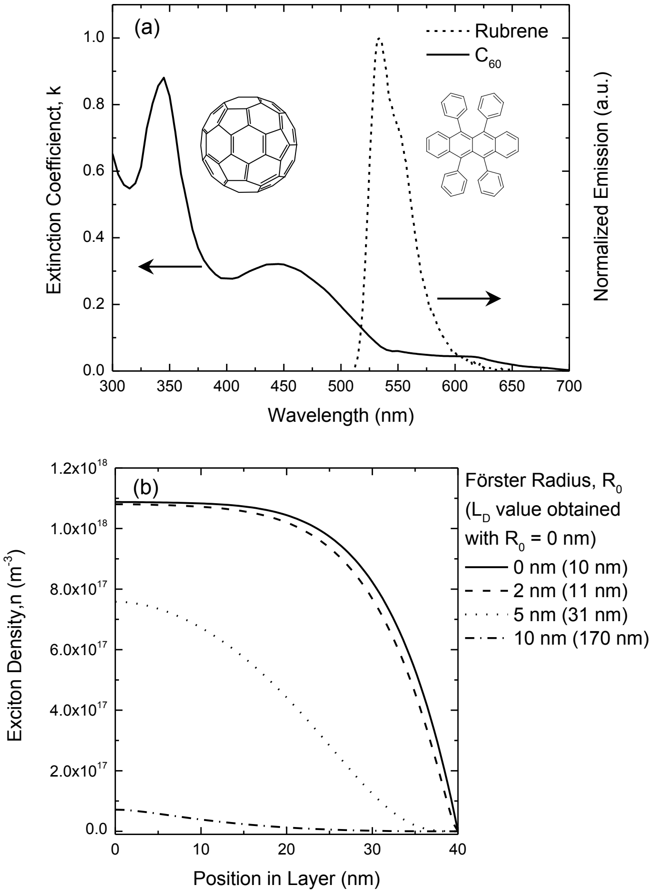

Figure 3.10 (a) Extinction coefficient (k) for C_{60}, a common exciton quenching molecule, and fluorescence for rubrene, a prototypical organic, electron donating molecule. (b) As a demonstration, simulated, quenched exciton densities are shown for various Förster radii (R_0) and a common L_D = 10 nm. Additionally, also shown are the *incorrect* values for L_D that would have been obtained if Förster energy transfer to the acceptor was ignored.

When the layer thicknesses used are much thicker than the optical absorption path length, generation profiles can be reduced to an exponential decay. Such a simplification allows for an analytical solution to Eq. 2.27 when only simple boundary conditions are involved. However, since the L_D for most organic semiconductors is short, the use of thin layers disrupts this assumption because optical interference will generate non-trivial optical fields inside the layer structure. To account for this, Eq. 2.27 can be solved numerically where a transfer matrix formalism is used to accurately determine the optical-electric field responsible for exciton generation. Note that a numerical solution is also required when adding in long range energy transfer to the quencher. Incorrectly modeling the generation profile for a given system can result in both under and over estimates for L_D. Use of a transfer matrix formalism to calculate the optical field does require, however, knowledge of the explicit optical constants for all materials in the system and that the system have smooth interfaces that do not scatter light.

Transient photoluminescence quenching is a useful variation of photoluminescence quenching, typically applied to polymeric systems. Solving Eq. 2.27 in the time domain is usually done by assuming a uniform generation profile. Transfer matrix simulations of the optical field should be performed to ensure this a reasonable approximation. To simplify the experiment, quenching materials can be uniformly dispersed throughout the material of interest at very low concentrations. This allows for a spatially independent solution to Eq. 2.27 where quenching is accounted for by adding a decay term that is dependent on D, since exciton motion to the quenching sites determines the relative amount of quenching. The concentration of the quenching material can also be varied to provide additional confidence, but care should be taken to account for non-linear effects such as aggregation and phase separation.

In a similar manner to transient photoluminescence quenching, transient absorption spectroscopy (TAS) can also be used to extract L_D [77]. In TAS, an organic film is pulsed with a monochromatic excitation followed by a variable wavelength probe excitation. By measuring the differential absorption on timescales shorter than the excited state lifetime, a fine determination of exciton dynamics is achievable. Typically, TAS spectra are collected for a variety of excitation densities. In a similar manner to transient photoluminescence quenching, exciton motion to quenching events can be modeled and fit to determine D. When large excitation densities are used, both quenching to extrinsic sites and exciton-exciton annihilation should be considered. Eq. 2.27 can be further updated to reflect bimolecular recombination events by adding terms of order n^2. Assessing the mechanism and activation of bimolecular recombination is often complex and extracted interaction lengths are not necessarily directly attributed to L_D. A distinct advantage of TAS is its ability to measure inhomogeneity in exciton energy transfer on the scale of the exciton lifetime and shorter. This is in stark contrast to the steady state photoluminescence quenching measurements described earlier in this section.

3.5.2. Charge carrier techniques

Charge carrier techniques to measure L_D are useful when the material of interest does not emit light, as required by photoluminescence quenching techniques. Perhaps the simplest incarnation is to fabricate bilayer, planar heterojunction organic photovoltaic device and fit the measured external quantum efficiency (η_{EQE}) spectra using a transfer matrix formalism coupled to a solution to the exciton diffusion equation (Eq. 2.27). Instead of forming a PL ratio, however, the exciton flux to the quenching interface is transformed into a prediction for the η_{EQE}. Iterative fits between calculated and measured η_{EQE} will result in measurements for L_D as depicted in Figure 3.11. While device-based techniques offer estimations for L_D they are additionally sensitive to other loss pathways such as a non-unity charge carrier collection efficiency [78]. Not accounting for losses in charge carrier collection would results in underestimates for L_D. For example, the fit value of L_D in Figure 3.11 for boron subphthalocyanine chloride (SubPc) is an underestimate, lower than what is measured for SubPc using photoluminescence quenching techniques. Device based analytic techniques to measure parameters like collection efficiency are available and devices can be fabricated in such a way to minimize these losses, but device based measurements should only be used as a zero-order method for estimating L_D.

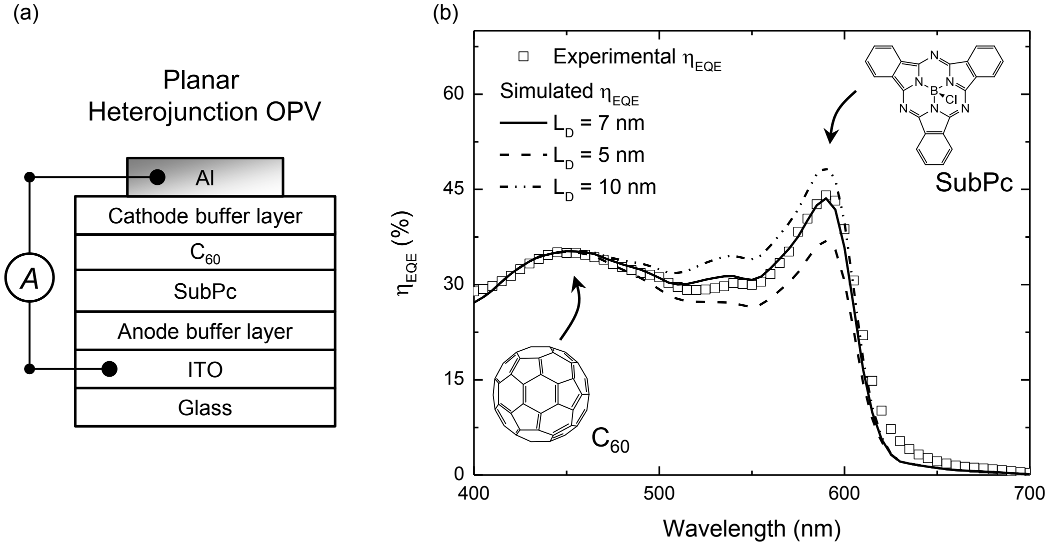

Figure 3.11 (a) Typical planar heterojunction organic photovoltaic device that would be used in modeling of external quantum efficiency (η_{EQE}) for measurement of L_D. (b) Modeling results in the fitting of η_{EQE} for the measurement of L_D.

Time-resolved microwave conductivity is another technique that is sensitive to photogenerated charge carriers [79]. This technique is advantageous because it does not require the collection of charge carriers. This electrode-less technique measures the time dependent change in reflected power from a microwave cavity, inside of which a quenched film is located. Changes in the charge carrier density in the quenching medium are proportional to the reflected power. While this technique is not sensitive to charge carrier collection losses, it does require that the quenching medium, often TiO_2, be more conductive than the material of interest. Since this method does not require an unquenched reference sample, care should be taken to precisely determine the optical field incident upon the structure. Doing so will allow for accurate determination of photon absorption and exciton generation.

3.5.3. Imaging exciton diffusion

In terms of accurately measuring L_D, all the techniques described hereto are equally dependent on the exact formulation and usage of the exciton diffusion equation (Eq. 2.27). If an incorrect or over-simplified form is utilized, errors is measuring L_D will result. Alternatively, directly imaging exciton density distributions is highly advantageous since solving Eq. 2.27 is not directly required [80,81]. For this technique, the excitation light should be as spatially focused and uniform as possible. Focusing a laser beam through microscope objectives is relatively straightforward, and the sample emission can then be focused onto a CCD camera for imaging, though scanning techniques may be employed as well. One limiting condition for this technique is that the L_D for the system to be longer than the spatial resolution of the optical imaging technique. Typically, resolution below ~1 μm becomes increasingly difficult. Recent developments in sub-diffraction limit imaging may be able to reduce this limit further. As with many of the techniques discussed hereto, this technique also requires the material to be emissive. The simplicity is attractive, though, as the mean squared displacement versus time for the exciton can be directly measured and fit with a simple diffusive model akin to Eq. 2.33.

3.5.4. Comparison of L_D measurement techniques

When comparing the available techniques to measure exciton diffusion, one must balance the desired resolution with the ability to satisfy critical requirements for the accurate measurement of L_D. To aide researchers in this decision, Table 3.1 classifies and compares the techniques discusses hereto based on typical measurement ranges, advantages, common constraints, and assumptions [82].

Table 3.1 Comparison of techniques commonly used to measure the L_D of organic semiconductors. Adapted with permission from [37].

Method	Detection Scheme	Measurement Range	Advantages, Constraints, and Assumptions
Photoluminescence Quenching	Photons	1 nm	Can be carried out at steady state, Requires emissive organic semiconductor
Transient Absorption Spectroscopy	Photons	1 nm	Information at short time ($<10^{-9}$ s) scales, Requires fast detection electronics
Imaging	Photons	1 μm	Simplified data treatment, Requires emissive organic semiconductor and long diffusion length
Time Resolved Microwave Conductivity	Charge carriers	1-10 nm	Electrode-less technique, Requires quenching layer more conductive than organic semiconductor
Surface Photoconductivity	Charge carriers	1 μm	Requires large surface photoconductivity, Typically paired with organic single crystals
Device Modeling	Charge carriers	1-10 nm	Typically paired with planar OPVs with well-defined interfaces, Requires assumptions for other device related charge loss pathways

4. Exciton diffusion in dilute systems: SubPc

To begin understanding the nature of the typically short exciton diffusion length (L_D), it is critical to first understand the underlying nanoscopic energy transfer events that mediate exciton transport. In the case of a fluorescent molecule like boron subphthalocyanine chloride (SubPc), energy transfer is thought to be predominantly controlled by self-Förster energy transfer as SubPc has a relatively long self-Förster radius (self-R_0~1 nm) compared to the average intermolecular separation (<1 nm) [72]. Inspection of the Förster radius (Eq. 2.24) reveals that, among others, the photoluminescence efficiency (η_{PL}) is a key parameter [33]. Interestingly, η_{PL} has long been optimized in phosphorescent organic light-emitting devices (OLEDs) [25]. In an OLED, diluting an emissive phosphorescent guest molecule into a wide energy-gap host matrix suppresses non-radiative exciton decay pathways, enabling near unity η_{PL} at dopant concentrations <5–10 wt.% [83]. If η_{PL} can be increased, it stands to reason that the self-R_0 and L_D can be increased as well. Overall, understanding the concentration dependence of exciton transport may also be useful as a probe for the dominant mechanisms for nanoscopic energy transfer in organic thin-films.

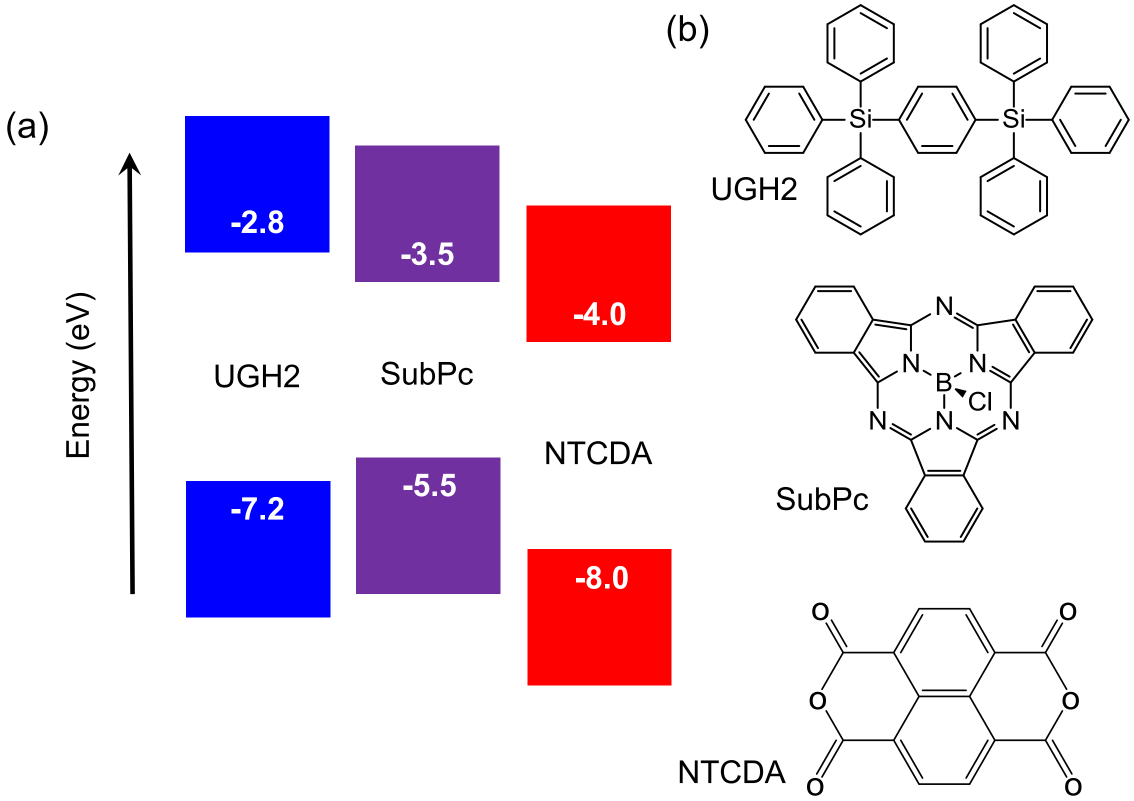

Figure 4.1 Molecular energy levels (a) and molecular structures (b) for SubPc, UGH2, and NTCDA.

4.1. Concentration dependence of exciton transport

As the rate of Förster energy transfer is inversely proportional to the average intermolecular separation (d), increases in d reduce the rate of energy transfer to neighboring molecules (Eq. 2.23). All other parameters remaining the same, increases in d resulting from dilution reduce the rate of energy transfer, diffusivity (D), and L_D. The concentration dependence of η_{PL}, however, as well as other parameters that affect Förster energy transfer suggests there may be a more complex relationship between L_D and concentration.

4.1.1. Mesoscopic diffusion

To begin, the L_D for SubPc was measured as a function of concentration by dilution in the wide energy-gap host material p-bis(triphenylsilyl)benzene

(UGH2) [84,85]. The wide energy-gap of UGH2 (E_g~4.4 eV) ensures that excitons photogenerated on SubPc neither quench nor energy transfer to UGH2. Figure 4.1 shows the energy levels and molecular structures for SubPc and UGH2 [84,86]. Importantly, the energy levels of SubPc are nested within those of UGH2. The concentration dependence of L_D for SubPc diluted in UGH2 was measured with thickness dependent photoluminescence (PL) quenching. Naphthalene-1,4,5,8-tetracarboxylic acid dianhydride (NTCDA) is used as the exciton quencher due to its favorable alignment for electron transfer from SubPc and its large energy-gap (E_g~4 eV) [43]. The large energy-gap prevents long-range Förster energy transfer to the quencher, ensuring that all dissociation of photogenerated excitons and reduction in PL is the result of direct charge transfer at the dissociating interface. Figure 4.1 also shows the energy levels and molecular structure for NTCDA. Figure 4.2 shows the experimentally measured PL ratios for 100, 50, 25, and 10 wt.% SubPc diluted in UGH2. Also shown are the corresponding fits and the fit values for L_D. Here, L_D=(10.7 ± 1.0) nm is found for a neat film of SubPc, consistent with previously reported values [43,72]. The L_D is measured to increase continuously with dilution to a maximum value of L_D=(15.3 ± 1.5) nm for a film containing 25 wt.% SubPc. The increase in L_D is observed despite the concomitant increase in the average intermolecular spacing, and is larger than the value measured in a pure film for all dilutions investigated. For reference, d increases from d=0.48 nm for a pure film of SubPc to d=0.8 nm for a film containing 25 wt.% SubPc corresponding the concentration with the longest measured L_D (Figure 4.3). This counterintuitive result further confirms that the nanoscopic energy transfer events that mediate exciton diffusion have a non-trivial dependence on concentration, warranting further investigation.

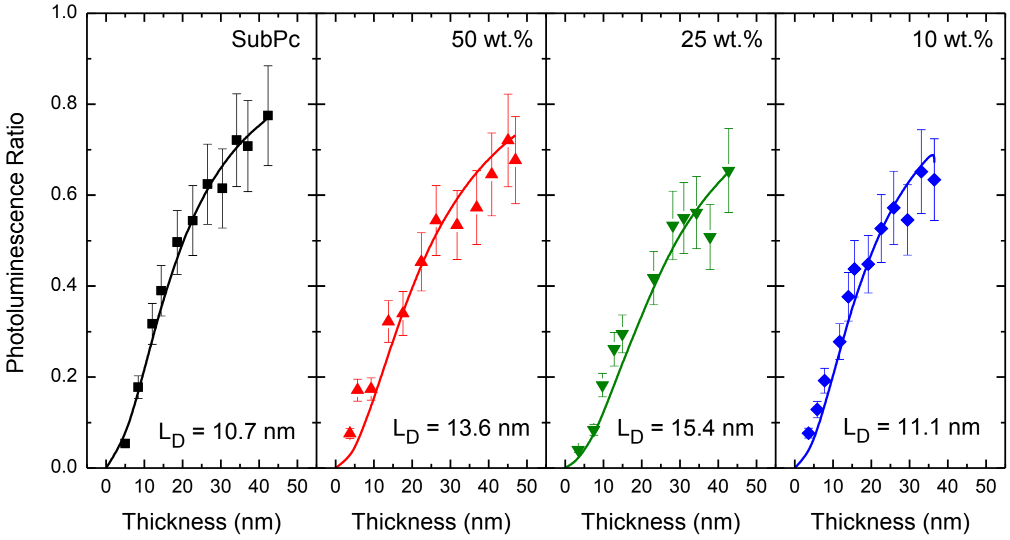

Figure 4.2 Experimental and simulated photoluminescence (PL) ratios for various concentrations of SubPc diluted in UGH2. Also shown are the corresponding fits and fit values for L_D at each concentration. Adapted with permission from [87].

4.1.2. Nanoscopic energy transfer

In order to quantitatively understand the role of dilution on L_D, a simple model connecting the mesoscopic diffusion and nanoscopic Förster energy transfer can be employed. For a simple cubic lattice where only nearest neighbor interactions are considered the L_D can be rewritten from Eq. 2.26 as:

$$\text{Eq. 4.1} \qquad L_D = \sqrt{A}\frac{R_0^3}{d^2}$$

where A accounts for disorder within the films. By accounting for disorder in this way, it is assumed that the degree of disorder is relatively small compared to thermal energy at room temperature (~25 meV) and can be averaged over during the lifetime of the exciton. A more detailed account of disorder is required when the degree of disorder is larger or the temperature is reduced (Chapter 9). Separate measurements of the photoluminescence spectrum, index of refraction (n), extinction coefficient, and η_{PL} at various concentrations allows for the tabulation of the concentration dependent self-R_0 (Eq. 2.24).

The absorption cross-section is defined as the absorption coefficient divided by the molecular density (ρ) of the film and is independent of the film concentration. The ρ is typically extracted from the bulk powder density and molecular weight (Appendix). For SubPc, $\kappa = 0.845\sqrt{2/3}$, appropriate for an amorphous film with randomly oriented, rigid dipoles [88]. The value for n is taken at the wavelength corresponding to the maximum value of the spectral overlap integral (Eq. 2.24). The d is taken as the Wigner-Seitz radius for a molecular thin film evaluated as:

Eq. 4.2 $$d = \left(\frac{3}{4\pi\rho}\right)^{1/3}$$

and shown as a function of dilution in Figure 4.3.

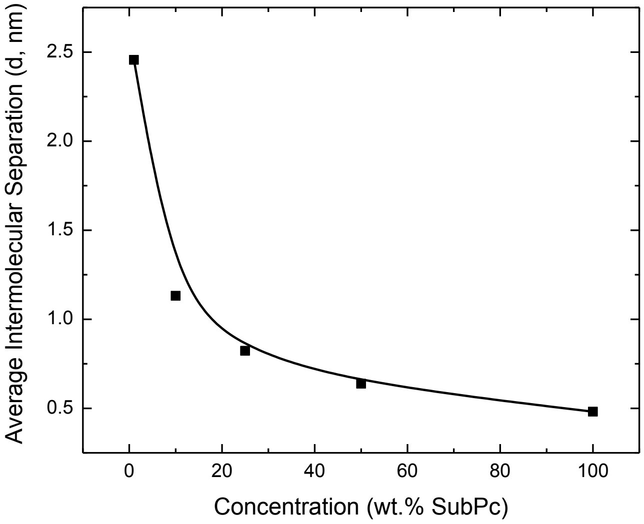

Figure 4.3 Average intermolecular separation for SubPc diluted in UGH2 over the range of concentrations investigated.

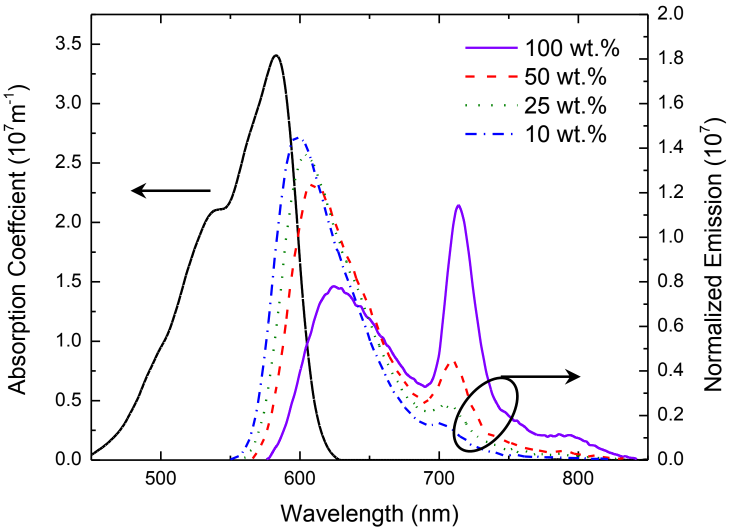

Figure 4.4 Absorption coefficient for SubPc along with the area-normalized photoluminescence spectra at four various concentrations of SubPc diluted in UGH2.

Figure 4.4 shows the absorption coefficient for SubPc along with the normalized photoluminescence spectra for four concentrations of SubPc diluted in UGH2. Interestingly, the photoluminescence spectra shift towards shorter wavelengths upon dilution. This can be attributed to a solid-state solvation effect where higher energy, polar excited states are stabilized in less polar solvents [89–91]. The low dielectric constant of UGH2, owing to is non-polar nature, creates a favorable environment for higher energy excitons on SubPc, increasing the spectral overlap upon dilution (Figure 4.5). Additionally, the low dielectric constant of UGH2 serves to reduce n at the wavelength of maximum spectral overlap which is found to decrease nearly 20% for films containing 1 wt.% SubPc in UGH2 compared to pure film (Figure 4.5).

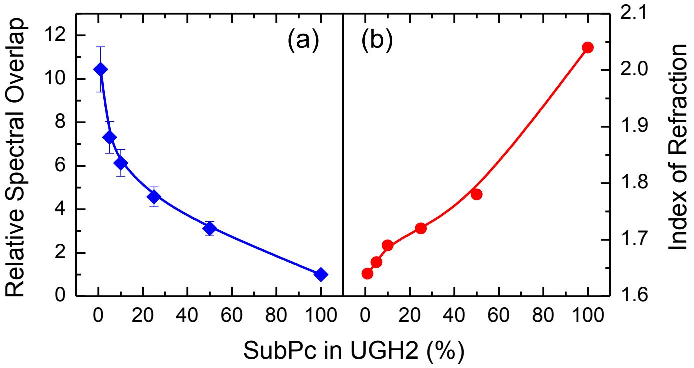

Figure 4.5 Relative spectral overlap (a) and index of refraction at the wavelength of maximum spectral overlap (b) for SubPc as a function of concentration diluted in UGH2. Adapted with permission from [87].

Examination of the photoluminescence spectra in Figure 4.4 also reveals that the peak located at wavelength λ~710 nm decreases in intensity upon dilution. The narrow linewidth and reduced energy suggest it may represent a dimer or aggregate state where the excitonic wavefunction is delocalized over one or several molecules [92]. The presence of such a state is in qualitative agreement with the concentration dependent photoluminescence spectra as dilution in a host matrix may disrupt dimerization or aggregation.

The η_{PL} and exciton lifetime (τ) were also separately measured as a function of concentration [93]. Interestingly, the η_{PL} is observed to increase from a value of η_{PL}=(1.0 ± 0.1)% in neat film to η_{PL}=(22.0 ± 3.0)% in a dilute film containing 1 wt.% SubPc (Figure 4.6). Additionally, the exciton lifetime is observed to increase from a value of τ=(0.5 ± 0.1) ns in neat film to τ=(3.0 ± 0.4) ns at 1 wt.% SubPc. Using Eq. 2.19 and Eq. 2.20, the radiative decay rate is tabulated to range from k_R=(20 ± 4)x10^6 s^{-1} in neat film to k_R=(70 ± 10)x10^6 s^{-1} in films containing 1 wt.% SubPc, while the non-radiative decay rate decreases from a value of k_{NR}=(2.0 ± 0.3)x10^9 s^{-1} in neat film to k_{NR}=(0.26 ± 0.1)x10^9 s^{-1} in films containing 1 wt.% SubPc.

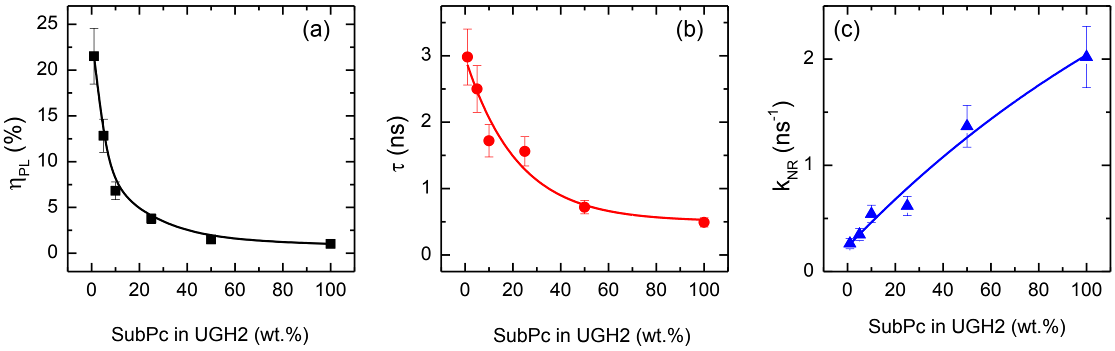

Figure 4.6 (a) Photoluminescence efficiency (η_{PL}), (b) exciton lifetime (τ), and (c) non-radiative decay rate (k_{NR}) for SubPc as a function of dilution in UGH2. Adapted with permission from [87].

With all the concentration dependent variables in Eq. 2.24 separately measured, the tabulated value of the self-R_0 is found to increase from $R_0=(1.0 \pm 0.1)$ nm in neat film to $R_0=(3.8 \pm 0.4)$ nm for films containing 1 wt.% SubPc in UGH2 (Figure 4.7).

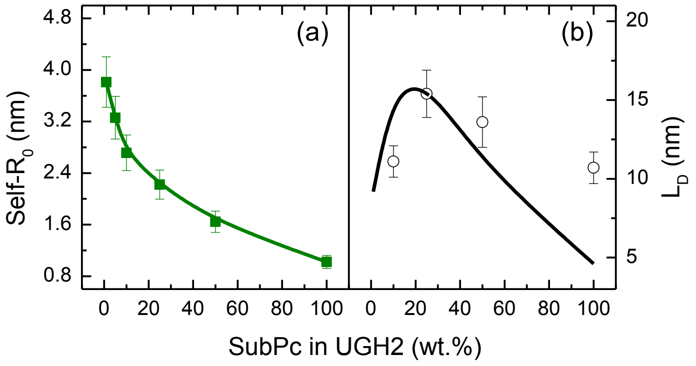

Figure 4.7 Self-Förster radius (a) and L_D (b) for SubPc as a function of concentration diluted in UGH2. Also shown is the L_D predicted from Eq. 4.1. Adapted with permission from [87].

Using Eq. 4.1, the tabulated values for the self-R_0 with a value of A=1.0 can be used to predict the concentration dependence for L_D. Figure 4.7 compares the predicted and measured values for SubPc L_D as a function of concentration. Good agreement is found between for the majority of concentrations investigated. Deviations from this simple model observed for neat film may reflect the limitations of the Förster model in describing short transfer distances and the need to consider shorter-range Dexter energy transfer hopping events.

4.2. Role of the wide energy-gap host

To determine the role of host matrix, the L_D for SubPc was measured as a function of concentration in another wide energy-gap host, bathophenanthroline (BPhen) [94]. The molecular structure and energy levels for BPhen as compared to SubPc can be seen in Figure 4.8. BPhen was selected as it preserves the same energy level relationship with SubPc, yet has a different molecular weight and bulk powder density. As with UGH2, the L_D was measured with thickness dependent photoluminescence quenching utilizing NTCDA as the exciton quencher. Figure 4.8 also shows the experimental PL ratios along with the corresponding fits and fit values for L_D at 100, 75, 50, and 25 wt.% SubPc in BPhen. Interestingly, SubPc diluted in BPhen shows a similar to enhancement in L_D upon dilution as is found with the UGH2 host. The L_D was measured to increase to L_D=(15.3 ± 1.0) nm for films containing 25 wt.% SubPc in BPhen. As in the case of UGH2, the L_D is optimized at 25 wt.% SubPc.

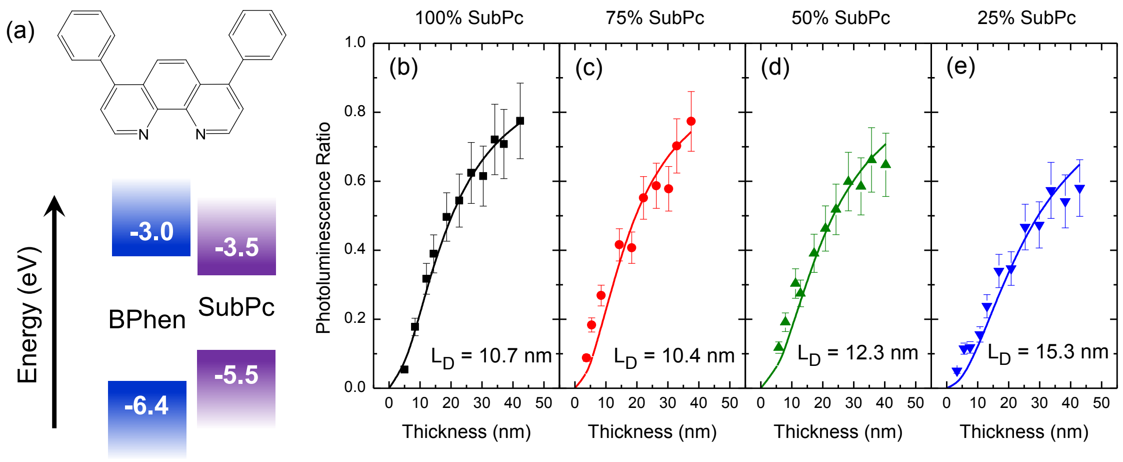

Figure 4.8 (a) Molecular structure and energy levels for BPhen as compared to SubPc. (b) Experimental photoluminescence ratios and corresponding fits and fit values for L_D at four concentrations of SubPc diluted in BPhen.

To deconvolute the difference in molecular density between UGH2 ($\rho=1.2\times10^{27}$ m^{-3}) and BPhen ($\rho=2.0\times10^{27}$ m^{-3}), the L_D for SubPc in each host is shown as a function of molecular concentration in Figure 4.9. Clearly, the host plays an important role in the determining the concentration dependence of L_D. Figure 4.9 also shows the relationship between the self-R_0^3 and d^2 for each host. If R_0^3 increases faster than d^2, enhanced L_D will be achieved with dilution (Eq. 4.1). While dilution in both hosts leads to an increase in L_D, the self- for SubPc in a BPhen host exhibits a smaller increase for concentrations >25 wt.% SubPc as compared to the UGH2 host. This leads to the later onset in peak L_D upon dilution. Inspection of the parameters that control the self-R_0 reveal that both the spectral overlap integral and η_{PL} are likely responsible for the delayed onset. The host, then, dictates the balance between R_0 and d as it determines both the stabilization of the excited state and deactivation of non-radiative decay pathways upon dilution. It is also important to note that both UGH2 and BPhen are non-polar. A more polar host may reduce the spectral overlap and increase the n at the wavelength at maximum overlap upon dilution, thereby reducing enhancements in L_D.

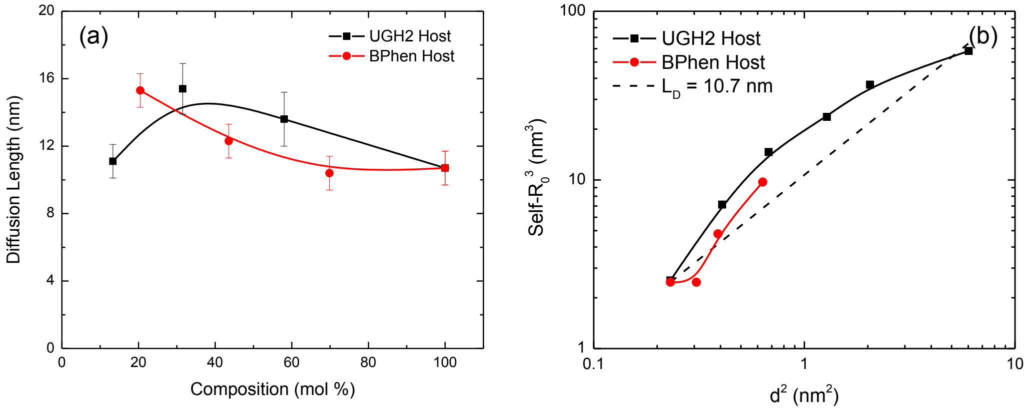

Figure 4.9 (a) Comparison of L_D versus molecular composition for SubPc in BPhen versus UGH2. (b) Self-Förster radius (R_0^3) versus average intermolecular spacing (d^2) for SubPc with in both BPhen and UGH2 hosts.

4.3. Solution photoluminescence of SubPc

To confirm the presence of the solid state solvation effect, solution photoluminescence was recorded for SubPc as a function of concentration in two common solvents, benzene and dimethyl sulfoxide (DMSO). Benzene was selected for its vanishingly small molecular dipole, and DMSO was selected for its relatively large dipole moment (~13 Debye) [95]. If the dielectric environment affects the photoluminescence energy in the solid state, a similar effect should be seen in solution as the dielectric environment is varied. Photoluminescence spectra for SubPc in benzene and DMSO over a range of concentrations are shown in Figure 4.10. In each experiment, the concentration was gradually reduced until the wavelength of peak photoluminescence remained constant. At this point, the SubPc photoluminescence is independent of concentration and representative of the interaction between the molecular excited state and the solvent's dielectric environment.

Interestingly, the wavelength of peak photoluminescence (λ_{MAX}) is shorter in benzene (λ_{MAX}~572 nm) than in DMSO (λ_{MAX}~578 nm). As was seen in the solid state, the less polar dielectric environment stabilizes higher energy excited states, confirming the presence of a solvation effect in solution and suggesting the possibility of a similar solid state solvation effect in the thin-films. Of additional interest is the lack of a lower energy, narrow linewidth feature at λ~710 nm as was measured in films of pure SubPc. In fact, only the solution photoluminescence spectrum recorded in DMSO at the solubility limit of SubPc shows possible evidence for this state in solution. The lack of this state in solution further suggests its assignment as a dimer or aggregate state.

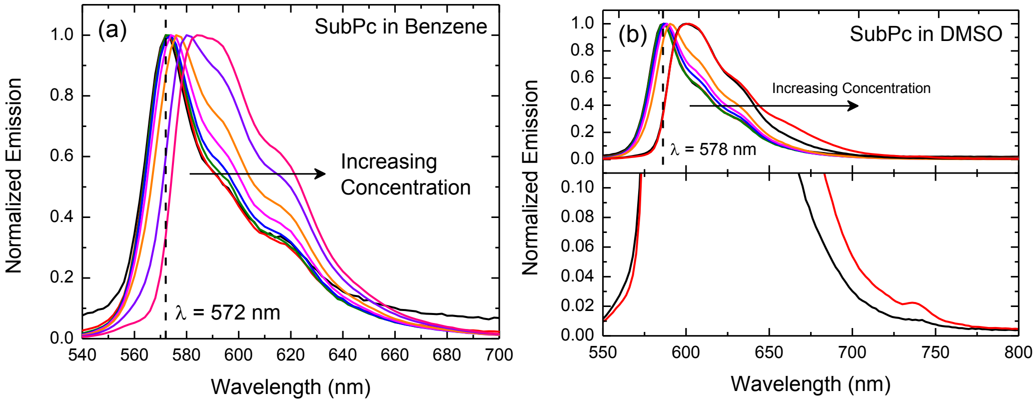

Figure 4.10 Solution photoluminescence spectra recorded for SubPc solvated in benzene (a) and DMSO (b). The wavelength of maximum photoluminescence at the lowest concentration is denoted with the dashed line.

4.4. OPVs incorporating dilute SubPc donor layers

In order to test whether the enhanced L_D of SubPc translates to an improvement in organic photovoltaic device (OPV) performance, planar heterojunction devices were constructed incorporating a dilute donor layer of SubPc in UGH2.

4.4.1. Enhanced electrical performance

Devices were constructed on indium-tin-oxide (ITO) coated glass substrates with the following layer structure: a 10-nm-thick buffer layer of MoO_x [96], a 12-nm-thick dilute donor layer consisting of SubPc dispersed in UGH2 with variable composition, a 5-nm-thick donor layer of SubPc, a 35-nm-thick acceptor layer of C_{60}, and a 10-nm-thick exciton blocking layer of bathocuproine (BCP) [55]. Devices were capped with a 65-nm-thick Al cathode. The inclusion of a thin, neat layer of SubPc at the donor-acceptor (D-A) interface increases the overall absorption efficiency of the device. Being close to the interface, however, an enhanced L_D is not necessary for efficient exciton diffusion this layer. The performance of OPVs containing a dilute donor layer is compared to that of a separately optimized planar heterojunction OPV consisting of a 13-nm-thick layer of SubPc and a 35-nm-thick layer of C_{60}. It is important to note that an OPV containing a dilute donor layer with SubPc composition <66.7 wt.% will contain less SubPc than the control device. The layer structures for OPVs based on both dilute and conventional donor layers are shown in Figure 4.11.

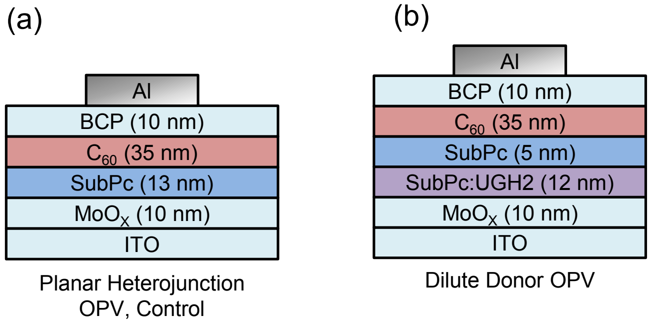

Figure 4.11 Device schematics for the planar heterojunction OPV control device (a) and the dilute donor OPV (b). Adapted with permission from [87].

Current density-voltage characteristics for OPVs containing dilute donor layers of varying composition and the control device are shown in Figure 4.12 under AM1.5G illumination at (134 ± 5) mW/cm^2. A clear increase in the short-circuit current density (J_{SC}) is observed relative to the control device for a dilute donor layer OPV containing 50 wt.% SubPc. The J_{sc} increases as a function of dilution with an eventual roll-off as the concentration of SubPc is reduced below 25 wt.% SubPc. This roll-off is attributed to a reduction in the donor absorption efficiency as well as a reduction in L_D. Impressively, the J_{sc} is maximized for dilute donor layer OPVs containing 50 wt.% SubPc, despite the fact that the device contains 15% less SubPc than the control device. No significant change in the open-circuit voltage (V_{OC}) is observed upon dilution, and only the 10 wt.% dilute donor device shows any reduction in fill factor. The constant fill factor observed for OPVs containing ≥25 wt.% SubPc suggests that there is no significant change in the charge collection efficiency under forward bias over this range of compositions. Additionally, no change in the magnitude or shape of the dark current density-voltage response is observed over the same range of film compositions, with only the case of 10 wt.% SubPc showing a reduced current, indicating an increase in resistance (Figure 4.13). Figure 4.12 shows the dependence of the power conversion efficiency (η_P) on dilution, reaching a peak value of η_P=(4.4 ± 0.3)% for dilute donor OPVs containing 50 wt.% SubPc in UGH2. For comparison, the efficiency of the optimized control device is η_P=(3.3 ± 0.3)%, consistent with previous reports [97]. The performance of the dilute donor OPV rivals that of other reported bulk heterojunctions based on SubPc-C_{60} [98]. While the observation of such a substantial increase in efficiency with dilution may seem counterintuitive, this result highlights the unrealized potential for further performance gains in simple, planar heterojunction OPVs with directed optimization of L_D. The potential for increased photocurrent with less absorbing material may also have a significant impact on the design of multi-junction OPVs where multiple sub-cells in series often compete for absorption in overlapping regions of the solar spectrum [99].

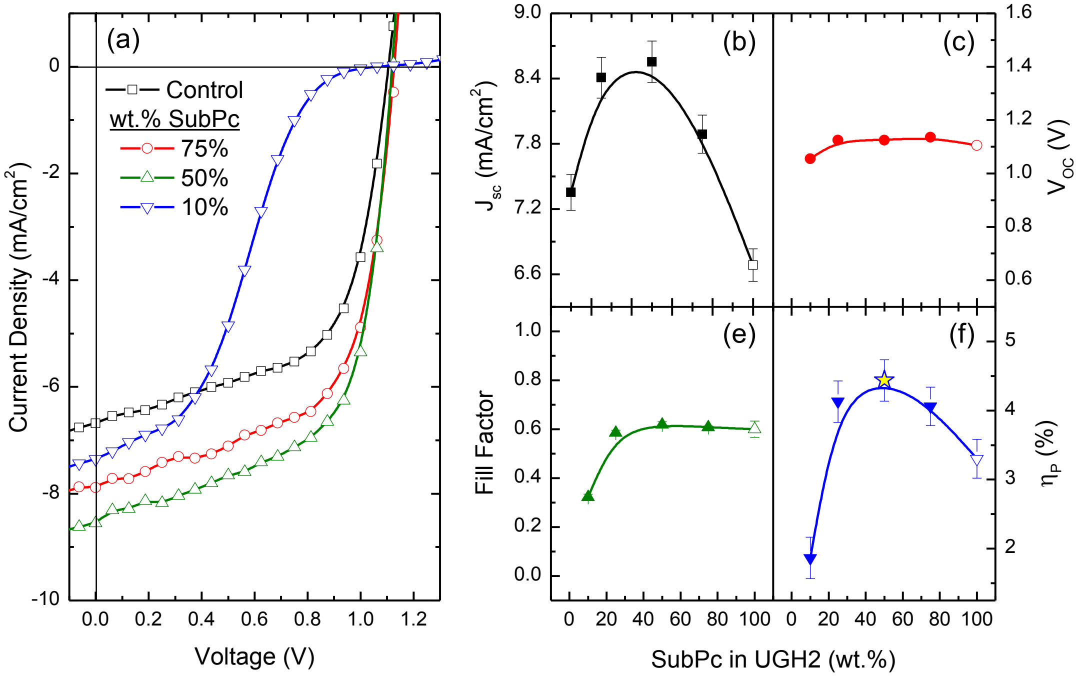

Figure 4.12 (a) Current-density voltage characteristics the control OPV device as well as dilute donor OPVs at three concentrations under AM1.5G solar simulated illumination at 134 mW/cm^2. (b) Extracted short-circuit current density (J_{SC}), open-circuit voltage (V_{OC}), fill factor, and power conversion efficiency (η_P). Adapted with permission from [87].

It is important to note the dilute donor OPVs with similar device architectures were fabricated incorporating BPhen as the inert host material in replacement of UGH2. These devices, however, displayed very poor electrical characteristics and demonstrated very low V_{OC}, fill factor and η_P. It is suspected that the high charge carrier mobilities in

BPhen with respect to SubPc led to increased non-geminate recombination which, in turn, leads to reduced V_{OC} and charge collection efficiency [100].

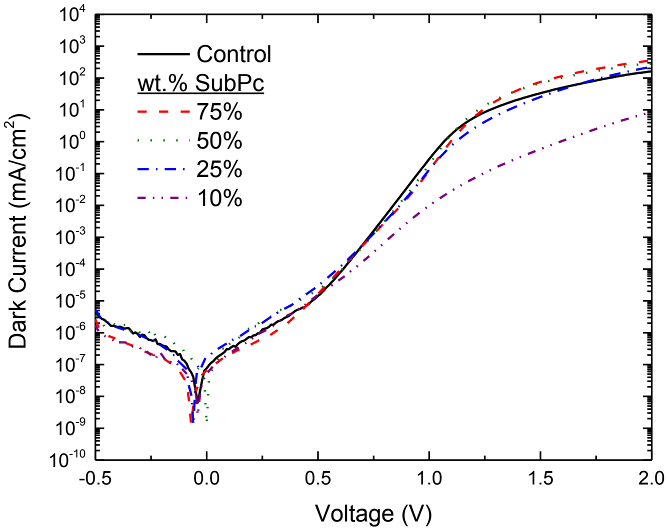

Figure 4.13 Dark current-density voltage characteristics for the control OPV device as well as dilute donor OPVs at four different concentrations.

In order to confirm that the increase in performance with dilution comes from an increase in L_D for SubPc, Figure 4.14 compares the external quantum efficiency (η_{EQE}) of the best performing dilute donor layer OPVs with that of the control. The η_{EQE} is further defined as the product of the absorption efficiency (η_A) and the internal quantum efficiency (η_{IQE}). The photoresponse from SubPc in the η_{EQE} spectrum is observed to increase with dilution while the C_{60} photoresponse remains unchanged. In order to access the potential role of an enhanced L_D, it is essential to decouple changes in η_A from the $\eta_{EQE,}$ thereby investigating changes in the η_{IQE}, which characterizes the product of the exciton diffusion, dissociation, and charge collection efficiencies. In order to account for the varying η_A of SubPc in these structures, the reflectivity is measured through the ITO anode, reflecting off the Al cathode. With negligible optical transmission through the cathode, one minus reflectivity (1-R) offers a measure of the relative η_A (Appendix). Figure 4.14 also shows 1-R for each device structure. Due to optical losses in the electrodes, 1-R is an overestimate of η_A, and the data in Figure 4.15 is therefore an underestimate to the actual η_{IQE}. Assuming that the charge collection efficiency is unchanged for moderate levels of dilution, the observed increase in η_{IQE} reflects an increase in the diffusion efficiency for excitons created on SubPc. This is consistent with the observation that the η_{IQE} is only enhanced for λ>500 nm, a range of the spectrum corresponding predominantly to optical absorption in SubPc. Excitingly, relative η_{IQE} is measured to achieve values over 80% in the dilute donor OPVs incorporating a 25 wt.% layer of SubPc diluted in UGH2.

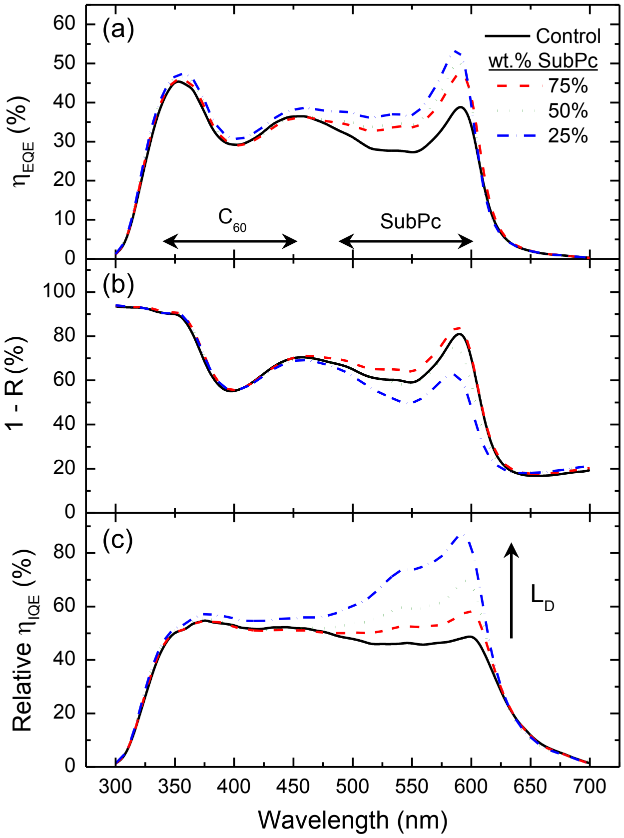

Figure 4.14 External quantum efficiency (η_{EQE}), one minus reflection (1-R), and relative internal quantum efficiency (η_{IQE}) for the optimized dilution donor OPVs as a function of dilute layer concentration. Adapted with permission from [87].

4.4.2. Optical modeling

In analyzing improvements to device performance with dilution, it is also important to also include the impact of changes to the optical field in the device. By reducing optical absorption away from the D-A interface with dilution, the intensity of the optical field can be enhanced in the thin 5-nm-thick layer of SubPc at the D-A interface (Figure 4.11). Increased absorption nearer to the interface reduces the distance an exciton must diffuse, and can enhance the η_{IQE} with no increase in L_D. In order to decouple this possibility from increases in L_D with dilution, optical simulations utilizing transfer matrix formalism were performed for the optical field at λ=590 nm and the rate of absorbed photons per unit volume under AM1.5G solar illumination at 134 mW/cm^2 (Figure 4.15). The results indicate that there is an 11% increase in photons absorbed across the 5-nm-thick SubPc layer in the dilute device with respect to the control device. If all of these additional excitons are harvested, the increased absorption would lead to only an additional 0.3 mA/cm^2 in J_{SC}. Since the dilute donor devices show an increase of 1.8 mA/cm^2 in J_{SC} (Figure 4.12), a majority of the increase in photocurrent can be attributed to an increase in exciton diffusion. Interestingly, these dilute layers could be considered akin to the optical spacer layers reported previously with the distinction that photocurrent can still be generated and efficiently collected from the dilute layers. This effect will be considered in more detail in Chapter 5.

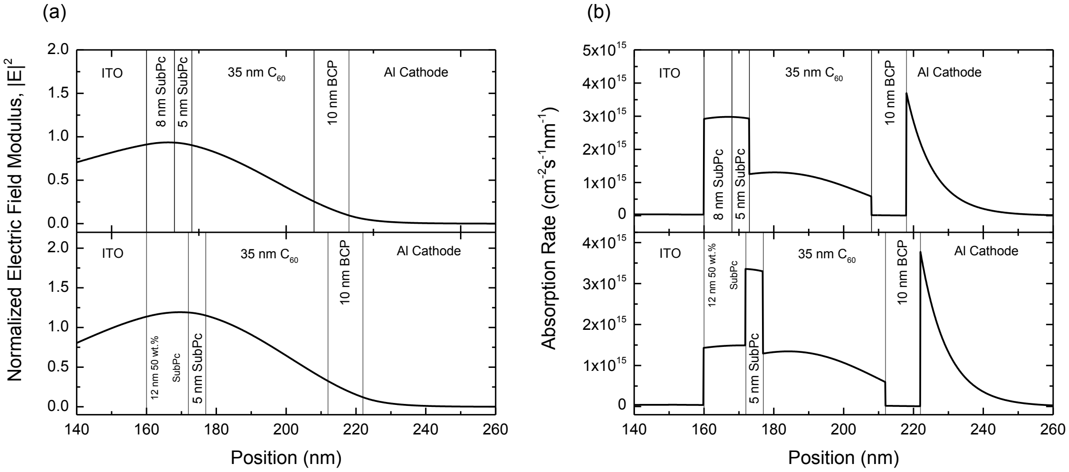

Figure 4.15 Transfer matrix simulations of the optical field at λ=590 nm and the optical absorption rate for the control device and best performing dilute donor device incorporating a 25 wt.% SubPc in UGH2 layer.

4.5. Summary

In conclusion, significantly enhanced exciton diffusion lengths can be realized in SubPc by directly optimizing the molecular separation and the degree of molecular interaction. Investigation of the key photophysical properties of SubPc as a function of dilution into a wide energy gap spacer material reveal increases in η_{PL}, τ, and connect the resulting increases in self-R_0 to L_D. This increase in exciton diffusion length translates to a substantial improvement in device efficiency via increases in the short-circuit current density. Impressively, this technique allows for a peak power conversion efficiency of (4.4 ± 0.3)% in a simple, planar architecture, rivaling the performance of bulk heterojunction OPVs based on SubPc. This work suggests that the optimum molecular separation for efficient exciton diffusion is not necessarily realized in neat film, and that further fundamental improvements in performance can be achieved by engineering molecular separation. While in this chapter, control over the molecular separation is realized via the physical method of dilution, the concepts presented here are general, and similar results may also be achieved through thoughtful molecular design [101].

5. Optical spacing in OPVs incorporating dilute C_{60} acceptor layers

In planar heterojunction organic photovoltaic devices (OPVs), each wavelength of the incident, broadband optical field peaks at a different location in the multilayer stack. Consequently, an important consideration for efficient OPV operation is the optimization of the optical field such that the locations of peak intensity for a given wavelength of light overlap with layers or materials with high absorption at the same wavelength, maximizing the absorption efficiency (η_A). Furthermore, shifting the location of peak intensity toward the dissociating interface can enhance the exciton diffusion efficiency (η_D) in cases where the exciton diffusion length (L_D) is shorter than the layer thickness. Optimization of the optical field is often achieved by varying OPV layer thicknesses, for example the thickness of the exciton blocking layer between the acceptor layer and the cathode, and is generally referred to as the optical spacing effect [102–107]. Given the optical constants for the materials in the device and L_D for the respective donor and acceptor layers, transfer matrix modeling combined with simple, analytical solutions to the first order exciton diffusion equation can used to predict the short circuit current density (J_{SC}) in planar heterojunction OPVs [41]. While optical spacing effects have been well described for neat active layers, the results are quite different for active layers that have been wholly or partially diluted. By diluting regions of the active layers that are furthest from the donor-acceptor interface, enhanced absorption nearest the donor-acceptor interface is possible (Chapter 4). In this chapter, the effectiveness of diluting the archetypical electron accepting molecule fullerene C_{60} into the wide energy gap host material p-bis(triphenylsilyl)benzene (UGH2) [84,85] is demonstrated and the results are discussed in terms of the optical spacing effect and the exciton diffusion efficiency (η_D) [108].

5.1. Optical spacing effect

In order to demonstrate the difference between optimizing the optical field by acceptor dilution versus blocking layer thickness, the total power absorbed over the solar spectrum (AM1.5G) was simulated for the device architectures shown in Figure 5.1. The layer stack for the device in Figure 5.1a consists of a 10-nm-thick layer of MoO_x [96,109] on indium-tin-oxide (ITO) coated glass, a 13-nm-thick layer of the electron donor boron subphthalocyanine chloride (SubPc) [97], a 20-nm-thick layer of the electron acceptor C_{60}, a 20-nm-thick layer of C_{60} diluted into UGH2 of varying composition, followed by a 10-nm-thick exciton blocking layer bathocuproine (BCP). For the device in Figure 5.1b, a 40-nm-thick layer of C_{60} is used followed by a layer of BCP whose thickness is varied between 5 and 20 nm. Both devices are capped by a 60-nm-thick cathode layer of Al.

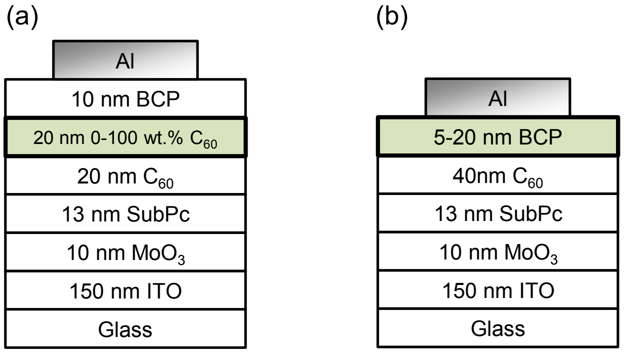

Figure 5.1 Device architectures for OPVs where the optical field is optimized by varying the acceptor layer concentration (a) or exciton blocking layer thickness (b). Adapted with permission from [108].

Figure 5.2 shows the simulated absorbed power for the devices of Figure 5.1. Diluting the outer half of the acceptor reduces absorption away from the donor-acceptor interface, leading to increased absorption for the inner half of the acceptor layer. Note that the integrated acceptor layer absorption decreases from 30.5×10^{19} photons/m^2/s for a neat C_{60} outer half to 21.7×10^{19} photons/m^2/s for a neat UGH2 outer half. In contrast, optimizing the BCP layer thickness serves to shift the peak towards the donor-acceptor interface but does not strongly impact the absorption intensity in the acceptor layer. In fact the total acceptor layer absorption stays nearly constant at a value between 29-31×10^{19} photons/m^2/s. Both of these techniques serve to increase the η_D because they are minimizing the distance between the average point of exciton generation and the donor-acceptor interface.

Optimization of the optical spacing in the acceptor layer also affects the corresponding donor layer as well, but the direction of the effect will depend directly on the overlap of the donor and acceptor absorption spectra. In this case, SubPc and C_{60} have a reasonable amount of overlapping absorption and in both cases the absorption in the SubPc layer increases upon diluting C_{60} or decreasing the BCP layer thickness. This need not be the case for other donor materials, especially for lower energy gap donors that have less overlap with C_{60}.

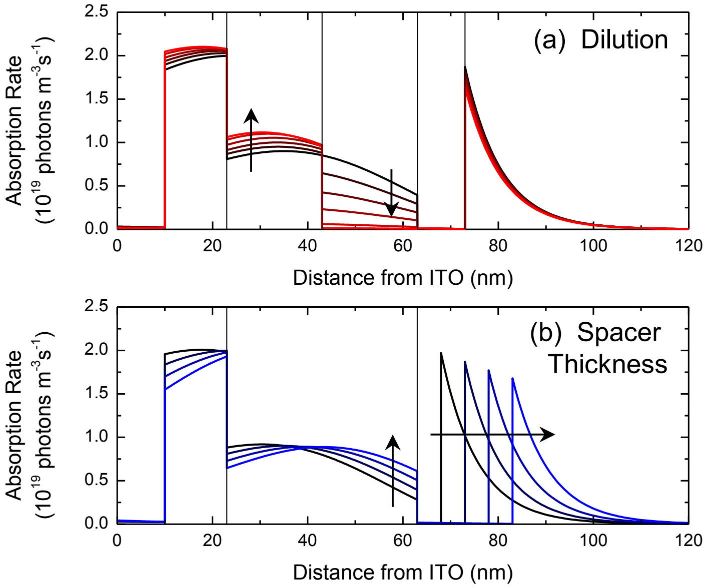

Figure 5.2 Absorption rate for the device architectures described in Figure 5.1 where the outer half of the acceptor layer is diluted (a) or the thickness of the exciton blocking layer varied (b). Arrows indicate increased dilution and spacer layer thickness, respectively. Adapted with permission from [108].

5.2. OPVs incorporating dilute C_{60} acceptor layers

In order to experimentally achieve optical spacing via dilution, several sets of OPVs were fabricated based on the acceptor-host pairing of C_{60} and UGH2 (Figure 5.3). Devices were fabricated on glass substrates coated with a 150-nm-thick layer of ITO having a sheet resistance of 15 Ω/☐. Substrates were degreased and cleaned with solvents and treated in UV-ozone ambient prior to film deposition. All organic layers were grown using vacuum thermal evaporation ($<10^{-7}$ Torr) at a nominal rate of 0.2 nm/s. The 10-nm-thick anode buffer layer of MoO_x serves to reduce device dark current [109,110]. For consistency, all devices contain a 13 nm-thick-layer of SubPc. As shown in Figure 5.1a, the first device architectures has two acceptor layers consisting of a

20 nm-thick-layer of neat C_{60} followed by a 20 nm-thick-layer of variable concentration C_{60} diluted into UGH2. Further sets of devices employ 0, 10, and 20 nm-thick-layers of 50 wt.% C_{60}:UGH2 dilute acceptor across a wide range of neat C_{60} layer thicknesses.

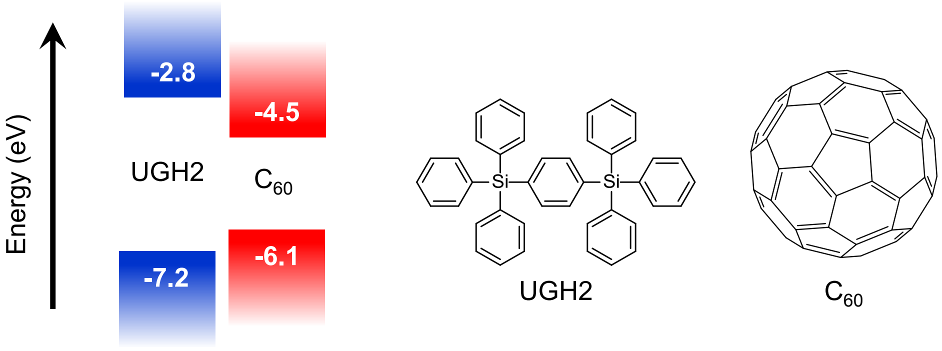

Figure 5.3 Molecular orbital energy levels for UGH2 and C_{60} along with the corresponding molecular structures.

Current density-voltage characteristics were measured under AM1.5G at an illumination of (100±5) mW/cm^2. Figure 5.4 shows the responsivity and fill factor for the set of devices described in Figure 5.1 as a function of dilute layer concentration. A slight increase in device responsivity is observed upon diluting the outer half of the acceptor layer from pure C_{60} to approximately 40-50 wt.% C_{60} in UGH2. Interestingly, the fill factor in this range of dilution is remarkably constant, even increasing slightly for dilution in the 60-70 wt.% C_{60} in UGH2 devices. With no change in the device open circuit voltage (V_{OC}), an increase in η_P from (2.8 ± 0.2)% for a neat acceptor layer to (3.0 ± 0.3)% for a 70 wt.% C_{60} in UGH2 dilute acceptor layer is realized. While the increase in total device responsivity is small, it occurs despite the concomitant decrease in acceptor η_A by ~15%, obtained by comparing the integrated spatial absorption rates in Figure 5.2. The increasing responsivity and decreasing η_A signal an increase in internal quantum efficiency (η_{IQE}). Assuming no change in charge collection efficiency (η_{CC}) or exciton dissociation by charge transfer efficiency (η_{CT}), the increase in responsivity is attributed to a resultant increase in η_D for the acceptor layer. Assuming η_{CT} to be invariant is likely a good assumption since the donor-acceptor interface is unchanged between all devices studied. The assumption of a constant η_{CC} is assessed later in this chapter. Regardless, C_{60} concentrations >50% appear suitable to achieve optical spacing while retaining efficient charge collection pathways. Further, the non-trivial dependence of fill factor on dilution may not be general for broader families of organic semiconductors. Similar work for other host-guest systems suggests that dilute layers, at a minimum, can be electrically robust in amorphous mixtures and in some cases be beneficial for reducing exciton/charge interactions [111].

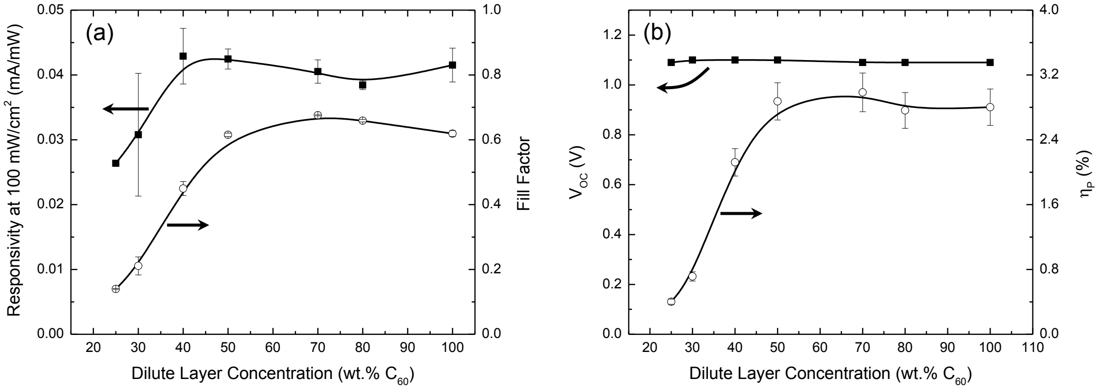

Figure 5.4 Responsivity at 100 mW/cm^2, fill factor, open-circuit voltage (V_{OC}), and power conversion efficiency (η_P) for the device described in Figure 5.1 as a function of dilute layer concentration. Adapted with permission from [108].

In the previously reported device measurements of dilute donor devices consisting of SubPc and C_{60} (Chapter 4), photoluminescence (PL) quenching measurements were used to show that the dilution of SubPc in UGH2 lead to enhanced L_D owing to optimized Förster energy transfer between SubPc molecules [87]. In contrast, the weak emission of C_{60} in thermally deposited thin-films makes difficult the use of PL quenching to directly study the impact of dilution on exciton transport.

In order to model diffusion in these structures, it is assumed that no photocurrent is collected from the dilute layer. This would be the case, for instance, if the dilute C_{60} layer had an L_D much shorter than the layer thickness. To verify this assumption, the J_{SC} was measured for two sets of devices containing (1) variable thickness neat acceptor layers near the donor-acceptor interface and (2) 10- and 20-nm-thick layers of 50 wt.% C_{60} in UGH2 nearest the Al cathode. This concentration is used since it strikes a balance between optimizing the absorption/diffusion profile and the need for efficient charge collection. For the modeling of photocurrent, the exciton flux is simulated using dissociating boundary conditions at the donor-acceptor interface and reflecting boundary conditions at the SubPc/MoO_x interface for the donor and neat C_{60}/dilute C_{60} interface for the acceptor. A non-reflecting, non-quenching boundary condition is more appropriate for the acceptor/dilute acceptor interface, however it cannot be included *a priori*. Since there is an imbalance in destination sites for exciton hopping at this interface, a reflecting boundary condition is a suitable choice. In these simulations, the L_D for SubPc is set to L_D=10.7 nm and the L_D for C_{60} and η_{CC} are set as fitting parameters.

Figure 5.5 displays the experimental and simulated J_{SC} for devices combining variable thickness neat C_{60} layers with 10- and 20-nm-thick 50 wt.% C_{60} in UGH2 dilute layers. Good agreement is found between the experimental and simulated values of J_{SC} with a C_{60} L_D=45 nm and η_{CC}=72.5%. The maximum J_{SC} for a control device, containing no dilute layer and a 50-nm-thick C_{60} layer, is shown for comparison. The optimum neat layer thickness decreases as the dilute layer thickness increases. Interestingly, the total optimized acceptor layer thickness remains relatively constant at approximately 40 nm. Since there is good agreement is for neat layers approaching and equal to 0-nm-thick, there is likely no appreciable photocurrent coming from the dilute C_{60} layer. This may signify that the L_D in dilute C_{60} is indeed short, validating the selection of boundary conditions. The short L_D for dilute films of C_{60} may reflect the presence of Dexter-type energy transfer, which has a strong dependence on intermolecular separation and requires direct electronic wavefunction overlap between adjacent molecules [36].

The optimum neat layer thickness for a given set of devices depends directly on the L_D of C_{60} and is independent of η_{CC}, which only serves to modulate the magnitude of the J_{SC}. The uniqueness and independence of these fitting variables, combined with wide agreement across many devices gives a reasonable degree of confidence for these values, in contrast to only fitting a single device where the η_{CC} and L_D for C_{60} would be convoluted.

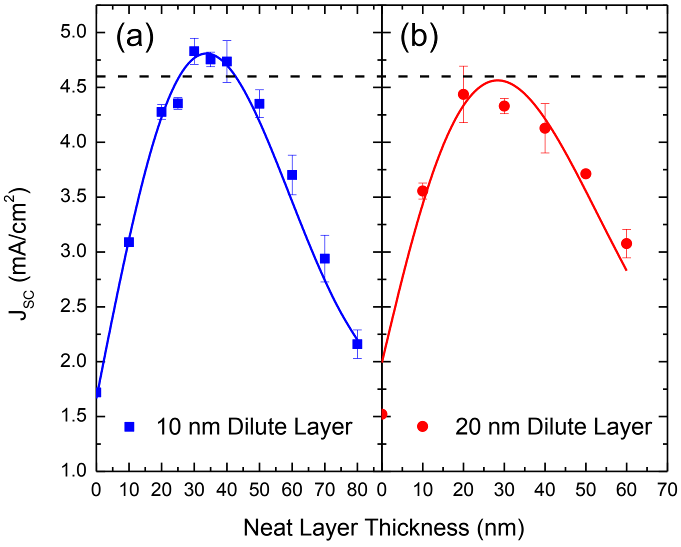

Figure 5.5 Short-circuit current densities (J_{SC}) for OPVs incorporating 50 wt.% C_{60} in UGH2 dilute, outer acceptor layers as a function of the thickness for the neat C_{60} inner layer. The dashed line represents the optimized control device. Adapted with permission from [108].

5.3. Measurements of internal efficiency for OPVs with dilute acceptor layers

In order to quantitatively probe changes in η_D, experimental measurements for the η_{EQE} are combined with simulations of the η_A in order to extract η_{IQE}. Figure 5.6 displays the η_{EQE} spectrum for a device with a 35-nm-thick neat C_{60} acceptor layer and a device with a 25-nm-thick neat C_{60} acceptor layer combined with a 10-nm-thick 50 wt.% C_{60} in UGH2 dilute acceptor layer. From the η_{EQE} in Figure 5.6 and the values of J_{SC} in Figure 5.5, it is clear that these devices have very *similar* values of J_{SC}. However, these devices have *different* values of η_A. The modeled η_A for each device as well as the predicted η_{IQE}, obtained by dividing the measured η_{EQE} by the modeled η_A. No change in the η_{IQE} for the portion of the spectrum with predominantly SubPc absorption (525–600 nm) is found. This is consistent with the use of a constant SubPc donor layer thickness in all devices. There is, however, a marked increase in the C_{60} dominant region of the spectrum (350–475 nm) for the diluted device. The 45% increase in η_{IQE} from ~55% in the neat device to ~80% in the dilute device is attributable to an increase in the η_D, corresponding to the realization of optimized optical spacing via dilution.

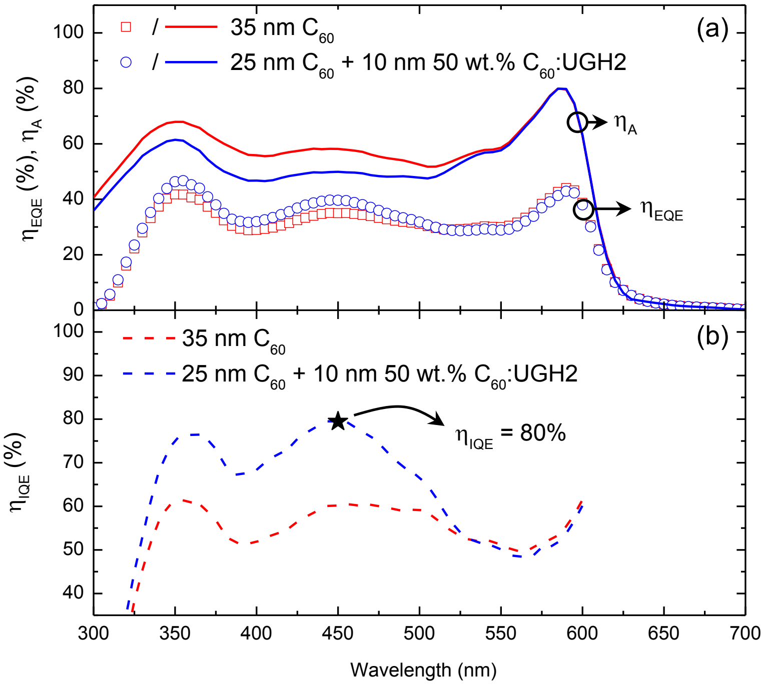

Figure 5.6 External quantum efficiency (η_{EQE}), absorption efficiency (η_A), and internal quantum efficiency (η_{IQE}) for OPVs incorporating a 35-nm-thick C_{60} acceptor layer and a partially diluted 35-nm-thick acceptor layer. Adapted with permission from [108].

5.4. Summary

The results presented in this chapter demonstrate the effectiveness of the dilute active layers and the optical spacing effect to drastically increase the exciton diffusion efficiency of an OPV device. In fact, a nearly 50% increase in the internal quantum efficiency was achieved for the archetypical electron acceptor C_{60} when diluted in the wide-energy gap material UGH2. While the enhancement of internal efficiency comes at the expense of the overall absorption efficiency, more efficient host-guest OPVs may be possible if the host and guest molecules absorbed in the solar spectrum. This relationship will be explored in Chapter 7. Further, dilute active layers with optimized optical spacing may be a useful tool for the global optimization of tandem OPVs where individual sub-cells compete for absorption [99]. The ability to achieve an enhanced internal efficiency with a reduced absorption efficiency can, therefore, reduce the constraints on materials selection and help maintain balanced photocurrent between the individual sub-cells.

6. Directed energy transfer resulting from exciton permeable interfaces

Inspection of the organic photovoltaic devices incorporating dilute layers in both Chapter 4 and Chapter 5 reveals the presence of an interface between a neat layer and a dilute layer. In order to build a complete model for exciton diffusion and transport across these interfaces an appropriate boundary condition must be developed that reflects the non-destructive exciton flux that occurs as excitons move between layers, a so-called exciton permeable interface. Recall from Chapter 2 that excitons in a homogeneous landscape move diffusively. Incorporation of this interface, however, can lead to inhomogeneity in exciton transport and result in anomalous diffusion. In this chapter, the impact of exciton permeable interfaces on organic photovoltaic device (OPVs) performance is described and quantified. In particular, while gains in exciton harvesting are possible with enhanced bulk exciton diffusion length (L_D) [87,101,112–115], a more effective approach may involve introducing exciton permeable interfaces that intentionally bias energy transfer toward the donor-acceptor (D-A) interface. These interfaces break the symmetry associated with normal diffusion and exploit transport in a super-diffusive regime to realize large diffusion efficiencies (η_D) [116].

6.1. Exciton permeable interfaces

An exciton permeable interface may be realized in practice at the interface between two materials (Figure 6.1) where there exists an imbalance in the forward and reverse exciton energy transfer rates across the interface. This imbalance may arise from a number of different material or device configurations. For example, *Material 1* in Figure 6.1 may be a donor material with a larger energy gap than *Material 2* [117,118]. In such a structure, an exciton to the left of the interface has a nonzero probability of moving either left or right, while an exciton on the right of the interface may only move to the right due to conservation of energy. Thus, an interface of this type relies on an energetic asymmetry to realize the required rate imbalance.

A second configuration that can lead to a similar asymmetry in rates requires an interface between dilute and neat layers of a single molecular species [87]. Using the schematic of Figure 6.1, *Material 1* is a layer of donor material diluted into a wide energy gap matrix while *Material 2* is a neat layer of the same donor. In this configuration, there is no energetic asymmetry as the exciton is confined to the donor species on both sides of the interface. There is however, a difference in the molecular site density between the dilute and neat materials, creating the required asymmetry. For an exciton immediately to the left of this interface, dilution reduces the number of molecular destination sites in the dilute layer relative to the neat layer, and the same holds for excitons on the right side of the interface. Since the rate of hopping is proportional to the number of sites, the site imbalance creates an asymmetry in hopping rates (Eq. 2.26).

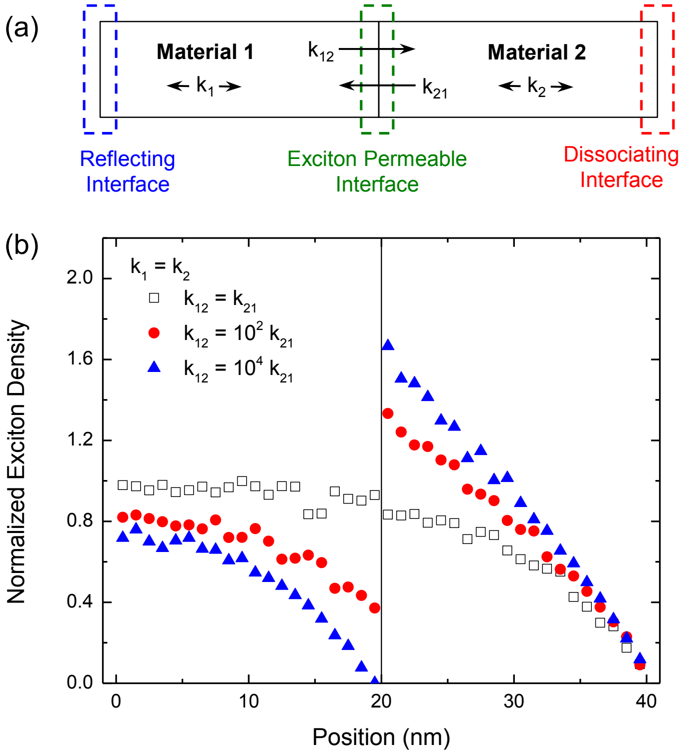

Figure 6.1 (a) Schematic representation describing an exciton permeable interface. The rate of energy transfer at the interface from Material 1 to Material 2 is defined as k_{12} and vice versa. (b) The resulting exciton density profiles across the layer when the rates of energy transfer at the interface between *Material 1* and *Material 2* are the same or different. Adapted with permission from [116].

In the following sections, results demonstrating enhanced exciton transport for architectures exploiting both the energetic and site density asymmetries will be presented. In order to isolate the role of the interface in determining the overall efficiency of exciton transport, a Kinetic Monte Carlo (KMC) formalism is developed to solve the 1-D exciton diffusion equation across exciton permeable interfaces. The advantage of this stochastic solution is that the boundary condition for the permeable interface does not need to be known *a priori*, and can be, instead, constructed by identifying the imbalance in exciton energy transfer rates at the interface. Other device related boundary conditions, such as exciton reflecting and dissociating, may also be easily incorporated as appropriate. Care is taken to ensure that the KMC solutions agree identically with analytical solutions for cases without permeable interfaces. Further information regarding the KMC model can be found in the appendix.

Figure 6.1 demonstrates the drastic effect that an imbalance in energy transfer rates can impart on the steady state exciton density in a model organic photovoltaic (OPV) multilayer system. Here, k_{12} and k_{21} are the energy transfer rates to *Material 2* and *Material 1*, respectively. When the rates are equal, no imbalance is present and the conventional, continuous solution for the exciton density profile is retained. The presence of imbalance, however, leads to a discontinuity in the exciton density at the permeable interface. The discontinuity reflects a depletion and pile-up of excitons, with a net movement towards the side of the interface to which energy transfer is favored. The gating of excitons in this model system is beneficial for exciton motion rightwards, thereby also increasing the flux of excitons toward the dissociating interface adjacent to *Material 2*.

6.2. Imbalance in molecular density

As discussed, the interface between dilute and neat layers of donor material forms an exciton permeable interface due to an asymmetry in transfer rates. The dilute donor OPVs presented in Chapter 4 show a 30% enhancement in power conversion efficiency (η_P) relative to undiluted control devices [87]. In these devices, dilute layers of the archetypical electron donating molecule boron subphthalocyanine chloride. (SubPc) [72,92,97] dispersed in the wider energy-gap host material p-bis(triphenylsilyl)benzene (UGH2) [84,85] show a 50% increase in the L_D for SubPc owing to optimized Förster energy transfer and intermolecular interaction (Figure 4.7).

The increase in bulk L_D leads to an enhancement in the exciton diffusion efficiency (η_D) when incorporated as part of a multilayer donor structure. Notably, an exciton permeable interface exists between the 12-nm-thick dilute layer of variable concentration and the 5-nm-thick layer of neat SubPc (Figure 6.2). The control device consists of separately optimized 13-nm-thick donor layer of SubPc [97]. The enhancement in η_D for these structures is, consequently, a combination of both bulk diffusion and interface effects. In order to understand the balance of these effects and model exciton migration in these devices, proper consideration of energy transfer at the permeable interface is critical. In addition to the imbalance in molecular site density, the variation in average intermolecular separation ($\bar{d}_1 > \bar{d}_2$) manifests imbalance across the permeable interface through the concentration dependence of the self Förster radius (self-R_0) and the distance dependence for the rate of Förster energy transfer. These contributions are pictured schematically in the inset of Figure 6.2.

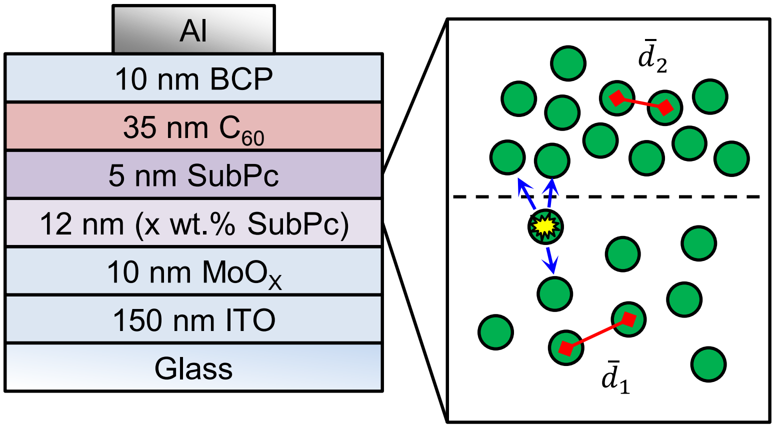

Figure 6.2 Dilute donor OPV schematic detailing the imbalance in donor molecular density at the interface between the dilute and neat donor layers. Adapted with permission from [116].

To confirm the validity of this model, photoluminescence quenching experiments and complementary simulations were performed for a two-layer system where the outer layer consists of a 20-nm-thick layer of 50 wt.% SubPc dispersed in UGH2 while the 10-nm-thick inner layer has a variable SubPc concentration (Figure 6.3). Photoluminescence (PL) is measured with and without the presence of an adjacent 10-nm-thick layer of naphthalene-1,4,5,8-tetracarboxylic acid dianhydride (NTCDA). Experimental photoluminescence ratios are defined as the ratio between quenched photoluminescence (PL_Q) and unquenched photoluminescence (PL_{UQ}).

Simulated PL ratios are generated using the KMC approach for two situations namely, with and without the rate imbalance (gating) at the exciton permeable interface. A transfer matrix formalism was used to determine the optical field and rate of exciton generation within the structure. Hopping rates within each layer were determined from measured values of L_D as a function of concentration. The imbalance in energy transfer at the interfaces was captured by explicitly including the effects of both the imbalance in molecular site density and intermolecular separation. Care was taken to include the effect of variable photoluminescence efficiency (η_{PL}) between the layers. The KMC modeling also allows for the tabulation of the exciton diffusion efficiency (η_D) as a function of interlayer concentration. Modeling the experimental PL ratios, consequently, provides a direct confirmation for the presence and sources of the rate imbalance.

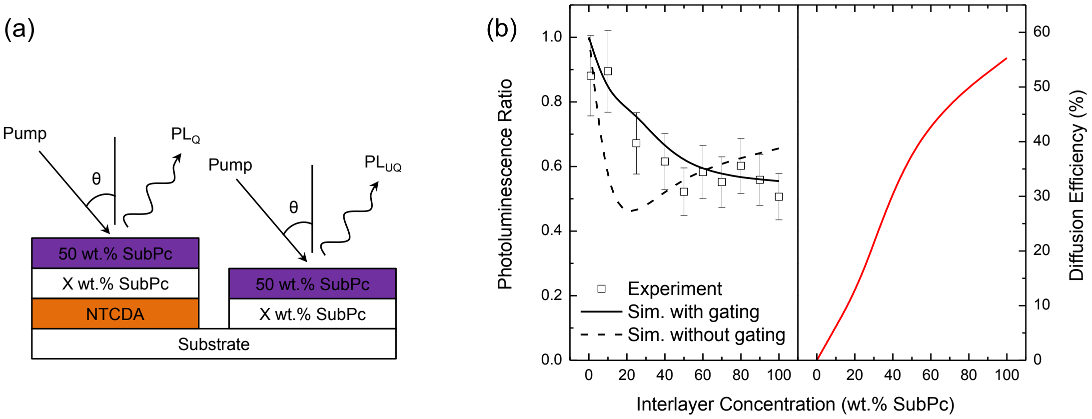

Figure 6.3 (a) Photoluminescence (PL) quenching experiment where the concentration of the inner layer was varied. (b) Resulting PL ratios along with the corresponding fit from Kinetic Monte Carlo simulations. Also shown is the associated exciton diffusion efficiency. Adapted with permission from [116].

Agreement between experimental and simulated PL ratios is only achieved when imbalance (gating) at the permeable interface is included. Interestingly, when the effect of the exciton permeable interface is correctly applied, η_D is optimized for an inner layer comprised of undiluted SubPc. This counterintuitive result contrasts the notion that exciton harvesting is optimized by incorporating active materials with the longest L_D and confirms that the interface plays a critical role in driving excitons toward the D-A interface.

Figure 6.4 shows the measured external quantum efficiency (η_{EQE}) at a wavelength λ = 590 nm, corresponding mainly to SubPc absorption, as measured from the devices in Chapter 4. A transfer matrix formalism is employed to model the incident optical field responsible for photon absorption and exciton generation. Simulated η_{EQE}, absorption efficiency (η_A), and η_D calculated using the KMC model are also shown as a function of dilute layer concentration in Figure 6.4. Excellent agreement with experiment is found when an additional, concentration independent loss term equal to 0.85 is included. Here, $\eta_{EQE} = \eta_A \eta_D \eta_{CT} \eta_{CC} = 0.85 \eta_A \eta_D$ where η_{CT} and η_{CC} are the charge transfer and charge collection efficiencies, respectively. Losses are expected and may reflect exciton quenching at the MoO_x anode buffer layer and non-unity η_{CC}. Further, previous work shows concentration-independent acceptor η_{EQE} and fill factor for devices incorporating dilute layers ≥25 wt.% SubPc, confirming that UGH2 does not have a concentration-dependent effect on the η_{CC} [87].

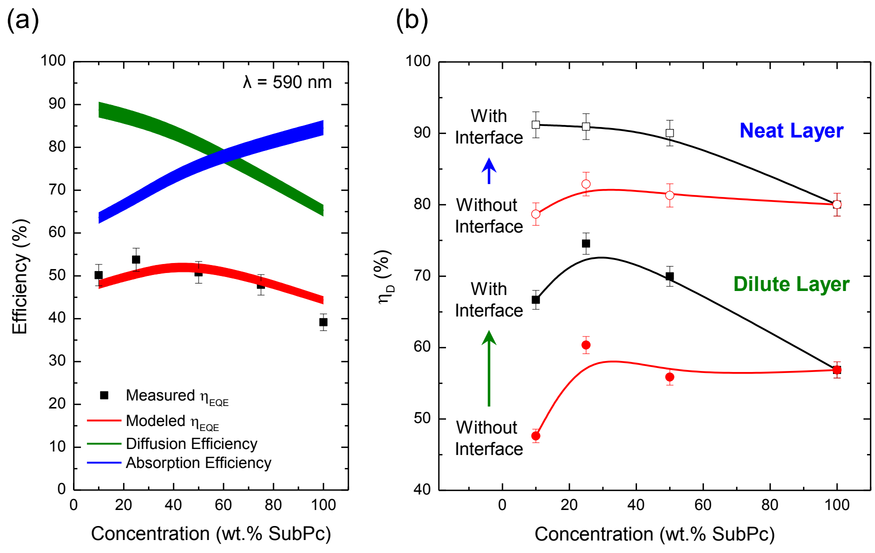

Figure 6.4 (a) Measured and modeled external quantum efficiency along with the modeled absorption and diffusion efficiencies for the dilute donor device of Figure 6.2. (b) Separated exciton diffusion efficiencies for the neat and dilute layers with and without adding the exciton gating effects. Adapted with permission from [116].

Interestingly, η_D increases continuously upon dilution. To confirm the origin of the enhanced η_D, Figure 6.4 displays the separated dilute and neat layer η_D as a function of concentration. Furthermore, the separate values of η_D are simulated for the actual device with a rate imbalance at the interface as well as for an artificial device where no imbalance is present. For the latter, the hopping rates within and between each layer in the artificial device are identical, and the exciton lifetimes are adjusted to reflect the proper bulk L_D. The simulation of the artificial devices allows for the determination of η_D based solely on changes to the bulk L_D. Dilution, however, is capable of achieving very large imbalances (k_{12}/k_{21} ~ 100–1,000) in energy transfer, yielding η_D^{Dilute} and η_D^{Neat} that are significantly larger than values obtained from solely considering increases in bulk L_D. The η_D^{Neat} increases upon dilution owing to more effective reflection at the gating interface. The η_D^{Dilute} increases from η_D^{Dilute}=(56.9 ± 1.1)% to η_D^{Dilute}=(74.6 ± 1.5)%. Of this enhancement, 20% results from changes in bulk L_D with the remainder resulting from the effect of the gating interface. It should be noted that the increase in η_D^{Dilute} would be ~20% larger if compared to an identically thick control device instead of the optimized control device. Remarkably, a total donor layer η_D>85% is achieved.

6.3. Imbalance in energy-gap

As another common example of a passive exciton gate, energy-cascade OPVs derive an imbalance in energy transfer from differences in energy-gap. In such a configuration, downhill and sometimes long-range energy transfer [42,119] can take place from a larger energy-gap donor to a lower energy-gap donor as is the case for SubPc (E_g=2.0 eV) to boron subnapthalocyanine chloride (SubNc, E_g=1.8 eV) [120,121]. Förster-type energy transfer from SubPc to SubNc is favorable due to their complementary photoluminescence and absorption spectra. Tabulated predictions for the Förster radius (R_0) from SubPc to SubNc yield R_0=2.1 nm, whereas the reverse transfer is very improbable with R_0~0 nm. Therefore, a perfect imbalance can be achieved leading to enhanced η_D in both donor layers. In this chapter, energy-cascade OPVs are fabricated according to the layer structure in Figure 6.5 where the total donor layer consists of a 10-nm-thick layer of SubPc followed by a variable thickness layer of SubNc. A 42-nm-thick

C_{60} acceptor layer is used followed by a 10-nm-thick bathocuproine (BCP) exciton blocking layer and a 100-nm-thick Al cathode. Measurements of the power conversion efficiency (η_P) reveal that these devices can be quite efficient with η_P=(4.7 ± 0.2)% when incorporating a 6-nm-thick SubNc layer. The current-density-voltage characteristics of the champion cell are shown in Figure 6.5. For comparison, the η_P for single, neat donor planar heterojunction OPVs paired with a C_{60} acceptor based on SubPc and SubNc are η_P=3.3% and η_P=2.4%, respectively.

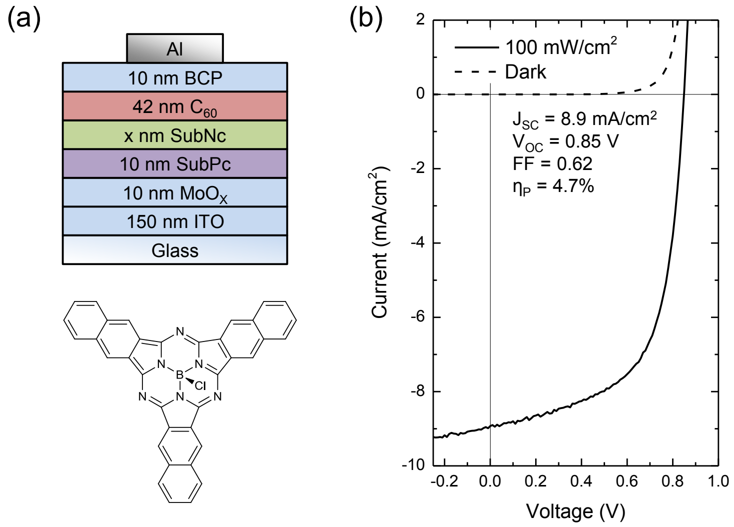

Figure 6.5 (a) Device schematic for energy-cascade OPV along with the molecular structure for SubNc. (b) Current-density voltage characteristics for the energy cascade device incorporating a 6-nm-thick layer of SubNc at 100 mW/cm^2 under AM1.5G solar simulated illumination. Adapted with permission from [116].

The KMC model for exciton diffusion in cascade structures incorporating exciton permeable interfaces allows for the accurate prediction of the η_{EQE}. Here, the η_{EQE} is modeled for SubPc and SubNc at λ=590 nm and λ=700 nm, respectively, corresponding to regions of predominant absorption for each material, respectively (Figure 6.6). The KMC model accurately reproduces the experimentally obtained η_{EQE} with L_D=15 nm for

SubNc and the previously measured value of L_D=10.7 nm for SubPc. A thickness independent loss term of 0.75 is needed to make the KMC predicted η_{EQE} agree with the measured η_{EQE}. Such a loss term is expected since the KMC model does not address charge collection losses, similar to the dilute devices discussed previously.

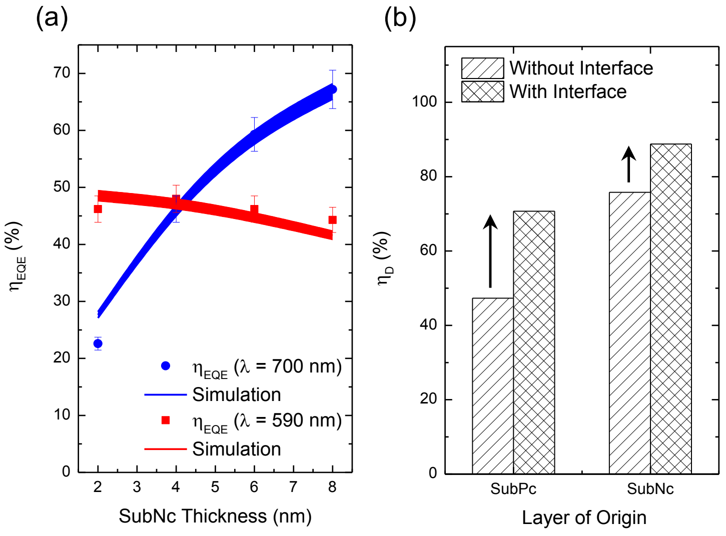

Figure 6.6 (a) Measured and modeled external quantum efficiency (η_{EQE}) as a function of SubNc layer thickness. (b) Separated SubPc and SubPc exciton diffusion efficiencies (η_D) with and without adding the exciton gating effects. Adapted with permission from [116].

To directly investigate the effect of the exciton permeable interface on η_D in this energy-cascade structure, η_D is separately simulated for each donor layer and compared to a device where no imbalance is present at the interface. Only excitons generated in SubPc will contribute to the η_D^{SubPc}, with the same being true for excitons generated on SubNc and the η_D^{SubNc}. As can be seen from Figure 6.6, the addition of the interface increases the diffusion efficiency for the SubPc and SubNc layers by 50% and 20%, respectively. The increase in the η_D^{SubPc} is a result of directed energy transfer to the SubNc layer at the exciton permeable interface. Since there can be no reverse energy transfer from SubNc to SubPc, excitons that are generated in the SubNc layer experience effective reflection at the permeable interface, thereby also increasing η_D^{SubNc}. Such drastic effects on η_D, and ultimately device photocurrent, can only be quantified by correctly modeling the imbalance in energy transfer at the exciton permeable interface.

6.4. Advanced structures

So far, only systems incorporating a single permeable interface have been studied, warranting further investigation into multiple interface systems. Inspection of the mean-squared displacement as a function of time elucidates the connection between number of permeable interfaces and the degree of anomalous diffusion. To do so, a generic system consisting of 16 1-nm-thick bins is modeled. The first interface is introduced by discretizing the system into two layers, one representing a very dilute layer (e.g. 1 wt.%) with L_D=10 nm and one representing a nearly undiluted layer (e.g. 99 wt.%) with L_D=1 nm, depicted schematically in Figure 6.7. Rates are extracted from L_D with a lifetime of τ=1 ns. A simple molecular site density rationale is used for quantifying the imbalance in energy transfer at the interface(s). To inspect the mean-squared displacement versus time, a large population of excitons is injected through a 5-nm-thick layer of the most dilute layer into the multiple interface system. Importantly, the simulation is ended when the first excitons reach the opposite side of the structure. The system is further discretized into 4, 8, and 16 layers containing 3, 7, and 15 exciton permeable interfaces, respectively. A linear interpolation is used to determine the specific rates of energy transfer and relevant molecular concentrations for each layer. For example, the 4-layer system would contain layers with concentrations of 1, 34, 67, and 100 wt.% with corresponding L_D of 10, 8.2, 5.8, and 1 nm, respectively.

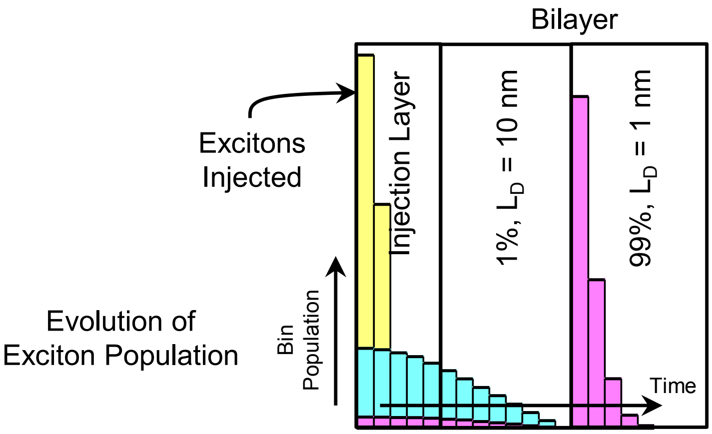

Figure 6.7 Description of a model experiment where the exciton trajectory is tracked in timer for multilayer structures as a function of the number of permeable interfaces. Adapted with permission from [116].

Figure 6.8 shows the mean-squared displacement versus time for the various multilayer structures. At short times, the structures behave nearly identically. This is consistent since they all contain an identical, 5-nm-thick injection layer whereby the excitons are all sampling an identical, diffusive environment at very short times. However, when the first excitons reach the permeable interface 10-30 ps after injection, the mean-squared displacement begins increasing faster, especially for the systems with a larger number of permeable interfaces. In fact, regions of the plot with slopes greater than unity indicate super-diffusive behavior. To verify, Figure 6.8 displays the derivative of the mean-squared displacement where α, the slope, is defined from $\langle x^2 \rangle = \beta t^{\alpha}$. Values of $\alpha>1$ and $\alpha<1$ signify super- and sub-diffusive motion, respectively. Clearly, the structures with the greatest number of permeable interfaces show the largest degree of super-diffusive motion, with α reaching a peak value of $\alpha \sim 1.5$. Furthermore, the peak in α occurs at increasingly shorter times as the number of permeable interfaces is increased.

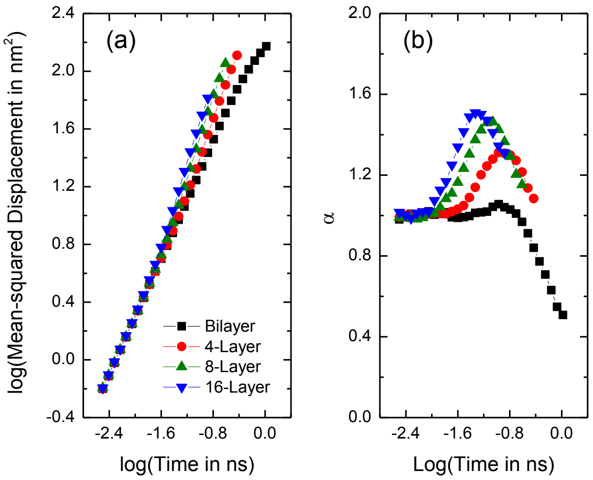

Figure 6.8 (a) Mean-squared displacement and (b) slope of the mean-squared displacement versus time for excitons traversing the structures described in Figure 6.7. Adapted with permission from [116].

In order to investigate how efficiently an exciton can practically traverse the various multilayer structures from Figure 6.7, excitons are again injected into the most dilute layer. However now, no injection layer is included, and the excitons are allowed to decay according to their natural lifetime. Excitons that reach the opposite end of the layered system are said to be collected, characterized by a transport efficiency (η_T). The time taken by the excitons to traverse the system is denoted as the transit time. This experiment is depicted schematically in Figure 6.9.

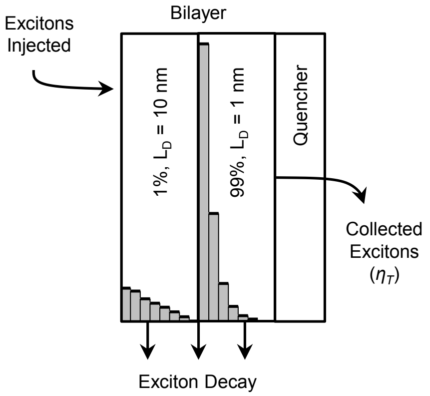

Figure 6.9 Description of a model experiment where the transport efficiency of excitons traversing a multilayer structure is recorded as a function of the number of permeable interfaces. Adapted with permission from [116].

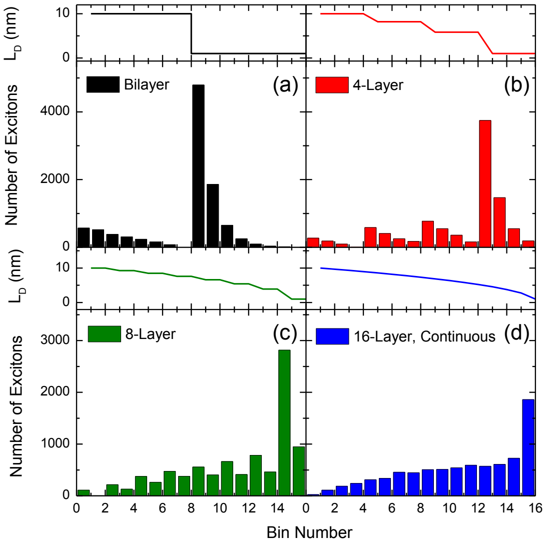

Figure 6.10 Histogram of the steady state exciton distribution for the multilayer structures described in Figure 6.9. Also shown is the dispersion in L$_D$ for each structure across the binned structure. Adapted with permission from [116].

A histogram of final exciton location for each of the structures is presented in Figure 6.10. Exciton gating occurs on the more concentrated side of each permeable interface. Additionally, as the number of permeable interfaces increases, the relative difference in exciton density between adjacent bins decreases. This is likely due to smaller imbalances in energy transfer rates across the interface since the changes in concentration occur in finer steps as more interfaces are added. In the 16-layer system, where the rates change continuously, there is a constant increase in exciton number density across the structure.

Coupled to the deeper penetration of excitons into this system is a concomitant increase in the η_T (Figure 6.11). Indeed, nearly 20% of excitons injected into bin 1 are able to traverse the 16 nm layer structure in the 16-layer system even though the average L_D is only ~6 nm. Furthermore, these excitons are collected on a dramatically shorter time scale with the majority being transported below their natural exciton lifetime of τ=1 ns. Beyond designing systems for optimal exciton collection, exciton permeable interfaces could also be designed to confine or redistribute excitons faster than could normally be achieved with purely diffusive motion.

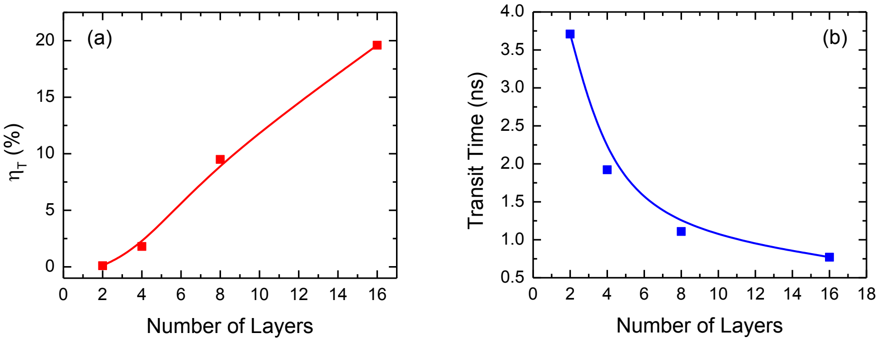

Figure 6.11 (a) Exciton transport efficiency (η_T) and (b) transit time for excitons traversing the multilayer structures described in Figure 6.9. Adapted with permission from [116].

6.5. Summary

This chapter has developed the formalism to properly model and characterize exciton transport in multilayer structures that contain exciton permeable interfaces. When optimized, exciton permeable interfaces can create passive exciton gates that enhanced exciton diffusion to the dissociating interface. This effect was quantified in two model systems incorporating exciton permeable interfaces, namely, dilute donor and energy-cascade OPVs. It was further demonstrated that incorporating multiple exciton permeable interfaces in a multilayer structure can result in apparent super-diffusive behavior and significant enhancements in exciton transport efficiency and transit time. Taken together, directed exciton motion resulting from exciton permeable interfaces may be harnessed to realize efficient exciton transport in OPVs and other organic optoelectronic devices beyond the diffusive limit.

7. Host-guest architectures for energy cascade OPVs

In planar heterojunction organic photovoltaic devices (OPVs), broad spectral coverage can be realized by incorporating multiple molecular absorbers in an energy-cascade architecture [117,118]. By definition, energy-cascade OPVs require energy transfer between donor or acceptor species in order for efficient exciton dissociation, depicted schematically in Figure 7.1. While energy-cascade OPVs can be fabricated in planar, multilayer configurations, host-guest configurations are also possible which are reminiscent of the dilute donor OPVs presented in Chapter 4. Importantly, energy-cascade OPV architectures retain a single donor-acceptor (D-A) interface. This is in contrast to charge cascade architectures which contain more than one exciton dissociating interface (Figure 7.1) [86,122,123].

In this chapter, energy-cascade architectures are combined with the host-guest donor layer architecture previously shown to optimize exciton transport for the fluorescent organic semiconductor boron subphthalocyanine chloride (SubPc) when diluted in an optically transparent host [87]. The consequences of the host-guest donor layer architecture will be developed, providing insight regarding the continued optimization of planar heterojunction OPVs. This chapter also demonstrates progress toward the effective separation of functionality between constituent OPV materials [113].

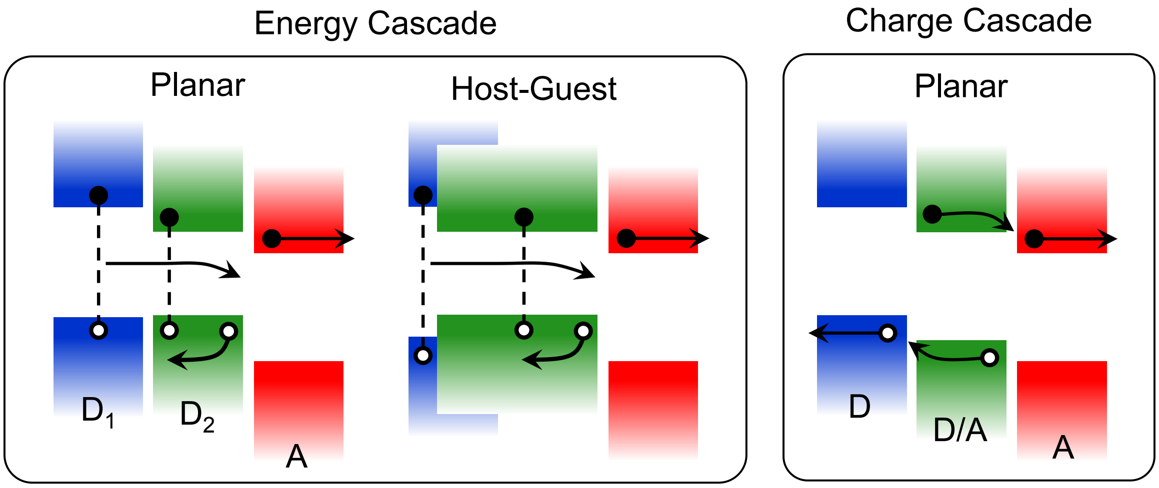

Figure 7.1 Exciton pathways for planar and host-guest energy cascade organic photovoltaic devices (OPVs) as well as the charge pathways for charge cascade OPVs.

7.1. Host-guest pairing of SubPc and SubNc

Variation of the intermolecular spacing can optimize the rate of intermolecular Förster energy transfer through photophysical properties such as the photoluminescence efficiency (Chapter 4). An enhancement in energy transfer rate can be further translated to enhancements in the exciton diffusion length (L_D). Previous work experimentally demonstrates this effect by diluting the electron-donating species, boron subphthalocyanine chloride (SubPc) [72,92,97] into a wide energy-gap host material, p-bis(triphenylsilyl)benzene (UGH2) [84,85]. The L_D is increased from L_D=10.7 nm in a neat film of SubPc to L_D=15.4 nm for a film containing 25 wt.% SubPc diluted in UGH2. Devices constructed using a dilute layer of SubPc in UGH2 show a 30% enhancement in power conversion efficiency (η_P). Increases in both the short-circuit current density (J_{SC})

and η_P were observed *despite* a concomitant ~30% decrease in donor absorption. The decrease in absorption efficiency results from the wide-energy gap of UGH2, suggesting that there is the potential for increased photocurrent if the host material were also photoactive.

Boron subnaphthalocyanine chloride (SubNc) [86,117,121] was selected as a guest material to integrate with a photoactive host of SubPc. SubPc and SubNc have been previously used as complimentary absorbers in tandem OPVs [99,117]. Figure 7.2 shows the extinction coefficient and molecular orbital energy levels for SubNc, SubPc, and UGH2. Owing to its wide energy-gap (E_g =4.4 eV), UGH2 does not strongly absorb in the solar spectrum. Excitons generated on SubPc (E_g=2 eV) neither energy transfer to UGH2 nor dissociate in the presence of UGH2, creating a single pathway for exciton transport. SubNc also strongly absorbs in the visible spectrum with a reduced energy-gap relative to SubPc (E_g=1.8 eV).

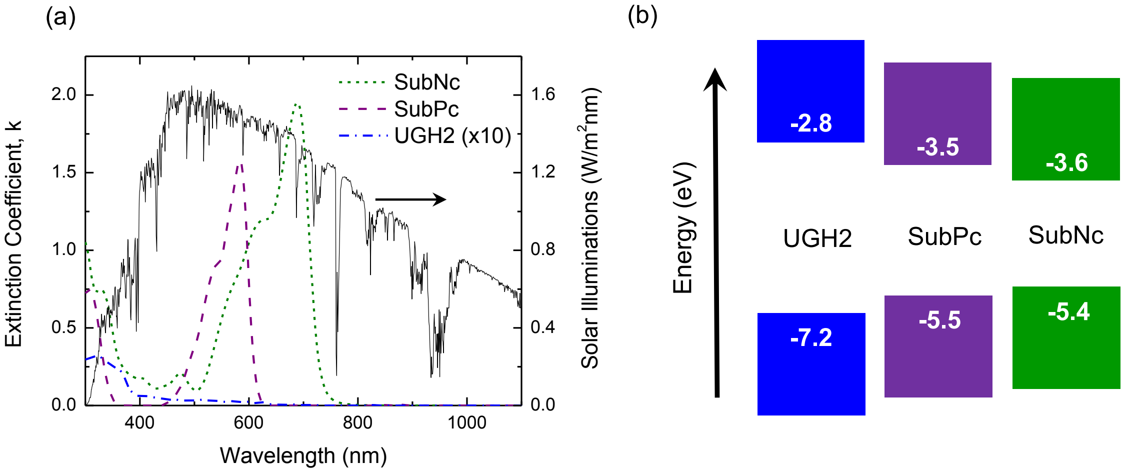

Figure 7.2 (a) Extinction coefficients for SubNc, SubPc, and UGH2 as compared to AM1.5G solar simulated radiation. (b) Molecular orbital energy levels for UGH2, SubPc, and SubNc. Adapted with permission from [118].

When SubNc is diluted in SubPc, two donor exciton harvesting pathways coexist. Similar to the case of dilute SubPc, excitons generated on SubNc diffuse along a pathway comprised of SubNc molecules toward the donor-acceptor interface. The difference in energy-gap between SubNc and SubPc is much larger than the ambient thermal energy (~25 meV), ensuring that excitons generated on SubNc do not energy transfer to SubPc. In this way, SubPc acts analogously to UGH2. A second pathway is also present for excitons that originate on SubPc. Efficient Förster energy transfer from SubPc to SubNc occurs rapidly [117], and excitons may follow the same route to the interface as those originally generated on SubNc. Overall, all photogenerated excitons are quickly confined to molecules of SubNc followed by short range exciton energy transfer toward the donor-acceptor interface where excitons are dissociated. Here, the host-guest donor layer is distinct from composite donor layers formed from multilayer stacks as the photogenerated charges remain solely on the guest species (SubNc) during transport towards the anode.

7.2. Exciton diffusion in SubNc

The exciton transport properties of dilute SubNc films were separately investigated in order to determine if a dilute donor enhancement in L_D is also observed for SubNc. This characterization provides guidance for selecting appropriate dilute film concentrations to be used during device fabrication. The diffusive behavior of excitons in films of SubNc as a function of concentration is measured via spectrally resolved photoluminescence quenching (SRPLQ) [46,73] as a function of dilution in UGH2. Figure 7.3 shows the measured photoluminescence emission and excitation spectra for 50, 25, and 10 wt.% SubNc diluted in UGH2. The shape of the excitation spectra change arising from differences in the optical absorption and interference. As in the case of SubPc diluted in UGH2, the photoluminescence spectra shift towards shorter wavelengths upon dilution. As SubNc is more polar than UGH2, a solid-state solvation effect is likely responsible [89–91].

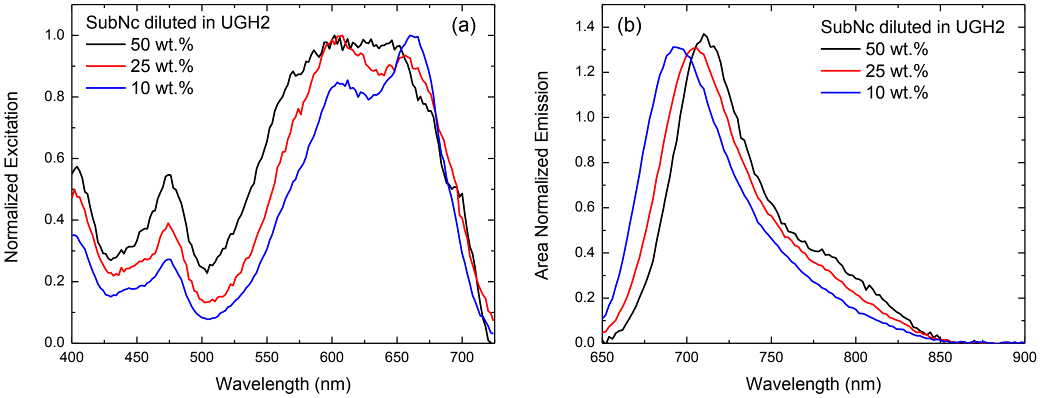

Figure 7.3 Excitation (a) and emission (b) spectra for various concentrations of SubNc diluted in UGH2. Adapted with permission from [118].

Experimental photoluminescence quenching ratios (PL ratios) are constructed by measuring the photoluminescence excitation spectrum of a SubNc:UGH2 film deposited on a 15-nm-thick quenching layer of 1,4,5,8,9,11-hexaazatriphenylene hexacarbonitrile (HATCN) [124] and dividing it by the excitation spectrum of an identical film of SubNc:UGH2 deposited on a glass substrate. Optical transfer matrix simulations combined with analytical solutions to the exciton diffusion equation allow for the simulation of predicted PL ratios which are sensitive to the L_D of the film [41]. Iterative fitting of the measured and predicted PL ratios allows for the determination of L_D. SRPLQ measurements were performed over a range of film thicknesses between 75 and 125 nm. The experimental PL ratios and respective fits for various thicknesses of 5, 10, 25, and 50 wt.% SubNc in UGH2 films are shown in Figure 7.4. Good fits to the measured PL ratios were obtained in spectral regions corresponding to strong SubNc absorption (~550–700 nm). For example the resulting fit values for L_D are L_D=25.8, 26.5, and 34.0 nm for film that are 75, 100, and 125-nm-thick, respectively.

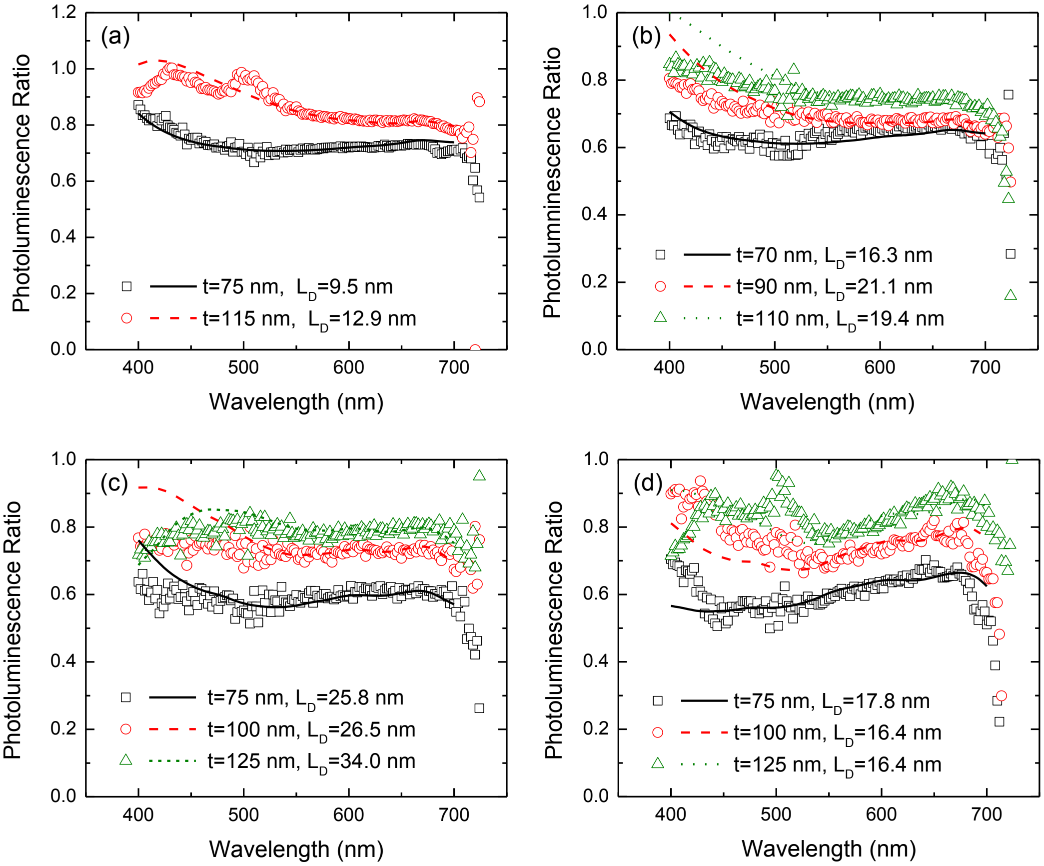

Figure 7.4 Experimentally measured photoluminescence ratios along with the corresponding fits for 5 (a), 10 (b), 25 (c), and 50 (d) wt.% SubNc diluted in UGH2 at various thicknesses.

Deviations observed in the shorter wavelength spectral regions (~400–550 nm) are likely due to the low signal intensity characteristic of spectral bands with low extinction coefficients. These deviations are then propagated into the overall fit value for L_D and result in a broader range of L_D values for a given concentration than typically obtained using thickness-dependent photoluminescence quenching-based techniques [37]. Figure 7.5 summarizes the measured values of L_D versus film concentration where each data point reflects a different film thickness at a given concentration. Also shown is the average L_D for each concentration where the error bars reflect the standard deviation. SRPLQ measurements of neat SubNc were not possible due to the low photoluminescence efficiency (η_{PL}) of films of pure SubNc ($\eta_{PL} \leq 0.25\%$). However, preliminary device-based measurements combined with modeling of the external quantum efficiency (η_{EQE}) suggest the L_D for pure SubNc is L_D~11 nm. This result, however, is susceptible to error where, for example, a non-unity charge collection efficiency (η_{CC}) will lead to an underestimate of L_D [37,78]. Interestingly, the L_D of SubNc exhibits a dependence on concentration. As in the case of SubPc, diffusion is not optimized in neat films of SubNc, and a near tripling of L_D is found in 25 wt.% SubNc in UGH2 films compared to the approximate L_D in pure films.

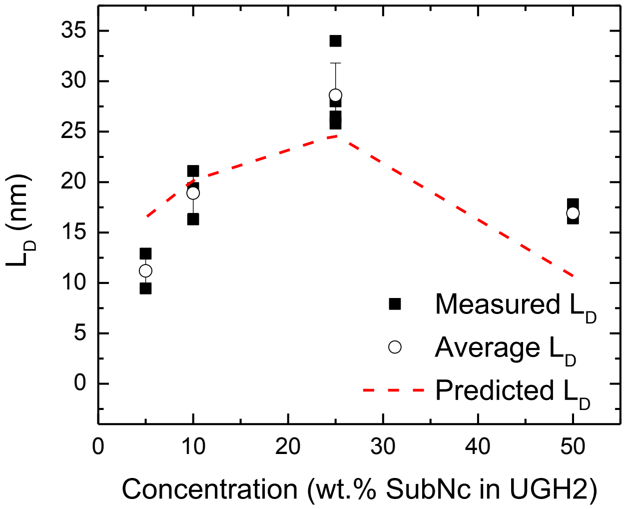

Figure 7.5 Summary of the fit values for L_D as a function of concentration for SubNc diluted in UGH2. Also shown is the average measured L_D at each concentration along with the predicted L_D from Förster theory. Adapted with permission from [118].

For fluorescent organic semiconductors, the Förster theory of energy transfer has been successfully applied to a variety of systems. Here, Förster theory is utilized to describe exciton diffusion in SubNc as a function of dilution in UGH2. By assuming that exciton diffusion is dominated by nearest neighbor Förster energy transfer, predictions for the L_D of SubNc as a function of concentration can be made. The L_D as predicted from this simple interpretation of Förster energy transfer is written as:

$$\text{Eq. 7.1} \qquad L_D = \frac{{R_0}^3}{d^2} = \frac{1}{d^2}\sqrt{\frac{9\eta_{PL}\kappa^2}{128\pi^5 n^4}\int \lambda^4 F_D(\lambda)\sigma_A(\lambda)d\lambda}$$

where R_0 is the self-Förster radius, d is the average intermolecular separation, κ is the dipole orientation factor, n is the index of refraction at maximum absorption-emission overlap, λ is the wavelength, F_D is the area normalized fluorescence, and σ_A is the absorption cross section. Here, randomly oriented rigid dipoles are used to approximate the amorphous nature of the films with $\kappa = 0.845\sqrt{2/3}$ [88]. The value of n is determined from separate measurements of the optical constants via spectroscopic ellipsometry. The absorption cross-section is defined as the absorption coefficient divided by the molecular density of the film (ρ). Here, d is taken to be the Wigner-Seitz radius as tabulated from $d = \sqrt[3]{3/(4\pi\rho)}$. The tabulated predictions for the SubNc L_D when dispersed in UGH2 are shown in Figure 7.5, showing good agreement with the experimentally measured L_D values.

7.3. Neat SubNc Devices

Optimization was performed for OPVs incorporating neat donor layers of SubNc as a function of donor layer thickness. Figure 7.6 shows the device schematic where a 10-nm-thick layer of MoO_x [96,109,110] and a 10-nm-thick layer of bathocuproine (BCP) [55] act as the anode and cathode buffer layer, respectively. A 150-nm-thick layer of indium tin oxide (ITO) acts as the anode and a 100-nm-thick layer of Al acts as the cathode. The electrical characteristics are shown in Figure 7.6 and summarized in Figure 7.7.

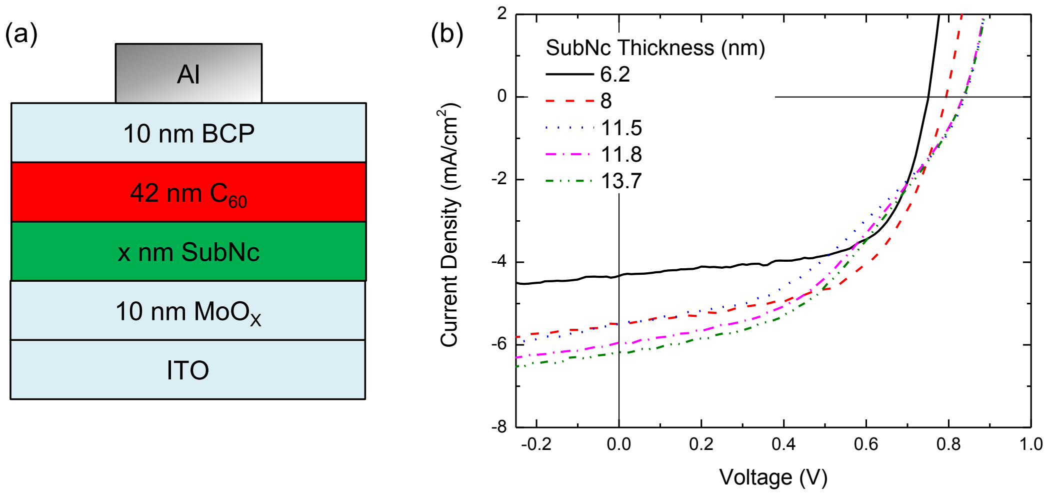

Figure 7.6 Device schematic (a) and current-density voltage characteristics (b) for planar SubPc OPVs as a function of SubNc donor layer thickness.

An increase in both J_{SC} and V_{OC} is observed with increasing SubNc donor layer thickness. The increasing dependence of J_{SC} likely signals an L_D of >10 nm for SubNc. A decreasing trend for fill factor versus donor layer thickness is observed, plateauing to a value of ~0.45 for donor layers >10-nm-thick. The low fill factors observed suggest that these simple planar heterojunction OPVs suffer from poor charge collection under forward bias. In order to maintain adequate charge collection and high fill factors, only thin neat layers of SubNc should be incorporated in the OPV architecture. With increases to the J_{SC} and V_{OC} combined with a decrease in the fill factor, the η_P is found to be relatively constant as a function of SubNc thickness at a value of η_P=2–2.5%.

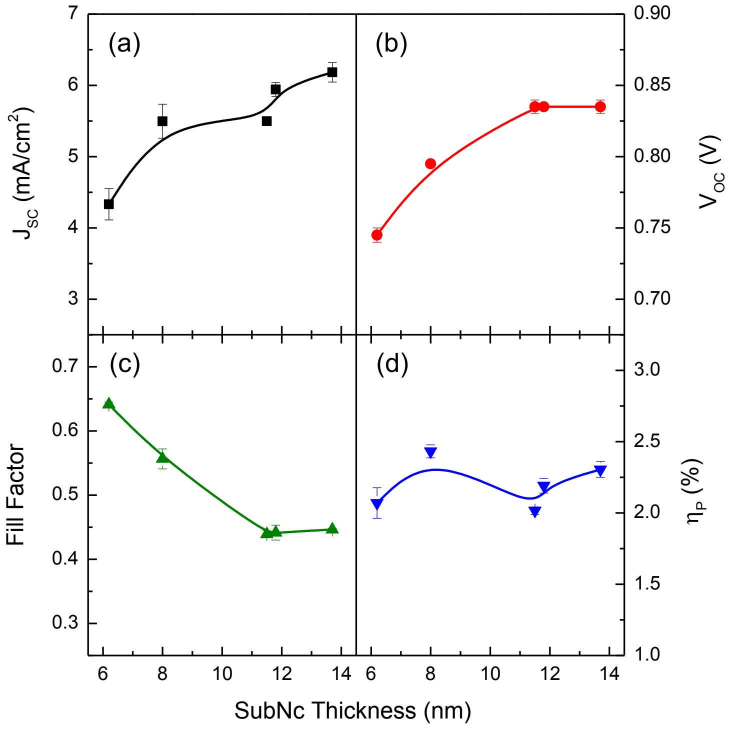

Figure 7.7 Short-circuit current density (J_{SC}), open-circuit voltage (V_{OC}), fill factor, and power conversion efficiency (η_P) for the devices described in Figure 7.6 as a function of SubNc donor layer thickness.

7.4. Dilute SubNc devices with a non-absorbing host

In order confirm the robustness of photoconversion in SubNc to dilution, host-guest OPVs were fabricated incorporating UGH2 as the host material (Figure 7.8). A multilayer donor scheme consisting of a 10-nm-thick dilute layer followed by a 3-nm-thick neat layer of SubNc constitutes the effective donor layer. A thin, neat layer of SubNc is inserted at the donor-acceptor interface. This partially offsets the reduction in absorption efficiency upon dilution and is placed in a location where exciton harvesting is already efficient in neat film. Figure 7.9 displays the short-circuit current density (J_{SC}), open-circuit voltage (V_{OC}), fill factor, and η_P as a function of the dilute layer concentration collected at an intensity of 100 mW/cm^2 under AM1.5G solar simulated illumination. The open symbols correspond to a neat film of SubNc and represent a control device with a single donor layer consisting of a 13-nm-thick layer of SubNc.

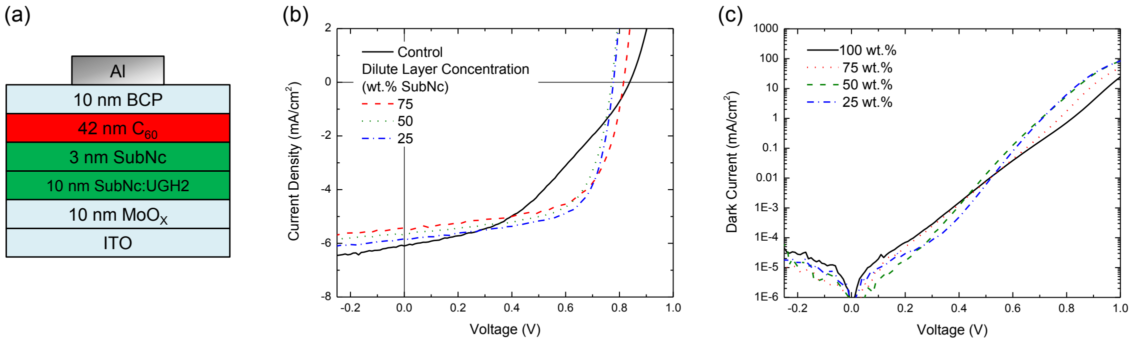

Figure 7.8 Device schematic (a), current-density voltage characteristics (b) and dark current-density voltage characteristics (c) for the host-guest OPVs based on SubNc diluted in the wide energy-gap UGH2.

Interestingly, the J_{SC} is relatively constant versus dilute layer concentration, despite a ~50% reduction in the number SubNc molecules in the total donor layer. This trend indicates that the internal efficiency increases with dilution. The reduction in V_{OC} upon dilution is corroborated by an increase in forward-bias dark current upon dilution. Of additional interest, the fill factor increases with dilution in the control device to 75 wt.% SubNc and remains constant upon further dilution. A similar trend has been reported previously for dilutions of C_{60} in UGH2 (Chapter 5) [108]. This may suggest a shift in the steady state charge density upon dilution at voltages below V_{OC}, thereby reducing either non-geminate recombination at the donor-acceptor interface or exciton-polaron annihilation near the extraction layers [111,125]. Overall, the η_P is optimized at $\eta_P=(3.0 \pm 0.1)\%$ for a dilute layer concentration of 75 wt.% SubNc. As in the case of host-guest donor layers consisting of SubPc and UGH2, the optimum η_P is achieved when the donor layer is partially diluted.

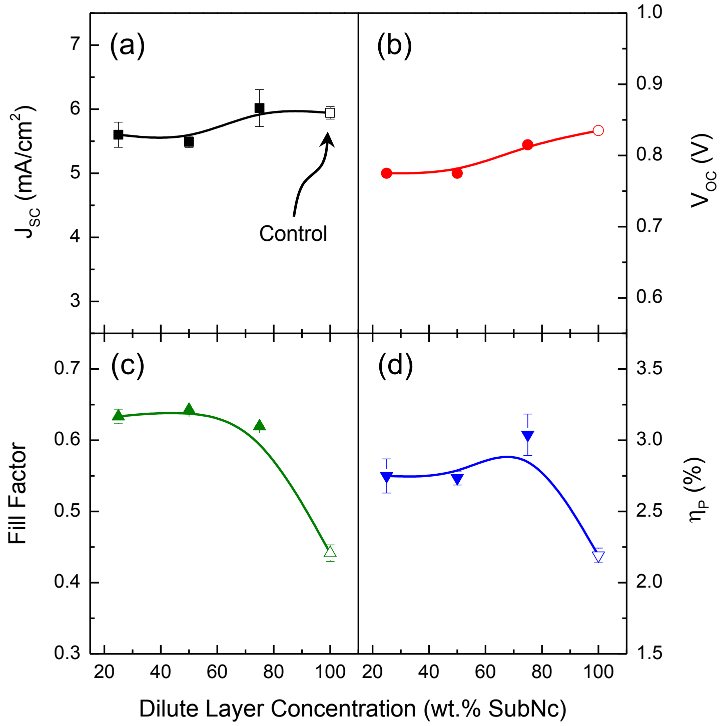

Figure 7.9 Short-circuit current density (J_{SC}), open-circuit voltage (V_{OC}), fill factor, and power conversion efficiency (η_P) for the devices described in Figure 7.8 as a function of dilute layer concentration. Adapted with permission from [118].

7.5. Dilute SubNc devices with an absorbing host

In order to recover the lost absorption that occurs in host-guest donor layers containing UGH2, devices employing a photoactive host of SubPc were examined. Recall from Figure 7.2 that the molecular orbital energy levels for SubNc are favorably nested within those of SubPc, similar to the host-guest relationship between UGH2 and SubPc (SubNc). The device architecture is shown in Figure 7.10, with the dilute layer consisting of a 10-nm-thick layer of 25 wt.% SubNc in SubPc.

7.5.1. Current-density voltage characteristics

As can be seen from the current density-voltage characteristics, the use of a photoactive host increases the J_{SC} from J_{SC}=(5.6 ± 0.2) mA/cm^2 to J_{SC}=(6.2 ± 0.1) mA/cm^2 for devices using an UGH2 host. Interestingly, the V_{OC} increases from V_{OC}=(0.78 ± 0.01) V to V_{OC}=(0.85 ± 0.01) V upon replacing UGH2 with SubPc, similar to the value measured for the undiluted control device and consistent with the measured reduction in forward bias dark current. In contrast, the fill factor for devices containing a SubPc host is larger than that measured for the control device with a value of fill factor=(0.62 ± 0.01), similar to that of the device incorporating UGH2 as the host material. Incorporating SubPc as the photoactive host retains the best characteristics of the control and host-guest OPVs containing UGH2 while also leading to enhanced J_{SC} compared to both devices. The η_P is also enhanced at a value of η_P=(3.2 ± 0.1)%. The J_{SC} and η_P can be further enhanced by utilizing a 40-nm-thick layer of C_{70} as the acceptor layer [126–128]. This strategy is common in the OPV literature as C_{70} has broader absorption than C_{60}. With C_{70}, the J_{SC} increases to J_{SC}=(8.7 ± 0.5) mA/cm^2 and the η_P increases to η_P=(4.3 ± 0.2)%. These represent significant enhancements relative to a SubNc / C_{70} planar heterojunction control device that shows J_{SC}=(6.0 ± 0.1) mA/cm^2, V_{OC}=(0.83 ± 0.01) V, fill factor=(0.43 ± 0.01), and η_P=(2.2 ± 0.1)% under AM1.5G solar simulated illumination at an intensity of 100 mW/cm^2 (Figure 7.11).

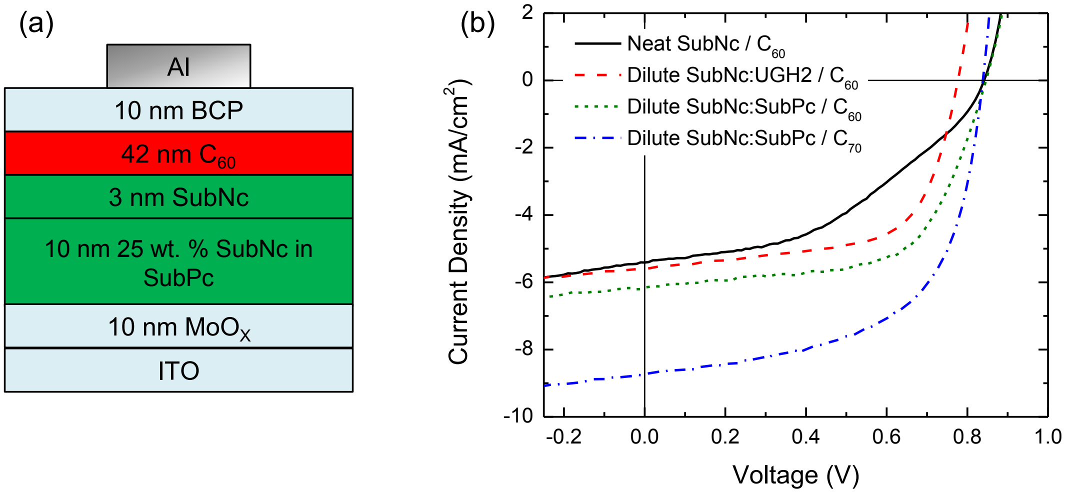

Figure 7.10 (a) Device schematic for the energy-cascade, host-guest OPV based on SubNc and the photoactive host SubPc. (b) Current-density voltage characteristics for various energy-cascade, host-guest OPVs described in this Chapter. Adapted with permission from [118].

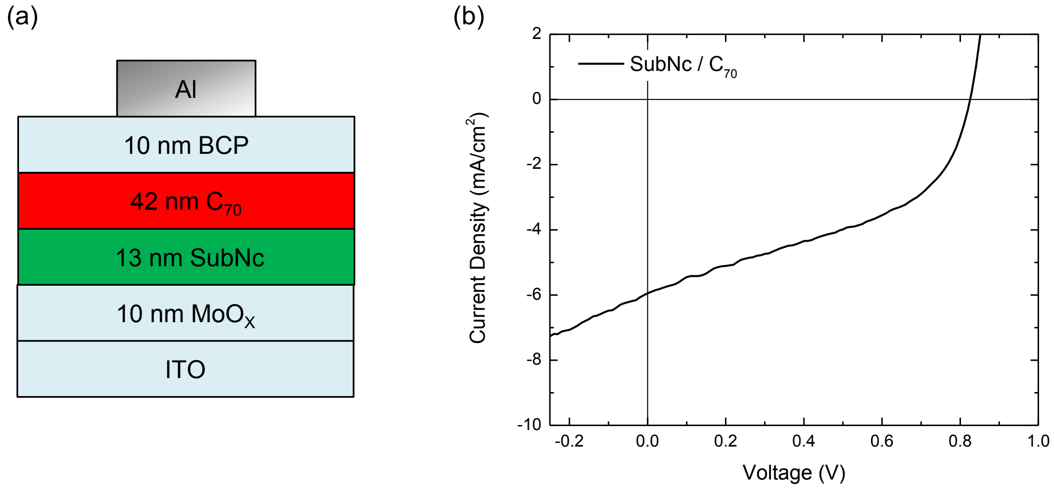

Figure 7.11 Device schematic (a) and current-density voltage characteristics (b) for the reference OPV incorporating a neat SubPc donor layer and a C_{70} acceptor layer.

7.5.2. External and internal quantum efficiency

In order to examine changes in the internal quantum efficiency (η_{IQE}) of the host-guest OPVs presented hereto, the η_{EQE} and reflectivity (R) are separately measured. The reflectivity is measured at an incident angle of 15° and 1-R is taken as an approximate measurement of the optical absorption within the OPV. The relative η_{IQE} is calculated by dividing the η_{EQE} by 1-R (Appendix). Transfer matrix simulations of the internal optical field permit the estimation of absorption losses within the cathode, anode, and surrounding buffer layers which can be further subtracted from 1-R to provide a more accurate estimation for the absorption in the photoactive layers. Figure 7.12 shows the η_{EQE}, 1-R, and relative η_{IQE} spectra for the SubNc control device consisting of a 13-nm-thick total donor layer and a host-guest OPV consisting of a 10-nm-thick layer of 25 wt.% SubNc diluted in SubPc and a 3-nm-thick neat layer of SubNc.

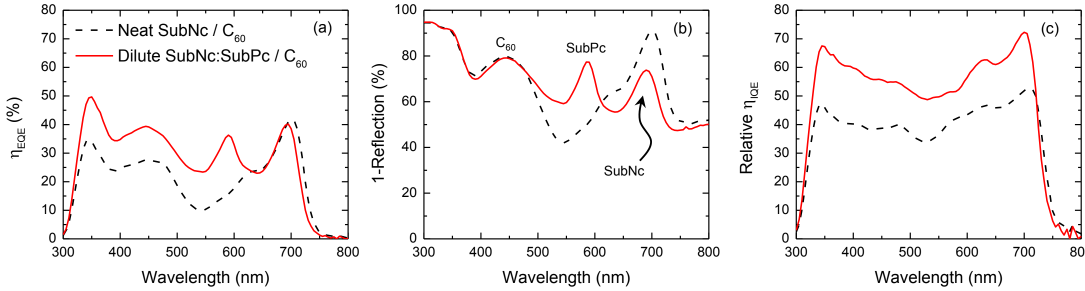

Figure 7.12 External quantum efficiency (η_{EQE}) (a), 1-Reflection (b), and relative internal quantum efficiency (η_{IQE}) for a control OPV incorporating an 8-nm-thick neat SubNc donor layer compared to an energy-cascade, host-guest OPV incorporating a dilute SubNc in SubPc donor layer. Adapted with permission from [118].

Recall, both devices contain a 42-nm-thick film of C_{60} as the acceptor. Inspection of the η_{EQE} reveals enhancements in both the C_{60} and SubPc regions of the spectrum. The latter is clearly rationalized since the control device does not contain any SubPc. The former is likely due to an increase in the η_{CC} for the device. Since the C_{60} acceptor layer thickness and donor-acceptor interface remain constant between the control and dilute devices, changes in the acceptor exciton diffusion (η_D) and exciton dissociation efficiencies are likely minimal. Consequently, η_{CC} is the only remaining component of the η_{IQE} likely to be affected. Inspection of the dependence of fill factor on concentration for the SubNc:UGH2 host-guest OPVs further suggests that η_{CC} is not constant. Figure 7.12 shows 1-R for these two devices and confirms that the response from SubNc is indeed reduced upon the addition of SubPc, as marked by a decrease in 1-R at a wavelength λ=690 nm (SubNc) and an increase in 1-R at λ=590 nm (SubPc). The relative η_{IQE} are shown in Figure 7.12, with broadband enhancement observed for the host-guest OPV with a photoactive host relative to the control device. From the earlier discussion of η_{CC}, the broadband enhancement in the relative η_{IQE} seems to be mainly a result of an enhanced η_{CC}. This is in contrast to the result obtained with SubPc:UGH2 host-guest OPVs reported previously which show large enhancements in the relative η_{IQE} upon dilution due to increases in the η_D. Though the peak relative η_{IQE} >70% is similar to the peak relative η_{IQE} reported for SubPc:UGH2, this result may indicate that there is no significant enhancement in L_D for SubNc when diluted in SubPc.

Such a contrast in the dependence of L_D on concentration between hosts suggests that the choice of the host material is critical (Chapter 4). Moreover, the host material may serve a broader role in energy transfer than simply varying the average intermolecular separation. Here, SubPc is a less advantageous host material when comparing its impact on the L_D of SubNc relative to UGH2. Inspection of the parameters that control exciton diffusion via Förster energy transfer lends intuition (Eq. 7.1). For example, SubPc has n~2.3 in the region of SubNc spectral overlap whereas UGH2 has n~1.6. The larger n serves to reduce the rate of energy transfer and therefore L_D. Additionally, the more polar nature of SubPc as compared to UGH2 may redshift the photoluminescence of SubNc upon dilution owing to a solid-state solvation effect. This effect would reduce the spectral overlap integral and also reduce the L_D of SubNc when diluted in SubPc as compared to UGH2. Beyond exciton transport, the host species may also affect charge transport. For a donor layer, the interplay of host and guest molecular orbital energy levels will dictate the most efficient charge carrier pathway. The mixing ratio provides a route towards optimizing this interplay for a given pair of materials.

7.6. Summary

In this chapter, the effectiveness of host-guest mixtures in energy-OPVs has been demonstrated and explored. Overall, while enhancements in power conversion efficiency were realized, the potential for further enhancements remain. For the host-guest pairing of SubPc and SubNc, the polar nature of SubPc likely counteracts the measured enhancements in L_D for SubNc upon dilution. Transient absorption spectroscopy, for instance, may be useful in characterizing the rate of energy transfer from SubPc to SubNc as well as measuring the diffusivity for excitons residing on SubNc. More than likely a more promising host would be non-polar in nature, similar to UGH2, yet absorb strongly in the solar spectrum.

8. Spin-dependent exciton transport

Engineering excitonic spin has been an enabling step in the design of many organic optoelectronic devices. Dopants for organic light-emitting devices (OLEDs), for example, display enhanced quantum efficiencies by overcoming exciton spin limitations [129,130]. In an OLED, electrical excitation results in the production of singlet and triplet excitons [25]. When electrons and holes of random spin combine, approximately one singlet exciton is generated for every three triplet excitons [131]. For traditional, fluorescent OLEDs, the triplet exciton is non-radiative and the internal efficiency of the device is immediately reduced by ~75% owing to these unfavorable spin statistics [132].

In a molecule exhibiting thermally activated delayed fluorescence (TADF), the singlet and triplet exciton energy splitting (E_{ST}) is very small (E_{ST}<100 meV) [26,133]. Since the energy difference is similar to the thermal energy present at room temperature, triplet excitons are able to efficiently reverse intersystem cross, transforming into radiative, singlet excitons. Remarkably, efficient intersystem crossing can proceed in these materials without the incorporation of heavy atoms as would typically be required for large spin-orbit coupling (Eq. 2.3). Successful manipulation of singlet and triplet excitonic pathways has led to improved OLED device performance [26,134]. In the past years, considerable work has been completed to design molecules with a small singlet-triplet energy splitting and low triplet non-radiative loss [135].

In the organic photovoltaic (OPV) community, long standing questions remain regarding the usefulness of triplet excitons and exciton spin [37,80,113,136–143]. The long triplet exciton lifetime (τ_T~10^{-6}–10^{-3} s) is attractive because it may be correlated to long exciton diffusion lengths (L_D). To date, however, devices harnessing these long lifetimes have only been achieved in organic single crystals [81,144,145]. More commonly, the L_D is limited in disordered organic thin-films (L_D~1–10 nm) owing to a substantially reduced D for triplet excitons (D~10^5–10^8 nm^2s^{-1}) [146,147]. In contrast, singlet excitons have exhibit larger diffusivities (D~10^{10}–10^{11} nm^2s^{-1}) owing to the possibility of longer-range Förster energy transfer [42,43,148]. Organic semiconductors exhibiting TADF provide a unique test-bed for understanding the role of exciton spin in energy transfer and diffusion. In an analogous method to the investigation of boron subphthalocyanine chloride (SubPc) [87], the effect of intermolecular separation on L_D in the archetypical TADF molecule 1,2,3,5-tetrakis(carbazol-9-yl)-4,6-dicyanobenzene (4CzIPN) is investigated [26].

8.1. Dependence of L_D on concentration

The L_D for 4CzIPN was measured as a function of concentration when diluted in the wide energy-gap host material p-bis(triphenylsilyl)benzene (UGH2) [84,85] using thickness dependent photoluminescence quenching. The molecular structure and molecular orbital energy levels as compared to UGH2 are shown in Figure 8.1. As with

SubPc, the wide energy-gap of UGH2 effectively confines photogenerated excitons to 4CzIPN (Figure 8.1).

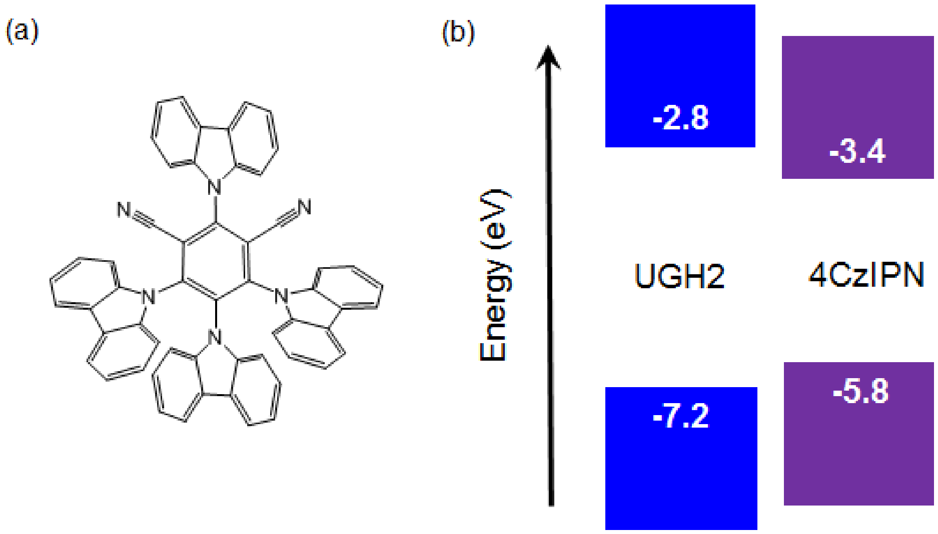

Figure 8.1 (a) Molecular structure of 4CzIPN. (b) Molecular orbital energy levels for 4CzIPN as compared to UGH2.

Experimentally measured and simulated photoluminescence (PL) ratios are shown in Figure 8.2 along with the corresponding fits and fit values for L_D. Interestingly, the L_D increases upon dilution and is maximized at L_D=(8.4 ± 1) nm for 10 wt.% 4CzIPN diluted in UGH2. This represents a 30% enhancement over pure film with an L_D=(6.3 ± 0.8) nm. The trend of L_D versus concentration alone, however, does not provide much insight regarding the interplay between the coexisting singlet and triplet excitons. These competing pathways for exciton transport require a more comprehensive model for L_D than was required for molecules such as SubPc (Chapter 4) and boron subnaphthalocyanine chloride (SubNc) (Chapter 7) where exciton transport occurs primarily along a single state.

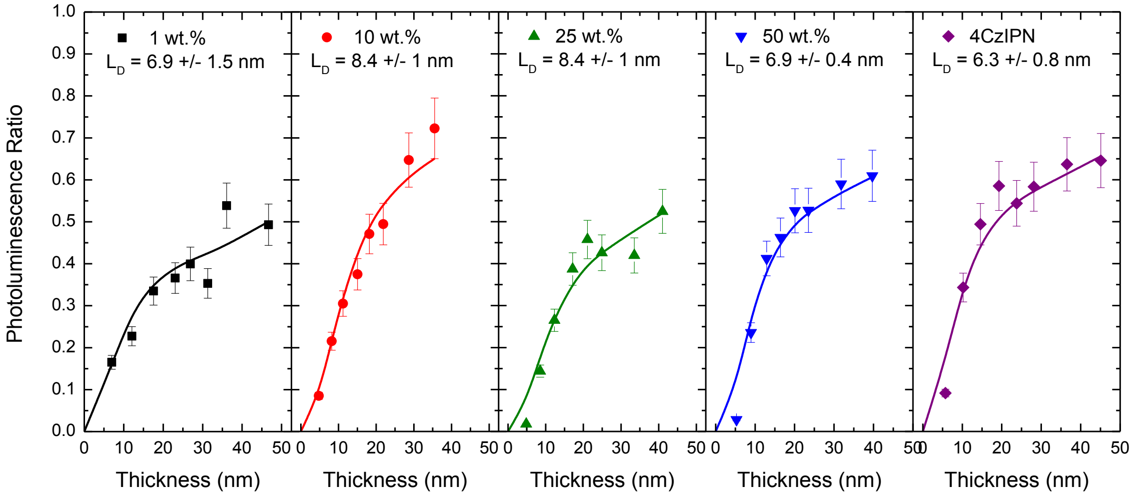

Figure 8.2 Experimentally measured photoluminescence (PL) ratios along with corresponding fits and fit values for L_D for 4CzIPN as a function of dilution in the wide energy-gap host UGH2.

8.2. Modeling exciton diffusion along competing pathways

Modeling exciton transport in molecules exhibiting delayed fluorescence requires care as an exciton can exist in more than one spin-state and each spin-state will have a unique rate of energy transfer to neighboring molecules. In this way, two competing pathways are formed: singlet excitons hopping between nearest and next-nearest neighboring molecules and triplet excitons hopping between nearest neighboring molecules. The measured L_D, consequently, represents a combination of these two pathways, and a proper model for exciton transport in delayed fluorescent systems needs to reflect information regarding how these two pathways interact. In this section, a model for exciton transport in molecules that exhibit TADF is developed. It should be noted that the resulting equations can, in fact, be amended to describe transport in any two-state system as long as the particles move independently of one another (i.e. no second order effects such as triplet-triplet annihilation).

8.2.1. Photophysical pathways for 4CzIPN

The exciton state diagram in Figure 8.3 summarizes the relevant exciton generation, energy transfer, and decay pathways present upon illumination for a generic organic semiconductor [15]. Upon photogeneration to the singlet excited state (S_1), relaxation to the lowest energy state within S_1 is assumed to occur rapidly.

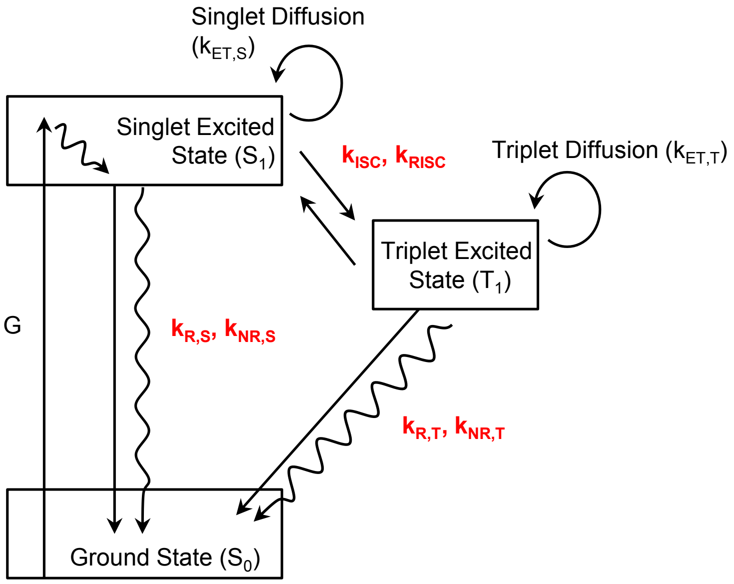

Figure 8.3 Schematic description of the two-state system representative of a typical organic semiconductor. Shown are the relevant excitonic pathways for photogeneration (G), radiative ($k_{R,S}$) and non-radiative ($k_{NR,S}$) singlet decay, radiative ($k_{R,T}$) and non-radiative ($k_{NR,T}$) triplet decay, intersystem crossing (k_{ISC}), reverse intersystem crossing (k_{RISC}), singlet energy transfer ($k_{ET,S}$), and triplet energy transfer ($k_{ET,T}$).

The separated, time-dependent singlet and triplet population functions are written as:

Eq. 8.1 $$\frac{dn_S[x]}{dt} = D_S\frac{\partial n_S{}^2}{\partial x^2} - \frac{n_S[x]}{\tau_{S'}} - n_S k_{ISC} + n_T k_{RISC} + G[x]$$

Eq. 8.2 $$\frac{dn_T[x]}{dt} = D_T\frac{\partial n_T{}^2}{\partial x^2} - \frac{n_T[x]}{\tau_{T'}} + n_S k_{ISC} - n_T k_{RISC}$$

where n_S and n_T are the singlet and triplet exciton densities, D_S and D_T are the singlet and triplet diffusion coefficients, $\tau_{S'}$ and $\tau_{T'}$ are the singlet and triplet exciton lifetimes in the *absence* of intersystem crossing, k_{ISC} and k_{RISC} are the rates of intersystem and reverse intersystem crossing, and G is the rate of exciton photogeneration. The *total* singlet lifetime (τ_S) and triplet lifetime (τ_T) are written as:

Eq. 8.3 $$\tau_S = \frac{1}{k_{R,S}+k_{NR,S}+k_{ISC}}$$

Eq. 8.4 $$\tau_T = \frac{1}{k_{R,T}+k_{NR,T}+k_{RISC}}$$

where $k_{R,S}$ and $k_{NR,S}$ are the radiative and non-radiative singlet decay rates and $k_{R,T}$ and $k_{NR,T}$ are the radiative and non-radiative triplet decay rates.

In 4CzIPN, all measured photoluminescence corresponds to emission from S_1 ($k_{R,T} = 0$) [26]. The photoluminescence efficiency (η_{PL}) can then be separated into two parts. The prompt photoluminescence efficiency ($\eta_{PL,P}$) represents the radiative decay from S_1 to S_0. The delayed photoluminescence efficiency ($\eta_{PL,D}$) represents the radiative decay from S_1 to S_0 after one or more cycles of intersystem and reverse intersystem crossing have occurred. The total photoluminescence efficiency ($\eta_{PL,T}$) is the sum of the prompt and delayed components [149].

Eq. 8.5 $$\eta_{PL,P} = \frac{k_{R,S}}{k_{R,S}+k_{NR,S}+k_{ISC}} = k_{R,S}\tau_S$$

Eq. 8.6 $$\eta_{PL,D} = \sum_{k=1}^{\infty}(\Phi_{ISC}\Phi_{RISC})^k\eta_{PL,P}$$

Eq. 8.7 $$\eta_{PL,T} = \sum_{k=0}^{\infty}(\Phi_{ISC}\Phi_{RISC})^k\eta_{PL,P}$$

Here, Φ_{ISC} and Φ_{RISC} represent the efficiencies of intersystem and reverse intersystem crossing as:

Eq. 8.8 $$\Phi_{ISC} = \frac{k_{ISC}}{k_{R,S}+k_{NR,S}+k_{ISC}}$$

Eq. 8.9 $$\Phi_{RISC} = \frac{k_{RISC}}{k_{R,T}+k_{NR,T}+k_{RISC}}$$

8.2.2. Modeling transient photoluminescence

In order to extract information from transient photoluminescence measurements, the set of differential equations (Eq. 8.1 and Eq. 8.2) must be solved. Assuming that an exciton has already been generated (i.e. set G=0) and a spatially uniform exciton density, the resulting eigenvalues for the system of first order differential equation are:

Eq. 8.10 $$k_{1,2} = -\frac{1}{2}(k_{ISC} + k_{RISC} + k_S + k_T) \pm \sqrt{(k_{ISC} + k_S + k_T)^2 - 4(k_{RISC}k_{ISC} + k_{ISC}k_T + k_S k_T)}$$

where k_S and k_T are the sum of the radiative and non-radiative singlet and triplet decay rates, respectively. Importantly, these time constants can be extracted from measurements of the transient photoluminescence. Note that these time constants are not necessarily τ_S and τ_T. Assuming that the rates of k_S and k_{ISC} are larger than k_T and k_{RISC}, $k_{1,2}$ can be expressed as the rate of prompt decay (k_P) and delayed decay (k_D) as:

Eq. 8.11 $$k_P = k_S + k_{ISC}$$

Eq. 8.12 $$k_D = k_T + \left(1 - \frac{k_{ISC}}{k_S + k_{ISC}}\right) k_{RISC}$$

If Eq. 8.1 and Eq. 8.2 are solved in the steady-state with a non-zero rate of generation, some important quantities can also be derived. First, the steady state populations of the singlet and triplet state can be expressed as:

Eq. 8.13 $$n_S = \frac{G(k_{RISC} + k_T)}{k_{RISC}k_S + k_{ISC}k_T + k_S k_T}$$

Eq. 8.14 $$n_T = \frac{G(k_{ISC})}{k_{RISC}k_S + k_{ISC}k_T + k_S k_T}$$

The balance between the singlet and triplet exciton densities becomes:

Eq. 8.15 $$\frac{n_S}{n_T} = \frac{k_{RISC} + k_T}{k_{ISC}}$$

If the rate of triplet radiative and non-radiative decay is much slower than reverse intersystem crossing, Eq. 8.15 can be simplified to:

Eq. 8.16 $$\frac{n_S}{n_T} = \frac{k_{RISC}}{k_{ISC}}$$

The fraction of singlet (f_S) and fraction of triplet (f_T) excitons as steady-state are:

Eq. 8.17 $$f_S = \frac{n_S}{n_S+n_T} = \frac{1}{1+\frac{k_{ISC}}{k_{RISC}}} \quad \text{and} \quad f_T = \frac{n_T}{n_S+n_T} = \frac{1}{1+\frac{k_{RISC}}{k_{ISC}}}$$

8.2.3. Modeling steady-state transport

In similar way as the derivation of the photoluminescence efficiency, the singlet mean-squared displacement (MSD_S) and triplet mean-squared displacement (MSD_T) can be expressed as:

Eq. 8.18 $$MSD_S = D_S \tau_S \sum_{k=0}^{\infty} (\Phi_{ISC} \Phi_{RISC})^k$$

Eq. 8.19 $$MSD_T = D_T \tau_T \Phi_{ISC} \sum_{k=0}^{\infty} (\Phi_{ISC} \Phi_{RISC})^k$$

where D_S and D_T are the singlet and triplet exciton diffusion coefficients, respectively. Evaluation of the infinite sum leads to simplified expressions for MSD_S and MSD_T.

Eq. 8.20 $$MSD_S = D_S \frac{(k_{RISC}+k_T)}{k_{RISC}k_S+k_{ISC}k_T+k_S k_T} = D_S \frac{n_S}{G}$$

Eq. 8.21 $$MSD_T = D_T \frac{(k_{ISC})}{k_{RISC}k_S+k_{ISC}k_T+k_S k_T} = D_S \frac{n_T}{G}$$

At steady state:

Eq. 8.22 $$G = n_S k_S + n_T k_T$$

and

Eq. 8.23 $$MSD_S = D_S \left(\frac{1}{k_S+\frac{n_T}{n_S}k_T}\right)$$

Eq. 8.24 $$MSD_T = D_T \left(\frac{1}{k_T+\frac{n_S}{n_T}k_S}\right)$$

The total exciton diffusion length can be written as:

Eq. 8.25 $$L_D = \sqrt{MSD_S + MSD_T}$$

Importantly, the total L_D is not solely dependent on the respective diffusivity and lifetime for each state. The balance of intersystem and reverse intersystem crossing dictate effective lifetimes for excitons in each state that also affect the total L_D. This derivation clears the way for a connection between measured photophysical parameters (e.g. η_{PL}, k_P, and k_D) and the measured L_D.

8.3. 4CzIPN photophysical characterization

The photophysical parameters required to connect energy transfer in 4CzIPN to exciton diffusion were measured as a function of concentration.

8.3.1. Steady-state photoluminescence

To begin, the steady state photoluminescence spectra were measured as a function of concentration when diluted in the wide energy-gap host, UGH2 (Figure 8.4). Figure 8.4 also shows the tabulated absorption cross-section for 4CzIPN as extracted from the extinction coefficient measured from spectroscopic ellipsometry. Similar to SubPc and SubNc, the photoluminescence spectra shift towards shorter wavelengths upon dilution. This behavior suggests that 4CzIPN also has polar character, likely reflecting the charge-transfer nature of the exciton [26].

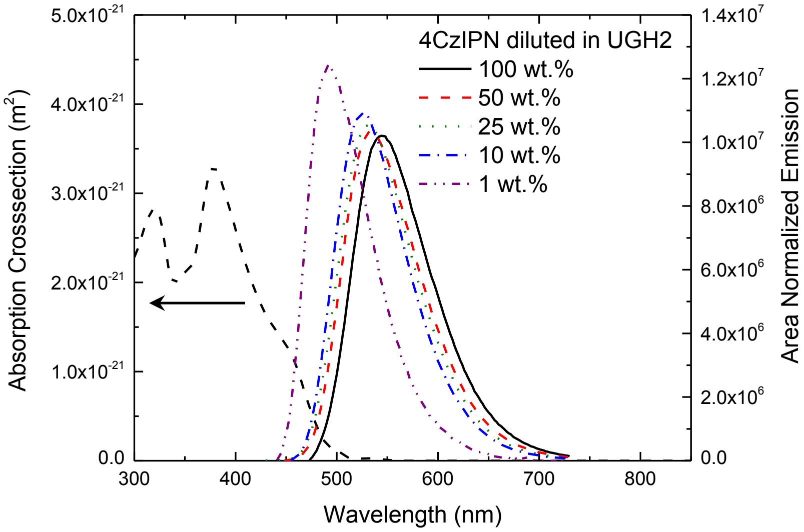

Figure 8.4 Photoluminescence spectra for various concentrations of 4CzIPN diluted in UGH2.

Upon dilution, the η_{PL} is measured to increase. Figure 8.5 shows the concentration dependence of η_{PL} which reaches values near unity at 1 wt.% 4CzIPN diluted in UGH2. Similar to SubPc and SubNc, this behavior may signal a reduction in non-radiative decay upon dilution [150]. The question remains, however, as to what are the individual contributions from both the prompt and delayed components. To provide insight, the characterization of the transient photoluminescence is required in order to deconvolute the prompt and delayed contributions to the total photoluminescence.

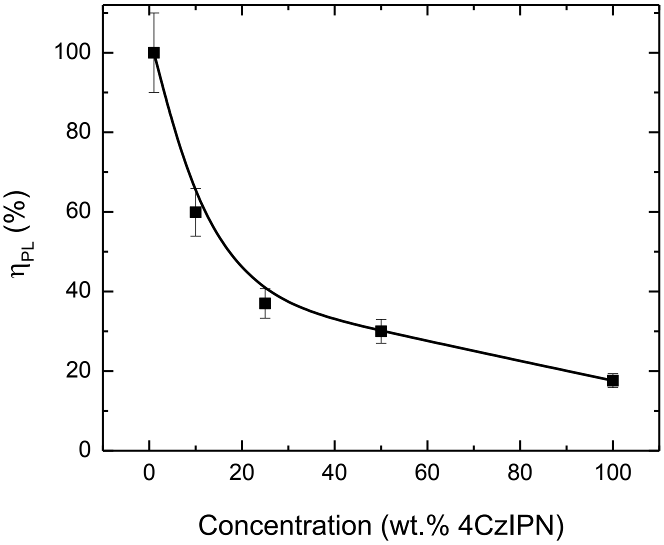

Figure 8.5 Photoluminescence efficiency (η_{PL}) versus concentration for 4CzIPN diluted in UGH2.

8.3.2. Transient photoluminescence

The transient photoluminescence decay was measured as a function of concentration to compliment the steady state photoluminescence spectra and η_{PL}. A N_2 laser was used as the source of illumination at a wavelength (λ) of λ=337 nm and a pulse width of <1 ns. A fast, silicon photodiode was used to record the photoluminescence with a response time of <1 ns. Importantly, a 337 nm band-stop filter was placed directly in front of the detector to ensure that scatter from the N_2 laser was not measured. The output of a 1 ns response-time photodiode under reverse bias was recorded on an oscilloscope across a 50 Ω input. The illumination power was varied with neutral density filters, summarized in Table 8.1.

Table 8.1 Summary of illumination energy density of fluence used for the measurements of transient photoluminescence in 4CzIPN

Filter	Energy Density (μJ/cm^2)	Fluence (10^{13} photons/cm^2)
1	700	119
2	185	31.4
3	70.2	11.9
4	21.7	3.7
5	8.5	1.4

Figure 8.6 shows the measured transient photoluminescence decays for thin-films of 4CzIPN diluted in UGH2 at various concentrations. The four most concentrated films were measured at a pump fluence of 3.7×10^{13} photons/cm^2 and the 1 wt.% film of 4CzIPN in UGH2 was measured at a pump fluence of 11.9×10^{13} photons/cm^2. Low pump fluences were used to ensure that second-order effects like exciton-exciton annihilation do not adversely affect the extracted data. The decays were well-fit with a bi-exponential function. Figure 8.7 summarizes the fit values across the fluences investigated. Largely, the fit values for the prompt and delayed lifetimes are independent of pump fluence, confirming the absence of second order effects. As was derived earlier in this chapter, the short component corresponds to prompt fluorescence from the singlet state. The delayed component corresponds to excitons that have undergone one or more cycles of intersystem and reverse intersystem crossing.

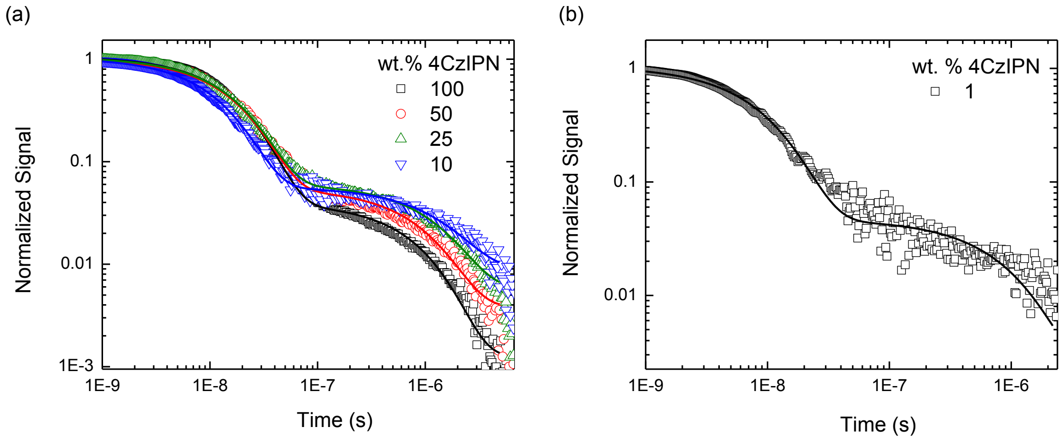

Figure 8.6 Experimental transient photoluminescence decays for various concentrations of 4CzIPN diluted in UGH2 along with the corresponding bi-exponential fits. The peak photodiode signal for each decay was normalized to unity.

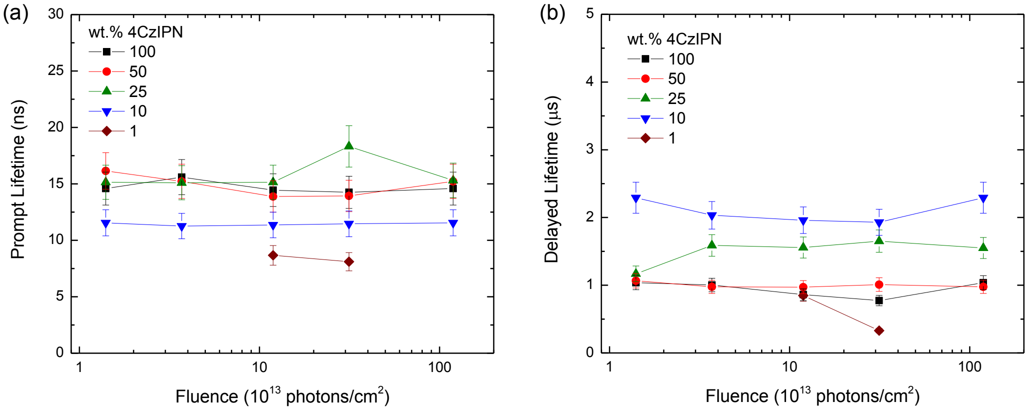

Figure 8.7 Prompt (a) and delayed (b) lifetimes as a function of concentration and pump fluence. The independence of the prompt and delayed lifetimes on the pump fluence confirm the absence of second order annihilation effects such as exciton-exciton annihilation.

Figure 8.8 summarizes the extracted prompt and delayed exciton lifetimes from Figure 8.6. These lifetimes correspond exactly with the time constants described in Eq. 8.10. Interestingly, the prompt and delayed lifetimes appear to be relatively insensitive to changes in concentration. This is in contrast to the concentration dependent η_{PL}.

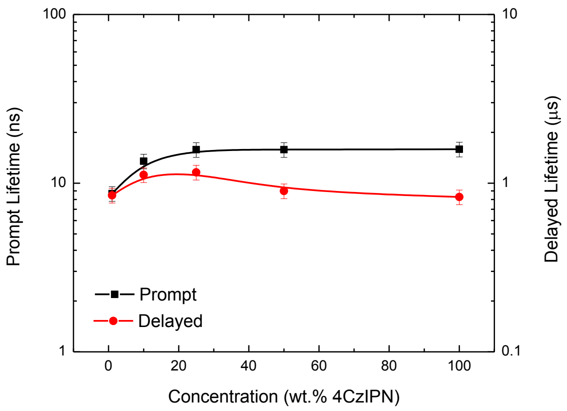

Figure 8.8 Extracted prompt and delayed exciton lifetimes for 4CzIPN as a function of dilution in UGH2.

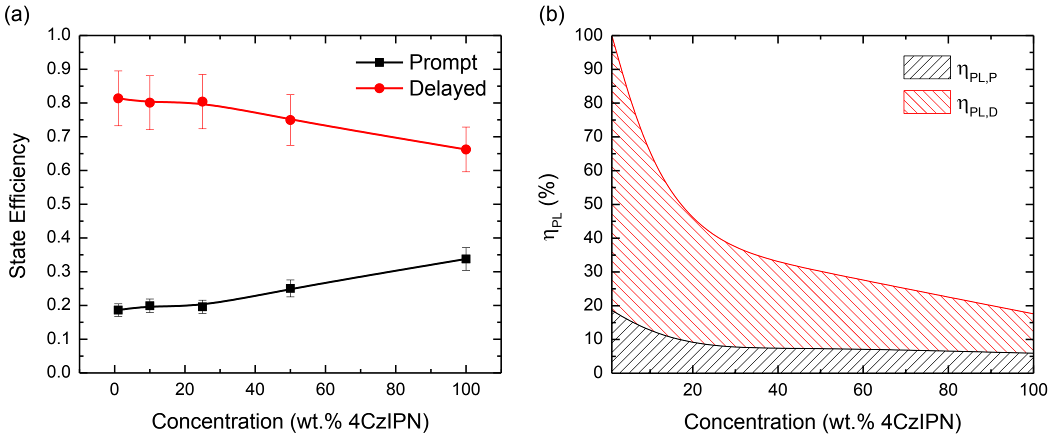

Figure 8.9 State efficiency (a) and separated prompt and delayed photoluminescence efficiencies (b) as a function of concentration for 4CzIPN diluted in UGH2.

Separate integration of the prompt and delayed transient photoluminescence decays allows for the determination of $\eta_{PL,P}$ and $\eta_{PL,D}$ (Figure 8.9). The state efficiency refers to the proportion of radiated excitons that underwent prompt or delayed fluorescence. Multiplication of the state efficiency and the total η_{PL} produces $\eta_{PL,P}$ and $\eta_{PL,D}$. Delayed fluorescence is found to be more prominent for all concentrations investigated. Further, the proportion of delayed fluorescence increases upon dilution and is responsible for the majority of the measured increase in total η_{PL}.

Earlier, it was postulated that the increase in η_{PL} upon dilution was due to a reduction in non-radiative decay. While this is possible scenario, a reduction in k_{NR} cannot be categorically separated from, for instance, a reduction in k_{ISC}. Decreases to k_{NR} and k_{ISC} both result in an increase to $\eta_{PL,P}$ and $\eta_{PL,D}$. Since the state efficiency reveals an increase in the competitiveness for Φ_{ISC} upon dilution, k_{NR} is likely decreasing faster than k_{ISC}. It should be noted, however, that other plausible scenarios for the evolution of rate constants upon dilution may exist. This may be the case, for example, if $k_{R,S}$ is highly concentration dependent. Regardless, it is clear that concentration is an effective tool for mediating the balance between intersystem and reverse intersystem crossing in 4CzIPN.

8.4. Temperature dependent photophysical properties

To examine the thermally activated nature of reverse intersystem crossing in 4CzIPN, steady-state and transient photoluminescence was measured as a function of temperature between 78K and 290K. Figure 8.10 shows the steady-state photoluminescence spectra for 4CzIPN as a function of temperature. Upon cooling, the photoluminescence intensity increases by a factor of ~1.5 with only small changes to the spectral width and peak wavelength. With only small changes in the spectral nature of photoluminescence upon cooling, fluorescence likely remains the dominant radiative decay pathway.

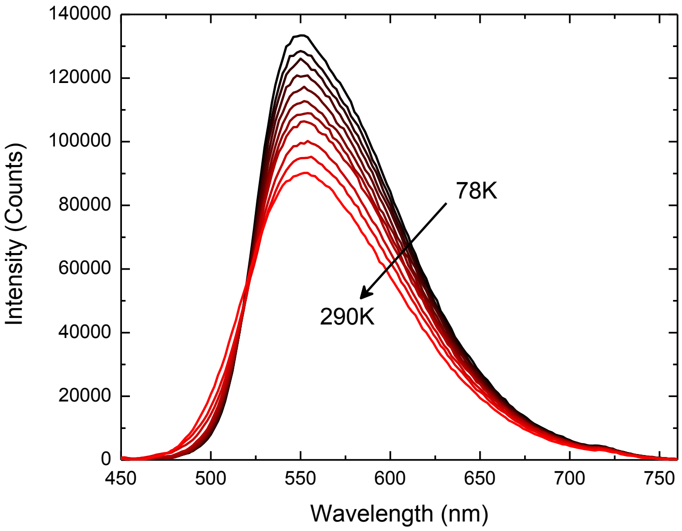

Figure 8.10 Steady state photoluminescence spectra for 4CzIPN as a function of temperature.

In order to probe the evolution of the prompt and delayed decay components, transient photoluminescence was also characterized. Figure 8.11 shows the transient photoluminescence for 4CzIPN as a function of temperature. Transient photoluminescence was recorded at a fluence of 1.2×10^{13} photons/cm^2. Figure 8.11 also shows a summary of the corresponding fit values for the prompt and delayed lifetimes extracted from a bi-exponential fit. The increase in τ_P upon cooling is consistent with an expected reduction in the non-radiative singlet decay. Since τ_D is controlled by Φ_{ISC} and Φ_{RISC}, the slight decrease in τ_D is consistent with a decrease in k_{ISC} upon cooling. Since a reduction in k_{ISC} would also increase τ_P, reductions in k_{ISC} and $k_{NR,S}$ cannot be categorically distinguished.

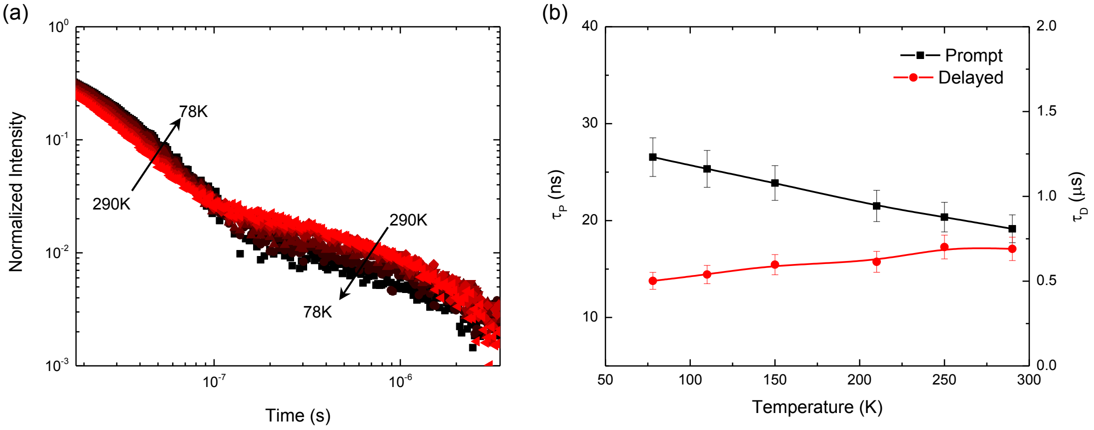

Figure 8.11 (a) Transient photoluminescence and (b) extracted prompt and delayed lifetimes for 4CzIPN as a function of temperature.

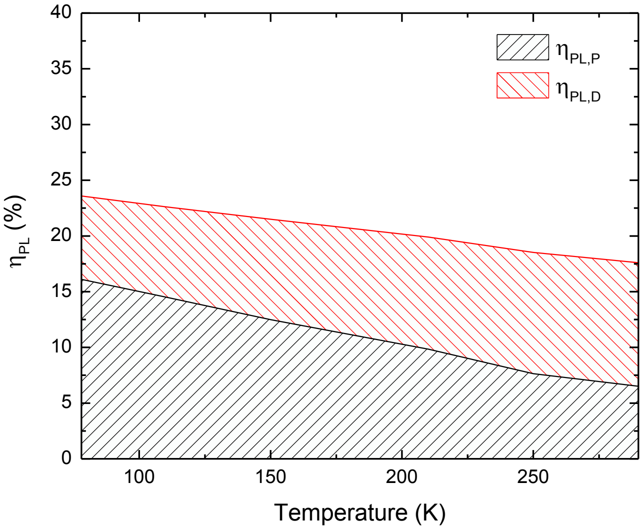

Figure 8.12 Prompt and delayed photoluminescence efficiency (η_{PL}) for 4CzIPN as a function of temperature.

With the prompt and delayed lifetimes measured, the prompt and delayed η_{PL} can be separated from the total η_{PL}. Figure 8.12 shows that the $\eta_{PL,P}$ increases upon cooling, consistent with the increase in τ_P and decrease in non-radiative, singlet decay. In contrast the $\eta_{PL,D}$ decreases upon cooling. Since Φ_{RISC} is likely close to unity, a decrease in Φ_{ISC} is needed to explain the reduction in $\eta_{PL,D}$. Since decreases in non-radiative, singlet decay will increase Φ_{ISC}, k_{ISC} is likely decreasing at low temperatures—in qualitative agreement with the analysis of the prompt and delayed lifetimes. As such, a reduction in k_{ISC} upon cooling will be used as a working hypothesis.

8.5. Reverse intersystem crossing

To investigate the dependence of reverse intersystem crossing versus both concentration and temperature, Eq. 8.26 can be used to extract k_{RISC} as [26]:

$$k_{RISC} = \frac{k_P k_D}{k_{ISC}} \frac{\eta_{PL,D}}{\eta_{PL,P}} \qquad \text{Eq. 8.26}$$

where k_P and k_D are the prompt and delayed decay rates, respectively. Figure 8.13 shows the tabulated k_{RISC} versus concentration and temperature assuming a constant rate of intersystem crossing of $k_{ISC}=4\times10^7$ s^{-1}. Since this assumption is likely invalidated over the full range of temperatures investigated, the high-temperature range (T>200K) is fit with an Arrhenius relationship to establish an upper bound for the activation energy for reverse intersystem crossing (E_A). It is inferred that this activation energy corresponds to E_{ST}. The corresponding fit value is $E_A=(33 \pm 1)$ meV. Interestingly, the tabulated k_{RISC} decreases upon dilution by a factor of ~2 from neat film to films containing 1 wt.% 4CzIPN. This decrease could potentially be captured by an increase in E_A upon dilution to E_A~50–60 meV, a value consistent with experimental measurements of E_{ST} for 4CzIPN diluted in other wide energy gap hosts [26]. Here, the non-polar nature of UGH2 reduces the dielectric constant of the local surrounding environment. In turn, reductions in the dielectric constant have been correlated to a larger E_{ST}. [151]

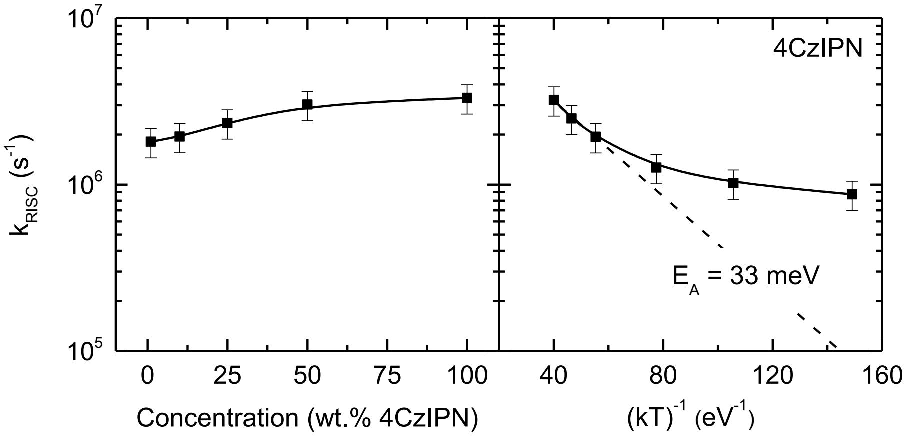

Figure 8.13 Rate of reverse intersystem crossing (k_{RISC}) for 4CzIPN versus both dilution in UGH2 and temperature.

8.6. Energy transfer and diffusion

As was demonstrated in Chapters 4 and 7, a simple model for the exciton diffusion coefficient can be employed assuming nearest-neighbor hopping on a simple cubic lattice. The D_S and D_T can be separately expressed as:

Eq. 8.27 $$D_S = d^2 k_{ET,S}$$

Eq. 8.28 $$D_T = d^2 k_{ET,T}$$

where d is the average intermolecular separation.

For the singlet state, Förster energy transfer likely dominates the nearest-neighbor hopping events, and the rate of Förster energy transfer can be tabulated from the measured photophysical parameters. Using Eq. 2.24, the self-Förster radius (R_0) for 4CzIPN as a function of dilution in UGH2 is shown in Figure 8.14. Importantly, $\eta_{PL,P}$ is used in Eq. 2.24, as the product of η_{PL} and τ_S must produce $k_{R,S}$ in order for the rate of Förster energy transfer ($k_{ET,S}$) to accurately model hopping along the singlet state. Incorrectly using $\eta_{PL,T}$ in Eq. 2.24 results in an overestimate for the R_0 and $k_{ET,S}$. Consistent with previous modeling for amorphous films [46,87,101,118], the dipole orientation factor (κ) is held constant versus concentration at a value of κ=0.69, representative of randomly oriented, rigid dipoles [88]. The index of refraction at the wavelength of maximum overlap and the absorption cross-section are extracted from measurements of the optical constants with spectroscopic ellipsometry. The absorption cross-section is defined as the absorption coefficient divided by the molecular density. The molecular density for 4CzIPN was taken from literature.

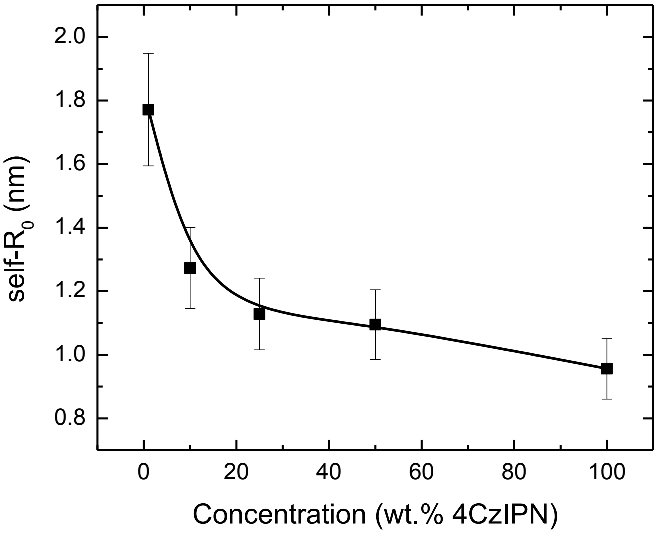

Figure 8.14 Self Förster radius (self-R_0) for 4CzIPN as a function of dilution in UGH2.

From Eq. 8.25, the only missing piece of information required to model L_D is the rate of triplet energy transfer as a function of concentration. In a similar form to the rate of Dexter energy transfer (Eq. 2.25), the concentration dependent rate of triplet energy transfer is modeled as $k_{ET,T} = KJexp(-\beta d)$ where KJ and β are set as fitting parameters. Figure 8.15 compares tabulated $k_{ET,S}$ and the resulting fit values for $k_{ET,T}$ with KJ=1.8×10^8 s^{-1} and β=0.08 $Å^{-1}$as a function of average intermolecular separation (d).

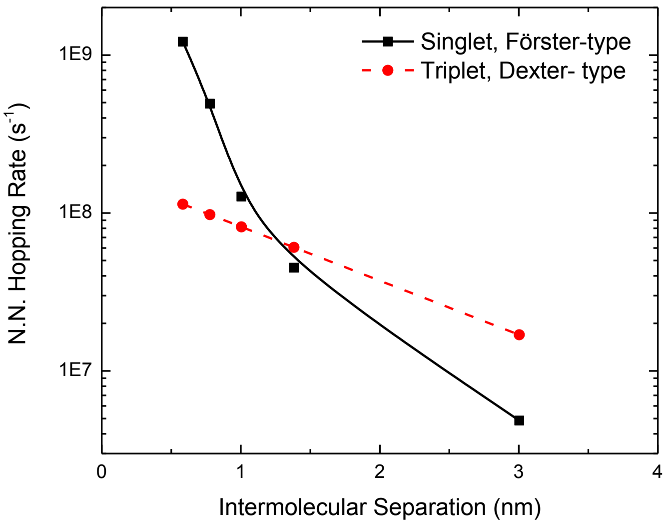

Figure 8.15 (a) Singlet and triplet rates of energy transfer as a function of intermolecular separation. (b) Ratio of n_S to n_T and k_S for 4CzIPN as a function of dilution in UGH2.

Figure 8.16 shows the experimentally measured and fit L_D for 4CzIPN as a function of concentration. Excellent agreement is found suggesting the accuracy of the two-state model described in this Chapter. Also shown are the separated MSD_S and MSD_T. Interestingly, exciton transport is evenly shared between the spin states for pure 4CzIPN. At low concentrations, however, the triplet state dominates exciton transport. This occurs for two reasons. First, k_F decreases more rapidly upon dilution, with increases to d, than the fit values for k_D. In fact, at concentrations less than 10 wt.% 4CzIPN, triplet, Dexter energy transfer proceeds at a faster rate. Second, the τ_T increases from τ_T=(0.3 ± 0.1) μs for a neat film of 4CzIPN to τ_T=(0.6 ± 0.1) μs for a film of 1 wt.% 4CzIPN diluted in UGH2. An increase in τ_T coupled with the weaker concentration dependence for k_D results in longer range triplet diffusion in 4CzIPN at dilutions between 1 and 25 wt.% 4CzIPN. This surprising result contrasts with the typical notion of Dexter energy transfer as being short-range and inefficient at longer distances greater than 10

Å [37]. Correspondingly, the value for β^{-1} is approximately as large (β^{-1}~1.3 nm) as the predicted molecular diameter, suggesting that the triplet excited state wavefunction may be delocalized along the perimeter of the molecule [152,153].

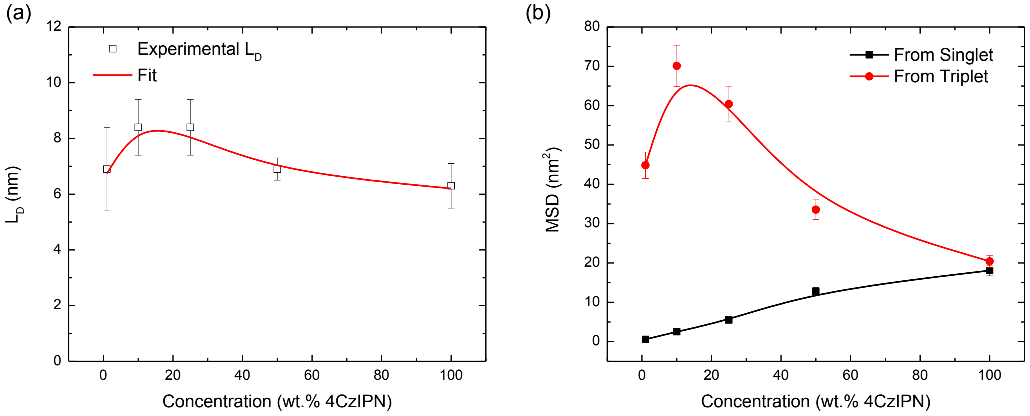

Figure 8.16 (a) Experimental and fit L_D showing excellent agreement. (b) Separated mean-squared displacement (MSD) for the singlet and triplet exciton states.

8.7. Summary

Taken together, the concentration dependent molecular photophysics and exciton diffusion provide unique insight into exciton transport along multiple spin states in a molecule exhibiting thermally activated delayed fluorescence. In 4CzIPN both the E_A for reverse intersystem crossing and the relative magnitude of singlet and triplet exciton transport are found to be concentration dependent. These results highlight the role concentration plays in determining the dielectric environment and, subsequently, balance between intersystem and reverse intersystem crossing. In the broader scope of organic optoelectronics, this work highlights the role concentration can play in mediating spin-dependent excitonic pathways.

9. Role of energetic disorder and thermal activation in exciton transport

As has been shown hereto in this dissertation, the movement of excitons underpins organic optoelectronic device design. Accordingly, exciton transport warrants a further increased fundamental understanding in order to enable new paradigms for enhanced capability and performance. In this chapter, temperature dependent measurements for the exciton diffusion length (L_D) are utilized to probe the fundamental processes limiting L_D in organic semiconductor thin-films. Combined experimental, theoretical, and stochastic results suggest the presence of two transport regimes: activated and non-activated [154–156]. Upon evaluation of the temperature dependence for L_D, the role of energetic disorder and thermal activation can be identified and separated in terms of their relative effect on exciton transport.

9.1. Energetic disorder

In previous chapters, the energetic landscape for excitons has been treated as homogeneous. The assumption, however, is over simplistic when going forward and inspecting the temperature dependence of L_D. A more realistic picture accounts for energetic disorder. This type of disorder has many origins. For instance, the local conformation of neighboring molecules may change the local dielectric environment. A change in the local dielectric environment then alters the energy of an exciton residing on that specific conjugation center. Over an entire film, many different site energies may then be realized, resulting in a continuous distribution. A common distribution function describing disorder in organic thin-films is the Gaussian distribution function (g[E]) written as:

Eq. 9.1 $$g[E] = \frac{1}{\sigma\sqrt{2\pi}}\exp[-\frac{E}{2\sigma^2}]$$

where σ is the disorder parameter, σ^2 is the variance, and E is the energy. In combination with the molecular density of the film (N_D), the density of states (ρ) is expressed as:

Eq. 9.2 $$\rho[E] = N_D g[E]$$

Importantly, the disorder being represented with this function is assumed to be static where the fluctuation in site energies is very long compared to the rate of energy transfer and diffusion.

Other options exist when selecting a distribution function [48,157]. If only the tail of a distribution needs to be considered, an exponential distribution function may be appropriate. If a large number of outliers need to be considered, a Lorentz distribution function may be appropriate. In this chapter, the Gaussian distribution function will be utilized.

Consider the generation of an exciton randomly within the density of states (DOS). At higher temperatures, excitons quickly relax through the DOS and establish a population in thermodynamic equilibrium [154]. Equilibrium is established quickly because nearly all neighboring molecules are energetically accessible. Continuous hopping at equilibrium then takes place since there is sufficient thermal energy for an exciton to access a majority of neighboring sites. In this activated regime, the L_D is temperature dependent and sensitive to the degree of energetic disorder (σ) present in the system. At very low temperatures, relaxation through the DOS becomes frustrated since thermally-activated, upward hops become disallowed, reducing the number of energetically accessible, neighboring sites. The distance an exciton can travel is therefore limited by either trapping in the tail of the DOS or recombination owing to a finite τ [158]. Figure 9.1 schematically describes the activated and non-activated regimes by showing the reduction in relaxation pathways when thermal energy in the system is reduced. While both regimes exhibit sub-diffusive motion, especially at lower temperatures, an effective L_D can be derived that is representative of exciton transport [154,159]. These regimes have been used to qualitatively assess measurements of L_D versus temperature; however direct quantitative fits have not been explored in detail [160,161].

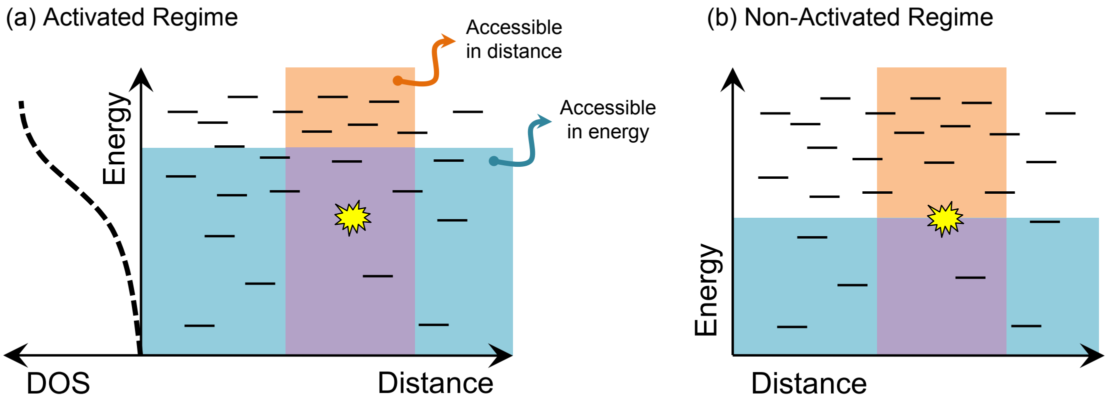

Figure 9.1 Schematic representation of the number of energetically and spatially accessible neighboring sites for an exciton near the tail in the density of states (DOS) in the temperature activated (a) and non-activated (b) regimes.

9.1.1. Theoretical treatment for activated hopping

This section summarizes a previous derivation for the L_D representative of activated hopping described by Athanasopoulos *et. al.* [154]. In a similar manner to Miller-Abrahams hopping, the energy transfer rate Γ(E,E',r), here combined with a Förster-type mechanism, between a molecule or conjugation center with energy E to a target molecule or conjugation center of energy E' separated by distance d can be written as:

Eq. 9.3 $$\Gamma[E',E,r] = \frac{1}{\tau}\left(\frac{R_0}{d}\right)^6 \begin{cases} exp\left[-\frac{E'-\mathrm{E}}{k_BT}\right], & \mathrm{E}'-\mathrm{E} > 0 \\ 1, & \mathrm{E}'-\mathrm{E} < 0 \end{cases}$$

where R_0 is the Förster radius (Eq. 2.24), τ is the exciton lifetime, k_B is the Boltzmann constant, and T is the temperature. In this formalism, upward hops are weighted by a Boltzmann factor. Importantly, R_0 is assumed to be temperature independent. Accordingly, increases in τ do not affect L_D as τ confers the time dependence to the overall transfer rate. To simply the solution, the hopping rate can be rewritten as [154]:

Eq. 9.4 $$\Gamma = \frac{1}{\tau}\exp[-u]$$

where:

Eq. 9.5 $$u[E,E',r] = 6\ln\left[\frac{r}{R_0}\right] + \frac{\eta[E'-E]}{k_BT}$$

Here, η is the Heaviside function. The mean-squared displacement is expressed as:

Eq. 9.6 $$\langle r^2[E]\rangle = \frac{4\pi\int_0^{R_0\exp\left[\frac{u}{6}\right]} r^2 r^2 dr \int_{-\infty}^{E+kT(u-6\ln\left[\frac{r}{R_0}\right]]} g[E']dE'}{4\pi\int_0^{R_0\exp\left[\frac{u}{6}\right]} r^2 dr \int_{-\infty}^{E+kT(u-6\ln\left[\frac{r}{R_0}\right]]} g[E']dE'}$$

$$\cong {R_0}^2\exp[\frac{\langle u[E]\rangle}{3}]$$

where $\langle u[E]\rangle$ is an average hopping parameter. The equilibrium diffusion coefficient is obtained by multiplying the mean-squared displacement with the hopping rate averaged over E. The L_D results as:

Eq. 9.7 $$L_D = \sqrt{D\tau} = R_0 \left(\frac{\int_{-\infty}^{\infty} g[E] \exp\left[-\frac{E}{kT}\right] \exp\left[-\frac{2}{3}\langle u[E]\rangle\right] dE}{\int_{-\infty}^{\infty} g[E] \exp\left[-\frac{E}{kT}\right] dE} \right)^{\frac{1}{2}}$$

As a result, the L_D in the activated regime will be sensitive to the size and shape of the DOS. Increases to N_D will increase L_D whereas increases to σ will decrease L_D.

9.1.2. Theoretical treatment for non-activated hopping

This section summarizes a previous derivation for the L_D representative of non-activated exciton hopping described by Arkhipov *et. al* [162]. In this regime, excitons can only make downward hops in energy. The available part of the density of states (N[E]) is then:

Eq. 9.8 $$N[E] = \int_{-\infty}^{E} g[E']dE'$$

A non-activated exciton energy distribution function can be derived as:

Eq. 9.9 $$f[E,r,t] = A[t]r^2\rho[E]N[E]\exp[-\frac{4\pi r^3}{3}N[E] - \frac{t}{\tau}\left(\frac{R_0}{r}\right)^6]$$

where t is the time until the exciton decays and A[t] is a normalization constant:

Eq. 9.10

$$A[t] = \exp[-\frac{t}{\tau}]\left\{\int_0^{\infty} r^2 dr \int_{-\infty}^{\infty} \rho[E]N[E] \exp\left[-\frac{4\pi r^3}{3}N[E] - \frac{t}{\tau}\left(\frac{R_0}{r}\right)^6\right] dE\right\}^{-1}$$

The L_D is calculated from the mean-squared displacement, $\langle r^2\rangle$, and the total number of hops, n[t=0]. The $\langle r^2\rangle$ can be determined from the distribution function as:

Eq. 9.11 $$\langle r^2 \rangle = \frac{1}{\tau}\int_0^{\tau} dt \int_0^{\infty} r^2 dr \int_{-\infty}^{\infty} f[E,r,t] dE$$

The n[t=0] can be determined by integrating the total jump rate Γ_T from t=0 to infinity where:

Eq. 9.12 $$\Gamma_T[t] = \frac{1}{\tau}\int_0^{\infty} dr \int_{-\infty}^{\infty} \left(\frac{R_0}{r}\right)^6 f[E,r,t] dE$$

Eq. 9.13 $$L_D = \sqrt{\langle r^2 \rangle n[t=0]}$$

Importantly, the non-activated L_D is not dependent on the degree of disorder (σ). Increases to σ result in slower, yet longer, hops. Rather, it is dependent on the R_0 and N_D.

9.1.3. Extended Boltzmann approximation

In Eq. 9.3, the site energy and temperature dependence of the exciton transfer rate within the DOS is approximated by a Boltzmann distribution. The exact energy (wavelength) dependence, however, can be expressed via F_0 as [33]:

Eq. 9.14 $$F_0^6 = \frac{9\kappa^2}{128\pi^5 n^4}\int \lambda^4 F_D[\lambda]\sigma_A[\lambda] d\lambda$$

where κ^2 is the dipole orientation factor, λ is the wavelength, F_D is the area-normalized photoluminescence spectrum, σ_A is the absorption cross-section, and n is the index of refraction at the wavelength of maximum spectral overlap. Note that F_0 is nearly identical to R_0 (Eq. 2.24) except the photoluminescence efficiency (η_{PL}) has been removed. Assuming that energetic disorder leads to similar shifts in F_D and σ_A, upward hops become *less* favorable owing to a reduced spectral overlap integral—in agreement with Eq. 9.3. Downward hops will also become *more* favorable owing to an increase in the spectral overlap integral—behavior not captured in Eq. 9.3. Implementing this exact relationship is difficult, however, without precise knowledge of the purely homogeneously broadened molecular photoluminescence and absorption spectra [163].

If the Boltzmann distribution is extended over the entire energy spectrum, the resulting exciton landscape correctly favors downhill exciton energy transfer and can be used to approximate Eq. 9.14. It should be noted that this approximation remains consistent with the notion of spectral diffusion where a time-dependent shift for the peak photoluminescence wavelength immediately after excitation characterizes the energetic evolution of excitons through the DOS [155,158,164,165].

9.2. Thermal activation of Förster energy transfer

In the previous sections, F_0 was assumed to be constant when considering hopping through the inhomogeneously broadened DOS. Temperature can affect F_0, however, through the spectral overlap integral. As the spectral linewidth for molecular absorption and photoluminescence is approximately proportional to T [166], the spectral overlap integral is expected to increase with increasing temperature. To capture this behavior, F_0^6 can be modeled with an Arrhenius relationship as:

Eq. 9.15 $$F_0{}^6 = F_{0,C}^6 \exp\left[-\frac{E_A}{kT}\right]$$

where $F_{0,C}^6$ is a temperature independent constant and E_A is the activation energy for Förster energy transfer. If the radiative lifetime (τ_{rad}) is assumed be temperature independent, changes in τ can be excluded from the total transfer rate. In this new scheme, the exciton transfer rate is expressed as:

Eq. 9.16 $$\Gamma[E, E', d] = \frac{F_{0,C}^6}{d^6 \tau_{rad}} \exp\left[-\frac{E_A}{kT}\right] \exp\left[-\frac{E'-E}{kT}\right]$$

where the rightmost exponential term represents the extended Boltzmann approximation.

9.3. Kinetic Monte Carlo simulations

Kinetic Monte Carlo (KMC) can be employed to connect the exciton transfer rate with the disordered energetic landscape and simulate L_D as a function of temperature [167]. Importantly, the temperature dependence of τ is separately measured and used as an input to the KMC simulations. The use of KMC to model temperature dependent exciton transport is advantageous because the activated and non-activated behavior, and transition between, emerges naturally without explicit definition.

With an expression for the rates of energy transfer and the measured τ as a function of temperature, KMC simulations are employed to simulate the temperature dependence of L_D where $F_{0,C}^6/\tau_{rad}$, E_A, and σ are set as floating parameters. Excitons are randomly generated on a cubic lattice with a lattice constant of 0.5 nm, $(50)^3$ lattice sites, and periodic boundary conditions. Site energies are selected from a Gaussian distribution and exciton hopping is proceeds according to the site-selective rates described in Eq. 9.16 while considering the nearest neighbors within a $(20)^3$ cubic surrounding centered at the current lattice position of the exciton. When the exciton decays, the mean-squared displacement is recorded and the L_D is tabulated by averaging the mean-squared displacement over 10,000 trials. In this work, contributions from spatial and orientational disorder are not explicitly included in the model and manifest in $F_{0,C}^6/\tau_{rad}$.

9.4. Alq_3, DCV3T, and SubPc

The temperature dependence of L_D and τ were measured for three archetypical organic molecules: aluminum tris-(8-hydroxyquinoline) (Alq_3), dicyanovinyl-terthiophene (DCV3T), and boron subphthalocyanine chloride (SubPc) [43,87,163,168]. Organic thin-films approximately 60-nm-thick were fabricated on pre-cleaned quartz substrates by vacuum thermal evaporation ($<10^{-6}$ Torr) at an approximate rate of 1–2 nms^{-1}. The L_D was measured by spectrally resolved photoluminescence quenching (SRPLQ) where the photoluminescence of a film deposited on a 15-nm-thick exciton quenching layer of 1,4,5,8,9,11-hexaazatriphenylene hexacarbonitrile (HATCN) is compared to that of an identical film deposited directly on the quartz substrate [46,169]. A photoluminescence ratio (PL Ratio) is defined as the photoluminescence at a given emission wavelength (λ_{em}) for the quenched sample divided by that of the unquenched sample. PL Ratios are collected as a function of excitation wavelength (λ_{ex}). Transfer matrix modeling for the internal optical fields combined with solutions to the exciton diffusion equation are used to fit the experimental PL ratios and extract L_D [41]. Time correlated single photon counting was performed as a function of temperature to extract τ. All temperature dependent measurements were performed in a liquid-N_2 cooled optical cryostat.

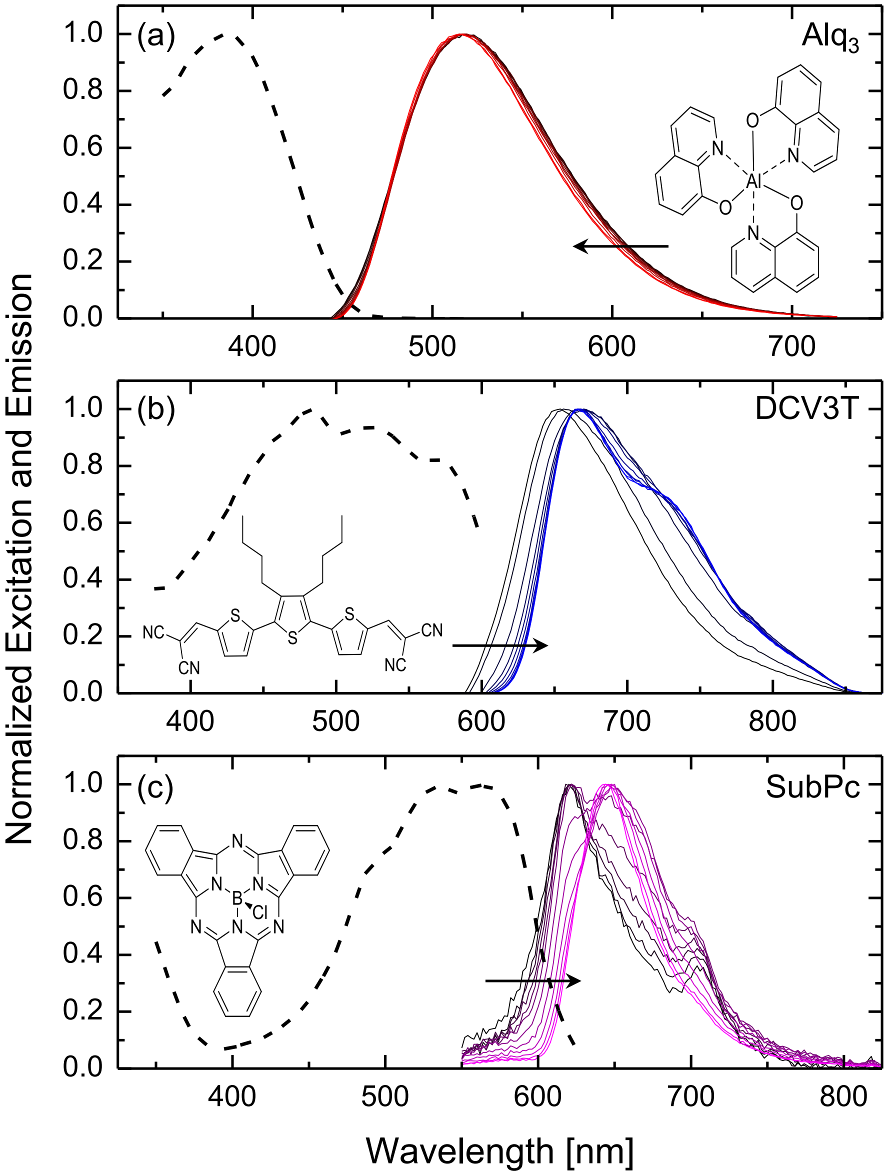

Figure 9.2 Temperature dependent photoluminescence spectra for Alq_3, DCV3T, and SubPc. Arrows indicate decreasing temperature from 295K to 78K. Also shown are representative excitation spectra and molecular structures.

Figure 9.2 shows the peak normalized, steady-state photoluminescence for Alq_3, DCV3T, and SubPc along with the normalized excitation spectra and molecular structures. The arrow denotes decreasing temperature from 295–78K. Both DCV3T and SubPc exhibit bathochromic shifts in photoluminescence upon cooling to 78K, consistent with the qualitative picture of a shift in steady-state exciton population towards lower energies in the DOS. In contrast, Alq_3 photoluminescence exhibits a weaker dependence on temperature, suggesting the steady-state exciton population within the DOS does not change significantly in this temperature range. Consequently, Alq_3 excitons may migrate in a non-activated regime throughout the range of the temperatures investigated.

Figure 9.3a shows time correlated singlet photon counting at room temperature for Alq_3, DCV3T, and SubPc along with the corresponding fits. Figure 9.3b summarizes the extracted values for τ as a function of temperature from 78–295K. For all three materials, τ increases approximately linearly with decreasing temperature. Importantly, these values will be used as a direct input for KMC simulations for L_D.

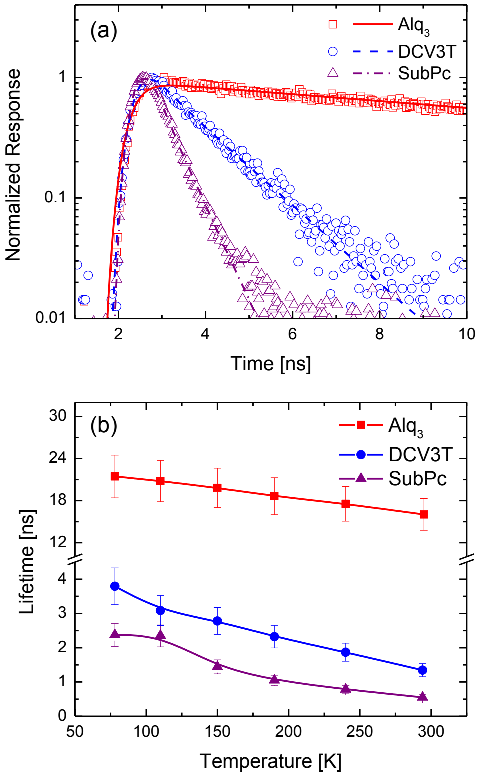

Figure 9.3 (a) Time correlated single photon counting for Alq_3, DCV3T, and SubPc taken at room temperature along with the corresponding fits. (b) Summary of extracted exciton lifetimes (τ) as a function of temperature.

Figure 9.4 shows the photoluminescence ratios measured from SRPLQ of Alq_3, DCV3T, and SubPc at three representative temperatures: 295K, 210K, and 78K. The direction of the arrow denotes decreasing temperature. Also shown are the corresponding fits and fit values for L_D as a function of temperature. Both DCV3T and SubPc exhibit decreasing L_D upon cooling. The L_D for DCV3T is measured to decrease from $L_D=(7.1 \pm 0.4)$ nm at 295K to $L_D=(1.3 \pm 0.4)$ nm at 78K. The L_D for SubPc is measured to decrease from $L_D=(9.4 \pm 0.3)$ nm at 295K to $L_D=(3.0 \pm 0.3)$ nm at 78K. In contrast, Alq_3 exhibits a significantly weaker dependence on temperature remaining nearly constant at $L_D=5.5$–6.1 nm between 295K and 78K. To understand these dependencies, KMC simulations were performed and $F_{0,C}^{6}/\tau_{rad}$, E_A, and σ were varied in order to capture the temperature dependent behavior. The resulting simulations that best reproduce the experimental data are shown as the solid lines in Figure 9.4. The dashed lines represent the maximum and minimum values from a set of corresponding simulations where $F_{0,C}^{6}/\tau_{rad}$, E_A, and σ were separately varied by 5%. The shaded region, consequently, represents the sensitivity of the simulated L_D to small changes in the input parameters. Table 9.1 summarizes the model parameters described by solid lines in Figure 9.4.

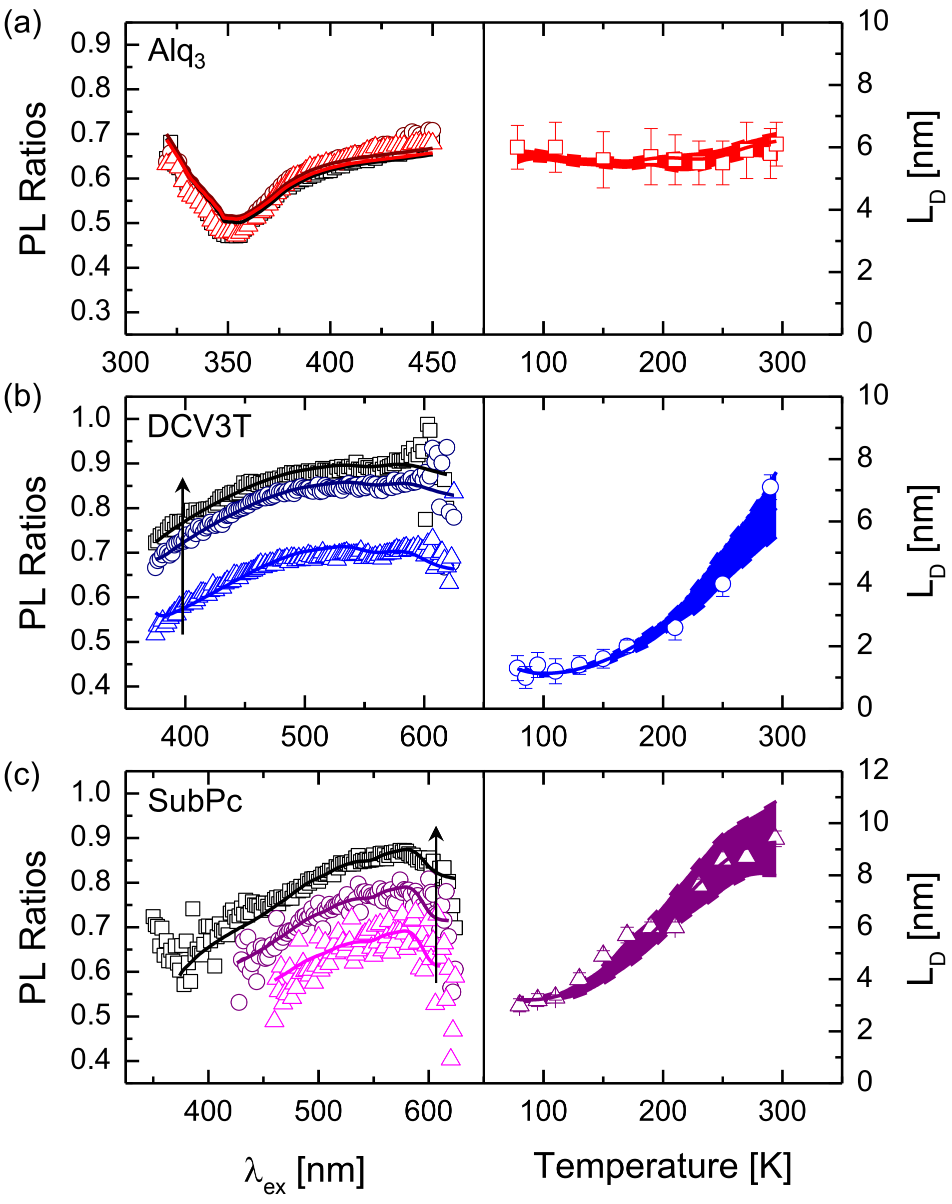

Figure 9.4 Spectrally resolved photoluminescence quenching for Alq_3, DCV3T, and SubPc at 295K, 210K, and 78K along with the corresponding fits. Also shown are the extracted L_D as a function of temperature and the corresponding KMC simulations representative of the L_D vs T behavior for each material.

To deconvolute the photophysical differences between each of the materials, the values for τ and separately measured values for η_{PL} at room temperature are used to calculate τ_{rad} and $F_{0,C}$ [93]. The resulting values for η_{PL}, τ_{rad}, and $F_{0,C}$ are also shown in Table 9.1.

Table 9.1 Model parameters for the KMC simulations predicting the temperature dependence of L_D.

Material	$F_{0,C}^6/\tau_{rad}$ (nm^6/ns)	E_A (meV)	σ (meV)	η_{PL} (%)	τ_{rad} (ns)	$F_{0,C}$ (nm)	d (nm)
Alq_3	2.3	3	150	16.2	99	2.5	0.53
DCV3T	1.7	80	33	8.0	17	1.8	0.54
SubPc	1.4	1	35	1.0	55	2.0	0.48

Inspection of Table 9.1 allows for an informed comparison of exciton diffusion in these three archetypical materials. In the case of Alq_3, where the L_D is relatively constant over the temperature range investigated, exciton diffusion is limited by the large degree of energetic disorder. As a consequence, exciton motion is likely remains in a non-activated regime. As the τ is relatively long as compared to most fluorescent materials, L_D is limited by the distance an exciton can migrate before reaching the tail of the DOS. For Alq_3, F_0 is found the decrease slight upon cooling from F_0=2.4 nm at 295K to F_0=2.3 nm at 78K. With a relatively long $F_{0,C}$, however, large enhancements in Alq_3 L_D may be realized if the energetic disorder could be minimized.

For DCV3T, the disorder is significantly smaller than was seen for Alq_3. The L_D for DCV3T is still shorter than that of Alq_3, especially at lower temperatures, owing to a significantly larger E_A. As a result, the Förster energy transfer rate falls steeply upon cooling—decreasing F_0 from F_0=1.5 nm at 295K to F_0=0.3 nm at 78K. Inspection of Figure 9.2b reveals that the steady-state photoluminescence spectra stops shifting for T<210K, signaling the onset of the non-activated hopping regime. Since the F_0 is still decreasing upon cooling, however, the non-activated L_D continues to decrease as smaller values for R_0 reduce the number of lower-energy, accessible neighbors.

The temperature dependent behavior for the L_D of SubPc was also well-represented with a lower degree of disorder than Alq_3. In contrast to DCV3T, however, E_A is found to be significantly smaller. This results in a very weak temperature dependence for F_0, staying nearly constant at F_0=1.8 nm over the temperatures investigated. Inspection of Figure 9.2c reveals that the steady-state photoluminescence stops shifting for T<110K. As a consequence, SubPc largely remains in the activated hopping regime from 110–295K. The strong decrease in L_D is therefore driven primarily by the energetic disorder in the system, to which the activated regime is strongly sensitive.

In these archetypical organic small molecules, simulating the temperature dependence of L_D allows separation of the competing roles of energetic disorder and thermal activation of energy transfer in exciton transport. The disorder parameter σ captures how dispersion in the local site energy impacts L_D. For a given F_0, the number of nearest neighbors within F_0 of similar or lower energy can limit transport and significantly reduce L_D—consistent to the picture developed for Alq_3. As organic single crystals exhibit reduced site energy dispersion [144], materials with large F_0 limited by a large σ may possess significantly enhanced L_D upon crystallization. Furthermore, this method may provide an *a priori* assessment of potential gains in L_D from efforts aiming to affect film morphology and crystalline order. In the absence of site energy dispersion, $F_{0,C}$ provides a measure for the rate of energy transfer in the limit of $kT>>E_A$. Parameters that affect $F_{0,C}$ include n and κ^2 (Eq. 2) along with the Stokes shift between molecular absorption and photoluminescence. Inspection of $F_{0,C}$ as compared to the average intermolecular separation (d) (Table 9.1) and τ_{rad} allows for meaningful comparisons of the total rate of energy transfer to be made. Accordingly, the long $F_{0,C}$ and short τ_{rad} for SubPc suggest that energy transfer in the absence of temperature induced dispersion and energetic disorder may proceed more rapidly in SubPc than Alq_3 and DCV3T.

While these three materials all exhibit Förster energy transfer, materials that exhibit Dexter energy transfer may also be probed using a similar rationale. At first estimate, Dexter materials may have a reduced length scale for energy transfer—a parallel of F_0—owing to the short-range nature of electron exchange transfer events. As a consequence, even small amounts of energetic disorder may strongly depress and limit L_D owing to a reduced number of accessible neighboring sites. It remains unclear, however, if this is a fundamental limiting factor as temperature-activated, phonon-assisted tunneling may allow for enhanced nearest neighbor energy transfer rate that can overcome any reduction in available destination sites [139,170].

9.5. Summary

Overall, the temperature dependence for the L_D of Alq_3, DCV3T, and SubPc are well-reproduced with stochastic simulations when accounting for the presence of energetic disorder in the inhomogeneously broadened density of states and thermal activation within the rate of intermolecular Förster energy transfer. Consequently, the role of energetic disorder and thermal activation in exciton transport can be effectively separated and compared. The extracted values for E_A and $F_{0,C}$ allow insight regarding the fundamental parameters limiting L_D in these materials. Knowledge of these fundamental limits allows for effective strategies to be employed aimed at, for example, enhancing L_D for application in organic photovoltaic cells.

10. Tunable, broadband organic photodetectors

This chapter represents a departure from the topic of exciton transport and covers work done towards the design of tunable, broadband organic photodetectors (OPDs). Organic photodetectors are a class of optoelectronic devices that are designed for the sensing of ultraviolet, visible, and near-infrared (NIR) photons. While similar in operation to the organic photovoltaic devices (OPVs) presented hereto in this dissertation, OPDs are ultimately characterized by their optical sensitivity and frequency response rather than power conversion efficiency.

10.1. Introduction

Organic photodetectors are of interest for a wide range of sensing applications including imaging, communications, surveillance systems, and biological sensing [171,172]. Photodetectors based on organic semiconductors are attractive for their compatibility with flexible substrates and broad, tunable absorption characteristics. Recent demonstrations have shown that broadband response can be realized in OPDs using a variety of organic and hybrid organic-inorganic systems [171,173–178]. Multilayer OPDs sensitive in the visible spectrum incorporating planar electron donor-acceptor (D-A) heterojunctions in series have been previously used to realize high quantum efficiencies and short response times [179,180]. Mixtures of D-A species, forming bulk heterojunctions, can also be employed; however the response times are typically slower [173,181].

Commonly, broadband response in an OPD is achieved by forming planar or bulk heterojunctions that incorporate a narrow energy gap electron donor material paired with a fullerene acceptor material. While these simple structures can exhibit high external quantum efficiencies and optical responsivities, the spectral tunability of these devices is intrinsically limited to the absorption profiles of the respective donor and acceptor materials. In fact, previous reports of spectral tunability refer to methods that serve only to shift the wavelength of peak response via optical engineering [182] or materials selection [183]. In order to realize both broadband response and inter-band spectral tunability, it is necessary to incorporate additional active materials such that the overall OPD response is the superposition of multiple narrow absorption profiles instead of a single broad absorption profile. In this chapter, broadband OPDs incorporating three donors having complementary absorption extending into the NIR, permitting spectral tunability without sacrificing broadband response, are examined [184]. These qualities are realized in a single photodetector by stacking, in tandem, multiple D-A bulk heterojunction photodetectors, with each sub-cell tuned to a different absorption band. In contrast to typical tandem OPV device architectures, this device architecture does not require highly conductive recombination layers between the stacked bulk heterojunctions.

This approach permits the realization of a broadband photodetector whose spectral response is highly tunable and can be tailored depending on the application.

10.2. Panchromatic absorbing materials

Broadband OPDs were fabricated using three electron donor materials with complementary optical absorption: boron subphthalocyanine chloride (SubPc) [98], chloroaluminum phthalocyanine (ClAlPc) [185], and tin naphthalocyanine dichloride ($SnNcCl_2$) [175]. The absorption coefficients for SubPc, ClAlPc, and $SnNcCl_2$ are shown in Figure 10.1 as determined from spectroscopic ellipsometry.

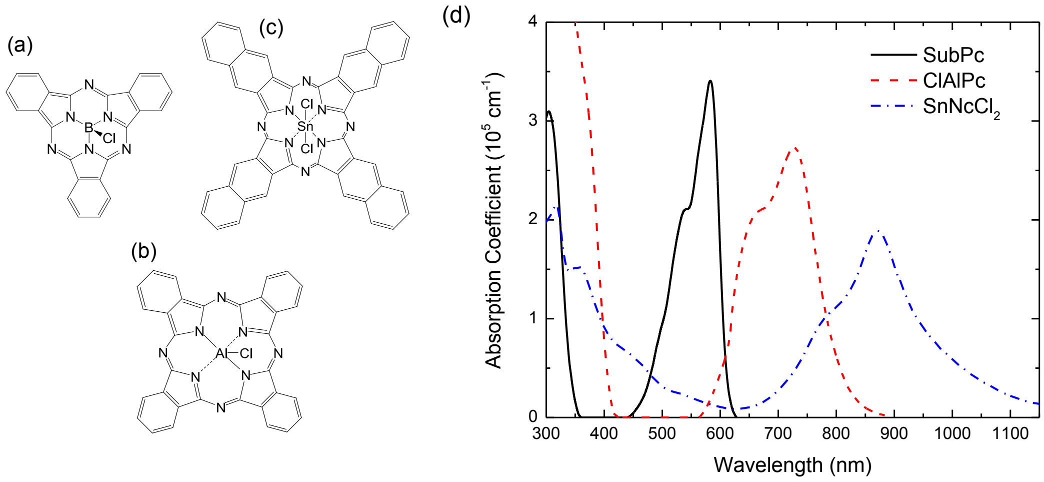

Figure 10.1 Molecular structures for SubPc (a) ClAlPc (b) and $SnNcCl_2$ (c). (d) Absorption coefficient for SubPc, ClAlPc, and $SnNcCl_2$ as determined from spectroscopic ellipsometry and demonstrating complementary absorption. Adapted with permission from [184].

10.3. Single heterojunction OPDs

To characterize the OPD performance of each donor with C_{60}, single-donor bulk heterojunction OPDs were fabricated and characterized. For each OPD, the active layer consisted of an 80-nm-thick 1:1 mixture of the donor and C_{60}. Active layers were deposited on a glass slide coated with a 150-nm-thick layer of indium tin oxide (ITO) and a 10-nm-thick layer of MoO_x. Devices were capped with a 10-nm-thick layer of bathocuproine (BCP) and a 60-nm-thick Al cathode. Figure 10.2 summarizes the device architecture and shows the responsivity for each device at a reverse bias of -6 V, demonstrating that each OPD has a narrow wavelength range of peak response, reflecting the absorption spectra of Figure 10.1.

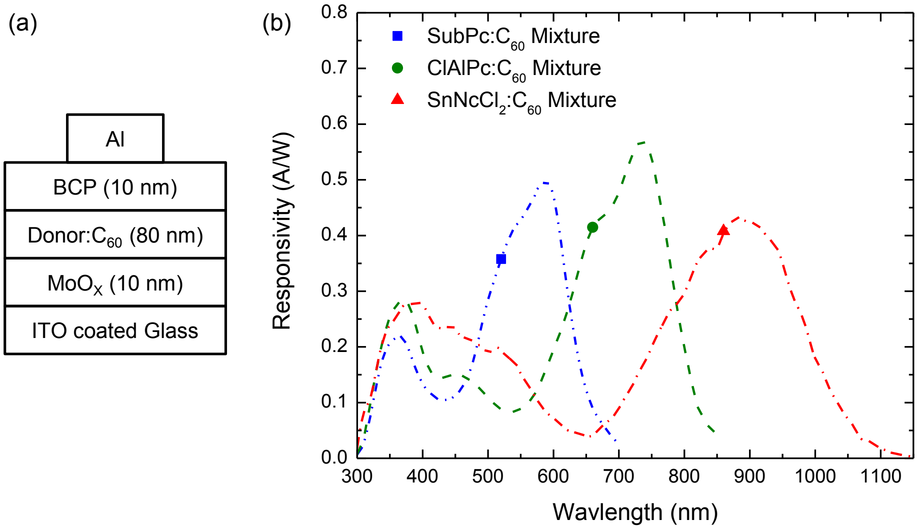

Figure 10.2 Device schematic (a) and responsivity at a reverse bias of -6V (b) for single heterojunction OPDs based on mixtures of SubPc, ClAlPc, and $SnNcCl_2$ and C_{60}. Adapted with permission from [184].

10.4. Broadband, tandem OPDs

In order to realize broadband response in a single device, mixtures of each donor and C_{60} were stacked in tandem with the following active layer structure: a 22-nm-thick layer of 1:1 SubPc:C_{60}, a 27-nm-thick layer of 1:1 ClAlPc:C_{60}, and a 40-nm-thick layer of 1:1 $SnNcCl_2$:C_{60}. The device structure is shown in Figure 10.3. The layer thicknesses were chosen to maintain a similar optical density for each individual donor, ignoring any effects due to optical interference. The responsivity for this tandem OPD at a reverse bias of -6 V is shown in Figure 10.3 and clearly reflects the absorption behavior of each individual donor. Optical responsivities >0.2 A/W are achieved across the visible and NIR, demonstrating the panchromatic, broadband response of this architecture.

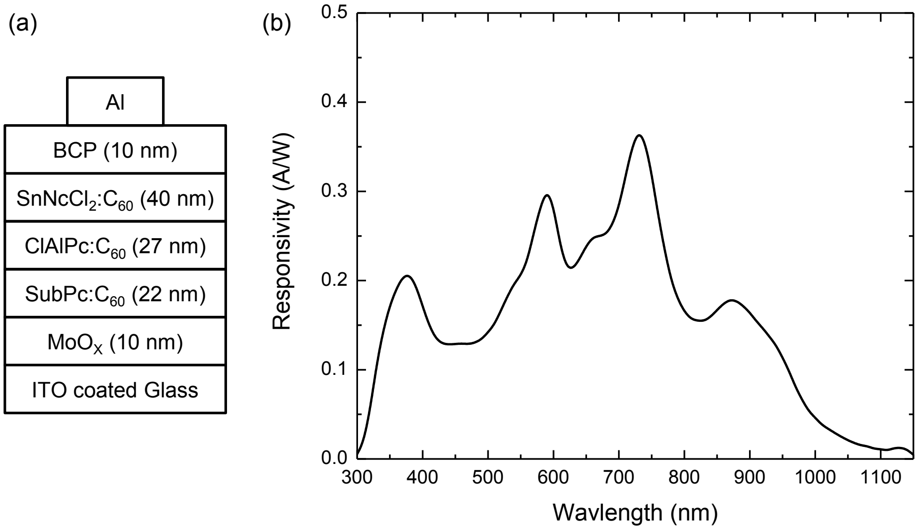

Figure 10.3 Device schematic (a) and device responsivity at a reverse bias of 6V for a tandem, broadband OPD. Adapted with permission from [184].

The highest occupied molecular orbital energy levels (HOMOs) for SubPc and ClAlPc are -5.6 eV and -5.4 eV, respectively [186,187]. While the HOMO level of $SnNcCl_2$ has not been previously measured, it is expected to be shallower than that of ClAlPc since photovoltaic cells constructed using $SnNcCl_2$ show a significantly smaller open-circuit voltage than those constructed using ClAlPc. In order to observe efficient hole collection under zero applied bias, it is necessary to reverse the ordering of the heterojunctions with respect to the tandem OPD in Figure 10.3, hereafter referred to as the control.

10.5. Effect of layer ordering on photomultiplication

Figure 10.4 shows the η_{EQE} as a function of reverse bias for each absorption band for both of the control and reverse structure where the mixtures containing SubPc and

$SnNcCl_2$ are exchanged so that the bulk heterojunction containing $SnNcCl_2$ is closest to the anode. Figure 10.4 shows that the inverted active layer ordering leads to a moderate amount of photomultiplication, signaled by $\eta_{EQE} > 100\%$. Photomultiplication is a gain phenomenon common in OPDs corresponding to situations where more than one electron and hole are collected per incident photon absorbed. [188] It generally arises due to the presence of intrinsically or extrinsically trapped charge carriers, giving rise to imbalanced charge transport and the subsequent injection of additional carriers which lead to additional photocurrent. [189] The reversed ordering shows photomultiplication at reverse biases greater than a few volts and at wavelengths of λ=360 nm and λ=740 nm, corresponding to the optical absorption bands of C_{60} and ClAlPc, respectively. Here, the photomultiplicative gain present in the reversed structure is likely the result of trapped carriers inside the device. In contrast, the control shows no signs of photomultiplication as the η_{EQE} at all wavelengths plateaus to a value less than 100% under reverse bias. While the existence of such a gain mechanism clearly increases the optical response, it can also decrease the speed of the OPD and is found to be difficult to control. Since the purpose is to examine the spectral tunability of the tandem OPD architecture, focus is hereafter placed on the control OPD structure that does not exhibit photomultiplication.

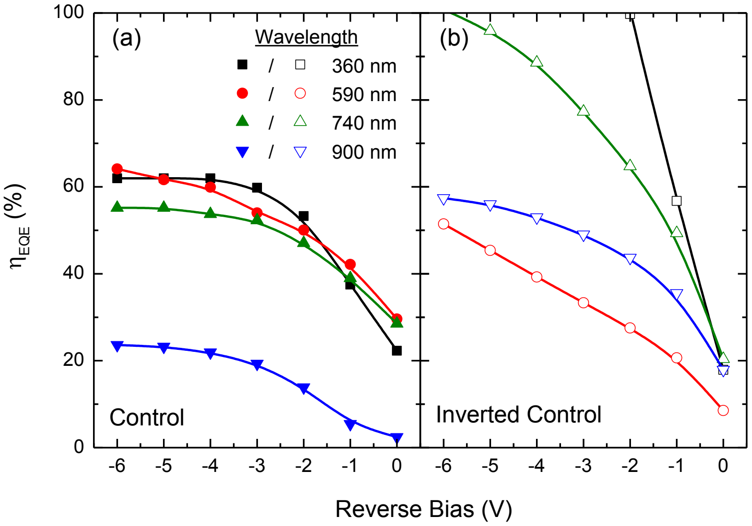

Figure 10.4 Single wavelength external quantum efficiencies (η_{EQE}) for the tandem control OPD (a) and an inverted control OPD (b). Adapted with permission from [184].

10.6. Demonstration of OPD tunability

In order to demonstrate the tunability of tandem, multi-donor OPDs, devices were constructed where the thickness of each individual bulk heterojunction is reduced by 50% relative to the control. Here, OPD-SubPc has the following layer structure: an 11-nm-thick layer of 1:1 SubPc:C_{60}, a 27-nm-thick layer of 1:1 ClAlPc:C_{60}, and a 40-nm-thick layer of 1:1 $SnNcCl_2$:C_{60}. Similarly, OPD-ClAlPc and OPD-$SnNcCl_2$ contain bulk heterojunctions of ClAlPc:C_{60} and $SnNcCl_2$:C_{60}, respectively, whose thickness is reduced by half relative to the control. Figure 10.5 compares the responsivities of these structures to that of the control at a reverse bias of -6 V. Halving the thickness of the SubPc:C_{60} mixed layer (OPD-SubPc) decreases the response from SubPc (λ~590 nm) likely reflecting a reduction in SubPc absorption. The enhancement in responsivity for ClAlPc (λ~740 nm) and $SnNcCl_2$ (λ~900 nm) is likely the result of improved hole collection to the ITO anode. Similarly, OPD-ClAlPc shows a reduction in responsivity for response from ClAlPc, (λ~725 nm) again reflecting a reduction in ClAlPc absorption. The minimal changes in the SubPc and $SnNcCl_2$ absorption peaks signals that the reduction in thickness of the ClAlPc:C_{60} mixed layer does not strongly alter hole collection in this architecture. OPD-$SnNcCl_2$ shows a decrease in responsivity for the $SnNcCl_2$ absorption band (λ~900 nm) attributed to a reduction in $SnNcCl_2$ absorption. The decrease in the ClAlPc dominant absorption band is due to a decrease in the optical electric field at λ=740 nm in the ClAlPc:C_{60} layer as suggested by modeling the optical electric field using transfer matrix formalism. These results demonstrate that spectral tunability can be easily achieved with simple consideration of the mixed layer thicknesses, HOMO landscape, and optical field inside the device.

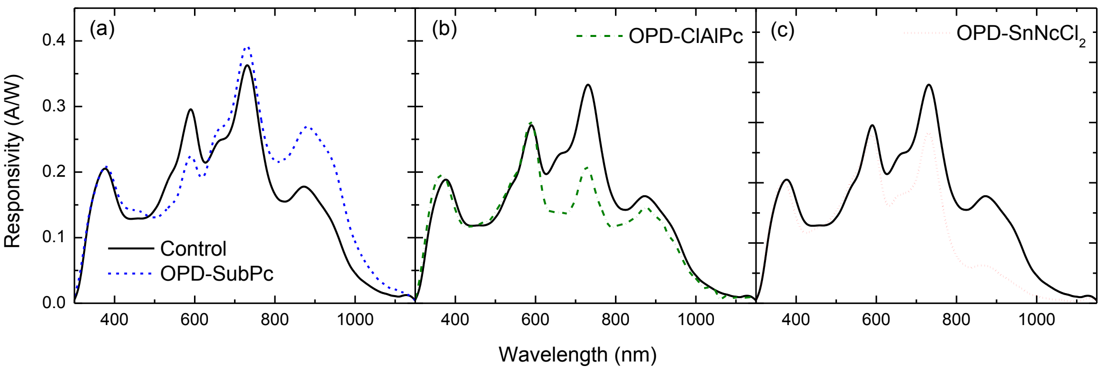

Figure 10.5 Device responsivities for OPDs where the SubPc (a), ClAlPc (b), and $SnNcCl_2$ layer thicknesses are individually halved and compared to the control OPD. Responsivities shown were collected at a reverse bias of -6 V. Adapted with permission from [184].

10.7. Noise equivalent power and detectivity

In order to further characterize the utility of tandem OPDs, the noise equivalent power (NEP) was calculated for the control OPD. The NEP represents the minimum incident optical power than can be detected over the noise. The inverse of the NEP is defined as the detectivity. When the shot noise from the dark current is the most significant contribution to the noise, the specific detectivity normalized for the detector area and detection frequency can be expressed as [171]:

$$D^{*} = R/(2eJ_d)^{1/2} \qquad \text{Eq. 10.1}$$

where R is the responsivity, e is the electron charge, and J_d is the dark current density. The dark current density for the control OPD is 10^{-6} mA/cm^2 at 0 V and 10^{-1} mA/cm^2 at -3 V and shown in Figure 10.6 alongside the dark current densities for the tunable counterparts.

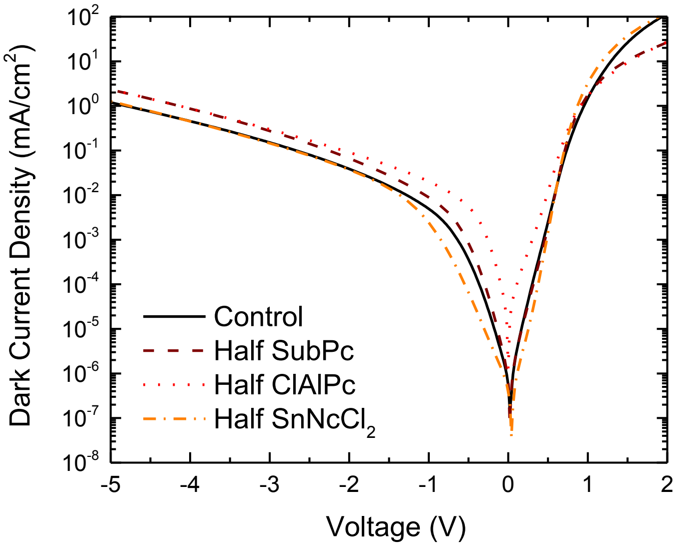

Figure 10.6 Dark current density versus voltage for the control OPD and the OPDs where the noted active layer thickness was halved.

Detectivities for the control OPD were calculated using Eq. 10.1 and are summarized in Table 10.1 for selected excitation wavelengths representative of each active material. These reported values are competitive with detectivities that have been reported for other organic and quantum dot photodetectors across the visible and NIR portions of the electromagnetic spectrum. Further increases in detectivity could be realized by reducing the dark current under reverse bias with the selection of more suitable blocking layers as well as directly optimizing for enhanced photomultiplication.

Table 10.1 Detectivity for the control OPD. Adapted with permission from [184].

Wavelength (nm)	D* (10^{10} Jones)	
	0 V	-3 V
360	340	2.7
590	800	4.3
740	990	5.3
900	100	2.2

10.8. Summary

The chapter has described the design of OPD architectures that demonstrate broadband, tunable optical response. These devices exhibit high η_{EQE} and responsivity at moderate reverse biases across the visible and near-IR spectrum. Broadband response is achieved by incorporating three distinct donor materials with complimentary absorption into three discrete bulk heterojunctions without the requirement of a recombination layer. Tunability is achieved by simple manipulation the heterojunction thicknesses coupled with a consideration for how these changes affect both the optical and charge carrier dynamics within the OPD. These structures are suitable for a wide array of photodetection applications and allow for user specified spectral response.

11. Future work

Hereto in this dissertation, a strong connection between fundamental photophysical properties and exciton transport has been developed. Looking forward, future work can be envisioned that leverages these relationships to realize further enhancements in exciton transport and diffusion length (L_D). This chapter will begin by describing experiments to verify the simulated enhancements in exciton transport efficiency predicted in Chapter 6 for multilayer, organic heterostructures incorporating exciton permeable interfaces. Efforts towards the controlled orientation and orientation of organic semiconductors and the corresponding effect on L_D will also be presented. The chapter will close by examining the usefulness of organic semiconductors that exhibit thermally activated delayed fluorescence (TADF) as electron donors and sensitizers in organic photovoltaic devices (OPVs).

11.1. Experimental evidence for enhanced transport efficiency

In Chapter 6, Kinetic Monte Carlo (KMC) simulations for exciton transport predicted large enhancements in the transport efficiency (η_T) for excitons traversing a 16-nm-thick layer of boron subphthalocyanine chloride (SubPc) [72,97,98] diluted in p-bis (triphenylsilyl)benzene (UGH2) [84,85] upon inclusion of exciton permeable interfaces [116]. At these interfaces, an imbalance in SubPc molecular density and rate of energy transfer results in directed exciton motion into the more dilute layer. The largest enhancement in η_T was simulated for a gradient architecture where the concentration changes continuously from 1 wt.% SubPc to 99 wt. % SubPc at the endpoints. While the framework for the simulations is identical to models that accurately predict the external quantum efficiency (η_{EQE}) and short-circuit current density (J_{SC}) in OPV devices based on dilute donor layers incorporating SubPc and UGH2 [87], there is to-date no experimental verification for the simulated large enhancement in η_T as a function of the number of exciton permeable interfaces within a given structure. In this section, the challenges for designing organic heterostructures to verify these simulations will be addressed and two possible techniques will be presented: sensing layer-based and quenching layer-based.

11.1.1. Sensing layer-based

Consider a simple bilayer, planar heterojunction OPV device. The exciton diffusion efficiency (η_D) is defined as the probability that a photogenerated exciton is able to encounter the donor-acceptor interface whereby exciton dissociation can proceed efficiently. As excitons are photogenerated throughout the entirety of the donor and acceptor layers, especially if the layers are much thinner than the optical absorption path length (L_A typically $\geq$50 nm), the η_D reflects the L_D and the shape of the optical field profile (Chapter 5). In contrast, the η_T for a given organic heterostructure is defined for excitons traversing the entire layer(s) structure. To effectively measure η_T, a more precise way of injecting excitons into an organic heterostructure is required.

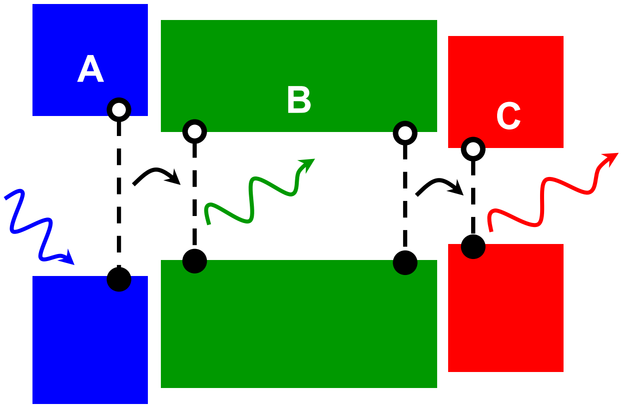

Figure 11.1 Schematic representation for the sensing layer-based approach for measuring the transport efficiency of excitons through an organic heterostructure (B). Excitons are selectively generated in the injection layer (A). Luminescence from the sensing layer (C) is a local probe of excitons on the destinations side of the organic heterostructure. Importantly the energy gaps of A, B, and C are selected such that efficient energy transfer can proceed at the interfaces.

A method to achieve a precise injection of excitons into a given organic system is shown in Figure 11.1. Here, the organic heterostructure of interest (B) is inserted between two additional layers: an injection layer (A) and a sensing layer (C). Importantly, the energy gap (E_g) of layer A is larger than B and the E_g of the heterostructure B is larger than C ($E_{g,A}>E_{g,B}>E_{g,C}$). By selectively pumping the injection layer excitons can subsequently energy transfer from layer A to heterostructure B. If short-range energy transfer occurs near the interface, exciton generation into the organic heterostructure of interest can be localized. Similar structures have been envisioned for preferentially injecting triplet excitons into an organic active layer and monitoring triplet exciton diffusion [138].

Exciton transport proceeds throughout the organic heterostructure of interest. If an exciton is able to traverse the entire structure, energy transfer from the heterostructure to the sensing layer is realized. Again, short-range energy transfer is preferred in order to locally probe excitons near the heterostructure–sensing layer interface. This ensures that long-range energy transfer from the heterostructure to the sensing layer does not overestimate the number of excitons able to traverse the entire heterostructure. Since the sensing layer has a reduced E_g, the red-shifted luminescence can be selectively monitored and compared across an array of heterostructure compositions to determine the relative degree of η_T.

An example set of materials that partially fulfill these requirements are shown in Figure 11.2 along with the corresponding extinction coefficient (k). Here, N,N'-di-1-naphthalenyl-N,N'-diphenyl-[1,1':4',1'':4'',1''']-quaterphenyl]-4,4'''-diamine (4P-NPB) [190,191] is used as the injection layer, SubPc is used within the organic heterostructure, and platinum tetrabenzo tetraphenylporphyrin (PtTPTBP) [46,192] is used as the sensing layer. Within this material set, selective excitation of the injection layer can be realized at an excitation wavelength (λ_{EX}) of λ_{EX}=355–375 nm. In this wavelength range, no excitons are generated on SubPc and PtTPTBP only exhibits weak absorption. Consequently, PtTPTBP luminescence (λ_{EM}~770 nm) should only result from excitons photogenerated on 4P-NPB and able to traverse the entire SubPc organic heterostructure.

Disadvantages of this material set are also apparent. First, long-range Förster energy transfer may occur from SubPc to PtTPTBP owing to the strong overlap between SubPc photoluminescence of PtTPTBP absorption. Long-range energy transfer reduces the sensitivity of the sensing layer and may result in over estimates for η_T. While Dexter energy transfer is typically of shorter-range than Förster energy transfer, care must be taken in selecting materials that undergo primarily Dexter energy transfer such that the dominant exciton spin-state matches that of the organic heterostructure of interest—in the case of SubPc, a singlet. Requiring spin-orbit coupling to change the exciton spin-state at the interface may significantly slow the rate of energy transfer and result in inefficient exciton injection and sensing. Note that PtTPTBP may also act as an triplet sensitizer, resulting in the population of triplets in SubPc at the interface and enabling SubPc phosphorescence [113,141].

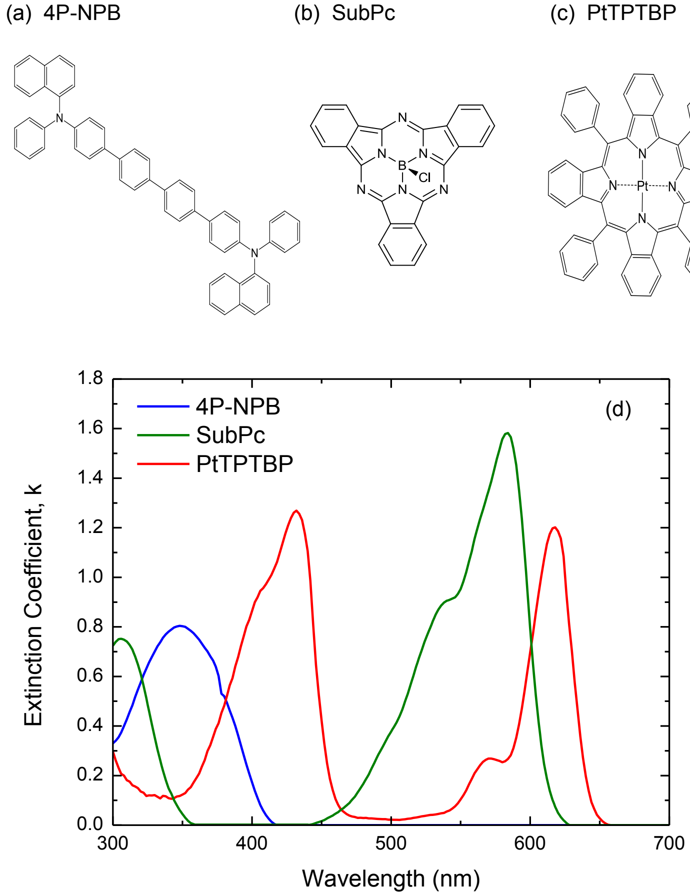

Figure 11.2 Molecular structures for 4P-NPB (a), SubPc (b), and PtTPTBP (c) along with the extinction coefficient for each molecule. The extinction coefficient spectrum for PtTPTBP was collected by Deepesh Rai (unpublished).

11.1.2. Quenching layer-based

In a similar configuration to the sensing layer-based approach, a quenching layer-based approach may also be useful for characterizing the η_T for an organic heterostructure. A schematic for the quenching layer-based approach can be seen in Figure 11.3. Again, an injection layer is used to localize the starting point for excitons traversing the heterostructure. In contrast, however, a quenching layer is found on the destination side of the heterostructure instead of a sensing layer. In this scheme, photoluminescence quenching between two identical structures, one with and one without the quenching layer, is performed. Only excitons that are able to traverse the entire structure are quenched and the generated photoluminescence ratio will be sensitive to the transport through the heterostructure. A wide E_g quenching material should be incorporated in order to reduce the amount of long-range Förster energy transfer [43].

In order to extract η_T, transfer matrix modeling combined with KMC simulations for transport in each structure will be required in order to model the experimentally measured photoluminescence ratios. An advantage of this approach is that direct measurements can be performed to extract absolute values of η_T for a single heterostructure. The sensing-layer approach, in contrast, can only give comparative information between two heterostructures and extract relative changes to the η_T. A Disadvantage of this approach, however, is that the photoluminescence efficiency for each layer within the organic heterostructure must be known in order to correctly convert the spatial profiles for the steady-state exciton density into photoluminescence ratios.

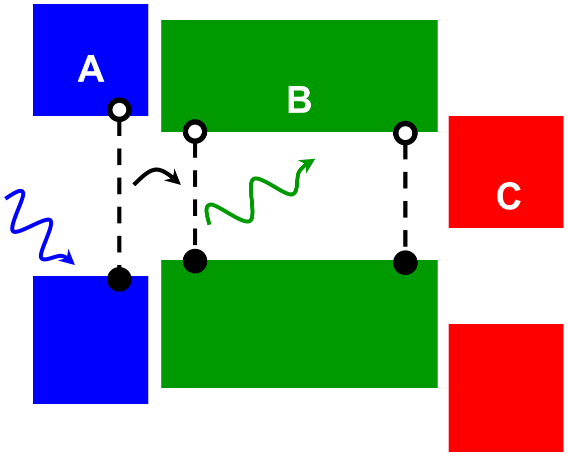

Figure 11.3 Schematic for the quenched layer-based approach to monitor the transport efficiency of excitons through an organic heterostructure (B). Exciton are selectively generated on the injection layer (A) and transferred to the heterostructure. Photoluminescence quenching measurements are then performed in the presence and absence of a quenching layer (C) located at the destination side of the organic heterostructure.

Overall, both of these approaches offer a plausible way to begin monitoring the efficiency of excitons traversing organic heterostructures that contain exciton permeable interfaces. Upon further design refinements and proper materials selection, each approach gives relevant information regarding the evolution of excitons in these structures at steady state. Transient photoluminescence based techniques may also be of interest for monitoring the transport time for excitons traversing the organic heterostructure.

11.2. Effect of uniaxial dipole alignment on L_D

While chemical and physical modifications to alter the primary photophysical rates of a molecular system offer insight and some solutions to the problem of the short L_D, a large body of work has been focused on the use of long range, crystalline ordering to achieve increases in L_D [144,193,194]. On one end of the spectrum lay organic single crystals where long range translational symmetry has been shown to correlate to extraordinary electron and hole mobilities as well as ultra-long L_D [144,195]. For amorphous, semicrystalline, and polycrystalline organic systems, researchers have shown how thermal annealing and molecular templating can be used to inject crystallinity, thereby enhancing L_D [114,196–198].

Recently, organic thin-films exhibiting uniaxially anisotropic optical properties have been demonstrated [58]. In these films, the molecules have random in-plane orientation and aligned out-of-the-plane orientation. This is typically achieved with molecules demonstrating a large aspect ratio. Some examples can be seen in Figure 11.4 [58,199,200]. Variable angle spectroscopic ellipsometry is an ideal tool for quantifying the degree of anisotropy in these materials. The question remains, however, how alignment and crystallinity rigorously affect exciton transport and L_D. In this section, effects of orientation will be discussed by inspecting the orientation factor present in the Förster radius and exploring the resulting impact upon L_D.

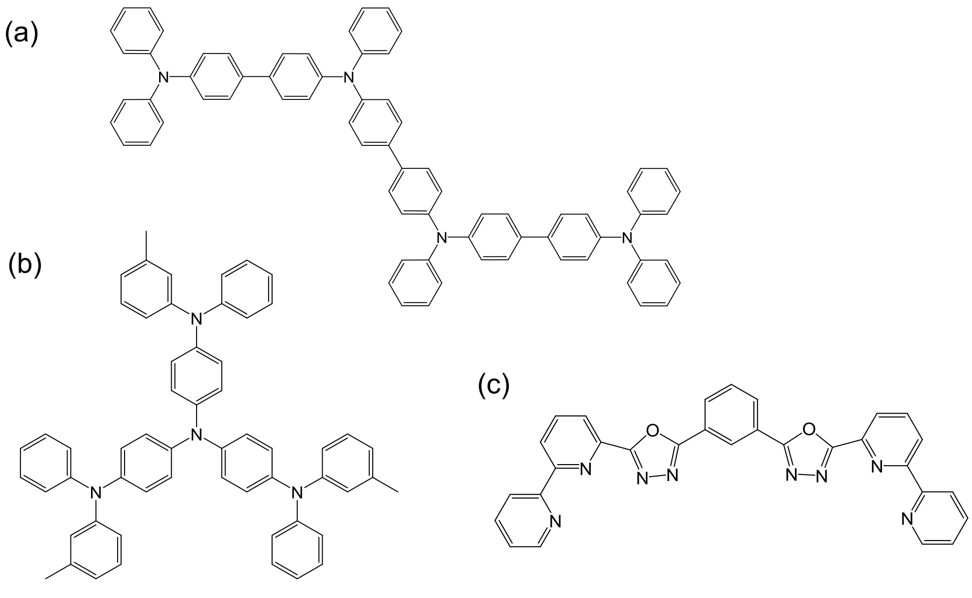

Figure 11.4 Molecular structures for TPT1 (a), m-MTDATA (b), and Bpy-OXD (c) which demonstrate varying degrees of uniaxially anisotropic optical constants.

11.2.1. Orientation Factor

In a Förster type energy transfer scheme, the order is mostly contained in the orientation between the transition dipole moments, κ^2, of the donor and acceptor molecules as summarized in Eq. 11.1, where φ_{AD} is the angle between the donor and acceptor dipoles and φ_A and φ_D are the angles between the respective dipole of the molecule and the molecular stacking direction.

Eq. 11.1 $$\kappa^2 = [\cos(\phi_{AD}) - 3\cos(\phi_A)\cos(\phi_D)]^2$$

The orientation factor is then rigorously bounded between zero and four. For simplicity, κ^2 is presented in Figure 11.5 for various orientations of in-plane dipole moments that are common for typical organic systems. For reference, randomly oriented rigid dipoles will have $\kappa^2 = 0.476$ [88]. For typical crystalline organic materials that form parallel stacks as seen in Fig 5a, increasing order only increases κ^2 for a certain range of angles with respect to the molecular stacking direction. Interestingly, κ^2 reduces to exactly zero for the magic angle at 54.7°. This is also true for the more obvious case of completely orthogonal transition dipole moments. This line of reasoning also extends beyond Förster type energy transfer as well. For Dexter type energy transfer, exciton hopping can only take place when there is direct electronic orbital overlap. Hence, if the electronic orbitals of two neighboring molecules are perfectly orthogonal there can be no energy transfer between the two. Note that the ideal ordering for Förster energy transfer need not necessarily be optimal for Dexter energy transfer. Predicting how orbital overlap changes with ordering is non-trivial and likely very system dependent, making it difficult to predict whether increased crystalline order will extend L_D in systems dominated by Dexter type energy transfer.

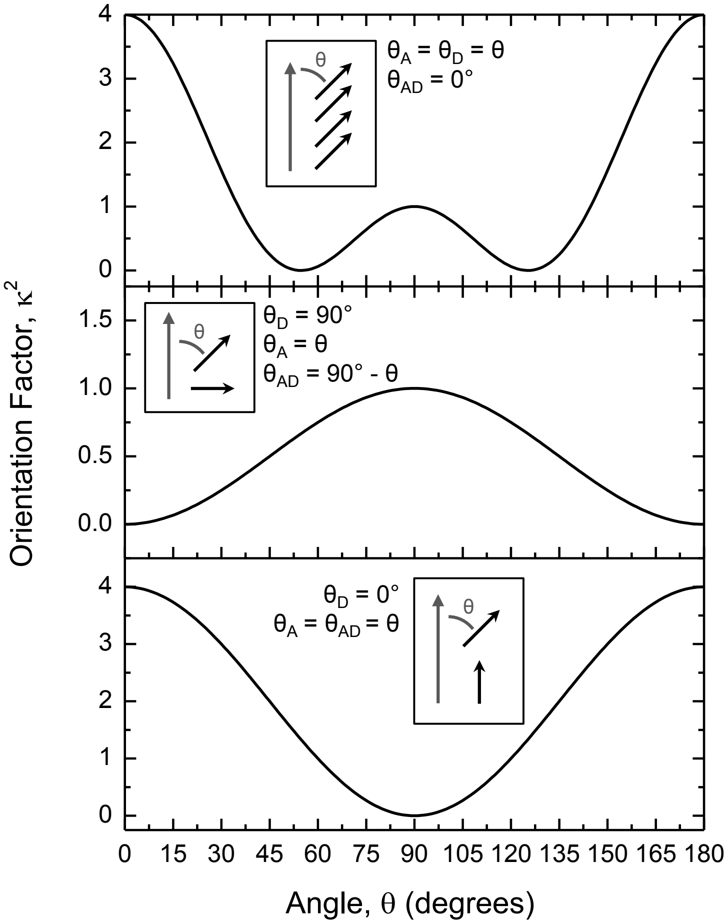

Figure 11.5 Orientation factor (κ^2) for three configurations of in-plane dipole moments as a function of angle (θ) from the stacking direction.

11.2.2. Uniaxially oriented thin-films

For uniaxially oriented thin-films, the dipole orientation factor can no longer taken from the isotropic limit used to represent amorphous films as demonstrated in Chapters 4, 7, and 8. Figure 11.6 clarifies this difference by showing a schematic representation for the transition dipole moments for an isotropic film and for a film with uniaxial symmetry. Isotropic alignment can be envisioned as selecting a random differential area on the surface of a unit sphere and drawing a vector that connects the differential area to the center of the sphere. In contrast, uniaxial alignment can be envisioned as selecting a differential area on the surface of an ellipsoid where there is more lateral area than vertical area.

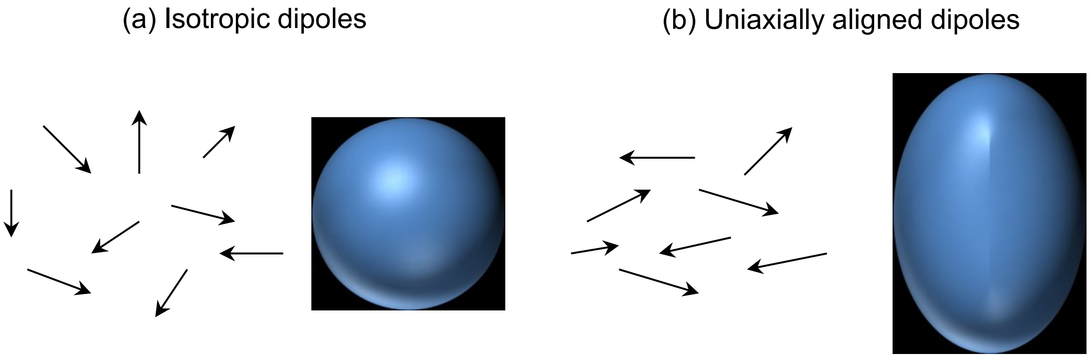
(a) Isotropic dipoles

(b) Uniaxially aligned dipoles

Figure 11.6 Schematic representation of molecular transition dipole moments for an amorphous film of random alignment (a) and for a film with uniaxially alignment.

The degree of anisotropy (χ) is then characterized by the ratio of the length of the long axis (c) by that of the short axes (a) as:

Eq. 11.2 $$\chi = \frac{c}{a}$$

The parametric equations that describe an ellipsoid are:

Eq. 11.3 $$x = \mathrm{a}\sin[\phi]\cos[\theta]$$

Eq. 11.4 $$y = \mathrm{a}\sin[\phi]\sin[\theta]$$

Eq. 11.5 $$z = c\cos[\phi]$$

where θ and φ are the in-plane and out-of-plane angles, respectively. The probability of selecting a small piece of area (dA) can be written as:

Eq. 11.6 $$\frac{dA}{A} = \frac{2\pi a\sin[\phi]\sqrt{c^2\sin^2[\phi]d\phi^2 + a^2\cos^2[\phi]d\phi^2}}{2\pi a^2 + \frac{\pi c^2}{e_1}\ln\left[\frac{1+e_1}{1-e_1}\right]}$$

where

Eq. 11.7 $$e_1 = \sqrt{1 - \frac{c^2}{a^2}} = \sqrt{1-\chi^2}$$

A connection between the parametric equations describing the spheroid and the orientation factor are required. For fluctuating dipoles [88]:

Eq. 11.8 $$\langle \kappa^2 \rangle = \int \kappa^2[V] \nu[V] dV$$

Where V represents the total volume of dipole configurations and υ is the normalized angular distribution. For static dipoles this equation is scaled as [88]:

Eq. 11.9 $$\langle \kappa^{\Delta/3} \rangle = \int (\kappa^2[V])^{\Delta/6} \nu[V] dV$$

For simplicity, an alternative definition for κ^2 is written in terms of unit vectors representing a first dipole moment ($\mathbf{r}_A$), a second dipole moment ($\mathbf{r}_B$) and the vector connecting r_A and r_B ($\mathbf{r}$).

Eq. 11.10 $$\kappa^2[V] = [\boldsymbol{r}_A \boldsymbol{r}_B - 3(\boldsymbol{r}_A \boldsymbol{r})(\boldsymbol{r}_B \boldsymbol{r})]^2$$

Finally,

Eq. 11.11

$$\nu[V] dV = \left(\frac{dA_A}{A_A}\right)\left(\frac{dA_B}{A_B}\right) dV =$$

$$\frac{d\theta_A d\theta_B d\phi_A d\phi_B}{(2\pi)^2} \left[\frac{2\pi a \sin[\phi_A]\sqrt{c^2 \sin^2[\phi_A] + a^2 \cos^2[\phi_A]}}{2\pi a^2 + \frac{\pi c^2}{e_1} \ln\left[\frac{1+e_1}{1-e_1}\right]}\right] \left[\frac{2\pi a \sin[\phi_B]\sqrt{c^2 \sin^2[\phi_B] + a^2 \cos^2[\phi_B]}}{2\pi a^2 + \frac{\pi c^2}{e_1} \ln\left[\frac{1+e_1}{1-e_1}\right]}\right]$$

By selecting **r** for different directions (e.g. in-plane or out-of-plane), κ^2 can be derived for uniaxial thin-films as a function of the degree of anisotropy (χ).

As a general result, thin-films with transition dipole moments aligned perfectly aligned in-plane will have κ^2 smaller in the out-of-plane direction than a film of randomly aligned transition dipole moments. This can be rationalized upon inspection Figure 11.5 where the optimum dipole orientation is head-to-tail. In a uniaxial thin-film, no head-to-tail alignment is present in the out-of-plane direction. In contrast, while randomly aligned dipoles have no overall order, some degree head-to-tail alignment is present and manifests in a larger overall κ^2 in the out-of-plane direction. Accordingly, the ideal configuration of transition dipole moments for a uniaxially aligned organic thin-film is depicted in Figure 11.7. If molecules that exhibit this alignment could be realized, large enhancements in L_D may be possible.

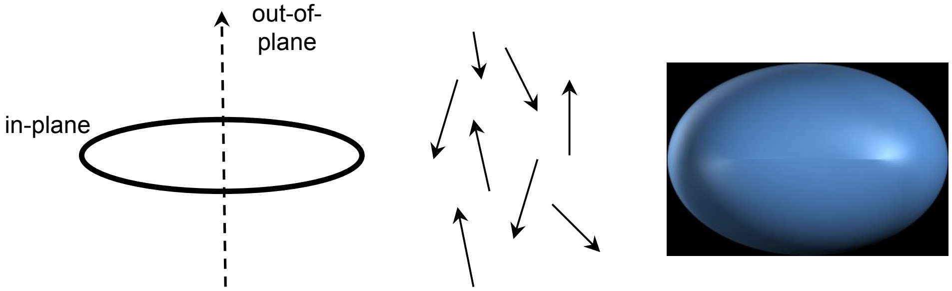

Figure 11.7 Schematic representation for the ideal alignment of transition dipole moments for a uniaxially aligned organic thin-film in order to maximize L_D.

11.3. New avenues for organic semiconductors exhibiting thermally activated delayed fluorescence

To date, organic semiconductors that exhibit TADF have been used primarily as dopants for organic light-emitting devices (OLEDs) [26,134,149]. In concert with the insight developed in Chapter 8, however, application of these unique materials in organic photovoltaic devices (OPVs) is also promising. In this section, potential OPV implementations of TADF materials will be presented and discussed.

11.3.1. Electron donating species

Perhaps the simplest implementation of these materials in an OPV is as a replacement for the electron donating species. Take, for example, 1,4-dicyano-2,3,5,6-tetrakis(3,6-diphenylcarbazol-9-yl)benzene (4CzTPN-Ph) which is a derivative of the TADF molecule explored in Chapter 8. Figure 11.8 shows the normalized photoluminescence and excitation spectrum for 4CzTPN-Ph along with the molecular structure. Unlike 1,2,3,5-tetrakis(carbazol-9-yl)-4,6-dicyanobenzene (4CzIPN), 4CzTPN-Ph has a reduced E_g and correspondingly stronger absorption in the blue and green regions of the visible spectrum. This absorption range may correlate to a large open-circuit voltage (V_{OC}) and make this material an adequate candidate for the top cell in tandem OPV architectures. Further, the relatively large degree of spectral overlap between emission and absorption may signal a long L_D.

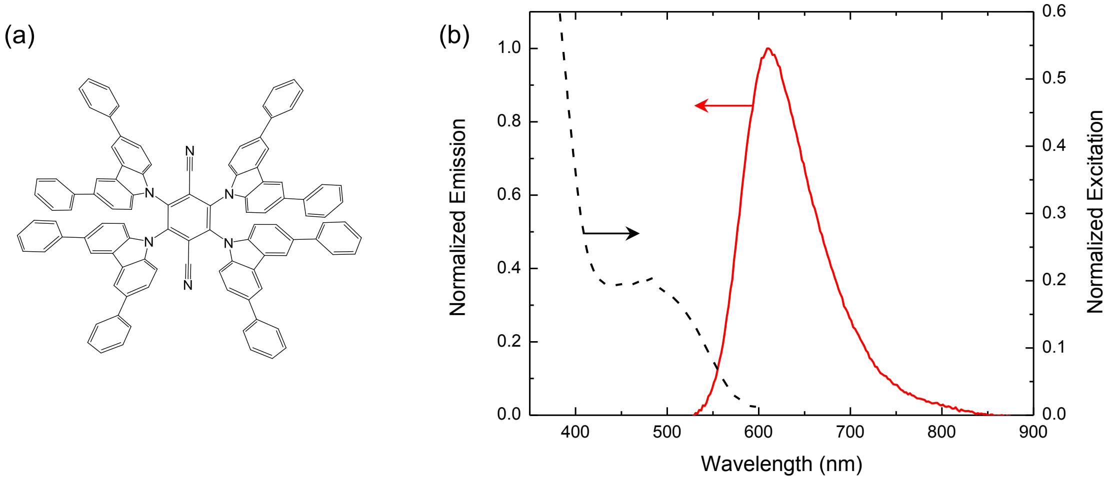

Figure 11.8 Molecular structure (a) along with the photoluminescence and excitation spectrum (b) for the TADF molecule 4CzTPN-Ph.

Unlike a conventional electron donating species, a molecule exhibiting TADF may have some distinct advantages. First, concentration can be used as a lever to manipulate the degree of singlet and triplet exciton energy transfer and diffusion. This may play an important role when combined with a dilute donor OPV architecture that also exhibits directed transport at exciton permeable interfaces (Chapters 4 and 6). Second, the higher-lying triplet exciton state may alleviate non-geminate recombination of photogenerated charge carriers [201]. In polymer OPVs, it has been shown that spin-uncorrelated electrons and holes can generate charge transfer states with both singlet and triplet character [202]. If the triplet charge transfer states are allowed to relax in to a low-lying triplet state on the donor molecule dissociation back to free charge carriers is strongly suppressed. In a TADF donor, however, the energy transfer from the triplet charge transfer state to the higher-lying triplet may be slow, rendering this deleterious pathway inefficient and allowing for an enhanced collection of photogenerated charge carriers. Such an enhancement should manifest as a large charge collection efficiency and fill factor.

11.3.2. Triplet sensitizers

A method of exploiting the long-lived triplet exciton is to incorporate a phosphorescent sensitizer into the active layer [113,141]. If the energy levels are appropriately chosen, a singlet exciton formed in the active layer can energy transfer to a nearby sensitizer, undergo intersystem crossing, and subsequently energy transfer back to the host molecule as a triplet. This can be seen schematically in Figure 11.9. In order for the sequence of events to proceed efficiently, the singlet and triplet exciton energies for the guest ($S_{1,G}$ and $T_{1,G}$) should be nested within the singlet and triplet exciton energies for the host ($S_{1,H}$ and $T_{1,H}$). Finding a suitable host-gest pairing that meets this requirement, however, tightly constrains the selection of OPV active materials, especially of those that have demonstrated other advantageous properties such as strong absorption and adequate charge mobility.

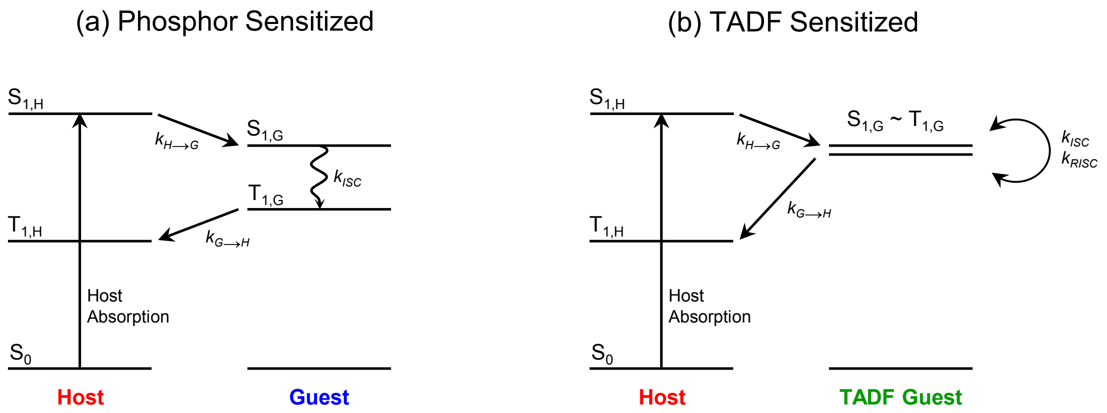

Figure 11.9 Schematic exciton energy landscape for a phosphor-sensitized OPV (a) and a TADF-sensitized OPV.

As an alternative guest species, TADF molecules can offer efficient intersystem crossing as well as relaxed constraints on the selection of suitable host-guest pairings. As the singlet-triplet energy splitting is small in a molecule exhibiting TADF, a broader range of host materials become accessible, especially those with higher-lying triplet exciton energies (Figure 11.9). As an example, consider the electron donor studied in Chapter 9, dicyanovinyl-terthiophene (DCV3T) that has an $S_{1,H}$~2.2 eV and $T_{1,H}$~1.5 eV [203]. With these energy levels, 4CzTPN-Ph is a good candidate as a triplet sensitizer as $S_{1,G}$ and $T_{1,G}$ are both ~1.9 eV [204]. Assuming that there is favorable energy transfer from $T_{1,G}$ to $T_{1,H}$, measurements for the L_D in pure and sensitized films of DCV3T may be able to elucidate the degree of exciton transport along the both the singlet and triplet excited state in DCV3T. If a longer L_D is realized in sensitized films, enhancements in the short-circuit current density (J_{SC}) are possible for OPVs that incorporate mixtures of DCV3T and 4CzTPN-Ph as compared to those that incorporate pure donor layers.

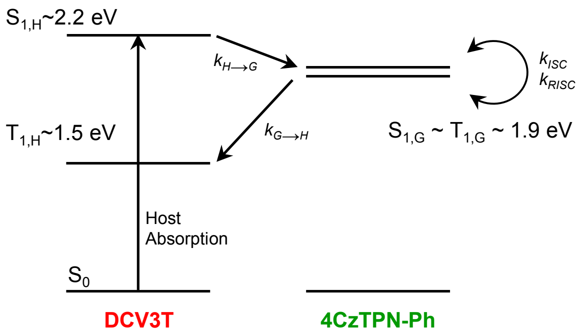

Figure 11.10 Exciton energy diagram for the host-guest pairing of DCV3T and 4CzTPN-Ph for application in a TADF-sensitized OPV.

11.4. Summary and Outlook

Overall, a strong connection between the fundamental photophysical properties of organic semiconductor thin-films and the operation of OPV devices has enabled new paradigms for OPV design and optimization. Building off the substantial body of work established over the past decades, this dissertation has focused explicitly on exciton transport—searching for methods to enhance L_D and direct exciton transport. In this search, the role of spin, energetic disorder, and thermal activation and their impacts on exciton diffusion have been highlighted. Moving forward, these projects represent promising pathways to continue leveraging the photophysical properties of excitons and organic semiconductors for enhanced OPV performance. Application of these fundamental connections may also be of importance in the design of next-generation organic optoelectronic devices such as electrically-driven, organic lasers.

12. References

[1] N. W. Ashcroft and N. D. Mermin, *Solid State Physics*, 33rd ed. (Holt, Reinhart, and Winston, 1976).

[2] P. Würfel and U. Würfel, *Physics of Solar Cells: From Basic Principles to Advanced Concepts* (John Wiley & Sons, 2009).

[3] W. Shockley and H. J. Queisser, J. Appl. Phys. **32**, 510 (1961).

[4] D. A. Neamen, *Semiconductor Physics and Devices: Basic Principles*, 3rd ed. (McGraw-Hill, New York, 2003).

[5] S. R. Wenham and M. A. Green, Prog. Photovoltaics **4**, 3 (1996).

[6] J. Jean, P. R. Brown, R. L. Jaffe, T. Buonassisi, and V. Bulović, Energy Environ. Sci. (2015).

[7] M. A. Green, Sol. Energy **76**, 3 (2004).

[8] M. A. Green, Prog. Photovoltaics Res. Appl. **9**, 123 (2001).

[9] G. Conibeer, Mater. Today **10**, 42 (2007).

[10] S. R. Forrest, Nature **428**, 911 (2004).

[11] S. E. Shaheen, D. S. Ginley, and G. E. Jabbour, MRS Bull. **30**, 10 (2005).

[12] C. J. Brabec, Sol. Energy Mater. Sol. Cells **83**, 273 (2004).

[13] F. C. Krebs, N. Espinosa, M. Hösel, R. R. Søndergaard, and M. Jørgensen, Adv. Mater. **26**, 29 (2014).

[14] S. Günes, H. Neugebauer, and N. S. Sariciftci, Chem. Rev. **107**, 1324 (2007).

[15] N. J. Turro, *Modern Molecular Photochemistry* (University Science Books, 1991).

[16] M. Pope and C. E. Swenberg, *Electronic Processes in Organic Crystals and Polymers* (Oxford University Press, New York, 1999).

[17] B. Kippelen and J. L. Brédas, Energy Environ. Sci. **2**, 251 (2009).

[18] M. Born and R. Oppenheimer, Ann. Phys. **20**, 457 (1927).

[19] P. W. Atkins and R. S. Friedman, *Molecular Quantum Mechanics* (Oxford University Press, 2011).

[20] P. I. Djurovich, E. I. Mayo, S. R. Forrest, and M. E. Thompson, Org. Electron. Physics, Mater. Appl. **10**, 515 (2009).

[21] J. Meyer, S. Hamwi, M. Kröger, W. Kowalsky, T. Riedl, and A. Kahn, Adv. Mater. **24**, 5408 (2012).

[22] M. Kasha, Discuss. Faraday Soc. **9**, 14 (1950).

[23] J. S. Wilson, A. S. Dhoot, A. J. Seeley, M. S. Khan, A. Köhler, and R. H. Friend, Nature **413**, 828 (2001).

[24] E. U. Condon and G. H. Shortley, *The Theory of Atomic Spectra* (Cambridge University Press, 1951).

[25] M. A. Baldo, D. F. O'Brien, Y. You, A. Shoustikov, S. Sibley, M. E. Thompson, and S. R. Forrest, Nature **395**, 151 (1998).

[26] H. Uoyama, K. Goushi, K. Shizu, H. Nomura, and C. Adachi, Nature **492**, 234 (2012).

[27] G. D. Scholes, Annu. Rev. Phys. Chem. **54**, 57 (2003).

[28] J. L. Brédas, D. Beljonne, V. Coropceanu, and J. J. Cornil, Chem. Rev. **104**, 4971 (2004).

[29] D. Beljonne, G. Pourtois, C. Silva, E. Hennebicq, L. M. Herz, R. H. Friend, G. D. Scholes, S. Setayesh, K. Mullen, and J. L. Brédas, Proc. Natl. Acad. Sci. U. S. A. **99**, 10982 (2002).

[30] J. Clark, C. Silva, R. H. Friend, and F. C. Spano, Phys. Rev. Lett. **98**, (2007).

[31] R. Silbey, Annu. Rev. Phys. Chem. **27**, 203 (1976).

[32] R. C. Powell and Z. G. Soos, J. Lumin. **11**, 1 (1975).

[33] T. Förster, Discuss. Faraday Soc. **27**, 7 (1959).

[34] D. L. Andrews, C. Curutchet, and G. D. Scholes, Laser Photonics Rev. **5**, 114 (2011).

[35] D. Beljonne, C. Curutchet, G. D. Scholes, and R. J. Silbey, J. Phys. Chem. B **113**, 6583 (2009).

[36] D. L. Dexter, J. Chem. Phys. **21**, 836 (1953).

[37] S. M. Menke and R. J. Holmes, Energy Environ. Sci. **7**, 499 (2014).

[38] S. Chandrasekhar, Rev. Mod. Phys. **15**, 1 (1943).

[39] S. N. Yaliraki and R. J. Silbey, J. Chem. Phys. **104**, 1245 (1996).

[40] W. Schrof, E. Betz, H. Port, and H. C. Wolf, Chem. Phys. Lett. **123**, 300 (1986).

[41] L. A. A. Pettersson, L. S. Roman, and O. Inganäs, J. Appl. Phys. **86**, 487 (1999).

[42] S. R. Scully, P. B. Armstrong, C. Edder, J. M. J. Fréchet, and M. D. McGehee, Adv. Mater. **19**, 2961 (2007).

[43] W. A. Luhman and R. J. Holmes, Adv. Funct. Mater. **21**, 764 (2011).

[44] J.-P. Bouchaud and A. Georges, Phys. Rep. **195**, 127 (1990).

[45] B. Movaghar, M. Grunewald, B. Ries, H. Bässler, and D. Wurtz, Phys. Rev. B **33**, 5546 (1992).

[46] R. R. Lunt, N. C. Giebink, A. A. Belak, J. B. Benziger, and S. R. Forrest, J. Appl. Phys. **105**, 053711 (2009).

[47] W. P. Su, J. R. Schrieffer, and A. J. Heeger, Phys. Rev. Lett. **42**, 1698 (1979).

[48] V. Coropceanu, J. Cornil, D. A. da Silva Filho, Y. Olivier, R. Silbey, and J. L. Brédas, Chem. Rev. **107**, 926 (2007).

[49] J. L. Brédas and G. Street, Acc. Chem. Res. **1305**, 309 (1985).

[50] T. Sakanoue and H. Sirringhaus, Nat. Mater. **9**, 736 (2010).

[51] V. Podzorov, E. Menard, A. Borissov, V. Kiryukhin, J. A. Rogers, and M. E. Gershenson, Phys. Rev. Lett. **93**, (2004).

[52] H. Sirringhaus, Adv. Mater. **17**, 2411 (2005).

[53] A. Miller and E. Abrahams, Phys. Rev. **120**, 745 (1960).

[54] F. C. Krebs, Sol. Energy Mater. Sol. Cells **93**, 394 (2009).

[55] P. Peumans, A. Yakimov, and S. R. Forrest, J. Appl. Phys. **93**, 3693 (2003).

[56] F. Jenkins and H. White, *Fundamentals of Optics*, 4th ed. (McGraw-Hill, 2001).

[57] R. D. L. Kronig, J. Opt. Soc. Am. **12**, 547 (1926).

[58] D. Yokoyama and C. Adachi, Appl. Phys. Lett. **43**, 137 (2010).

[59] G. A. Chamberlain, Sol. Cells **8**, 47 (1983).

[60] C. W. Tang, Appl. Phys. Lett. **48**, 183 (1986).

[61] B. A. Gregg and M. C. Hanna, J. Appl. Phys. **93**, 3605 (2003).

[62] M. Hiramoto, Y. Kishigami, and M. Yokoyama, Chem. Lett. 119 (1990).

[63] M. Hiramoto, H. Fujiwara, and M. Yokoyama, Appl. Phys. Lett. **58**, 1062 (1991).

[64] G. Yu, J. Gao, J. C. Hummelen, F. Wudl, and A. J. Heeger, Science (80-.). **270**, 1789 (1995).

[65] J. Halls, C. Walsh, N. C. Greenham, E. Marseglia, R. H. Friend, S. C. Moratti, and A. B. Holmes, Nature **376**, 498 (1995).

[66] A. J. Heeger, Adv. Mater. **26**, 10 (2014).

[67] M. A. Green, K. Emery, D. L. King, S. Igari, and W. Warta, Prog. Photovoltaics Res. Appl. **12**, 55 (2004).

[68] H. Ma, H.-L. Yip, F. Huang, and A. K. Y. Jen, Adv. Funct. Mater. **20**, 1371 (2010).

[69] S. R. Scully and M. D. McGehee, J. Appl. Phys. **100**, 034907 (2006).

[70] a. Haugeneder, M. Neges, C. Kallinger, W. Spirkl, U. Lemmer, J. Feldmann, U. Scherf, E. Harth, A. Gügel, and K. Müllen, Phys. Rev. B **59**, 15346 (1999).

[71] D. E. Markov, E. Amsterdam, P. W. M. Blom, A. B. Sieval, and J. C. Hummelen, J. Phys. Chem. A **109**, 5266 (2005).

[72] H. Gommans, S. Schols, A. Kadashchuk, P. Heremans, and S. C. J. Meskers, J. Phys. Chem. C **113**, 2974 (2009).

[73] K. J. Bergemann and S. R. Forrest, Appl. Phys. Lett. **99**, (2011).

[74] P. E. Shaw, A. Ruseckas, and I. D. W. Samuel, Adv. Mater. **20**, 3516 (2008).

[75] D. E. Markov, J. C. Hummelen, P. W. M. Blom, and A. B. Sieval, Phys. Rev. B - Condens. Matter Mater. Phys. **72**, (2005).

[76] Y.-X. Liu, M. a. Summers, S. R. Scully, and M. D. McGehee, J. Appl. Phys. **99**, 093521 (2006).

[77] E. Engel, K. Leo, and M. Hoffmann, Chem. Phys. **325**, 170 (2006).

[78] R. Pandey and R. J. Holmes, Appl. Phys. Lett. **100**, (2012).

[79] J. E. Kroeze, T. J. Savenije, M. J. W. Vermeulen, and J. M. Warman, J. Phys. Chem. B **107**, 7696 (2003).

[80] G. M. Akselrod, P. B. Deotare, N. J. Thompson, J. Lee, W. a Tisdale, M. A. Baldo, V. M. Menon, and V. Bulović, Nat. Commun. **5**, 3646 (2014).

[81] P. Irkhin and I. Biaggio, Phys. Rev. Lett. **107**, (2011).

[82] J. D. a. Lin, O. V. Mikhnenko, J. Chen, Z. Masri, A. Ruseckas, A. Mikhailovsky, R. P. Raab, J. Liu, P. W. M. Blom, M. A. Loi, C. J. García-Cervera, I. D. W. Samuel, and T.-Q. Nguyen, Mater. Horizons **1**, 280 (2014).

[83] Y. Kawamura, K. Goushi, J. Brooks, J. J. Brown, H. Sasabe, and C. Adachi, Appl. Phys. Lett. **86**, 1 (2005).

[84] R. J. Holmes, B. W. D'Andrade, S. R. Forrest, X. Ren, J. Li, and M. E. Thompson, Appl. Phys. Lett. **83**, 3818 (2003).

[85] X. Ren, J. Li, R. J. Holmes, P. I. Djurovich, S. R. Forrest, and M. E. Thompson, Chem. Mater. **16**, 4743 (2004).

[86] A. Barito, M. E. Sykes, B. Huang, D. Bilby, B. Frieberg, J. Kim, P. F. Green, and M. Shtein, Adv. Energy Mater. n/a (2014).

[87] S. M. Menke, W. A. Luhman, and R. J. Holmes, Nat. Mater. **12**, 152 (2013).

[88] J. Baumann and M. D. Fayer, J. Chem. Phys. **85**, 4087 (1986).

[89] V. Bulović, R. Deshpande, M. . Thompson, and S. R. Forrest, Chem. Phys. Lett. **308**, 317 (1999).

[90] M. A. Baldo, Z. G. G. Soos, and S. R. Forrest, Chem. Phys. Lett. **347**, 297 (2001).

[91] C. F. Madigan and V. Bulović, Phys. Rev. Lett. **91**, 247403 (2003).

[92] G. E. Morse and T. P. Bender, ACS Appl. Mater. Interfaces **4**, 5055 (2012).

[93] Y. Kawamura, H. Sasabe, and C. Adachi, Jpn. J. Appl. Phys. **43**, 7729 (2004).

[94] J. Huang, M. Pfeiffer, A. Werner, J. Blochwitz, K. Leo, and S. Liu, Appl. Phys. Lett. **80**, 139 (2002).

[95] V. Bulović, A. Shoustikov, M. A. Baldo, E. Bose, V. . Kozlov, M. . Thompson, and S. R. Forrest, Chem. Phys. Lett. **287**, 455 (1998).

[96] M. Kröger, S. Hamwi, J. Meyer, T. Riedl, W. Kowalsky, and A. Kahn, Appl. Phys. Lett. **95**, 10 (2009).

[97] H. Gommans, D. Cheyns, T. Aernouts, C. Girotto, J. Poortmans, and P. Heremans, Adv. Funct. Mater. **17**, 2653 (2007).

[98] R. Pandey, A. A. Gunawan, K. A. Mkhoyan, and R. J. Holmes, Adv. Funct. Mater. **22**, 617 (2012).

[99] T. Ameri, N. Li, and C. J. Brabec, Energy Environ. Sci. **6**, 2390 (2013).

[100] W. Tress, A. Petrich, M. Hummert, M. Hein, K. Leo, and M. Riede, Appl. Phys. Lett. **98**, (2011).

[101] T. K. Mullenbach, K. A. McGarry, W. A. Luhman, C. J. Douglas, and R. J. Holmes, Adv. Mater. **25**, 3689 (2013).

[102] P. Peumans, V. Bulović, and S. R. Forrest, Appl. Phys. Lett. **76**, 2650 (2000).

[103] J. Y. Kim, S. H. Kim, H. H. Lee, K. Lee, W. Ma, X. Gong, and A. J. Heeger, Adv. Mater. **18**, 572 (2006).

[104] J. Gilot, I. Barbu, M. M. Wienk, and R. A. J. Janssen, Appl. Phys. Lett. **91**, (2007).

[105] B. O'Connor, K. H. An, K. P. Pipe, Y. Zhao, and M. Shtein, Appl. Phys. Lett. **89**, (2006).

[106] A. Hadipour, B. De Boer, and P. W. M. Blom, J. Appl. Phys. **102**, (2007).

[107] J. Lee, S. Y. Kim, C. Kim, and J. J. Kim, Appl. Phys. Lett. **97**, (2010).

[108] S. M. Menke, C. D. Lindsay, and R. J. Holmes, Appl. Phys. Lett. **104**, (2014).

[109] I. Hancox, K. V. Chauhan, P. J. Sullivan, R. A. Hatton, A. Moshar, C. P. A. Mulcahy, and T. S. Jones, Energy Environ. Sci. (2010).

[110] Y. Zou and R. J. Holmes, Appl. Phys. Lett. **103**, (2013).

[111] A. N. Bartynski, C. Trinh, A. Panda, K. Bergemann, B. E. Lassiter, J. D. Zimmerman, S. R. Forrest, and M. E. Thompson, Nano Lett. **13**, 3315 (2013).

[112] B. Verreet, P. Heremans, A. Stesmans, and B. P. Rand, Adv. Mater. **25**, 5504 (2013).

[113] W. A. Luhman and R. J. Holmes, Appl. Phys. Lett. **94**, 153304 (2009).

[114] B. P. Rand, D. Cheyns, K. Vasseur, N. C. Giebink, S. Mothy, Y. Yi, V. Coropceanu, D. Beljonne, J. Cornil, J. L. Brédas, and J. Genoe, Adv. Funct. Mater. **22**, 2987 (2012).

[115] D. Yokoyama, Z. Q. Wang, Y. J. Pu, K. Kobayashi, J. Kido, and Z. Hong, Sol. Energy Mater. Sol. Cells **98**, 472 (2012).

[116] S. M. Menke, T. K. Mullenbach, and R. J. Holmes, ACS Nano 150323154650001 (2015).

[117] K. Cnops, B. P. Rand, D. Cheyns, B. Verreet, M. a Empl, and P. Heremans, Nat. Commun. **5**, 3406 (2014).

[118] S. M. Menke and R. J. Holmes, ACS Appl. Mater. Interfaces **7**, 2912 (2015).

[119] D. C. Coffey, A. J. Ferguson, N. Kopidakis, and G. Rumbles, ACS Nano **4**, 5437 (2010).

[120] B. Verreet, K. Cnops, D. Cheyns, P. Heremans, A. Stesmans, G. Zango, C. G. Claessens, T. Torres, and B. P. Rand, Adv. Energy Mater. **4**, (2014).

[121] B. Ma, C. H. Woo, Y. Miyamoto, and J. M. J. Fréchet, Chem. Mater. **21**, 1413 (2009).

[122] T. Ameri, P. Khoram, J. Min, and C. J. Brabec, Adv. Mater. **25**, 4245 (2013).

[123] M. C. Chen, D. J. Liaw, Y. C. Huang, H. Y. Wu, and Y. Tai, Sol. Energy Mater. Sol. Cells **95**, 2621 (2011).

[124] L. S. Liao and K. P. Klubek, Appl. Phys. Lett. **92**, (2008).

[125] B. Verreet, A. Bhoolokam, A. Brigeman, R. Dhanker, D. Cheyns, P. Heremans, A. Stesmans, N. C. Giebink, and B. P. Rand, Phys. Rev. B **90**, (2014).

[126] X. Wang, E. Perzon, F. Oswald, F. Langa, S. Admassie, M. R. Andersson, and O. Inganäs, Adv. Funct. Mater. **15**, 1665 (2005).

[127] S. Pfuetzner, J. Meiss, A. Petrich, M. Riede, and K. Leo, Appl. Phys. Lett. **94**, (2009).

[128] R. Pandey, Y. Zou, and R. J. Holmes, Appl. Phys. Lett. **101**, 033308 (2012).

[129] Y. Sun, N. C. Giebink, H. Kanno, B. Ma, M. E. Thompson, and S. R. Forrest, Nature **440**, 908 (2006).

[130] S. Reineke, F. Lindner, G. Schwartz, N. Seidler, K. Walzer, B. Lüssem, and K. Leo, Nature **459**, 234 (2009).

[131] M. Segal, M. A. Baldo, R. J. Holmes, S. R. Forrest, and Z. Soos, Phys. Rev. B **68**, (2003).

[132] S. Reineke and M. A. Baldo, Phys. Status Solidi Appl. Mater. Sci. **209**, 2341 (2012).

[133] A. Endo, K. Sato, K. Yoshimura, T. Kai, A. Kawada, H. Miyazaki, and C. Adachi, Appl. Phys. Lett. **98**, (2011).

[134] Q. Zhang, B. Li, S. Huang, H. Nomura, H. Tanaka, and C. Adachi, Nat. Photonics **8**, 1 (2014).

[135] F. B. Dias, K. N. Bourdakos, V. Jankus, K. C. Moss, K. T. Kamtekar, V. Bhalla, J. Santos, M. R. Bryce, and A. P. Monkman, Adv. Mater. **25**, 3707 (2013).

[136] S. R. Yost, E. Hontz, S. Yeganeh, and T. Van Voorhis, J. Phys. Chem. C **116**, 17369 (2012).

[137] S. T. Roberts, C. W. Schlenker, V. Barlier, R. E. McAnally, Y. Zhang, J. N. Mastron, M. E. Thompson, and S. E. Bradforth, J. Phys. Chem. Lett. **2**, 48 (2011).

[138] O. V. Mikhnenko, R. Ruiter, P. W. M. Blom, and M. A. Loi, Phys. Rev. Lett. **108**, (2012).

[139] A. Köhler and H. Bässler, J. Mater. Chem. **21**, 4003 (2011).

[140] Y. Shao and Y. Yang, Adv. Mater. **17**, 2841 (2005).

[141] B. P. Rand, S. Schols, D. Cheyns, H. Gommans, C. Girotto, J. Genoe, P. Heremans, and J. Poortmans, Org. Electron. **10**, 1015 (2009).

[142] E. B. Namdas, A. Ruseckas, I. D. W. Samuel, S. C. Lo, and P. L. Burn, Appl. Phys. Lett. **86**, 1 (2005).

[143] C. Wu, P. I. Djurovich, and M. E. Thompson, Adv. Funct. Mater. **19**, 3157 (2009).

[144] H. Najafov, B. Lee, Q. Zhou, L. C. Feldman, and V. Podzorov, Nat. Mater. **9**, 938 (2010).

[145] C. J. Bardeen, Annu. Rev. Phys. Chem. **65**, 127 (2014).

[146] N. C. Giebink, Y. Sun, and S. R. Forrest, Org. Electron. Physics, Mater. Appl. **7**, 375 (2006).

[147] O. V. Mikhnenko, M. Kuik, J. Lin, N. Van Der Kaap, T. Q. Nguyen, and P. W. M. Blom, Adv. Mater. **26**, 1912 (2014).

[148] K. Feron, W. J. Belcher, C. J. Fell, and P. C. Dastoor, Int. J. Mol. Sci. **13**, 17019 (2012).

[149] K. Goushi, K. Yoshida, K. Sato, and C. Adachi, Nat. Photonics **6**, 253 (2012).

[150] Y. Kawamura, J. Brooks, J. J. Brown, H. Sasabe, and C. Adachi, Phys. Rev. Lett. **96**, (2006).

[151] T. Imato, R. Ishimatsu, S. Matsunami, K. Shizu, C. Adachi, K. Nakano, and T. Imato, J. Phys. Chem. A **117**, 5607 (2013).

[152] V. Grosshenny, A. Harriman, and R. Ziessel, Angew. Chemie Int. Ed. English **34**, 1100 (1995).

[153] J. C. Ribierre, A. Ruseckas, K. Knights, S. V. Staton, N. Cumpstey, P. L. Burn, and I. D. W. Samuel, Phys. Rev. Lett. **100**, (2008).

[154] S. Athanasopoulos, E. V. Emelianova, A. B. Walker, and D. Beljonne, Phys. Rev. B **80**, 1 (2009).

[155] S. Athanasopoulos, S. T. Hoffmann, H. Bässler, A. Köhler, and D. Beljonne, J. Phys. Chem. Lett. **4**, 1694 (2013).

[156] A. K. Topczak, T. Roller, B. Engels, W. Brütting, and J. Pflaum, Phys. Rev. B - Condens. Matter Mater. Phys. **89**, (2014).

[157] A. Blumen and R. Silbey, J. Chem. Phys. **69**, 3589 (1978).

[158] S. T. Hoffmann, H. Bässler, J. M. Koenen, M. Forster, U. Scherf, E. Scheler, P. Strohriegl, and A. Köhler, Phys. Rev. B **81**, (2010).

[159] T. S. Ahn, N. Wright, and C. J. Bardeen, Chem. Phys. Lett. **446**, 43 (2007).

[160] O. V. Mikhnenko, F. Cordella, A. B. Sieval, J. C. Hummelen, P. W. M. Blom, and M. A. Loi, J. Phys. Chem. B **112**, 11601 (2008).

[161] F. B. Dias, K. T. Kamtekar, T. Cazati, G. Williams, M. R. Bryce, and A. P. Monkman, ChemPhysChem **10**, 2096 (2009).

[162] V. I. Arkhipov, E. V. Emelianova, and H. Bässler, Chem. Phys. Lett. **383**, 166 (2004).

[163] C. Madigan and V. Bulović, Phys. Rev. Lett. **96**, 1 (2006).

[164] S. Westenhoff, C. Daniel, R. H. Friend, C. Silva, V. Sundström, and A. Yartsev, J. Chem. Phys. **122**, (2005).

[165] F. Fennel and S. Lochbrunner, Phys. Rev. B **85**, (2012).

[166] J. G. Müller, U. Lemmer, G. Raschke, M. Anni, U. Scherf, J. M. Lupton, and J. Feldmann, Phys. Rev. Lett. **91**, 267403 (2003).

[167] J. A. Bjorgaard and M. E. Köse, RSC Adv. **5**, 8432 (2014).

[168] A. Holzhey, C. Uhrich, E. Brier, E. Reinhold, P. Bäuerle, K. Leo, and M. Hoffmann, J. Appl. Phys. **104**, 064510 (2008).

[169] Y.-K. Kim, J. W. Kim, and Y. Park, Appl. Phys. Lett. **94**, 63305 (2009).

[170] L. Sudha Devi, M. K. Al-Suti, C. Dosche, M. S. Khan, R. H. Friend, and A. Köhler, Phys. Rev. B - Condens. Matter Mater. Phys. **78**, (2008).

[171] X. Gong, M. Tong, Y. Xia, W. Cai, J. S. Moon, Y. Cao, G. Yu, C.-L. Shieh, B. Nilsson, and A. J. Heeger, Science (80-.). **325**, 1665 (2009).

[172] T. N. Ng, W. S. Wong, M. L. Chabinyc, S. Sambandan, and R. A. Street, Appl. Phys. Lett. **92**, (2008).

[173] Y. Yao, Y. Liang, V. Shrotriya, S. Xiao, L. Yu, and Y. Yang, Adv. Mater. **19**, 3979 (2007).

[174] M. Binda, A. Iacchetti, D. Natali, L. Beverina, M. Sassi, and M. Sampietro, Appl. Phys. Lett. **98**, 073303 (2011).

[175] I. H. Campbell, Appl. Phys. Lett. **97**, 033303 (2010).

[176] M. S. Arnold, J. D. Zimmerman, C. K. Renshaw, X. Xu, R. R. Lunt, C. M. Austin, and S. R. Forrest, Nano Lett. **9**, 3354 (2009).

[177] J. D. Zimmerman, E. K. Yu, V. V. Diev, K. Hanson, M. E. Thompson, and S. R. Forrest, Org. Electron. **12**, 869 (2011).

[178] J. P. Clifford, G. Konstantatos, K. W. Johnston, S. Hoogland, L. Levina, and E. H. Sargent, Nat. Nanotechnol. **4**, 40 (2009).

[179] P. Peumans, V. Bulović, and S. R. Forrest, Appl. Phys. Lett. **76**, 3855 (2000).

[180] T. Morimune, H. Kajii, and Y. Ohmori, IEEE Photonics Technol. Lett. **18**, 2662 (2006).

[181] M. Punke, S. Valouch, S. W. Kettlitz, N. Christ, C. Gärtner, M. Gerken, and U. Lemmer, Appl. Phys. Lett. **91**, (2007).

[182] K. H. An, B. O'Connor, K. P. Pipe, and M. Shtein, Org. Electron. Physics, Mater. Appl. **10**, 1152 (2009).

[183] B. Lamprecht, R. Thünauer, S. Köstler, G. Jakopic, G. Leising, and J. R. Krenn, Phys. Status Solidi - Rapid Res. Lett. **2**, 178 (2008).

[184] S. M. Menke, R. Pandey, and R. J. Holmes, Appl. Phys. Lett. **101**, (2012).

[185] R. F. Bailey-Salzman, B. P. Rand, and S. R. Forrest, Appl. Phys. Lett. **91**, 013508 (2007).

[186] K. L. Mutolo, E. I. Mayo, B. P. Rand, S. R. Forrest, and M. E. Thompson, J. Am. Chem. Soc. **128**, 8108 (2006).

[187] S. W. Cho, L. F. J. Piper, A. DeMasi, A. R. H. Preston, K. E. Smith, K. V. Chauhan, P. Sullivan, R. A. Hatton, and T. S. Jones, J. Phys. Chem. C **114**, 1928 (2010).

[188] J. Reynaert, V. I. Arkhipov, P. Heremans, and J. Poortmans, Adv. Funct. Mater. **16**, 784 (2006).

[189] W. T. Hammond and J. Xue, Appl. Phys. Lett. **97**, 073302 (2010).

[190] G. Schwartz, M. Pfeiffer, S. Reineke, K. Walzer, and K. Leo, Adv. Mater. **19**, 3672 (2007).

[191] G. Schwartz, S. Reineke, T. C. Rosenow, K. Walzer, and K. Leo, Adv. Funct. Mater. **19**, 1319 (2009).

[192] S. M. Borisov, G. Nuss, and I. Klimant, Anal. Chem. **80**, 9435 (2008).

[193] R. R. Lunt, J. B. Benziger, and S. R. Forrest, Adv. Mater. **22**, 1233 (2010).

[194] D. Kurrle and J. Pflaum, Appl. Phys. Lett. **92**, (2008).

[195] K. A. McGarry, W. Xie, C. Sutton, C. Risko, Y. Wu, V. G. Young, J. L. Brédas, C. D. Frisbie, and C. J. Douglas, Chem. Mater. **25**, 2254 (2013).

[196] W. Chen, L. Huang, X. Qiao, J. Yang, B. Yu, and D. Yan, Org. Electron. Physics, Mater. Appl. **13**, 1086 (2012).

[197] J. Yang, F. Zhu, B. Yu, H. Wang, and D. Yan, Appl. Phys. Lett. **100**, (2012).

[198] S. Singha Roy, D. J. Bindl, and M. S. Arnold, J. Phys. Chem. Lett. **3**, 873 (2012).

[199] D. Yokoyama, J. Mater. Chem. **21**, 19187 (2011).

[200] D. Yokoyama, A. Sakaguchi, M. Suzuki, and C. Adachi, Appl. Phys. Lett. **95**, (2009).

[201] P. C. Y. Chow, S. Gélinas, A. Rao, and R. H. Friend, J. Am. Chem. Soc. **136**, 3424 (2014).

[202] A. Rao, P. C. Y. Chow, S. Gélinas, C. W. Schlenker, C.-Z. Li, H.-L. Yip, A. K.-Y. Jen, D. S. Ginley, and R. H. Friend, Nature **500**, 435 (2013).

[203] H. Ziehlke, R. Fitzner, C. Koerner, R. Gresser, E. Reinold, P. Bäuerle, K. Leo, and M. K. Riede, J. Phys. Chem. A **115**, 8437 (2011).

[204] A. S. D. Sandanayaka, K. Yoshida, T. Matsushima, and C. Adachi, J. Phys. Chem. C **119**, 7631 (2015).

13. Appendices

A. List of publications

1. Menke, S. M., Pandey, R. & Holmes, R. J. Tandem organic photodetectors with tunable, broadband response. Appl. Phys. Lett. 101, (2012).
2. Menke, S. M., Luhman, W. A. & Holmes, R. J. Tailored exciton diffusion in organic photovoltaic cells for enhanced power conversion efficiency. Nat. Mater. 12, 152–7 (2013).
3. Pandey, R. et al. Tin naphthalocyanine complexes for infrared absorption in organic photovoltaic cells. Org. Electron. 14, 804–808 (2013).
4. Menke, S. M. & Holmes, R. J. Exciton diffusion in organic photovoltaic cells. Energy Environ. Sci. 7, 499 (2014).
5. Menke, S. M., Lindsay, C. D. & Holmes, R. J. Optical spacing effect in organic photovoltaic cells incorporating a dilute acceptor layer. Appl. Phys. Lett. 104, (2014).
6. Menke, S. M. & Holmes, R. J. Energy-Cascade Organic Photovoltaic Devices Incorporating a Host-Guest Architecture. ACS Appl. Mater. Interfaces 7, 2912–2918 (2015).
7. Menke, S. M., Mullenbach, T. K. & Holmes, R. J. Directing Energy Transport in Organic Photovoltaic Cells Using Interfacial Exciton Gates. ACS Nano (2015). doi:10.1021/acsnano.5b01160

B. List of presentations

1. Menke S.M., Holmes R.J. Energy-cascade organic photovoltaic devices incorporating a host-guest architecture, Materials Research Society Fall Meeting, 2014, Boston MA
2. Menke S.M., Holmes R.J. Enhancing exciton diffusion in organic photovoltaic cells incorporating dilute donor layers, IEEE PV Specialists Conference, 2014, Denver, CO.
3. Menke S.M., Mullenbach T.K., Holmes R.J. Passive exciton gating via directed energy transfer in organic photovoltaic cells, APS March Meeting, 2014, Denver, CO.

4. Menke S.M., Holmes R.J. Engineering Energy Flow at the Nano-Scale for Efficient Organic Solar Cells, Doctoral Dissertation Fellowship Seminar (Invited), 2013, Minneapolis, MN.
5. Holmes R.J., Menke S.M., Mullenbach T.K., McGarry K.A., Douglas C.J., Engineering energy transfer and exciton diffusion in organic semiconductors for application in photovoltaic cells, SPIE Optics + Photonics Annual Conference, 2013, San Diego, CA.
6. Mullenbach T.K., Menke S.M., Holmes, R.J. Understanding exciton energy transfer across complex interfaces using kinetic Monte Carlo technique, I-Prime Annual Meeting, 2013, Minneapolis, MN.
7. Menke S.M., Holmes R.J. Tandem organic photodetectors with tunable, broadband response, Materials Research Society Fall Meeting, 2012, Boston MA
8. Menke S.M., Holmes R.J. Tailoring exciton diffusion in organic photovoltaic cells for enhanced power conversion efficiency, 3M I-Prime Poster Session, 3M Corporate Headquarters, 2012, Woodbury MN.
9. Menke S.M., Luhman W.A., Holmes R.J. Tailoring exciton diffusion in organic photovoltaic cells for enhanced power conversion efficiency, I-Prime Annual Meeting, 2012, Minneapolis MN.
10. Menke S.M., Luhman W.A., Holmes R.J. Enhanced exciton diffusion and power conversion efficiency in organic photovoltaic cells containing a dilute, electron donor layer, Materials Research Society Spring Meeting, 2012, San Francisco CA.
11. Menke S.M., Luhman W.A., Holmes R.J. Measurement of exciton energy transfer and diffusion in organic photovoltaic cells, MRSEC program review, 2012, Minneapolis MN.

C. List of patents

1. "Photovoltaic devices with enhanced exciton diffusion" Holmes, R.J., Menke S.M., Luhman W.A., U.S. Patent Application 20120109. February 13, 2013.
2. "Spectrally tunable broadband photodetectors" Holmes, R.J., Menke S.M., Pandey R, U.S. Provisional Patent Application 61/665,153. June 27, 2012.

D. Copyright permissions

Chapter 3: All or portions of some figures were reproduced or adapted from "S. M. Menke and R. J. Holmes, Energy Environ. Sci. **7**, 499 (2014)." with permission from The Royal Society of Chemistry.

Chapter 4: All or portions of some figures were reproduced or adapted from "S. M. Menke, W. A. Luhman, and R. J. Holmes, Nat. Mater. **12**, 152 (2013)." with permission from Nature Publishing Group.

Chapter 5: All or portions of some figures were reproduced or adapted from "S. M. Menke, C. D. Lindsay, and R. J. Holmes, Appl. Phys. Lett. **104**, (2014)." Copyright 2014, AIP Publishing, LLC.

Chapter 6: All or portions of some figures were reproduced or adapted from "S. M. Menke, T. K. Mullenbach, and R. J. Holmes, ACS Nano 150323154650001 (2015)." Copyright 2015 American Chemical Society.

Chapter 7: All or portions of some figures were reproduced or adapted from "S. M. Menke and R. J. Holmes, ACS Appl. Mater. Interfaces **7**, 2912 (2015)." Copyright 2015 American Chemical Society.

Chapter 10: All or portions of some figures were reproduced or adapted from "S. M. Menke, R. Pandey, and R. J. Holmes, Appl. Phys. Lett. **101**, (2012)." Copyright 2012, AIP Publishing, LLC.

E. Simulation of 1-R for tabulation of relative internal quantum efficiency

In order to tabulate the relative internal quantum efficiency (η_{IQE}) for an organic photovoltaic device (OPV), a measured for the absorption efficiency of the OPV device must be obtained. As an approximation the complement of reflectivity (R) can be measured as schematically described in Figure 13.1. As very little light is expected to transmit through the >60-nm-thick Al cathode, 1-R approximates device absorption.

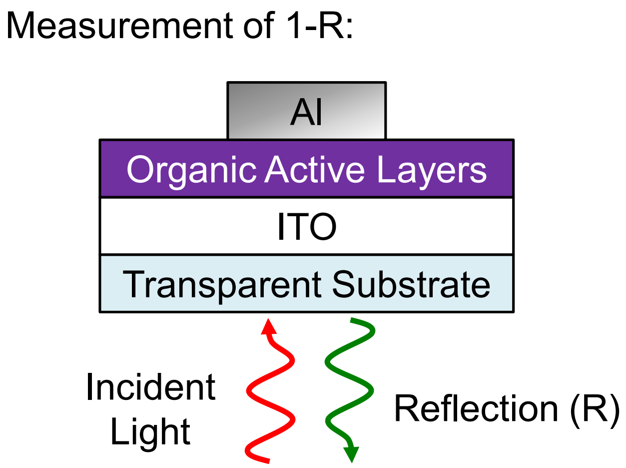

Figure 13.1 Schematic representation for the measurement of 1-R

In the tabulation of η_{IQE}, however, a measurement is required for the absorption in the organic active layers, discounting parasitic absorption from other regions of the device (e.g. cathode). In this regard, transfer matrix simulations for cathode absorption can be combined with measurement for 1-R to provide a good approximation for the active layer absorption in an OPV device.

F. Densities and molecular weights for selected materials

Table 13.1 Molecular weights and densities used for tabulation of average intermolecular separation as a function of dilution for selected materials

Material	Density (g/cm^3)	Molecular Weight (g/mol)
SubPc	1.53	431
SubNc	1.56	581
UGH2	1.2	595
BPhen	1.1	332
4CzIPN	1.2	789

G. Optical field simulation code

The following Matlab function uses transfer matrix formalism to generate the electric field profile for a given multilayer stack. The primary inputs to this function are the wavelength(s), thicknesses of the active layers, complex indices of refraction, layer discretization, absorption coefficients, incident optical field, relative fraction between s- and p-polarized light, and the incident angle of illumination. The code then outputs vectors for the optical field, the optical field intensity, absorbed power, reflection, and transmission.

```
function
[E_s,E_p,Intensity,Q,Reflection_s,Reflection_p,Transmission_s,Transmissi
on_p,S_s,S_p,S_prime_s,S_prime_p,S_doubleprime_s,S_doubleprime_p,xi,L,Tj
_s,Tj_p, Tj, tj_plus_s,Ijk_s,Ijk_p] =
GenerateElectricField(lambda,t,n,q,x,alpha,E0T,fraction,Ld,c,epsilon_0,p
hi)

%Declare size of variables for speed
xi = zeros(length(t),length(lambda));
L = zeros(2,2,length(t),length(lambda));
b = zeros(length(t),1);
rjk_s = zeros(length(lambda),length(t));
rjk_p = zeros(length(lambda),length(t));
tjk_s = zeros(length(lambda),length(t));
tjk_p = zeros(length(lambda),length(t));
Ijk_s = zeros(2,2,length(t),length(lambda));
Ijk_p = zeros(2,2,length(t),length(lambda));
S_s = zeros(2,2,length(lambda));
S_p = zeros(2,2,length(lambda));
Reflection_s = zeros(length(lambda),1);
Reflection_p = zeros(length(lambda),1);
Transmission_s = zeros(length(lambda),1);
Transmission_p = zeros(length(lambda),1);
S_prime_s = zeros(2,2,length(t),length(lambda));
S_prime_p = zeros(2,2,length(t),length(lambda));
S_doubleprime_s = zeros(2,2,length(t),length(lambda));
S_doubleprime_p = zeros(2,2,length(t),length(lambda));
E_s = zeros(length(t),101,length(lambda));
E_p = zeros(length(t),101,length(lambda));
E_x = zeros(length(t),101,length(lambda));
E_y = zeros(length(t),101,length(lambda));
E_z = zeros(length(t),101,length(lambda));
Intensity = zeros(length(t),101,length(lambda));
Q = zeros(length(t),101,length(lambda));
rj_prime_s = zeros(length(t),length(lambda));
rj_prime_p = zeros(length(t),length(lambda));
rj_dp_s = zeros(length(t),length(lambda));
rj_dp_p = zeros(length(t),length(lambda));
tj_prime_s = zeros(length(t),length(lambda));
tj_prime_p = zeros(length(t),length(lambda));
tj_dp_s = zeros(length(t),length(lambda));
tj_dp_p = zeros(length(t),length(lambda));
```

```
rjminus_prime_s = zeros(length(t),length(lambda));
rjminus_prime_p = zeros(length(t),length(lambda));
tj_plus_s = zeros(length(t),length(lambda));
tj_plus_p = zeros(length(t),length(lambda));
tj_minus_s = zeros(length(t),length(lambda));
tj_minus_p = zeros(length(t),length(lambda));
Tj_s = zeros(length(t),length(lambda));
Tj_p = zeros(length(t),length(lambda));
Tj = zeros(length(t),length(lambda));
rho_dp_s = zeros(length(lambda),length(t));
rho_dp_p = zeros(length(lambda),length(t));
delta_dp_s = zeros(length(t),length(lambda));
delta_dp_p = zeros(length(t),length(lambda));

for l = 1:length(lambda)

for j=1:1:length(t)

xi(j,l) = ((2*pi)*q(j,l))/lambda(l);
L(:,:,j,l) = [exp(-1i*xi(j,l)*t(j)) 0; 0 exp(1i*xi(j,l)*t(j))];
b(j) = (1/Ld(j));

end

%Fresnel complex reflection and transmission coefficients and Interface
Matrix;
for j=1:1:(length(t)-1);

%TE
rjk_s(l,j)=((q(j,l)-q((j+1),l)))/(q(j,l)+q((j+1),l));
tjk_s(l,j)=(2*q(j,l))/(q(j,l)+q((j+1),l));

%TM
rjk_p(l,j)=(-
1*(n(j+1,l))^2*q(j,l)+n(j,l)^2*q((j+1),l))/((n(j+1,l))^2*q(j,l)+n(j,l)^2
*q((j+1),l));
tjk_p(l,j)=(2*n(j,l)*n(j+1,l)*q(j,l))/((n(j+1,l))^2*q(j,l)+n(j,l)^2*q((j
+1),l));

%Interface Matrix
Ijk_s(:,:,j,l)=(1/tjk_s(l,j))*[1 rjk_s(l,j); rjk_s(l,j) 1];
Ijk_p(:,:,j,l)=(1/tjk_p(l,j))*[1 rjk_p(l,j); rjk_p(l,j) 1];

if cond(Ijk_s(:,:,j,l)) > 1E10
Ijk_s(:,:,j,l) = Ijk_s(:,:,j,l) + eye(2)*1E-5;
end

if cond(Ijk_p(:,:,j,l)) > 1E10
Ijk_p(:,:,j,l) = Ijk_p(:,:,j,l) + eye(2)*1E-5;
end

end

%Finding S total
S_s(:,:,l)=[1 0;0 1];
S_p(:,:,l)=[1 0;0 1];
for j=1:1:(length(t)-2);

S_s(:,:,l)=S_s(:,:,l)*Ijk_s(:,:,j,l)*L(:,:,j+1,l);
S_p(:,:,l)=S_p(:,:,l)*Ijk_p(:,:,j,l)*L(:,:,j+1,l);

end
```

```
S_s(:,:,l)=S_s(:,:,l)*Ijk_s(:,:,size(t,2)-1,l);
S_p(:,:,l)=S_p(:,:,l)*Ijk_p(:,:,size(t,2)-1,l);

%Finding R and T of Stack
Reflection_s(l) = abs(S_s(2,1,l)/S_s(1,1,l)).^2;
Reflection_p(l) = abs(S_p(2,1,l)/S_p(1,1,l)).^2;
Transmission_s(l) =
(real(q(length(t),l))./real(q(1,l))).*abs(1/S_s(1,1,l)).^2;
Transmission_p(l) =
(real(q(length(t),l))./real(q(1,l))).*abs(1/S_p(1,1,l)).^2;

%Finding S prime and double prime going layer by layer
for j = 2:(length(t))-1

%Finding S prime and S double prime
S_prime_s(:,:,j,l) = eye(2,2);
S_prime_p(:,:,j,l) = eye(2,2);
S_doubleprime_s(:,:,j,l) = eye(2,2);
S_doubleprime_p(:,:,j,l) = eye(2,2);

for k=1:1:(j-2)
S_prime_s(:,:,j,l) = S_prime_s(:,:,j,l)*Ijk_s(:,:,k,l)*L(:,:,k+1,l);
S_prime_p(:,:,j,l) = S_prime_p(:,:,j,l)*Ijk_p(:,:,k,l)*L(:,:,k+1,l);
end
S_prime_s(:,:,j,l) = S_prime_s(:,:,j,l)*Ijk_s(:,:,j-1,l);
S_prime_p(:,:,j,l) = S_prime_p(:,:,j,l)*Ijk_p(:,:,j-1,l);

for k=j:1:(length(t)-2)
S_doubleprime_s(:,:,j,l) =
S_doubleprime_s(:,:,j,l)*Ijk_s(:,:,k,l)*L(:,:,k+1,l);
S_doubleprime_p(:,:,j,l) =
S_doubleprime_p(:,:,j,l)*Ijk_p(:,:,k,l)*L(:,:,k+1,l);
end
S_doubleprime_s(:,:,j,l) =
S_doubleprime_s(:,:,j,l)*Ijk_s(:,:,(length(t)-1),l);
S_doubleprime_p(:,:,j,l) =
S_doubleprime_p(:,:,j,l)*Ijk_p(:,:,(length(t)-1),l);

end


for j = 2:length(t)-1

rj_prime_s(j,l) = S_prime_s(2,1,j,l)/S_prime_s(1,1,j,l);
rj_prime_p(j,l) = S_prime_p(2,1,j,l)/S_prime_p(1,1,j,l);
tj_prime_s(j,l) = 1/S_prime_s(1,1,j,l);
tj_prime_p(j,l) = 1/S_prime_p(1,1,j,l);
rj_dp_s(j,l) = S_doubleprime_s(2,1,j,l)/S_doubleprime_s(1,1,j,l);
rj_dp_p(j,l) = S_doubleprime_p(2,1,j,l)/S_doubleprime_p(1,1,j,l);
tj_dp_s(j,l) = 1/S_doubleprime_s(1,1,j,l);
tj_dp_p(j,l) = 1/S_doubleprime_p(1,1,j,l);
costhetaj(j,l) = q(j,l)/n(j,l);

rjminus_prime_s(j,l) = -1*S_prime_s(1,2,j,l)/S_prime_s(1,1,j,l);
rjminus_prime_p(j,l) = -1*S_prime_p(1,2,j,l)/S_prime_p(1,1,j,l);
tj_plus_s(j,l) = tj_prime_s(j,l)/(1-
(rjminus_prime_s(j,l)*rj_dp_s(j,l)*exp(2*1i*xi(j,l)*t(j))));
tj_plus_p(j,l) = tj_prime_p(j,l)/(1-
(rjminus_prime_p(j,l)*rj_dp_p(j,l)*exp(2*1i*xi(j,l)*t(j))));
tj_minus_s(j,l) = tj_plus_s(j,l)*rj_dp_s(j,l)*exp(1i*2*xi(j,l)*t(j));
tj_minus_p(j,l) = tj_plus_p(j,l)*rj_dp_p(j,l)*exp(1i*2*xi(j,l)*t(j));
interim_s = abs(tj_plus_s(j,l)).^2;
```

```
interim_p = abs(tj_plus_p(j,l)).^2;
Tj_s(j,l) = (real(q(j,l))/real(q(1,l)))*interim_s;
Tj_p(j,l) = (real(q(j,l))/real(q(1,l)))*interim_p;
rho_dp_s(j,l) = abs(S_doubleprime_s(2,1,j,l)/S_doubleprime_s(1,1,j,l));
rho_dp_p(j,l) = abs(S_doubleprime_p(2,1,j,l)/S_doubleprime_p(1,1,j,l));
delta_dp_s(j,l) =
angle(S_doubleprime_s(2,1,j,l)/S_doubleprime_s(1,1,j,l));
delta_dp_p(j,l) =
angle(S_doubleprime_p(2,1,j,l)/S_doubleprime_p(1,1,j,l));

for k = 1:1:101;

% Normalized Field profile (JAP Vol 86 p.487 Eq 20)
E_s(j,k,l) = ((S_doubleprime_s(1,1,j,l)*exp(-1i*xi(j,l)*(t(j)-
x(j,k)))+S_doubleprime_s(2,1,j,l)*exp(1i*xi(j,l)*(t(j)-
x(j,k))))/(S_prime_s(1,1,j,l)*S_doubleprime_s(1,1,j,l)*exp(-
1i*xi(j,l)*t(j))+S_prime_s(1,2,j,l)*S_doubleprime_s(2,1,j,l)*exp(1i*xi(j
,l)*t(j))));
E_p(j,k,l) = ((S_doubleprime_p(1,1,j,l)*exp(-1i*xi(j,l)*(t(j)-
x(j,k)))+S_doubleprime_p(2,1,j,l)*exp(1i*xi(j,l)*(t(j)-
x(j,k))))/(S_prime_p(1,1,j,l)*S_doubleprime_p(1,1,j,l)*exp(-
1i*xi(j,l)*t(j))+S_prime_p(1,2,j,l)*S_doubleprime_p(2,1,j,l)*exp(1i*xi(j
,l)*t(j))));

% Normalized Field profile (Pandey and Lunt)
E_z(j,k,l) =
(1/sqrt(cos(phi)))*(tj_plus_s(j,l)*exp(1i*xi(j,l)*x(j,k))+tj_minus_s(j,l
)*exp(-1i*xi(j,l)*x(j,k)));
E_y(j,k,l) =
(costhetaj(j,l)/sqrt(cos(phi)))*(tj_plus_p(j,l)*exp(1i*xi(j,l)*x(j,k))+t
j_minus_p(j,l)*exp(-1i*xi(j,l)*x(j,k)));
E_x(j,k,l) = (n(1,l)*sin(phi)/(n(j,l)*sqrt(cos(phi))))*(-
tj_plus_p(j,l)*exp(1i*xi(j,l)*x(j,k))+tj_minus_p(j,l)*exp(-
1i*xi(j,l)*x(j,k)));

Intensity(j,k,l) = fraction*(E_s(j,k,l)*conj(E_s(j,k,l)))+(1-
fraction)*(E_p(j,k,l)*conj(E_p(j,k,l)));
%Intensity(j,k,l) = fraction*(E_z(j,k,l)*conj(E_z(j,k,l)))+(1-
fraction)*((E_x(j,k,l)*conj(E_x(j,k,l)))+(E_y(j,k,l)*conj(E_y(j,k,l))));

% Time average of the energy dissipated per second in layer j
%Q(j,k,l) =
E0T(l)^2*.5*c*epsilon_0*alpha(j,l)*real(n(j,l))*(Intensity(j,k,l));
Q(j,k,l) = E0T(l)^2*alpha(j,l)*Tj_s(j,l)*(exp(-
1*alpha(j,l)*x(j,k))+rho_dp_s(j,l)^2*exp(-1*alpha(j,l)*(2*t(j)-
x(j,k)))+2*rho_dp_s(j,l)*exp(-
1*alpha(j,l)*t(j))*cos(4*pi*real(n(j,l))*(t(j)-
x(j,k))/lambda(l)+delta_dp_s(j,l)));
%Q(j,k,l) =
E0T(l)^2*.5*c*epsilon_0*alpha(j,l)*real((n(j,l))/real(n(1,l)))*(fraction
*(E_s(j,k,l)*conj(E_s(j,k,l)))+(1-
fraction)*(E_p(j,k,l)*conj(E_p(j,k,l))));

%Total Tj
Tj(j,l) = fraction*Tj_s(j,l)+(1-fraction)*Tj_p(j,l);

end

end

end
end
```

H. Analytical exciton diffusion simulation code

The following Matlab code is used to analytically solve the one-dimensional exciton diffusion equation for various boundary conditions. The expressions in the following code are reproduced, in part, from Pettersson *et. al.* The function requires inputs for the wavelength(s), layer thicknesses, complex indices of refraction, layer discretization, absorption coefficients, partial transfer matrices, boundary conditions, and exciton diffusion coefficients. The function outputs the photocurrent generated in the layer structure and the computed exciton density profiles.

```
function [J_photo,exden] =
AnalyticalModel(lambda,t,n,x,alpha,b,I0T,S_prime_s,S_doubleprime_s,xi,h,
c,cases,D,qe,Tj)

%Preallocate variables for speed
rho_dp = zeros(length(t),length(lambda));
delta_dp = zeros(length(t),length(lambda));
C1 = zeros(length(t),length(lambda));
C2 = zeros(length(t),length(lambda));
rj_prime = zeros(length(t),length(lambda));
tj_prime = zeros(length(t),length(lambda));
rj_dp = zeros(length(t),length(lambda));
tj_dp = zeros(length(t),length(lambda));
rjminus_prime = zeros(length(t),length(lambda));
tj_plus = zeros(length(t),length(lambda));
N = zeros(length(lambda),1);
EVA = zeros(length(t),length(lambda));
EVB = zeros(length(t),length(lambda));
Jphotox0 = zeros(length(t),length(lambda));
Jphotoxd = zeros(length(t),length(lambda));
J_photo = zeros(length(t),length(lambda));
exden = zeros(length(t),101,length(lambda));

for l = 1:length(lambda)

for j = 2:(length(t)-1)

%Finding C1, C2, EVA, and EVB (Petterson 29-32)
%This function assume light is s polarized (TE)
rho_dp(j,l) = abs(S_doubleprime_s(2,1,j,l)/S_doubleprime_s(1,1,j,l));
delta_dp(j,l) =
angle(S_doubleprime_s(2,1,j,l)/S_doubleprime_s(1,1,j,l));
C1(j,l) = (rho_dp(j,l)^2)*exp(-2*alpha(j,l)*t(j));
C2(j,l) = (((b(j)^2)-(alpha(j,l)^2))*2*rho_dp(j,l)*exp(-
1*alpha(j,l)*t(j)))/(b(j)^2+(4*pi*real(n(j,l))/(lambda(l)))^2);

rj_prime(j,l) = S_prime_s(2,1,j,l)/S_prime_s(1,1,j,l);
tj_prime(j,l) = 1/S_prime_s(1,1,j,l);
rj_dp(j,l) = S_doubleprime_s(2,1,j,l)/S_doubleprime_s(1,1,j,l);
tj_dp(j,l) = 1/S_doubleprime_s(1,1,j,l);
```

```
rjminus_prime(j,l) = -1*S_prime_s(1,2,j,l)/S_prime_s(1,1,j,l);
tj_plus(j,l) = tj_prime(j,l)/(1-
(rjminus_prime(j,l)*rj_dp(j,l)*exp(2*1i*xi(j,l)*t(j))));
N(l) = I0T(l)/(h*c/lambda(l));

%Finding Photocurrents

theta = 0;

%Disoc left, Disoc right
if cases(j) == 1

EVA(j,l) = ((exp(b(j)*t(j))-exp(-
1*alpha(j,l)*t(j)))+C1(j,l)*(exp(b(j)*t(j))-
exp(alpha(j,l)*t(j)))+C2(j,l)*(exp(b(j)*t(j))*cos(4*pi*real(n(j,l))*t(j)
/(lambda(l))+delta_dp(j,l))-cos(delta_dp(j,l))))/(exp(-b(j)*t(j))-
exp(b(j)*t(j)));
EVB(j,l) = -((exp(-b(j)*t(j))-exp(-alpha(j,l)*t(j)))+C1(j,l)*(exp(-
b(j)*t(j))-exp(alpha(j,l)*t(j)))+C2(j,l)*(exp(-
b(j)*t(j))*cos(4*pi*real(n(j,l))*t(j)/(lambda(l))+delta_dp(j,l))-
cos(delta_dp(j,l))))/(exp(-b(j)*t(j))-exp(b(j)*t(j)));

Jphotox0(j,l) = qe*alpha(j,l)*Tj(j,l)*N(l)*(-
b(j)*EVA(j,l)+b(j)*EVB(j,l)-
alpha(j,l)+alpha(j,l)*C1(j,l)+4*pi*real(n(j,l))*C2(j,l)*sin(4*pi*real(n(
j,l))*t(j)/lambda(l)+delta_dp(j,l))/lambda(l))/(b(j)^2-alpha(j,l)^2);
Jphotoxd(j,l) = qe*alpha(j,l)*Tj(j,l)*N(l)*(b(j)*EVA(j,l)*exp(-
b(j)*t(j))-b(j)*EVB(j,l)*exp(b(j)*t(j))+alpha(j,l)*exp(-
alpha(j,l)*t(j))-alpha(j,l)*C1(j,l)*exp(alpha(j,l)*t(j))-
4*pi*real(n(j,l))*C2(j,l)*sin(delta_dp(j,l))/lambda(l))/(b(j)^2-
alpha(j,l)^2);

J_photo(j,l) = J_photo(j,l) + Jphotox0(j,l);
J_photo(j,l) = J_photo(j,l) + Jphotoxd(j,l);
theta = 1;

end

%Non-Disoc right, Disoc left
if cases(j) == 2

EVA(j,l) = ((-alpha(j,l)*exp(-alpha(j,l)*t(j))-
b(j)*exp(b(j)*t(j)))+C1(j,l)*(alpha(j,l)*exp(alpha(j,l)*t(j))-
b(j)*exp(b(j)*t(j)))+C2(j,l)*(4*pi*real(n(j,l))*sin(delta_dp(j,l))/(lamb
da(l))-
b(j)*exp(b(j)*t(j))*cos(4*pi*real(n(j,l))*t(j)/(lambda(l))+delta_dp(j,l)
)))/(b(j)*(exp(b(j)*t(j))+exp(-b(j)*t(j))));
EVB(j,l) = -((-alpha(j,l)*exp(-alpha(j,l)*t(j))+b(j)*exp(-
b(j)*t(j)))+C1(j,l)*(alpha(j,l)*exp(alpha(j,l)*t(j))+b(j)*exp(-
b(j)*t(j)))+C2(j,l)*(4*pi*real(n(j,l))*sin(delta_dp(j,l))/(lambda(l))+b(
j)*exp(-
b(j)*t(j))*cos(4*pi*real(n(j,l))*t(j)/(lambda(l))+delta_dp(j,l))))/(b(j)
*(exp(b(j)*t(j))+exp(-b(j)*t(j))));

Jphotox0(j,l) = qe*alpha(j,l)*Tj(j,l)*N(l)*(-
b(j)*EVA(j,l)+b(j)*EVB(j,l)-
alpha(j,l)+alpha(j,l)*C1(j,l)+4*pi*real(n(j,l))*C2(j,l)*sin(4*pi*real(n(
j,l))*t(j)/lambda(l)+delta_dp(j,l))/lambda(l))/(b(j)^2-alpha(j,l)^2);

J_photo(j,l) = J_photo(j,l) + Jphotox0(j,l);
theta = 1;
```

```
end

%Disoc right, Non-Disoc left
if cases(j) == 3

EVA(j,l) = ((-alpha(j,l)*exp(b(j)*t(j))-b(j)*exp(-
alpha(j,l)*t(j)))+C1(j,l)*(alpha(j,l)*exp(b(j)*t(j))-
b(j)*exp(alpha(j,l)*t(j)))+C2(j,l)*(-
b(j)*cos(delta_dp(j,l))+(4*pi*real(n(j,l))*exp(b(j)*t(j))*sin(4*pi*real(
n(j,l))*t(j)/(lambda(l))+delta_dp(j,l))/(lambda(l)))))/(b(j)*(exp(b(j)*t
(j))+exp(-b(j)*t(j))));
EVB(j,l) = ((alpha(j,l)*exp(-b(j)*t(j))-b(j)*exp(-alpha(j,l)*t(j)))-
C1(j,l)*(alpha(j,l)*exp(-b(j)*t(j))+b(j)*exp(alpha(j,l)*t(j)))-
C2(j,l)*(b(j)*cos(delta_dp(j,l))+(4*pi*real(n(j,l))*exp(-
b(j)*t(j))*sin(4*pi*real(n(j,l))*t(j)/(lambda(l))+delta_dp(j,l))/(lambda
(l)))))/(b(j)*(exp(b(j)*t(j))+exp(-b(j)*t(j))));

Jphotoxd(j,l) = qe*alpha(j,l)*Tj(j,l)*N(l)*(b(j)*EVA(j,l)*exp(-
b(j)*t(j))-b(j)*EVB(j,l)*exp(b(j)*t(j))+alpha(j,l)*exp(-
alpha(j,l)*t(j))-alpha(j,l)*C1(j,l)*exp(alpha(j,l)*t(j))-
4*pi*real(n(j,l))*C2(j,l)*sin(delta_dp(j,l))/lambda(l))/(b(j)^2-
alpha(j,l)^2);

J_photo(j,l) = J_photo(j,l) + Jphotoxd(j,l);
theta = 1;

end

%Finding Exciton Density
for k = 1:1:101;
exden(j,k,l) = theta*alpha(j,l)*Tj(j,l)*N(l)*(EVA(j,l)*exp(-
b(j)*x(j,k))+EVB(j,l)*exp(b(j)*x(j,k))+exp(-
1*alpha(j,l)*x(j,k))+C1(j,l)*exp(alpha(j,l)*x(j,k))+C2(j,l)*cos(4*pi*rea
l(n(j,l))*(t(j)-x(j,k))/lambda(l)+delta_dp(j,l)))/(D(j)*(b(j)^2-
(alpha(j,l))^2));
end


end

end

J_photo = real(J_photo);

%end
```

I. Numerical exciton diffusion simulation code

The following Matlab code describes the function utilized to numerically solved the one-dimensional exciton diffusion equation. Numerical solutions were computed using a central difference method. The advantage of the numerical solution is that it can account for long-rang energy transfer to a quenching layer and can handle both TE and TM polarized light. The function requires inputs for the layer thicknesses, layer discretization, wavelength(s), boundary conditions, diffusion coefficients, optical power absorbed, Förster radii, and molecular densities. The function outputs the photocurrent for the layer structure and the computed exciton density profiles.

```
function [J,exden,M] =
NumericalModel(t,x,lambda,cases,D,Q,h,nu,Ld,qe,R0,MD)

%Determine stepsize for each layer
step = zeros(length(t));
for j = 1:length(t)
step(j) = x(j,2)-x(j,1);
end

C = zeros(length(t),101,length(lambda));
M = zeros(101,101,length(t),length(lambda));
exden = zeros(length(t),101,length(lambda));
J = zeros(length(t),length(lambda));
for l = 1:length(lambda)

for j = 2:length(t)-1

for k = 1:101

%C matrix in Mn=C (Units of (1/m^3))
C(j,k,l) = (-((step(j)^2)/(D(j)*h*nu(l)))*Q(j,k,l));

end

end

%Determine M Matrices
for j = 2:length(t)-1

%No Quenching
if cases(j) == 4

M(:,:,j,l) = diag(ones(101,1)*(-(2+(step(j)^2)/(Ld(j)^2)))) +
diag(ones(100,1)*1,1) + diag(ones(100,1)*1,-1);
M(1,2,j,l)=2;
M(101,100,j,l)=2;
```

```
Csolve = C(j,:,l)';
exden(j,:,l) = linsolve(M(:,:,j,l),Csolve);

end

%Quenching on both sides
if cases(j) == 1

M(:,:,j,l) = diag(ones(101,1)*(-(2+(step(j)^2)/(Ld(j)^2)))) +
diag(ones(100,1)*1,1) + diag(ones(100,1)*1,-1);
M(1,1,j,l) = 1;
M(1,2,j,l) = 0;
M(2,1,j,l) = 0;
M(101,101,j,l) = 1;
M(101,100,j,l) = 0;
M(100,101,j,l) = 0;
C(j,1,l) = 0;
C(j,101,l) = 0;

Csolve = C(j,:,l)';
exden(j,:,l) = linsolve(M(:,:,j,l),Csolve)';

J(j,l) = D(j)*(exden(j,2,l)-exden(j,1,l))*qe/step(j);
J(j,l) = D(j)*(exden(j,100,l)-exden(j,101,l))*qe/step(j)+J(j,l);

end

%Quenching on left side
if cases(j) == 2

M(:,:,j,l) = diag(ones(101,1)*(-(2+(step(j)^2)/(Ld(j)^2)))) +
diag(ones(100,1)*1,1) + diag(ones(100,1)*1,-1);
M(101,100,j,l)=2;
M(1,1,j,l) = 1;
M(1,2,j,l) = 0;
M(2,1,j,l) = 0;
C(j,1,l) = 0;

Csolve = C(j,:,l)';
exden(j,:,l) = linsolve(M(:,:,j,l),Csolve);

J(j,l) = D(j)*(exden(j,2,l)-exden(j,1,l))*qe/step(j);

end

%Quenching on right side
if cases(j) == 3

M(:,:,j,l) = diag(ones(101,1)*(-(2+(step(j)^2)/(Ld(j)^2)))) +
diag(ones(100,1)*1,1) + diag(ones(100,1)*1,-1);
M(1,2,j,l)=2;
M(101,101,j,l) = 1;
M(101,100,j,l) = 0;
M(100,101,j,l) = 0;
C(j,101,l) = 0;

Csolve = C(j,:,l)';
exden(j,:,l) = linsolve(M(:,:,j,l),Csolve);

J(j,l) = D(j)*(exden(j,100,l)-exden(j,101,l))*qe/step(j);
```

```
end

%Quenching on left side with Forster Energy transfer outgoing
if cases(j) == 5

M(:,:,j,l) = diag(ones(101,1)) + diag(ones(100,1)*1,1) +
diag(ones(100,1)*1,-1);
for z = 1:101
M(z,z,j,l) = (-(2+((step(j)^2)/(Ld(j)^2))*(1+(pi*MD(j-
1)*(R0(j))^6)/(6*(x(j,z))^3))));
end
M(1,1,j,l) = (-(2+((step(j)^2)/(Ld(j)^2))*(1+(pi*MD(j-
1)*(R0(j))^6)/(6*(0.0000000000001)^3))));
M(101,100,j,l)=2;
M(1,1,j,l) = 1;
M(1,2,j,l) = 0;
M(2,1,j,l) = 0;
C(j,1,l) = 0;

Csolve = C(j,:,l)';
exden(j,:,l) = linsolve(M(:,:,j,l),Csolve);

end

%Quenching on right side with Forster energy transfer outgoing
if cases(j) == 6

M(:,:,j,l) = diag(ones(101,1)) + diag(ones(100,1)*1,1) +
diag(ones(100,1)*1,-1);
for z = 1:101
zb = 102 - z;
M(z,z,j,l) = (-
(2+((step(j)^2)/(Ld(j)^2))*(1+(pi*MD(j+1)*(R0(j))^6)/(6*(x(j,zb))^3))));
end
M(101,101,j,l) = (-
(2+((step(j)^2)/(Ld(j)^2))*(1+(pi*MD(j+1)*(R0(j))^6)/(6*(0.0000000000001
)^3))));
M(1,2,j,l)=2;
M(101,101,j,l) = 1;
M(101,100,j,l) = 0;
M(100,101,j,l) = 0;
C(j,101,l) = 0;

Csolve = C(j,:,l)';
exden(j,:,l) = linsolve(M(:,:,j,l),Csolve);

end

%No quenching with Forster energy transfer outgoing on right side
if cases(j) == 7

M(:,:,j,l) = diag(ones(101,1)) + diag(ones(100,1)*1,1) +
diag(ones(100,1)*1,-1);
for z = 1:101
zb = 102 - z;
M(z,z,j,l) = (-
(2+((step(j)^2)/(Ld(j)^2))*(1+(pi*MD(j+1)*(R0(j))^6)/(6*(x(j,zb)+guess*1
e-9)^3))));
end
M(101,101,j,l) = (-
(2+((step(j)^2)/(Ld(j)^2))*(1+(pi*MD(j+1)*(R0(j))^6)/(6*(guess*1e-
9)^3))));
```

```
M(1,2,j,l)=2;
M(101,100,j,l)=2;

Csolve = C(j,:,l)';
exden(j,:,l) = linsolve(M(:,:,j,l),Csolve);

end

end

end

end
```

J. Kinetic Monte Carlo exciton diffusion simulation

The following strategy was used to simulate exciton diffusion for organic photovoltaic cells (OPVs) incorporating an exciton permeable interface in the donor layer. It does this by utilizing a Kinetic Monte Carlo approach to simulate exciton transport as dictated by local rates at each location (bin) in the donor layer. A flowchart depicting the relevant order of operations is shown below. The simulation operates by identifying the relevant rates of absorption, decay, and energy transfer (Figure 13.2a). These rates are then weighted by the population in each bin. A random number generator and searching algorithm is used to select the bin and operation. The operation is then performed by updating the exciton density population for the bins affected. The weighted rates are then recalculated and this cycle can continue. In this section of code which simulates an exact device, the external quantum efficiency at a given wavelength is tabulated after a given number of cycles. When the change in external quantum efficiency is below a target level, the system is declared to have reach steady state and the function output all relevant tabulated quantities. The spirit of this Kinetic Monte Carlo approach can be modified to incorporate many interfaces. It is important to note that for determination of the mean-squared displacement versus time, the excitons should not be allowed to decay.

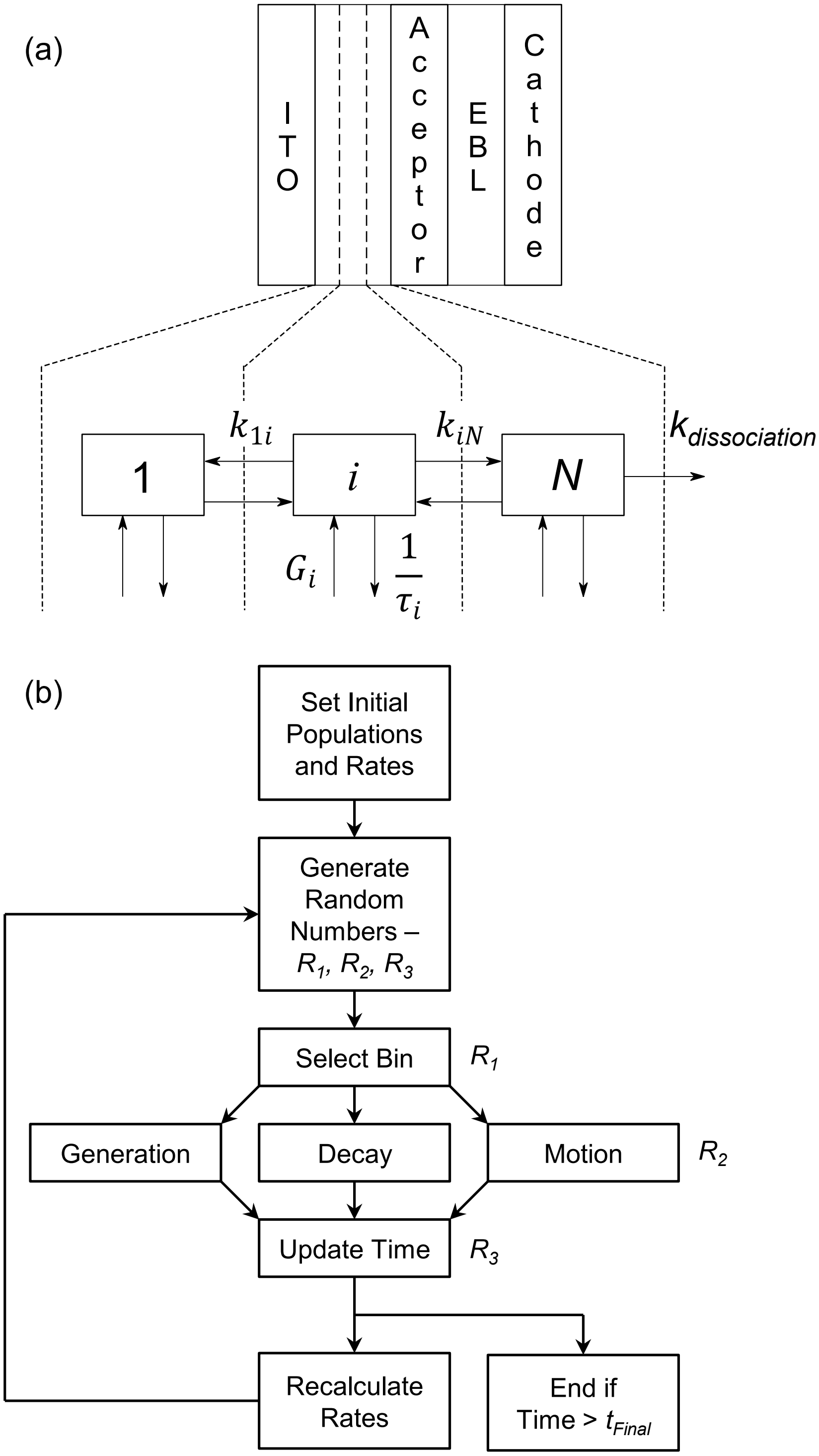

Figure 13.2 Schematic and flowchart for simulating exciton diffusion in a donor layer of an OPV utilizing Kinetic Monte Carlo.

To assess how quickly the KMC approach can approach steady-state behavior, the exciton flux at the dissociating interface can be modeled for a 20-nm-thick donor layer with an exciton diffusion length (L_D) of 10 nm (Figure 13.3). For a variety of initial bin populations, steady-state can be modeled after approximately 10^8 model iterations corresponding to 10^{-7} s, roughly 100 exciton lifetimes.

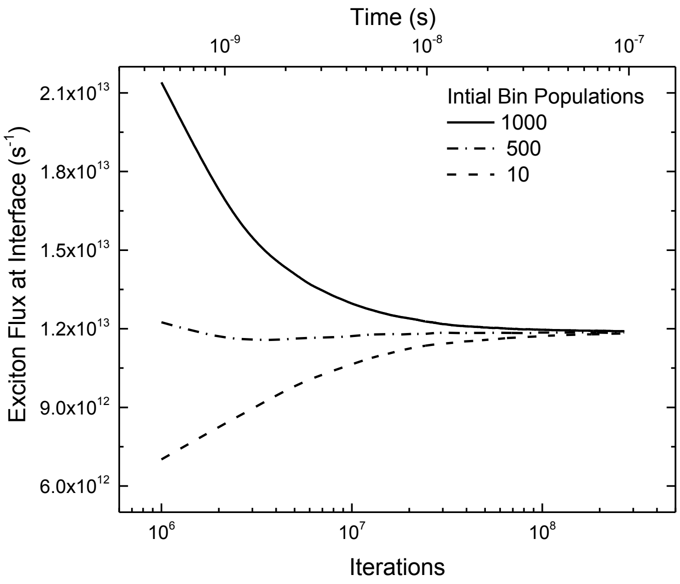

Figure 13.3 Exciton flux at the interface for a variety of initial conditions specifying the initial population within each bin.

Below is the C++ code used to model exciton diffusion for the dilute donor OPVs presented in Chapter 6. Beyond input of the L_D and lifetime for each layer, transfer matrix formalism is used to input the exact spatial dependence for exciton absorption/generation.

```
#include <fstream>
#include <iostream>
#include <sstream>
#include <string>
#include <vector>
#include <cmath>
#include "mtrand.h"
#include <iomanip>
using namespace std;

int main ()
{
double EQE[1];
```

```
double etaD[1];
double etaA[1];
for (int wavelengthloop = 0; wavelengthloop<1; wavelengthloop++)
{

clock_t tStart = clock();

////////////////////////////////////////////////////////////////////////////////////////////
////////////////////////////////////////////////////////////////////////////////////////////
////////////////////////////////////////////////////////////////////////////////////////////

double binthickness1 = 1;
double binthickness2 = 1;

double material1 = 8;
double material2 = 5;

double lifetime1 = 0.7907E-9;
double lifetime2 = .48E-9;

double kF1 = 234E9;
double kF2 = 234E9;

double kF12 = 234E9;//(9.1*1.434/1.167)*1E9;
double kF21 = 234E9;//(4.5*1.167/1.434)*1E9;

double kFnoneTrig = 0;

double R01_A = 0; //Currently R0 to second donor layer
//double R02_A = 0;

double MD_A = 1.44;

double goaltime = 1E-7;
double group = 1;

double absfactor1 = 0;
double absfactor2 = 1;

//For use when computing single wavelength EQE
double sunfactor[1];
sunfactor[0] = 1.37;

int nloadopt = 0;

double waves[1];
waves[0] = 590;

////////////////////////////////////////////////////////////////////////////////////////////
////////////////////////////////////////////////////////////////////////////////////////////
////////////////////////////////////////////////////////////////////////////////////////////
```

```
double *x;
double *Q;

//Load Q file
ifstream fp_in;
string lineHold;
int length=0;
int count=0;

fp_in.open("/Users/smenke2/Documents/University of Minnesota/Data/Monte
Carlo/Code/Q Values/Dilute 50/Q_dilute_50_590.txt");

while(fp_in.good()!=0)

{
getline(fp_in, lineHold);
length++;
}
length--;

//Return to the beginning of the input file stream
fp_in.clear();
fp_in.seekg(0);

x = new double[length+1];
Q = new double[length+1];

while(fp_in.good()!=0)
{
fp_in >> x[count];
fp_in >> Q[count];
count++;
}

fp_in.close();

///////////////////////////////////////////////////////////////////////////////////////////
///////////////////////////////////////////////////////////////////////////////////////////
///////////////////////////////////////////////////////////////////////////////////////////

double pi=3.14159;
double devicearea = pow(0.5E-3,2)*pi;

double materialtotal = material1 + material2;

const int numbins1 = floor(material1/binthickness1);
const int numbins2 = floor(material2/binthickness2);
const int numbins = numbins1 + numbins2;

cout << numbins1 << "     " << numbins2 << endl;
```

```
MTRand_closed mt(time(NULL));

//////////////////////////////////////////////////////////////////////////////////////////////////////////
//////////////////////////////////////////////////////////////////////////////////////////////////////////
//////////////////////////////////////////////////////////////////////////////////////////////////////////

//Fill binx

double binx[numbins+1];
for(int i = numbins; i>=(numbins-numbins2); i--)
{
binx[i] = materialtotal-binthickness2*(numbins-i);
}

binx[numbins-numbins2-1] = binx[numbins-numbins2]-(binthickness1+binthickness2)/2;

for(int i = numbins1-2; i>=0; i--)
{
binx[i] = binx[i+1] - binthickness1;
}

//////////////////////////////////////////////////////////////////////////////////////////////////////////
//////////////////////////////////////////////////////////////////////////////////////////////////////////
//////////////////////////////////////////////////////////////////////////////////////////////////////////

double data[6][numbins+1];

//Fill G from Q
for(int i = 0; i<=numbins1-1; i++)
{
int j = 0;
while(x[j]<binx[i])
{
j++;
}
data[0][i] = absfactor1*Q[j]*devicearea*binthickness1*1e-9;
//        data[0][i] = 1E9;
}

for(int i = numbins1; i<=numbins-1; i++)
{
int j = 0;
while(x[j]<binx[i])
{
j++;
}
data[0][i] = absfactor2*Q[j]*devicearea*binthickness2*1e-9;
//        data[0][i] = 1E9;
}
```

```
data[0][numbins] = 0;

//Fill L
for(int i = 0; i<=numbins1-1; i++)
{
data[1][i] = 1/lifetime1;
}

for(int i = numbins1; i<=numbins-1; i++)
{
data[1][i] = 1/lifetime2;
}

data[1][numbins] = 0;

//Fill kFs
for (int i = 0; i<=numbins1-2; i++)
{
data[2][i] = kF1;
data[3][i] = kF1;
data[4][i] = kFnoneTrig*kF1;
data[5][i] = (pow(R01_A,6)*MD_A*pi)/(lifetime1*6*pow((binx[numbins1]-binx[i]-
binthickness2/2),3));
}

data[2][numbins1-1] = kF12;
data[3][numbins1-1] = kF1;
data[4][numbins1-1] = kFnoneTrig*kF1;
data[5][numbins1-1] = (pow(R01_A,6)*MD_A*pi)/(lifetime1*6*pow((binx[numbins1]-
binx[numbins1-1]-binthickness2/2),3));

data[2][numbins1] = kF2;
data[3][numbins1] = kF21;
data[4][numbins1] = kFnoneTrig*kF2;
data[5][numbins1] = 0;//(pow(R02_A,6)*MD_A*pi)/(lifetime2*6*pow((binx[numbins]-
binx[numbins1]-binthickness2/2),3));

for (int i = numbins1+1; i<=numbins-1; i++)
{
data[2][i] = kF2;
data[3][i] = kF2;
data[4][i] = kFnoneTrig*kF2;
data[5][i] = 0;//(pow(R02_A,6)*MD_A*pi)/(lifetime2*6*pow((binx[numbins]-binx[i]-
binthickness2/2),3));
}

data[2][numbins] = 0.0;
//   data[2][numbins-1] = 0.0;
data[3][numbins] = 0.0;
data[3][0] = 0.0;
data[4][numbins] = 0.0;
```

```
data[5][numbins] = 0.0;

for(int i = 0; i <= 5; i++)
{
for(int j=0; j<=numbins; j++)
{
cout << setw(7) << setprecision(4) << scientific << data[i][j] << "\t";
}
cout << endl;
}

////////////////////////////////////////////////////////////////////////////////////////
////////////////////////////////////////////////////////////////////////////////////////
////////////////////////////////////////////////////////////////////////////////////////

//Intitalize n
double n[numbins+1];

if (nloadopt == 1)
{

fp_in.open("/Users/smenke2/Documents/University of Minnesota/Data/Monte
Carlo/Code/Monte Carlo/ExDen.txt");
length = 0;
while(fp_in.good()!=0)

{
getline(fp_in, lineHold);
length++;
}
length--;

//Return to the beginning of the input file stream
fp_in.clear();
fp_in.seekg(0);

double *nload = new double[length+1];

count = 0;
while(fp_in.good()!=0)
{
fp_in >> nload[count];
count++;
}

fp_in.close();

//Initalize n
for (int i=0; i<=numbins-1; i++)
{
n[i] = nload[i];
```

```
}
n[numbins] = 0;
}

if (nloadopt == 0)
{
//Initalize n
for (int i=0; i<=numbins-1; i++)
{
n[i] = 100;
}
n[numbins] = 0;
}

////////////////////////////////////////////////////////////////////////////////////////////
////////////////////////////////////////////////////////////////////////////////////////////
////////////////////////////////////////////////////////////////////////////////////////////

// Begin Iterations
int stable = 0;
double EQEcheck = 0.00001;
EQE[wavelengthloop] = 0;
double timer = 0;
double dataprob[6][numbins+1];
double cumsumdown[6][numbins+1];
double cumsumacross[numbins+1];
double random1, random2;
int k, o;
double counterdisoc = 0, countergen = 0;
int iterations = 0, iterationsloop = 0;
double disocrate[2001][3];

while (stable == 0)
{

double countero[6];
for(int i = 0; i<=6; i++)
{
countero[i] = 0;
}
double counterk[numbins];
for(int i = 0; i<=numbins; i++)
{
counterk[i] = 0;
}

//Update data to dataprob
for(int i = 0; i<=numbins; i++)
{
dataprob[0][i] = data[0][i];
}
```

```
for (int i = 1; i<=5; i++)
{
for(int j = 0; j<= numbins; j++)
{
dataprob[i][j] = n[j]*data[i][j];
}
}

//Calculate Cumulative Sums across bins
{
cumsumdown[0][0] = dataprob[0][0];
for (int j = 1; j<=5; j++)
{
cumsumdown[j][0] = dataprob[j][0]+cumsumdown[j-1][0];
}
cumsumacross[0] = cumsumdown[5][0];
}

for (int i = 1; i<=numbins; i++)
{
cumsumdown[0][i] = dataprob[0][i];
for (int j = 1; j<=5; j++)
{
cumsumdown[j][i] = dataprob[j][i]+cumsumdown[j-1][i];
}
cumsumacross[i] = cumsumdown[5][i]+cumsumacross[i-1];
}

//Begin Iterations
while (timer < goaltime)
{

//Generate First Random Number to choose bin
random1 = mt()*cumsumacross[numbins];
k = 0;
while (random1>cumsumacross[k])
{
k++;
}

//Generate Second Random Number to choose operation
random2 = mt()*cumsumdown[5][k];
o = 0;
while (random2>cumsumdown[o][k])
{
o++;
}

countero[o]++;
counterk[k]++;
```

```
if (o==0)
{
n[k] = n[k] + group;
countergen = countergen + group;
}

if (o==1)
{
n[k] = n[k] - group;
}

if (o==2)
{
n[k] = n[k] - group;
n[k+1] = n[k+1] + group;
if (k == numbins-1)
{
counterdisoc = counterdisoc + group;
}
}

if (o==3)
{
n[k] = n[k] - group;
n[k-1] = n[k-1] + group;
}

if (o==5)
{
n[k] = n[k] - group;
n[numbins1] = n[numbins1] + group;
//counterdisoc = counterdisoc + group;
}

//      if (n[k]==0)
//      {
//          cout << "Ran out of Excitons!" << endl;
//          return 0;
//      }

//Delete excitons is last bin
n[numbins] = 0;

//Determine Timestep
timer = timer - log(mt())/cumsumacross[numbins];

//Update dataprob, cumsumdown, and cumsum across

for(int j = 1; j<=5; j++)
{
dataprob[j][k] = n[k]*data[j][k];
```

```
cumsumdown[j][k]=dataprob[j][k]+cumsumdown[j-1][k];
}

if( o == 2)
{
for (int j = 1; j<=5; j++)
{
dataprob[j][k+1] = n[k+1]*data[j][k+1];
cumsumdown[j][k+1] = dataprob[j][k+1]+cumsumdown[j-1][k+1];
}
}

if( o == 3)
{
for (int j = 1; j<=5; j++)
{
dataprob[j][k-1] = n[k-1]*data[j][k-1];
cumsumdown[j][k-1] = dataprob[j][k-1]+cumsumdown[j-1][k-1];
}
}

cumsumacross[0] = cumsumdown[5][0];
for (int i = 1; i<=numbins; i++)
{
cumsumacross[i] = cumsumdown[5][i]+cumsumacross[i-1];
}

//If statement for recording vector of disocciation rate and iterations and timer
if( iterations == 1000000)
{
disocrate[iterationsloop][0] = (iterationsloop+1)*1000000;
disocrate[iterationsloop][1] = timer;
disocrate[iterationsloop][2] = counterdisoc/timer;
iterations = 0;
iterationsloop = iterationsloop + 1;
}
else
{
iterations = iterations + 1;
}

if( iterationsloop > 2000)
{
cout << "disocrate variable not long enrough" << endl;
return 0;
}

}
```

```
EQE[wavelengthloop] =
100*counterdisoc/(sunfactor[wavelengthloop]*devicearea*timer/(6.626E-
34*3E8/(waves[wavelengthloop]*1E-9)));
cout << EQE[wavelengthloop] << endl;
if (pow(pow(EQE[wavelengthloop]-EQEcheck,2),.5) < .1)
{
stable = 1;
}
else
{
EQEcheck = EQE[wavelengthloop];
iterations = 0;
iterationsloop = 0;
timer = 0;
counterdisoc = 0;
countergen = 0;
}

}

double current;
current = counterdisoc*1.6e-19/timer/devicearea/10;
EQE[wavelengthloop] =
100*counterdisoc/(sunfactor[wavelengthloop]*devicearea*timer/(6.626E-
34*3E8/(waves[wavelengthloop]*1E-9)));
cout << current << " mA/cm^2" << endl;
cout << "EQE = " << EQE[wavelengthloop] << " %" << endl;
cout << "Diffusion Efficiency = " << counterdisoc*100/countergen << " %" << endl;
cout << "Absorption Efficiency = " <<
countergen*100/(sunfactor[wavelengthloop]*devicearea*timer/(6.626E-
34*3E8/(waves[wavelengthloop]*1E-9))) << " %" << endl;
cout << counterdisoc << endl;
cout << countergen << endl;

etaD[wavelengthloop] = counterdisoc*100/countergen;
etaA[wavelengthloop] =
countergen*100/(sunfactor[wavelengthloop]*devicearea*timer/(6.626E-
34*3E8/(waves[wavelengthloop]*1E-9)));

printf("Time taken was %f seconds\n", (double)(clock() - tStart)/CLOCKS_PER_SEC);

//    stringstream ss (stringstream::in | stringstream::out);
//    ss << "/Users/smenke2/Documents/University of Minnesota/Data/Monte
Carlo/Code/Monte Carlo/ExDen.txt";
//    string str = ss.str();
//    ofstream f_out (str);
//
//      for (int i=0; i <= numbins; i++)
//    {
//        f_out << n[i] << endl;
//      }
```

```
//      f_out.close();
//
//    stringstream ss2 (stringstream::in | stringstream::out);
//    ss2 << "/Users/smenke2/Documents/University of Minnesota/Data/Monte
Carlo/Code/Monte Carlo/DisocRate.txt";
//    string str2 = ss2.str();
//    ofstream f_out2 (str2);
//
//      for (int i=0; i < iterationsloop; i++)
//    {
//        f_out2 << disocrate[i][0] << "\t" << disocrate[i][1] << "\t" << disocrate[i][2] << endl;
//      }
//      f_out2.close();

}

stringstream ss5 (stringstream::in | stringstream::out);
ss5 << "/Users/smenke2/Documents/University of Minnesota/Data/Monte
Carlo/Code/Monte Carlo/EQE.txt";
string str5 = ss5.str();
ofstream f_out3 (str5);

for (int i=0; i <=11; i++)
{
f_out3 << EQE[i] << "\t" << etaD[i] << "\t" << etaA[i] << endl;
}
f_out3.close();

return 0;

}
```

K. Kinetic Monte Claro temperature dependent exciton diffusion code

The following C++ code was used to simulate L_D as a function of temperature using a Kinetic Monte Carlo (KMC) algorithm. Similar to the previous section, KMC is used to simulate the diffusion of excitons along a 3D lattice with periodic boundary conditions. Upon decay, the final location of the exciton is stored and another exciton is launched. After a statistically significant number of excitons are launched, the program changes temperature, recalculates the nearest neighbor hopping rates, and repeats. Importantly, energetic disorder is accounted for by selecting site energies for each lattice point from a normal distribution of prescribed width.

```
#include <fstream>
#include <iostream>
#include <sstream>
#include <string>
#include <vector>
#include <cmath>
#include "mtrand.h"
#include <iomanip>
#include <random>
#include <ctime>
using namespace std;

double finaldistance[10000];
double finaltimes[10000];
double finalenergies[10000];

double intpow( double base, int exponent )
{
   int i;
   double out = base;
   for( i=1 ; i < exponent ; i++ )
   {
      out *= base;
   }
   return out;
}

int main(int argc, char *argv[])
{
   cout << "hello" << endl;
```

```
clock_t tStart = clock();

const int trialnum = 10000;
const int latticesize = 50;
double energy[51][51][51];

int xpos, xlat, xlatprime;
int ypos, ylat, ylatprime;
int zpos, zlat, zlatprime;

const int numnn = 10;

double e = 2.71;
double kb = 8.6E-5;
double T[] = {295, 270, 250, 230, 210, 190, 170, 150, 130, 110, 90, 78};
int lengthT = 12;
double tau[lengthT];
for (int i = 0; i<lengthT; i++)
{
    //tau[i] = 1;
    tau[i] = -.875576E-2*T[i]+3.183; // SubPc
    //tau[i] = -.0106*T[i]+4.574; // DCV3T
    //tau[i] = -.025*T[i]+23.375; // Alq3
    cout << tau[i] << " ";
}
cout << endl;

double lc = .5;
double Estart = 10;
double R0C = atof(argv[1]);
double EaR0 = atof(argv[2]);
double sigma = atof(argv[3]);

double R0[lengthT];
for (int i = 0; i<lengthT; i++)
{
    R0[i] = R0C*pow(e,-EaR0/6/kb/T[i]);
   cout << R0[i] << " ";
}
cout << endl;


////////////////////////////////////////////////////////////////////////////////////////////
////////////////////////////////////////////////////////////////////////////////////////////
////////////////////////////////////////////////////////////////////////////////////////////

MTRand_closed mt(time(NULL));
default_random_engine generator;
normal_distribution<double> distribution(0,sigma);

////////////////////////////////////////////////////////////////////////////////////////////
```

```
////////////////////////////////////////////////////////////////////////////
////////////////////////////////////////////////////////////////////////////

//Fill energy for each lattice point
//double energy[latticesize+1][latticesize+1][latticesize+1];

for (int i = 0; i<=latticesize; i++)
{
   for (int j = 0; j<=latticesize; j++)
   {
      for (int k = 0; k<=latticesize; k++)
      {
         energy[i][j][k] = distribution(generator);
      }
   }

}

////////////////////////////////////////////////////////////////////////////
////////////////////////////////////////////////////////////////////////////
////////////////////////////////////////////////////////////////////////////

double exciton;
double LDsum;
double LD[lengthT];
double data[numnn*2+1][numnn*2+1][numnn*2+1];
double predata[numnn*2+1][numnn*2+1][numnn*2+1];
double sumz[numnn*2+1];
double cumsumz[numnn*2+1];
double sumy[numnn*2+1];
double cumsumy[numnn*2+1];
double sumx[numnn*2+1];
double cumsumx[numnn*2+1];
double choice[2];
double randomchoice, randomz, randomy, randomx;
double timer;
int c, z, y, x;

//Loop over different Temperatures

for (int temps = 0; temps<lengthT; temps++)
{

   //Calculate nearest neighbor hopping rates for just lattice spacing
   for (int i = 0; i<=numnn*2; i++)
   {
      for (int j = 0; j<=numnn*2; j++)
      {
         for (int k = 0; k<=numnn*2; k++)
         {
```

```
                    predata[i][j][k] = intpow(R0[temps]/sqrt(lc*(-numnn+i)*lc*(-numnn+i)+lc*(-
numnn+j)*lc*(-numnn+j)+lc*(-numnn+k)*lc*(-numnn+k)),6);
                }
            }
        }
        predata[numnn][numnn][numnn] = 0;

        //Loop over number of trials

        for (int trials = 0; trials<trialnum; trials++)
        {
            //cout << trials << endl;

            finaldistance[trials] = 0;
            finaltimes[trials] = 0;

            exciton = 1;
            timer = 0;

            xlat = (mt()*40-20)+latticesize/2;
            ylat = (mt()*40-20)+latticesize/2;
            zlat = (mt()*40-20)+latticesize/2;
            while(energy[xlat][ylat][zlat] >= Estart)
            {
                xlat = (mt()*40-20)+latticesize/2;
                ylat = (mt()*40-20)+latticesize/2;
                zlat = (mt()*40-20)+latticesize/2;
            }
            xpos = 0;
            ypos = 0;
            zpos = 0;

            while (exciton == 1)
            {
                    while (xlat > latticesize)
                    {
                        xlat -= latticesize;
                    }
                    while (xlat < 0)
                    {
                        xlat += latticesize;
                    }
                    while (ylat > latticesize)
                    {
                        ylat -= latticesize;
                    }
                    while (ylat < 0)
                    {
                        ylat += latticesize;
                    }
                    while (zlat > latticesize)
```

```
                    {
                        zlat -= latticesize;
                    }
                    while (zlat < 0)
                    {
                        zlat += latticesize;
                    }

                //Calculate nearest neighbor hopping rates
                for (int i = 0; i<=numnn*2; i++)
                {
                    xlatprime = xlat+i-numnn;
                    while (xlatprime > latticesize)
                    {
                        xlatprime -= latticesize;
                    }
                    while (xlatprime < 0)
                    {
                        xlatprime += latticesize;
                    }

                    for (int j = 0; j<=numnn*2; j++)
                    {
                        ylatprime = ylat+j-numnn;
                        while (ylatprime > latticesize)
                        {
                            ylatprime -= latticesize;
                        }
                        while (ylatprime < 0)
                        {
                            ylatprime += latticesize;
                        }

                        for (int k = 0; k<=numnn*2; k++)
                        {

                            zlatprime = zlat+k-numnn;
                            while (zlatprime > latticesize)
                            {
                                zlatprime -= latticesize;
                            }
                            while (zlatprime < 0)
                            {
                                zlatprime += latticesize;
                            }

                            data[i][j][k]=predata[i][j][k]*exp((energy[xlat][ylat][zlat]-
energy[xlatprime][ylatprime][zlatprime])/kb/T[temps]);
                        }
                    }
                }
```

```
//Calculate Cumulative Sums across bins
for (int k = 0; k<=numnn*2; k++)
{
    sumz[k] = 0;
    for (int i = 0; i<=numnn*2; i++)
    {
        for (int j = 0; j<=numnn*2; j++)
        {
            sumz[k] += data[i][j][k];
        }
    }
}
partial_sum(sumz,sumz+(numnn*2+1),cumsumz);

//Decide energy transfer versus decay
choice[0] = cumsumz[numnn*2];
choice[1] = 1/tau[temps]+choice[0];
randomchoice = mt()*choice[1];
c = 0;
while(randomchoice > choice[c])
{
    c++;
}

//Calculate timestep
timer = timer + log(1/mt())/choice[1];

if(c==0)
{

    //Select z
    randomz = mt()*cumsumz[numnn*2];
    z = 0;
    while(randomz > cumsumz[z])
    {
        z++;
    }

    //Calculate Cumulative Sums for Selected Z
    for (int j = 0; j<=numnn*2; j++)
    {
        sumy[j] = 0;
        for (int i = 0; i<=numnn*2; i++)
        {
            sumy[j] += data[i][j][z];
        }
    }
    partial_sum(sumy,sumy+(numnn*2+1),cumsumy);

    //Select y
```

```
            randomy = mt()*cumsumy[numnn*2];
            y = 0;
            while(randomy > cumsumy[y])
            {
                y++;
            }

            //Calculate Cumulative Sums for Selected Z and Y
            for (int i = 0; i<=numnn*2; i++)
            {
                sumx[i] = data[i][y][z];
            }
            partial_sum(sumx,sumx+(numnn*2+1),cumsumx);

            //Select x
            randomx = mt()*cumsumx[numnn*2];
            x = 0;
            while(randomx > cumsumx[x])
            {
                x++;
            }

            //Update positions
            xpos += (x-numnn);
            ypos += (y-numnn);
            zpos += (z-numnn);
            xlat += (x-numnn);
            ylat += (y-numnn);
            zlat += (z-numnn);

        }

        if(c==1)
        {
            exciton = 0;
        }

    }

    finaldistance[trials] = sqrt((lc*xpos*lc*xpos)+(lc*ypos*lc*ypos)+(lc*zpos*lc*zpos));
    finaltimes[trials] = timer;
    finalenergies[trials] = energy[xlat][ylat][zlat];


}

//Calculate LD
LDsum = 0;
for (int i=0; i<trialnum; i++)
{
    LDsum = LDsum + finaldistance[i];
```

```
        }
        LD[temps] = LDsum/trialnum;
        cout << T[temps] << "K and " << LD[temps] << endl;

    }

    ////////////////////////////////////////////////////////////////////////////
    ////////////////////////////////////////////////////////////////////////////
    ////////////////////////////////////////////////////////////////////////////



//    stringstream ss (stringstream::in | stringstream::out);
//    ss << "/Users/smenke2/Documents/University of Minnesota/Data/Monte
Carlo/Code/Diffusion vs T/Data sigma_" <<sigma<< ".txt";
//    string str = ss.str();
//    ofstream f_out (str);
//
//    for (int i=0; i<trialnum; i++)
//    {
//        f_out << finaldistance[i] << "\t" << finaltimes[i] <<"\t" << finalenergies[i] << endl;
//    }
//    f_out.close();
//
//    stringstream ss1 (stringstream::in | stringstream::out);
//    ss1 << "/Users/smenke2/Documents/University of Minnesota/Data/Monte
Carlo/Code/Diffusion vs T/LD sigma_" <<sigma<< ".txt";
//    string str1 = ss1.str();
//    ofstream f_out1 (str1);
//
//    for (int i=0; i<lengthT; i++)
//    {
//        f_out1 << T[i] << "\t" << LD[i] << endl;
//    }
//    f_out1.close();

    printf("Time taken was %f seconds\n", (double)(clock() - tStart)/CLOCKS_PER_SEC);

    for (int i = 0; i<lengthT; i++)
    {
    cout << LD[i] << endl;
    }

    return 0;

}
```